

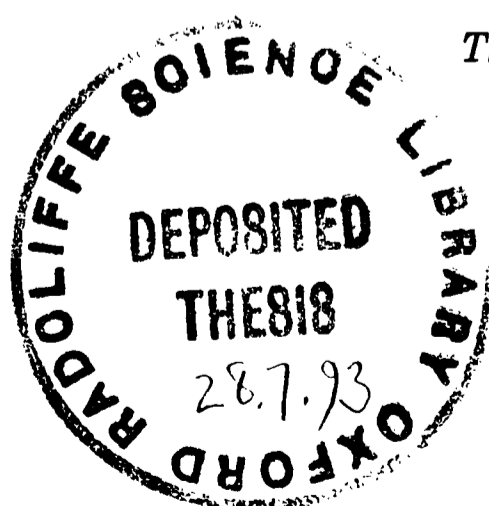
SOFT X-RAY CONTACT MICROSCOPY USING LASER GENERATED PLASMA SOURCES

by
J. H. FLETCHER

JESUS COLLEGE
OXFORD

*A thesis submitted for the degree
of Doctor of Philosophy at the
University of Oxford*

*The Clarendon Laboratory, Oxford
Hilary Term 1993*



ABSTRACT

**Soft X-ray contact microscopy using
laser generated plasma sources.**

J. H. Fletcher, Jesus College, Oxford.

*A thesis submitted for the degree of Doctor of Philosophy
at the University of Oxford, Hilary Term 1993.*

The ultimate objective of this project was to develop a small, transportable X-ray microscope which would be able to view a wide range of biological specimens without the need for any type of sample preparation at a resolution greater than that obtainable by conventional light microscopy (ie. about 250nm). Of the various possible implementations of X-ray microscopy currently being investigated, contact microscopy was chosen as being the most suitable for the development of such a small-scale instrument, while at the same time minimizing the effects on image quality of radiation damage to the biological specimen.

The requirement for a high brightness pulsed X-ray source of less than 50ns duration for illumination of the specimen was met by the production of laser generated plasmas. These were formed by focusing a 2.2J KrF laser beam, of wavelength 248nm and duration 20ns, onto the surface of one of a number of different target materials. In order to obtain the large intensities required for the production of a sufficiently high temperature plasma, a doubly pre-ionized, discharge-pumped amplifier KrF laser was developed. This was seeded by a smaller oscillator laser by means of a coupled unstable resonator configuration. A number of different cavity arrangements were investigated and an output beam divergence of 2.5 times the diffraction limit was achieved.

The plasmas generated by focusing the laser beam to an intensity of 10^{14}W/cm^2 onto carbon, titanium, molybdenum and tungsten targets were characterized as fully as was necessary for their use in the X-ray microscope. Preliminary investigations on the use of a grazing incidence ellipsoidal mirror to focus the emitted X-rays onto the specimen of the microscope were made and such an optical component was manufactured and tested.

Finally, numerous images of a number of different biological specimens were made and resolutions of better than 100nm were achieved. Images were read out using a Park Scientific Instruments atomic force microscope, which enabled the entire microscopy process to be carried out in a single working day. The system is now in routine use and can produce more than ten images per session.

ACKNOWLEDGEMENTS

It is a pleasure to offer my thanks to:

Professors R.A. Cowley and P.G.H. Sandars for the use of the facilities of the Clarendon Laboratory;

Professor Colin Webb for boundless enthusiasm for the whole field of Atomic Physics;

Dr. Tony Andrews for invaluable advice on the practicalities of conducting research at the Clarendon Laboratory;

Dr. Robin Cotton for aid too wide-ranging to possibly describe;

Dr. Tony Stead and Dr. Tom Ford of Royal Holloway and Bedford New College for providing biological specimens and interpreting images produced by the X-ray microscope.

Mr. George Matthews in the Clarendon Research Workshop for ensuring that hitting pieces of metal downstairs was doubly thoroughly enjoyable;

Adam Whybrew for agreement in general and excellent proof reading in particular;

Mr. Chris Goodwin for high quality optical coatings;

Past and present members of the Laser Group for occasional academic and frequent physical help with the running of the laser;

SERC and Jesus College for financial support;

And finally ... my parents and Sarah, many of my contemporaries, including but not necessarily limited to Suit, Dave Wren, Duncan, Dom, Alun and Katie, Llinos and Dave, Simon Hooker, the Happy Crowd Coterie of Bartlemas and their multifarious satellites, all co-editors past and present of *Y Cnychwr Defaid*, others too few to mention and anybody else who has been inadvertently overlooked.

CONTENTS

CHAPTER 1 INTRODUCTION

1.1	History	1
1.2	The laser system	2
1.3	Contact microscopy	3
1.4	Publications	4

CHAPTER 2 SOFT X-RAY CONTACT MICROSCOPY

2.1	Introduction	6
2.2	X-ray sources	9
2.3	Soft X-ray microscopes	12
2.4	The water window	14
2.5	Comparison of the techniques	16
2.6	Working microscope systems	20
2.7	Resolution	24
2.8	Secondary applications	32
2.9	Future prospects for X-ray microscopy	34

CHAPTER 3 THE KrF LASER SYSTEM

3.1	Introduction	36
3.2	The new laser electrical circuit	37
3.3	Initial '2 Joule' design	42
3.4	Second '2 Joule' design	43
3.5	Final '2 Joule' design	43
3.6	The new gas system	43
3.7	The new electrode structure	46
3.8	Optimization of the new laser system	52
3.9	Optimization with the final electrical circuit design	61
3.10	Gas optimization	62
3.11	Oscillator laser performance	66
3.12	Summary and further design improvements	66

CHAPTER 4 THE OPTICAL RESONATOR

4.1	Introduction	70
4.2	Unstable optical resonators	71
4.3	Injection seeding	84
4.4	Relative timing measurements	86
4.5	Optimization of the confocal cavities	90
4.6	Energy dependence on cavity	91
4.7	Divergence dependence on cavity	97
4.8	Summary	103

CHAPTER 5 LASER GENERATED PLASMAS

5.1	Introduction	105
5.2	Black body radiation	107
5.3	Plasma formation	108
5.4	Spectral dependence on Z	115

5.5	The target delivery system	117
5.6	Target alignment	121
5.7	Variation of X-ray emission with focal position	122
5.8	Variation of X-ray emission with seeding delay	124
5.9	Plasma emission spectra	125
5.10	Angular distribution of emission	131
5.11	Calculation of conversion efficiency	135
5.12	Measured conversion efficiencies	140
5.13	Variation of yield with laser energy	144
5.14	Pinhole camera images of the plasmas	147
5.15	Application of electric fields to the plasma region	156
5.16	Conclusions	160

CHAPTER 6 X-RAY OPTICS

6.1	Introduction	161
6.2	Zone plates	163
6.3	Multilayer mirrors	169
6.4	Grazing incidence optics	171
6.5	Use of X-ray optics	190
6.6	Conclusions	194

CHAPTER 7 SOFT X-RAY IMAGING

7.1	Introduction	196
7.2	The imaging technique	197
7.3	Resist dissolution rates	198
7.4	Use of the atomic force microscope	206
7.5	Biological imaging	208
7.6	Future biological investigations	221
7.7	Summary	223

REFERENCES	225
------------	-----

CHAPTER ONE

INTRODUCTION

- 1.1 HISTORY
- 1.2 THE LASER SYSTEM
- 1.3 CONTACT MICROSCOPY
- 1.4 PUBLICATIONS

1.1 HISTORY

The current soft X-ray contact microscope (SXCM) project at the Clarendon Laboratory began in 1987 when Dr. Webb was awarded £91,000 by the Royal Society's Paul Instrument Fund to develop, in collaboration with Dr. O'Neill of the Rutherford Appleton Laboratory (RAL), a transportable X-ray microscope which would be ultimately capable of imaging living biological specimens at sub-optical resolutions. Soft X-ray imaging had first been carried out by Spiller [1976], and by the time of the first international conference on X-ray microscopy, held at Göttingen in 1983 [Schmahl 1984], the development of several microscopes (almost all synchrotron based) had been initiated at various locations in Europe and America. At the second conference in this series, held at Brookhaven in 1987 [Sayre 1987], details of several microscopes based in Japan were given along with the first serious attempts at biological imaging. By that stage, the importance of user access to working microscopes had become apparent, and the need for a laboratory-based instrument had begun to be addressed. At the Clarendon Laboratory, R.A. Cotton started work on the development of such a microscope, and by the time of the completion of his D.Phil in 1990 [Cotton 1990], multiple-shot imaging of dry specimens had been achieved. Results were presented at the third X-ray microscopy conference in London in 1990 [Michette 1992].

As a result of the work being carried out at the Clarendon Laboratory, a valuable link was established with Dr. Tony Stead and Dr. Tom Ford of the Royal Holloway and Bedford New College (RHBNC) in Egham. As biologists, they had been active in the field of X-ray microscopy for some time, working with the contact

microscope at RAL. This was set up in TA2 and first came in to operation in 1984, using the 100J, 1.06 μ m Vulcan laser source, frequency doubled to obtain 30J of 0.53 μ m radiation. The target material used initially was carbon and the target chamber, specimen holders and method of resist development were all very similar to those of the current Oxford microscope. More recently, the target chamber of TA4 has been equipped with the X-ray microscope apparatus, making use of low energy (\sim 10J), 1.06 μ m laser pulses from Vulcan. Dr. Cotton took up a post-doctoral appointment at RHBNC to continue the development and improvement of the RAL microscope while this author set about upgrading the Oxford system to enable it to take single shot images of wet biological specimens. Once this had been achieved, work continued in parallel on the two systems, and a wide range of biological material has been studied [Fletcher 1993, Cotton 1993]. During this time, the relative merits of the two systems were assessed (ie. one a large central facility and the other a laboratory-based system), and each was able to benefit from technical advances made at the other since, apart from the very different laser sources, the two microscopes were almost identical.

1.2 THE LASER SYSTEM

The initial decision to construct a laboratory-designed KrF laser system was based on the lack of availability of a suitable commercial unit at that time. This continues to be the case today as the majority of commercial systems are designed for high repetition rate use, which, although having a high average power, give only a relatively small energy per pulse. For example, the highest pulse energy available from the Lambda Physik LPX301i excimer laser operating with a plane-plane cavity arrangement is 1J. Unstable resonator optics, which are necessary for this particular application, lead to a beam divergence of 400 μ rad (in comparison to a diffraction limit of \sim 8 μ rad), and a decrease in output energy to 400mJ. At present, this seems to be the most suitable commercially available system, and its cost in 1992 was £80,000, a sum almost equal to the total funds available for the SXCM project at the Clarendon Laboratory.

The initial KrF system, as developed by Cotton [1990], could deliver 875mJ

using an unseeded plane-plane cavity arrangement, and 650mJ when operated with a coupled confocal resonator. As it transpired that this was insufficient for the production of a plasma bright enough for single shot imaging, the first task in the current work was to upgrade the laser system to one which would give an output of 2J with a beam quality similar to that of the original system. A new amplifier electrode structure and external electrical circuit were constructed and a plane-plane cavity output of 2.24J was eventually achieved (chapter 3), a value unmatched, it is believed, by any KrF laser of an equally simple design currently in operation. A series of investigations was then made on various confocal cavity arrangements for the oscillator and amplifier lasers, which led to a seeded output energy of 2.22J being obtained in a beam which had a divergence only 2.5 times that of the diffraction limit (chapter 4).

1.3 CONTACT MICROSCOPY

Once the laser system had been upgraded, the production of laser generated plasmas (LGPs) was investigated with a view to obtaining the most appropriate X-ray source for use in the contact microscope. The laser beam was directed into a vacuum target chamber and focused onto the surface of a wire or thin ribbon target to an intensity of $\sim 10^{14} \text{W/cm}^2$. This resulted in the formation of a plasma at the surface, of approximately 20ns duration, which emitted soft X-rays into a large solid angle. Four different target materials were used and the plasmas generated by each were characterized as fully as necessary for use in the X-ray microscope (chapter 5). The use of some form of focusing X-ray optic was also considered and investigated in chapter 6, although time and resources unfortunately did not permit as full an evaluation as had been wished. The use of X-ray optics for contact microscopy had not previously been investigated, and the advantages to be gained in terms of image quality were considered. It is hoped to continue work in this field in the near future, with the ultimate aim of relaxing the source requirements of the laser used to produce the laser generated plasmas to a specification which could be met by a commercially available unit.

Finally, a number of biological studies were undertaken with the system, taking

advantage of the flexibility, very low running costs and immediate availability of the arrangement, which was entirely devoted to SXCM. The microscope is currently one of only a very small number of instruments which are not based at large, national facilities, which are readily accessible to potential users and which can image biological specimens without the need for any type of sample preparation. In a typical working day, a dozen resists could be exposed, each containing the images of up to one hundred micro-organisms. The microscopy process has also been greatly enhanced by the recent purchase of a Park Scientific Instruments atomic force microscope, only the second such machine in operation in Britain, which was used extensively to obtain the images presented in chapter 7.

1.4 PUBLICATIONS

A number of papers arising from the work described in this thesis have been published in various journals. These are:

- 1: "Recent advances in X-ray contact microscopy using laser generated plasmas."; R. A. Cotton, A. D. Stead, T. W. Ford, A. J. Jackson, A. Ridgeley, J. H. Fletcher and C. E. Webb, *Proc. Int. Conf. on progress and applications of plasma focus research*, New Jersey [1991].
- 2: "Dedicated soft X-ray source for contact microscopy."; R. A. Cotton, J. H. Fletcher, A. J. Andrews and C. E. Webb, 'X-ray Microscopy III', *Springer Series in Optical Sciences* 67, Eds. A. Michette et al, Publ. Springer-Verlag Berlin, pp209-211 [1992].
- 3: "Bringing soft X-ray contact microscopy to the biologist."; R. A. Cotton and J. H. Fletcher, *Proc. RMS* 27(2), pp77-80 [1992].
- 4: "Soft X-ray contact microscopy using laser generated plasma sources."; J. H. Fletcher, R. A. Cotton and C. E. Webb, *Proc. SPIE Conf. 'Soft X-ray microscopy'* 1741, pp142-153 [1992].
- 5: "Atomic force microscopy employed as the final imaging stage for soft X-ray contact microscopy."; R. A. Cotton, M. D. Dooley, J. H. Fletcher, A. D. Stead and T. W. Ford, *Proc. SPIE Conf. 'Soft X-ray microscopy'* 1741, pp204-212 [1992].

6: "Using soft X-rays from laser generated plasmas for the contact imaging of living biological specimens."; R. A. Cotton, M. D. Dooley, J. H. Fletcher, C. E. Webb, A. D. Stead and T. W. Ford, *Int. Conf. on X-ray optics and microanalysis XIII*, Manchester [1992].

In addition, two further papers are in preparation; 'A simple 2 joule KrF laser design' and 'An investigation of coupled confocal unstable cavities for an oscillator-amplifier KrF laser system'.

CHAPTER TWO

SOFT X-RAY CONTACT MICROSCOPY

2.1	INTRODUCTION
2.2	X-RAY SOURCES
2.2.1	Electron impact devices
2.2.2	Synchrotron radiation
2.2.3	Plasma devices
2.2.4	X-ray lasers
2.3	SOFT X-RAY MICROSCOPES
2.3.1	Contact microscopy
2.3.2	Full field transmission microscopy
2.3.3	Scanning X-ray transmission microscopy
2.4	THE WATER WINDOW
2.5	COMPARISON OF THE TECHNIQUES
2.5.1	Scanning transmission X-ray microscopy
2.5.2	Full field transmission microscopy
2.5.3	Contact microscopy
2.6	WORKING MICROSCOPE SYSTEMS
2.6.1	Synchrotron based microscopes
2.6.2	Pulsed plasma based microscopes
2.7	RESOLUTION
2.7.1	Penumbral blurring
2.7.2	Fresnel diffraction
2.7.3	Dosage statistics
2.7.4	Radiation damage and hydrodynamic motion
2.8	SECONDARY APPLICATIONS
2.8.1	Stereo imaging
2.8.2	Elemental mapping
2.9	FUTURE PROSPECTS FOR X-RAY MICROSCOPY

2.1 INTRODUCTION

The possibility of using X-rays as a microscope illumination source was first considered by Goby [1913] in an attempt to overcome the limitations of using visible light illumination. In a conventional microscope, the lateral resolution had been shown to be

$$d \sim 1.22\lambda / (NA_o + NA_c) \quad [2.1]$$

by Abbe [1884], where NA_o and NA_c are the numerical apertures of the objective and condenser lenses. This indicates that the resolution is effectively limited by the wavelength of the source illumination to values which for visible light are about 300nm.

The development of the confocal microscope in recent decades (as outlined by Hall [1991]), although aimed mainly at increasing longitudinal resolution, has enabled a lateral resolution of $\sim 200\text{nm}$ to be obtained by effectively reducing the field of view from the image plane by the use of a small pinhole. This is represented schematically in figure 2.1.

However, the type of microscope now most widely employed in situations where sub-100nm resolutions are required is the electron microscope, which can provide a resolution better than 1nm under ideal conditions. However, the study of biological material by electron microscopy is severely limited by several factors, the most

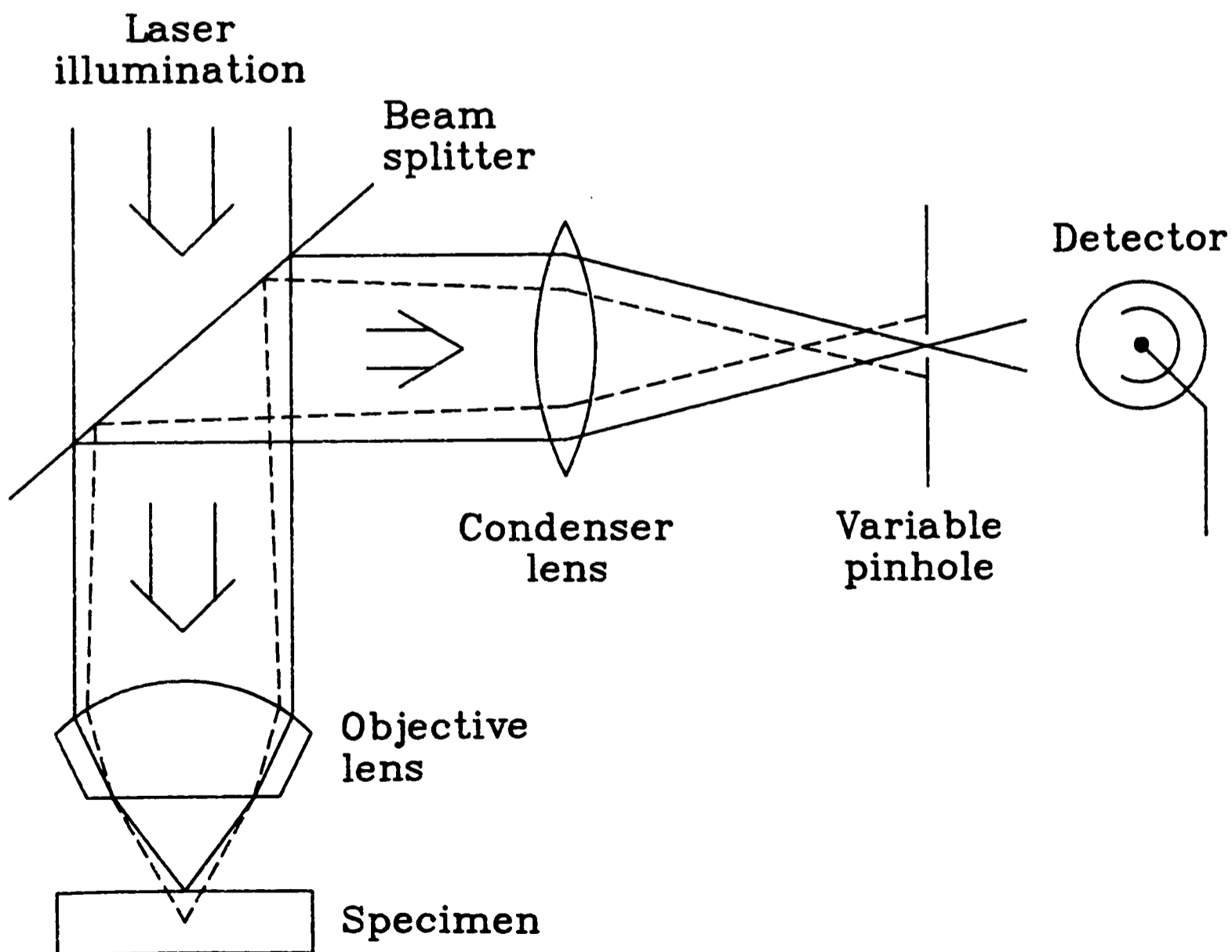


Figure 2.1: The scanning confocal optical microscope.

important of which are now outlined:

a) The specimen has to be dehydrated, as it will be placed in a vacuum inside the electron microscope. This vacuum is necessary to enable the accelerated beam of electrons to reach the specimen without being attenuated by collisions with air molecules and to avoid cathode poisoning. Although this clearly poses no problems for the study of inorganic materials, living biological tissue consists of well over 50% water, and this dehydration process will radically affect the structure of the specimen. Attempts to image hydrated biological material using electron microscopes have been made by, for example, Dupouy [1966] and Hui [1974], but they have been of relatively limited application in that it was the electron diffraction pattern, rather than a direct representation of the specimen itself, which was produced by the technique.

b) For viewing by transmission electron microscopy, the specimen has to be stained with a heavy metal in order to achieve sufficient contrast in the final image. This process of staining is required because the electron scattering coefficients for carbohydrate and protein are very similar to each other, leading to a very low natural contrast between different structures within a specimen. In the case of scanning electron microscopy, the specimen has to be thinly coated with a layer of metal (such as gold) to make it electrically conducting so that the probe electrons may be removed from the specimen to avoid a build up of electrical charge.

c) Since the scattering process by which the electron microscope probes the specimen is predominantly a surface phenomenon, scanning electron images are limited to the investigation of surface features only. Transmission electron microscope images may be obtained from very thin specimens (of only a few hundred nanometres) because of the large cross-sections for electron scattering shown by the materials of which biological specimens are composed.

The preparation procedures required for electron microscopy, such as dehydration, staining and fixing, will obviously distort features of a biological specimen, frequently introducing artifacts, thereby making the interpretation of images difficult and their conclusions possibly misleading (as noted by Stead [1993]). Interactions between the electron beam and the specimen may also result in damage to

its structure.

The technique of soft X-ray contact microscopy (SXCM) may be able to overcome these problems, in that it has the potential to offer:

a) A resolution greater than that currently available from other conventional forms of light microscopy.

b) The ability to look at sections of several microns thickness of living tissue in its natural aqueous environment without the need for staining. This arises from the fact that the absorption coefficients for X-rays are smaller than the electron scattering coefficients by a factor of ~ 10 in the cases of carbohydrate and protein. The dominant attenuating process for X-rays in these circumstances is photo-absorption.

If either of these two features are not realized however, then the techniques of confocal or electron microscopy will be able to offer more in terms of ease of use and resolution, in which case SXCM will have no rôle to play in the field. As yet, only a few members of the biological community have expressed any real interest in the technique, in as much as they have been convinced that it can offer any advantages over these other forms of microscopy. Unfortunately, this interest has been not been encouraged by the initial results of several soft X-ray microscopes (for example, as described in Schmahl [1984] and Sayre [1987]), which have often presented images of inorganic specimens with a resolution worse than $1\mu\text{m}$. Those specimens which were of a biological nature had needed to undergo damaging preparation such as dehydration or fixation.

2.2 X-RAY SOURCES

Initially, the development of all forms of X-ray microscopy was hampered by the lack of X-ray sources intense enough to provide adequate illumination of a specimen and which would enable an image to be recorded in a reasonably short time, by the lack of suitably sensitive detectors, and also by the difficulties in the fabrication of X-ray optical components. Over the past decade, the problem of obtaining a suitably bright source has been partially resolved in a number of manners. Potential sources are now outlined.

2.2.1 Electron impact devices

Electron impact X-ray sources include the familiar X-ray tube, where radiation is produced by the Bremsstrahlung process and also by the radiative decay of inner shell electrons of atoms excited by the incident electrons. The low conversion efficiency of incident electron energy to X-rays (less than 1%) and the resultant heating of the target material set a severe limit on the input power to such devices, leading to the generation of X-ray fluxes much smaller than those obtained from synchrotron sources. Materials which are suitable for use as the anode (ie. those which are able to withstand a high degree of heating) also emit characteristic spectral lines which do not fall within the wavelength range required for efficient X-ray microscopy. Compton [1935] showed that the conversion efficiency η of incident electron kinetic energy into continuum X-ray energy is given by

$$\eta = 1.1 \times 10^{-9} ZV \quad [2.2]$$

for a target material of atomic number Z and an accelerating voltage of V . In the case of the line spectra, Green [1961] has proposed the empirical expression

$$N = (\Delta + 2.8 \times 10^{-2} / AT^{0.37})(-1 + T/E_i)^{1.65} f(\chi) / (1 + 7.5 \times 10^5 / Z^4) \quad [2.3]$$

for the number N of $K\alpha$ photons emitted per steradian per incident electron from an infinitely thick target of atomic weight A and ionization energy E_i keV. The electron energy is T keV and Δ is a dimensionless factor to take account of the re-absorption of continuous X-rays which result in subsequent emission of $K\alpha$ lines. The function $f(\chi)$ represents the re-absorption of X-rays in the target material.

For a typical practical system, it is found that $\eta \sim 0.02\%$ and $N \sim 10^{-4}$. The sum of these contributions results in an X-ray flux which is far too low to be of any use in a practical imaging system, and consequently, conventional electron impact X-ray sources are not suitable for the current application.

2.2.2 Synchrotron radiation

When a charged particle is accelerated, it emits one or more quanta of radiation. This effect may be employed to produce radiation with a spectral intensity similar to that of black body radiation, by causing electrons to execute a closed

circular orbit at relativistic velocities (described by Winick [1987]). This method produces the highest average power of any soft X-ray source, in a well collimated beam, and with properties which may be quantified using only a small number of well defined parameters. For example, the angular distribution of the emitted radiation in the direction \underline{r} is given by

$$\frac{dP}{d\Omega}(\theta, \psi) = (e^2 a^2 / 16 \pi^2 \epsilon_0 c^3 \alpha^3) [1 - \{\sin(\theta) \cos(\psi) / \gamma \alpha\}^2] \quad [2.4]$$

where

$$\gamma = (1 - v^2/c^2)^{-1/2}, \quad \alpha = 1 - (v/c) \cos(\theta) \quad [2.5]$$

ψ is the angle between the acceleration, \underline{a} , and \underline{r} , θ is the angle between \underline{v} and \underline{r} , and ψ is consequently given by

$$\sin^2(\psi) = 1 - \sin^2(\theta) \cos^2(\psi) \quad [2.6]$$

Wigglers may be additionally be used to achieve higher spectral brightness. In these devices, the circulating electrons are made to traverse a periodic magnetic structure, causing them to follow a path with a decreased radius of curvature. Using this technique, the National Synchrotron Laboratory Source at the Brookhaven National Laboratory NY, for example, achieves an average spectral brightness of $\sim 10^{13}$ photons/s.mm².mrad² over a bandwidth of 0.1%. Such sources may be used for scanning transmission microscopes (described in section 2.3.3) and have also been used, with limited success, for contact microscopy [Kinjo 1992].

2.2.3 Plasma devices

Plasma devices rely on the production of a hot, dense plasma with a characteristic temperature of a few hundred electron volts. Such plasmas are strong emitters of X-rays, with a peak emission which may be made to fall in the soft X-ray region of the spectrum. There are two main techniques for producing plasma sources.

i) Z-pinch devices

In a Z-pinch, a very large current, of up to 10^6 A, is passed through a small sample of a suitable gas. The current creates a large magnetic field, causing a region of the gas to accelerate radially inwards due to the Lorentz force. The kinetic energy of

the gas particles is converted to thermal energy, forming a hot, dense plasma which emits line radiation characteristic of the gas used, superimposed on a background continuum. This type of source has been used for the full field transmission microscope operated by the Göttingen group [Schmahl 1992].

ii) Laser generated plasmas

If a laser pulse is focused with an intensity of at least $\sim 10^{12} \text{W/cm}^2$ onto the surface of a target material, then a plasma will be formed with a temperature of $\sim 10^6 \text{K}$. By choosing an appropriate target, this plasma can be made to emit in the soft X-ray region of the spectrum, either by line emission (for low Z targets) or electron capture and Bremsstrahlung, leading to a broadband spectrum (for high Z targets). Laser sources which are commonly used for this purpose are Nd:YAG and rare gas halide excimer lasers. It is this type of X-ray source which is currently the cheapest, most convenient and reliable for the application of X-ray contact microscopy.

2.2.4 X-ray lasers

At present, the deployment of X-ray lasers is limited to large national facilities to an even greater extent than synchrotron sources because of the specification requirements of the lasers needed to create plasmas of suitable density and geometries for the production of an X-ray laser beam. The technological difficulties of producing high reflectance mirrors in the water window range (as outlined in section 6.3) have also yet to be overcome. For example, the X-ray microscopy programme at the Lawrence Livermore National Laboratory, using the NOVA laser, currently operates at 4.5nm (ie. just outside the water window wavelength range, the importance of which is described in section 2.4) and is limited to obtaining just 70 laser shots per annum for their experiments [Da Silva 1992].

2.3 SOFT X-RAY MICROSCOPES

As might be expected, several different types of microscope have been developed which employ X-rays as their illuminating source. The most important of these so far

have been contact micro-radiography, or contact microscopy (SXCM), full field transmission imaging (FFT) and scanning transmission microscopy (STXM). A fourth technique, holographic microscopy, is unlikely to lead to any practically useful form of microscope until the development of more powerful X-ray lasers [Lindaas 1993].

2.3.1 Contact microscopy (SXCM)

Contact microscopy is the simplest implementation of X-ray microscopy and of the various methods, has been applied to the largest range of objects. The specimen, which needs neither to be dehydrated nor stained, is placed in close contact with an X-ray sensitive photoresist; in the present system, this is a 500nm thick layer of the polymer polymethyl methacrylate (PMMA), supported on a 1mm thick silicon wafer. The specimen is then illuminated by a measured dose of X-rays, so that the resist records the X-ray transmission map of the specimen at unity magnification - a 'contact print' in effect. The transmitted X-rays, when falling on the resist, act to break chemical bonds in the polymer chains and thus reduce its localized average molecular weight. The resist is then developed with methyl isobutyl ketone (MIBK), (diluted by isopropyl alcohol (IPA) to control the rate of development), which preferentially dissolves regions of lower average molecular weight. This results in a contour map being recorded in the resist, where its height at any one point represents the mass absorption of the specimen integrated perpendicular to the resist surface at that point. This may then be viewed with an SEM, or more recently an atomic force microscope (AFM), to obtain a magnified image of the resist.

2.3.2 Full field transmission microscopy (FFT)

The closest equivalent of a conventional light microscope is the full field transmission microscope, with condenser and objective lenses being replaced through necessity by zone plates. X-rays are focused onto the specimen by a condenser zone plate, and an objective zone plate is used to form a magnified image on a microchannel plate or photographic film; this arrangement is represented schematically in figure 2.2. Unfortunately, zone plates for soft X-rays are still only a few percent efficient (for the

reasons given in section 6.2), and so a strong source of X-rays is required in order to achieve a reasonable flux in the image plane; using a synchrotron source for example, the imaging process still takes several seconds. More importantly, the low efficiency of the system after the object plane necessitates a large irradiance of the specimen, which may well result in radiation damage before an image can be recorded.

2.3.3 Scanning transmission X-ray microscopy (STXM)

The problem of excessive X-ray dose to the specimen may be somewhat reduced by an arrangement in which a continuously emitting X-ray source (ie. synchrotron) is focused to as small a point as possible by the use of a zone plate, toroidal mirror, etc., and then used to scan the specimen in a raster pattern. (Turcu [1992] has investigated the use of a high repetition rate laser generated plasma source for STXM, which would, if successful, overcome the problem of restricted access to synchrotron sources.) At each point, a detector (commonly a CCD) placed behind the specimen produces a signal proportional to its transmittance at that point, which is passed to a computer to build up a complete picture of the specimen over a period of at least several seconds, as shown in figure 2.3. Since all of the imaging takes place on axis, aberrations are reduced and the absence of any post-specimen optics enables a high image formation efficiency to be obtained. The first practical STXM was developed by Horowitz [1972] at the Cambridge Electron Accelerator Synchrotron Source, USA.

2.4 THE WATER WINDOW

As mentioned previously, soft X-rays interact with matter predominantly by the photoelectric effect, where the strength of the interaction is characterized by the sum of the individual atomic cross-sections. Since biological specimens in their natural state are composed mainly of water, the water window region of the soft X-ray spectrum is of paramount importance in X-ray microscopy. This is because between the wavelengths of 2.3 and 4.4nm (539 to 282eV), the absorption cross-section of oxygen (and hence, water) is far smaller than that of organic materials such as protein. The transmission of 1 μ m thicknesses of water and protein are shown in figure 2.4 to

illustrate this effect. This indicates that if radiation of this wavelength range is used to illuminate a specimen then a natural contrast between biological features and their aqueous environment will result, and hence obviate the need to stain the sample.

In the current work on SXCM, parameters have been chosen so as to maximize

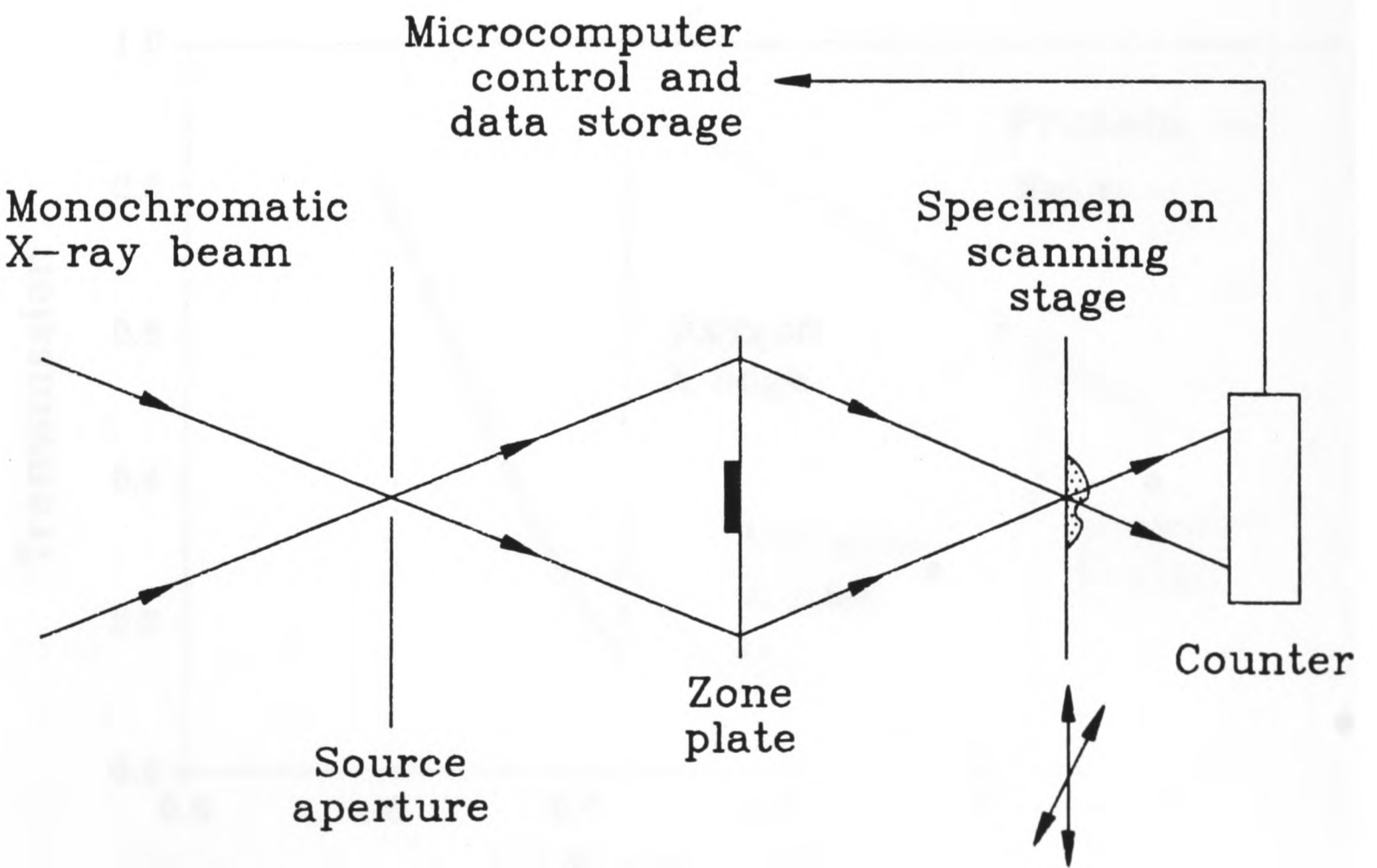
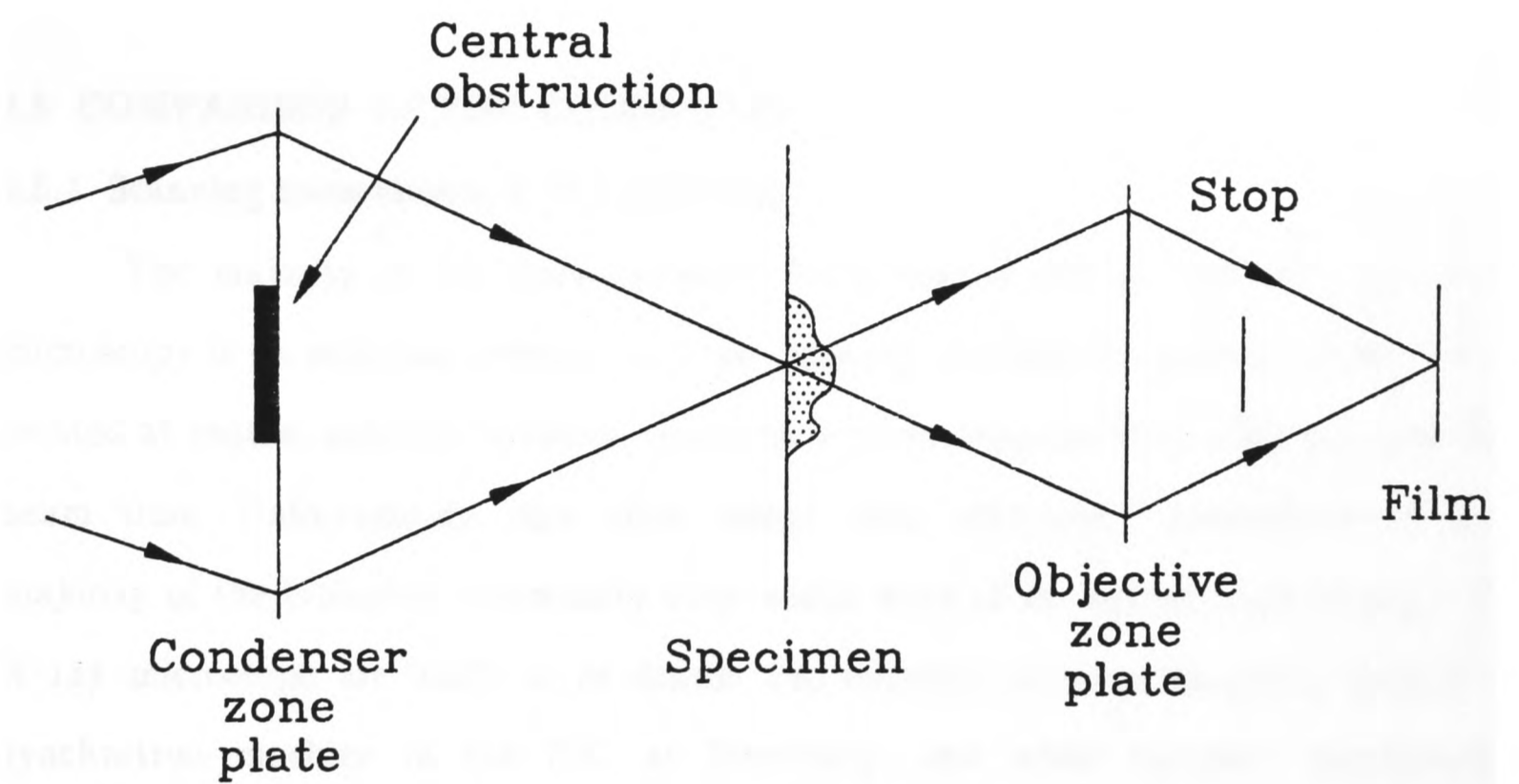


Figure 2.2: The full field transmission (FFT) X-ray microscope.

Figure 2.3: The scanning transmission X-ray microscope (STXM).

the proportion of X-rays in the illuminating flux falling within this region in, in order to obtain as great a contrast as possible in the final recorded image. On either side of the water window, water and protein have very similar absorption coefficients, and hence any contribution from X-rays of these wavelengths in the illumination will act to decrease the final contrast by 'fogging' the resultant image.

2.5 COMPARISON OF THE TECHNIQUES

2.5.1 Scanning transmission X-ray microscopy

The majority of the work currently being carried out in the field of X-ray microscopy is on scanning systems, the vast majority of which by necessity have to be located at central national facilities, where they must compete with other projects for beam time. Unfortunately, this often makes them effectively unavailable to the majority of the biological community from which most of the actual users of any soft X-ray microscope are likely to be drawn. For example, there is currently only one synchrotron machine in the UK, at Daresbury, and while compact commercial

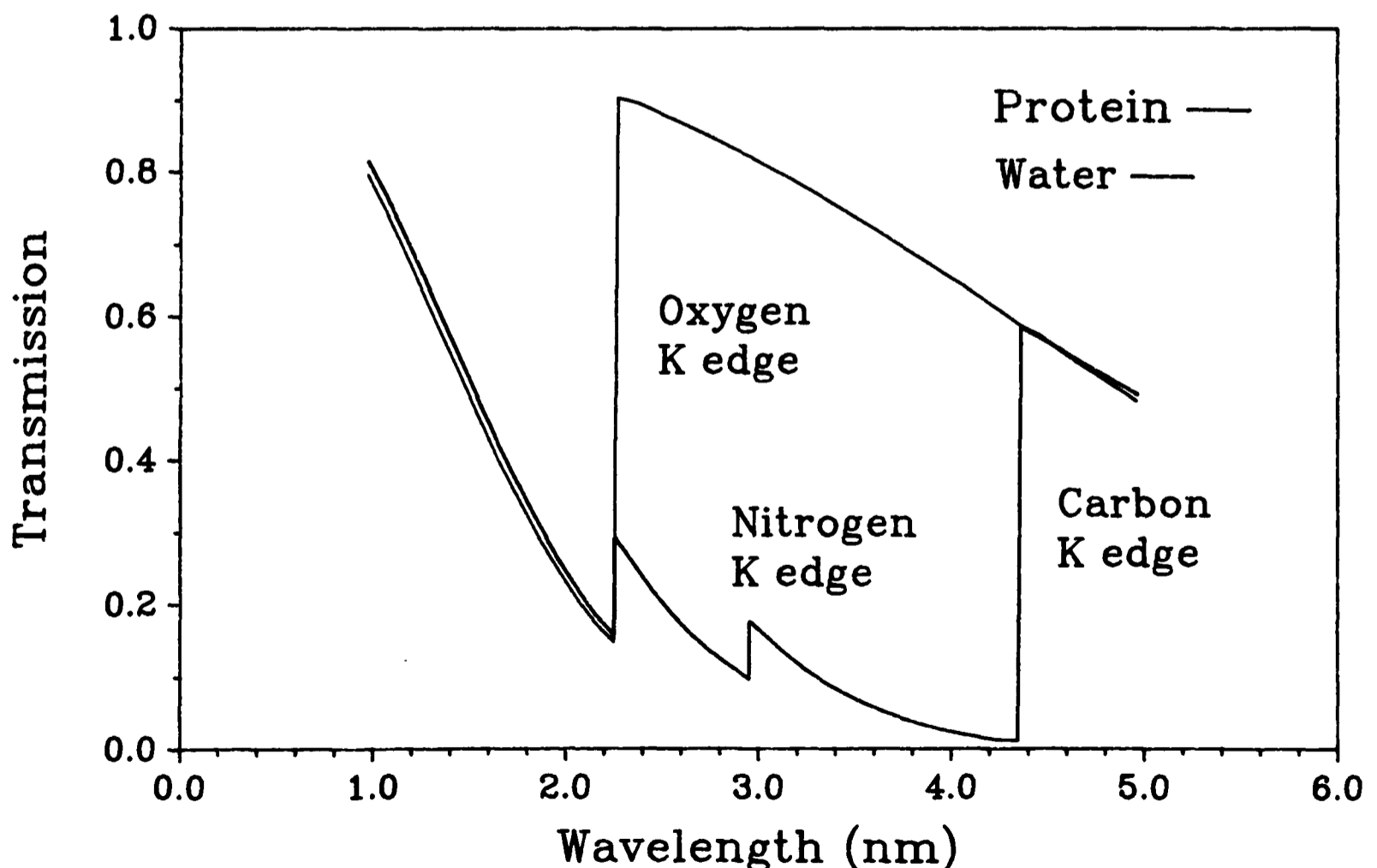


Figure 2.4: Transmission of $1\mu\text{m}$ sections of protein and water, illustrating natural contrast within the water window.

synchrotrons may soon become available, their cost is likely to exceed £1 million. If such machines were the only viable source of illumination, then X-ray microscopy would never become the routine imaging tool that optical and electron microscopies are today. Although the scanning arrangement has the advantage of giving a digital output directly (such that it may be immediately passed on for digital processing), the technique suffers from several fundamental drawbacks and technological difficulties, which are considered below.

In order to obtain sufficient flux at the CCD detector, the specimen has to be subjected to amounts of X-ray radiation which are several orders of magnitude greater than those which have been shown to severely damage many types of biological material (as shown by Folkard [1992]). Thus, as soon as the first point of the specimen is illuminated by the source, irreparable damage will be made to its structure on a time scale of microseconds. This would not be a significant problem but for the fact that the time required to scan a complete specimen and form a transmission image is several seconds, during which period the physiological effects of the radiation damage may become apparent, and thus adversely affect the recorded image. Irrespective of whether there are any radiation effects, the specimen still has to be fixed to avoid blurring due to natural movement during the imaging process. It is widely known to biologists that fixation processes can and do affect the structure of previously living specimens, as has recently been highlighted by Stead [1993].

Secondly, the resolution of a scanning X-ray microscope is almost entirely dependent on the size to which the X-rays may be focused, which for a zone plate system is equal to the width of the outer-most zone (as shown in section 6.2.1). Unfortunately, such components are very difficult to manufacture to the tolerances and dimensions required. A high proportion of the papers presented at the three X-ray Microscopy Conferences (Schmahl [1984], Sayre [1987] and Michette [1992]) were entirely concerned with the production of zone plates suitable for use in scanning X-ray microscopes. As is the case for multilayer mirrors, the need for such zone plates to operate within the water window region has led to further practical difficulties because of the need to avoid the use of carbon supporting foils. Grazing incidence

reflective optics have also been used, with the advantage that, unlike zone plates, radiation within the water window may be as readily focused as longer wavelengths, but difficulties still remain in obtaining sufficiently small spot sizes, which are usually larger than those obtained with zone plates.

Finally, scanning microscopes are generally very complicated and delicate instruments. Movement of the specimen stage is achieved by the use of piezoelectric transducers, which because of their inherent non-linearity and hysteresis have to be monitored by extremely sensitive and accurate position measuring devices. All of these obstacles fall in the way of the production of a reliable microscope which is easy to use with a wide range of biological specimens.

2.5.2 Full field transmission microscopy

In theory, full field transmission microscopy is the optimal solution to the problem of microscopy with X-rays, as it is a direct equivalent of the conventional light microscope. However, since the imaging process involves two zone plates, an exceptionally bright source would be required to make an exposure before the onset of radiation damage. Using a synchrotron source, Schneider [1992] required an exposure time of 30s, while Schmahl [1992] required 250 shots of a nitrogen Z-pinch to make one exposure. In both cases, the biological specimen had to be fixed and the low efficiency of the optical component after the object plane meant that the specimen would have been exposed to even greater amounts of radiation than those delivered in a scanning system.

2.5.2 Contact microscopy

In comparison, contact microscopy is currently the only implementation in which an image of the specimen is recorded before any radiation damage can become apparent. The exposure time of only a few nanoseconds is also short enough that any natural movement within the specimen will not cause blurring, and so there is no need to fix or dehydrate the subject. The source requirements may be met by a laboratory sized instrument; in this project, a relatively small, discharge-pumped KrF laser

system, delivering 1.4J of energy on target at 248nm in a time of 20ns FWHM, is used to produce a laser generated plasma of sufficient intensity that an image may be recorded in the resist in just one exposure. Tomie [1991] has also achieved single-shot imaging with a frequency-doubled Nd:glass laser delivering 2J in 500ps and a gold target, and, as mentioned in chapter 1, TA4 of the Vulcan laser system at the Rutherford Appleton Laboratory is currently equipped with a target chamber similar to that at the Clarendon Laboratory and has been made available for SXCM on a semi-permanent basis. A large number of images have been recorded with this system by Cotton [1992a, 1992b, 1993].

The main difficulties with this technique are ensuring a close contact between the specimen and the resist in order to reduce the effects of Fresnel diffraction and penumbral blurring (which are considered in section 2.7), and also in the development of the resist. The response of this recording medium is non-linear (as illustrated in section 7.3), and care has to be taken during development to avoid over-dissolution, which would result in the loss of smaller features recorded in the resist, while at the same time ensuring that development is sufficient for there to be large enough height variations in the surface between regions representing different parts of the specimen to be seen when viewed with an electron microscope or AFM. This problem may be overcome by the replacement of the resist by a photocathode, followed by accelerating and focusing fields to give a photoelectron magnification of the X-ray image (demonstrated by Polak [1987]), although this approach presents technical difficulties of its own.

A second drawback of the technique results from it being a two stage process; the resist, once exposed, has to be viewed with a secondary, high power microscope. Until recently, this has required the use of an SEM, and with even a fairly high specification model (for example, a Cambridge S100), it was frequently found that the resolution offered by the SEM (which had to be operated at a low accelerating voltage so as to avoid damaging the surface of the resist) did not match the resolution of the image in the resist itself. Also, the resist had to be coated with a thin metallic layer prior to viewing, which was a further drawback not only in terms of inconvenience, but

it also meant that the resist, once coated, could not be further developed in MIBK. It was often felt that this would have been desirable for a particular resist, since the development had to be monitored by light microscopy which offered only a rough guide to its progress and reaching the 'optimal' degree of development was often a rather hit and miss process.

More recently, the use of an AFM has increased the ease with which this second step may be performed, while also obviating the need for any resist coating. Using this type of microscope, a resist may be viewed with a resolution greater than the X-ray imaging process itself, without the risk of damage to the resist surface. After initial viewing, the resist may be further developed and then re-examined in the microscope. For example, using an image of *Schizosaccharomyces pombe* (fission yeast) taken at the RAL system, Cotton [1992a] was able to view the same image in a resist after various increasing degrees of development.¹⁾ As development progressed, it was possible to see the water in which the specimen was imaged 'dry down' to reveal a single yeast cell underneath.

2.6 WORKING MICROSCOPE SYSTEMS

2.6.1 Synchrotron based microscopes

Despite the interest shown by physicists in the technique of X-ray microscopy, which admittedly has yet to be shared by as many members of the biological community, there are relatively few X-ray microscopes currently in operation, and of these, only a small number are able to look at biological specimens. The majority are based by necessity at synchrotron sources, and a brief outline of those currently in operation is given below, together with details of the most recently published images.

¹⁾ Once the value of such an instrument in the process of SXCM had been shown, a consortium of groups within Oxford University (including Materials and Inorganic Chemistry) was awarded a University grant to purchase a Park Scientific Instruments AFM (costing £86,000) which is now located in the Chemical Crystallography Department, and is one of a very small number of such machines throughout the world which are in regular use for the study of SXCM resists. (The only other published work akin to this has been by Tomie [1991, 1993]).

i) **Photon Factory synchrotron source, Japan.** A full field transmission (FFT) microscope was built on the undulator beam line of this facility in 1987. To date [Kagoshima 1992] images of dry diatoms with a claimed resolution of 300nm have been made using radiation of wavelength 2.66nm and zone plate optics.

ii) **BESSY storage ring, FRG.** This national facility commenced operation in 1982, and an FFT microscope has been operated by the Göttingen group since 1983. At this location, several biological studies have been carried out [Guttmann 1993], for example on fixed but hydrated 3T3 mouse cells and chromosomes with 2.4nm radiation. However, exposure times have been large (over 30 seconds) with possible structural changes in the specimen associated with radiation damage. The resolution obtained with the instrument has not been given.

An STXM has been constructed for use at the storage ring, also operating at 2.4nm. To date, only dry diatoms have been imaged [Niemann 1992] with a scanning spot size of 100nm and thus an effective resolution of several times this value. An environmental chamber for wet cell experiments is currently being constructed.

iii) **UVSOR synchrotron source, Japan.** The UVSOR was constructed in 1983 and microscopy experiments have been conducted since 1987. An FFT microscope has been built using a zone plate condenser and objective and there has also been some work on the use of two Wolter Type I optics to replace these components. Watanabe [1992] has used this microscope to image various wet biological specimens, claiming a resolution of $1\mu\text{m}$. For these experiments, specimens were held between $4\mu\text{m}$ thick layers of polypropylene, $(\text{CH}_2\text{CHCH})_n$, which meant that imaging had to be carried out using radiation of wavelength 4.6nm, outside the water window region. At this wavelength, each polymer layer transmitted only 35% of the incident flux, and consequently, the specimens will have received a very large X-ray dose during the 2 second exposure. Additionally, there is very little natural contrast at this wavelength, which coupled with the high absorption of the specimen holder led to relatively poor quality images being obtained.

iv) **AURORA compact synchrotron source, Japan.** AURORA is a small, 1m diameter storage ring based on a single superconducting magnet, which became

operational in 1989. It was initially used for contact microscopy and images of fixed or dry chromosomes were made with 1.8nm radiation and exposure times of ~15s [Kinjo 1992]. The resolution obtained appears to be several hundred nanometres. More recently, the use of a Schwarzschild focusing optic has been investigated [Masui 1993] although biological imaging has yet to be carried out.

v) National Synchrotron Light Source (NSLS) at Brookhaven, USA. At NSLS, an undulator beamline has been built to supply radiation in the 1.5 to 5.0nm wavelength range to five experiments, one of which is an STXM. This has been used to study zymogen granules [Rothman 1992] using a pixel size of 32nm or greater (despite which, a resolution of 50nm was claimed from the 25-75% points on the image of a sharp knife edge) and an image acquisition time of several minutes. Fixed mitotic chromosomes have also been investigated [Jacobsen 1991] with an apparent resolution of ~80nm.

vi) Daresbury SRS. Workers from King's College, London have built an STXM for use on this synchrotron source, and the instrument was completed in 1986. A zone plate with an outer zone width of 75nm is used to focus water window radiation and a resolution of 150nm FWHM is claimed from the study of a sharp knife edge. Biological imaging has been limited to rabbit myofibrils at 3.27nm [Morrison 1992]; no other experimental details have been given.

2.6.2 Pulsed plasma based microscopes

There has also been some work on plasma based systems, where a 'stand alone' microscope can be built, independent of large synchrotron facilities, or at least only requiring a laser system of relatively modest specifications. The former includes the work being carried out at the Clarendon Laboratory, while the imaging being conducted at the Rutherford Appleton Laboratory by Cotton (as detailed in chapter 1) is an example of the latter. Those microscopes which have produced images of biological specimens are now outlined. (Projection microscopes, which are inevitably very low resolution instruments, and photoemission microscopes have not been included.)

i) **The Göttingen Group.** An FFT microscope has been built, of a similar design to that used on the BESSY storage ring but employing a nitrogen Z-pinch as the X-ray source. The resolution obtained with a high contrast gold target has been a few hundred nanometres and a fixed, dehydrated 3T3 fibroblast has been imaged with 2.5nm wavelength radiation with 400 plasma pulses [Schmahl 1992].

ii) **The Lawrence Livermore National Laboratory.** At LLNL, the large NOVA laser, operating at $0.53\mu\text{m}$, is brought to a line focus on a tantalum target foil to generate an X-ray laser beam at a wavelength of 4.483nm, just outside the water window. This is then used as the source for an FFT microscope, which has a multilayer mirror condenser and zone plate objective. This system has the advantage over all other FFT microscopes currently in operation in that an image can be obtained with a single 200ps pulse, thus eliminating the need for any specimen preparation and overcoming radiation damage problems; a facility unlikely to be matched by any FFT microscope which relies on either synchrotron or simple pulsed plasma sources. However, like a synchrotron source, the microscope is limited to the large national facility and only about 70 shots per year are available for X-ray microscopy experiments. A resolution of $\sim 100\text{nm}$ has been obtained with a gold test pattern and a specimen holder for biological material is currently being constructed after some discussion with Cotton and this author.

iii) **The Electrochemical Laboratory, Tsukuba, Japan.** At Tsukuba, a group led by Tomie has used a frequency-doubled Nd:glass laser, delivering 2J in 500ps, to generate a plasma source for SXCM. With a working distance of 6mm, single-shot images of wet, unfixed sea urchin sperm have been made, and a theoretical resolution of $\sim 70\text{nm}$ has been suggested. The resist, once developed, was viewed with an AFM [Tomie 1993]. It is intended to build an excimer laser in the near future, of a design similar to that at the Clarendon Laboratory, for plasma generation and it is apparent that this work most closely resembles that being conducted at Oxford, although fewer biological specimens have been studied with the system.

iv) **Tokyo Metropolitan Institute.** SXCM has also been investigated by Kinjo [1992], initially using the AURORA source. More recently, the problems associated

with long exposure times have been overcome by the use of a pulsed plasma source to view hydrated human chromosome fibres [Shinohara 1993].

v) **Princeton University.** The soft X-ray laser system at Princeton, employing a commercial 1kJ CO₂ laser as the pump source, has been used for SXCM experiments at 18.2nm. A single-shot image of a HeLa monolayer has been taken, with the developed resist viewed by SEM [Skinner 1990]. No indication of the resolution obtained was given however.

2.7 RESOLUTION

The final resolution obtained by the technique of SXCM is affected by a number of processes, ultimately limited by the wavelength of the radiation used to illuminate the specimen, ie. ~5nm. In current X-ray microscopy work, be it contact, scanning or direct imaging, the resolution of a particular instrument is frequently evaluated by the use of a metallic grid test object (for example, Trail [1989], Jacobsen [1991] and Kado [1991]). A value is obtained from the 25-75% points of the image of an extremely sharp high contrast edge. While this method often gives relatively small values, of several tens of nanometres, the result will unfortunately have little or no bearing on the resolution achieved when viewing biological specimens, in which interfaces between regions of varying carbon density have to be resolved, rather than an air-metal interface. For such subjects, the effective resolution will be degraded because of the decrease in contrast (section 2.7.3) and also possibly because of the effect of the spectral content of the illuminating radiation (section 2.4); 'knife edge' values for resolution can only be regarded as the ultimate limitation imposed by the microscope itself. The predominant factors affecting the resolution obtained by the technique of SXCM are now considered.

2.7.1 Penumbral blurring

Since not all of the specimen can be in complete contact with the recording medium, the image will be blurred because of the finite size of the illuminating source;

$$\Delta_p \sim 2rs/d \quad [2.7]$$

for a plasma of diameter $2r$ at a distance d from the specimen of thickness s (as shown in figure 2.5). For a $3\mu\text{m}$ thick specimen, plasma diameter of $100\mu\text{m}$ and plasma to resist distance of 9mm , this gives a limit of $\Delta_p=33\text{nm}$. This value could be significantly reduced by the use of an X-ray focusing optic (investigated in chapter 6) which would effectively increase the value of d .

2.7.2 Fresnel diffraction

The finite distance between the specimen and the resist will also lead to some degree of diffraction being recorded in the resist. To evaluate the severity of this effect, we first consider the Fresnel diffraction pattern created by a sharp opaque edge illuminated by a plane wave. At a distance s behind the object, we find an intensity distribution, I_p , described by the function

$$I_p(y) = \frac{1}{2}I_0 \left[\left[\frac{1}{2} - C(v) \right]^2 + \left[\frac{1}{2} - S(v) \right]^2 \right] \quad [2.8]$$

where

$$C(v) = \int_0^v \cos(\pi v^2/2) dv, \quad S(v) = \int_0^v \sin(\pi v^2/2) dv \quad [2.9]$$

$$v \equiv y \sqrt{2/\lambda s} \quad [2.10]$$

and y is the position of the screen in the plane perpendicular to the direction of illumination. The function was evaluated mathematically in terms of the parameter v , leading to the familiar Fresnel diffraction pattern of figure 2.6. Since the 'edge' of the

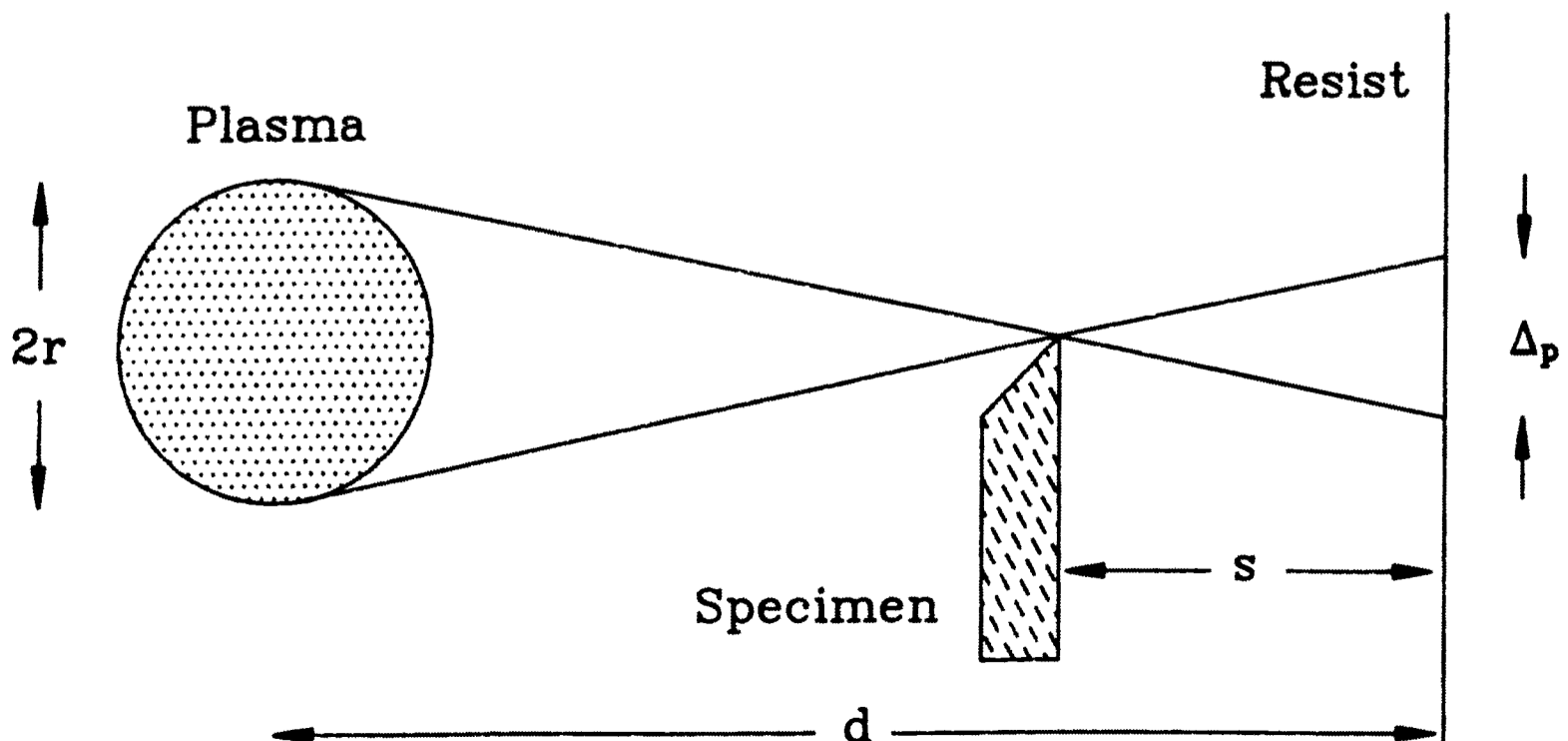


Figure 2.5: The effect of penumbral blurring on resolution.

function extends over a distance of approximately $v=1$, it is often concluded that this implies a resolution limit of

$$\Delta_f \sim \sqrt{\lambda s/2} \quad [2.11]$$

which gives a value of 70nm for a wavelength of 3nm and a $3\mu\text{m}$ thick specimen. More importantly in practice, it illustrates the presence of a very severe ‘ringing’ in the image, which could well cause problems in its subsequent interpretation and suggests an effective resolution of well over 70nm. However, this has assumed an infinitely sharp interface between one region of the specimen and another and also that the illuminating radiation is monochromatic. If we instead consider an interface whose transmission decreases sinusoidally from 1 to 0 between the positions y_1 and y_2 , we then obtain

$$I_p = \frac{1}{2} E_p^* E_p \quad [2.12]$$

where

$$E_p(\lambda) = (\alpha/s) e^{i(ks - \omega t)} (1+i) \left[[C(v) + iS(v)]_{v_2}^{\infty} + \int_{v_1}^{v_2} F(v) e^{i\pi v^2/2} dv \right] \quad [2.13]$$

and

$$F(v) = \frac{1}{2} \left[1 + \sin\{\pi(2v + v_2 - 3v_1)/2(v_2 - v_1)\} \right] \quad [2.14]$$

where the function $F(v)$ represents the sinusoidal variation and α is a constant. I_p was evaluated numerically for various values of $\Delta v = v_2 - v_1$, corresponding to the width of the sinusoidal section in real space, and assuming a Gaussian variation (of FWHM equal to the water window wavelength range) in the spectral intensity of the incident radiation. From figure 2.7, we can see that there is little evidence of any edge effects for the case of $\Delta v = 3.0$, and from equation [2.10], we may put

$$\Delta y(\text{nm}) \sim 116 \sqrt{s(\mu\text{m})} \quad [2.15]$$

which defines the sharpest feature for a given specimen thickness that can be viewed without any appreciable diffraction effects. Thus, for example, the image of a $5\mu\text{m}$ thick object could be faithfully recorded so long as its ‘edge fall-off’ was at least 260nm wide. This may seem a relatively large value, but for such a large specimen, conventional light microscopy would probably be more appropriate. If we instead consider a $1\mu\text{m}$ object, which would not be suitable for conventional light microscopy,

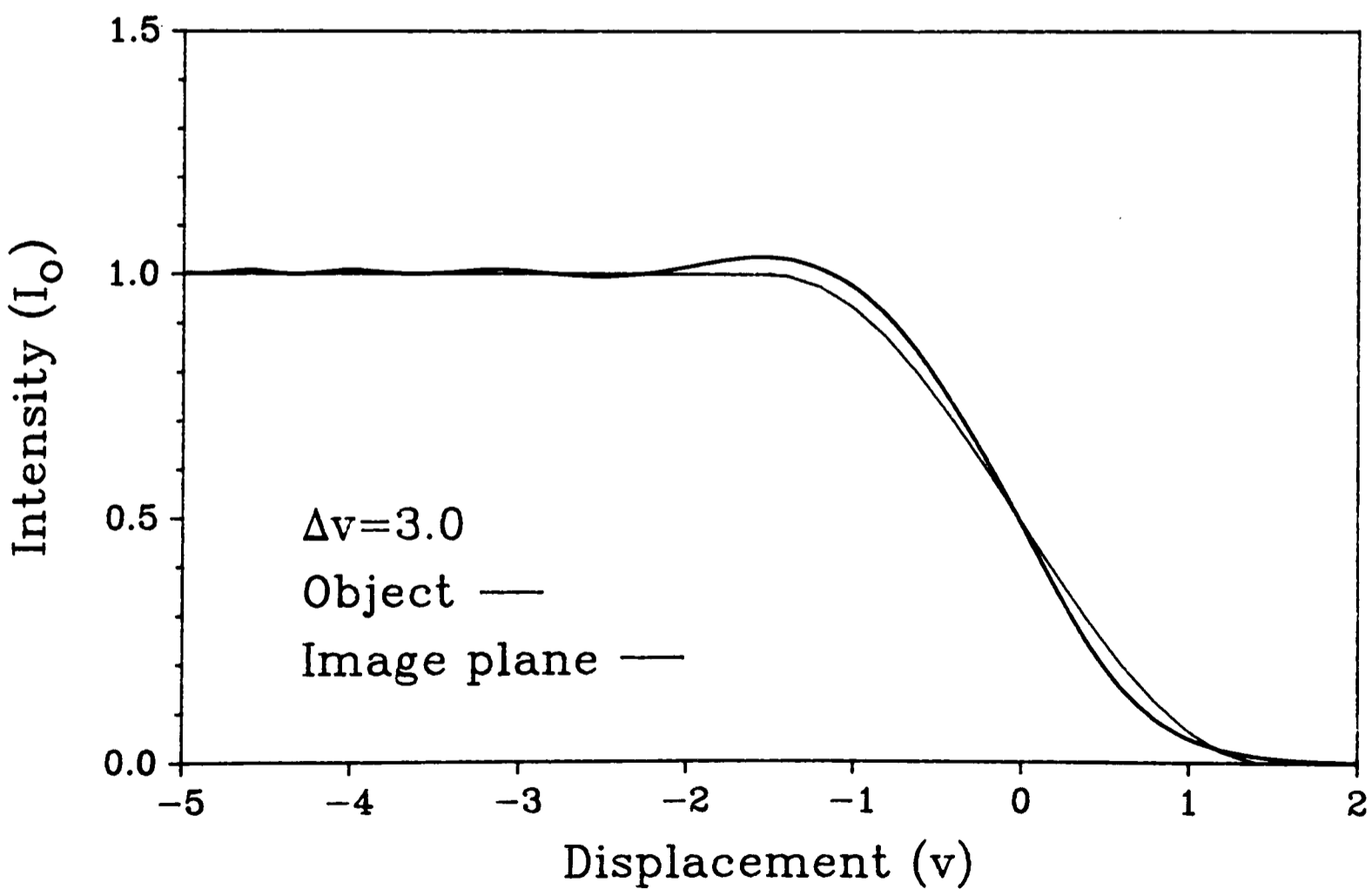
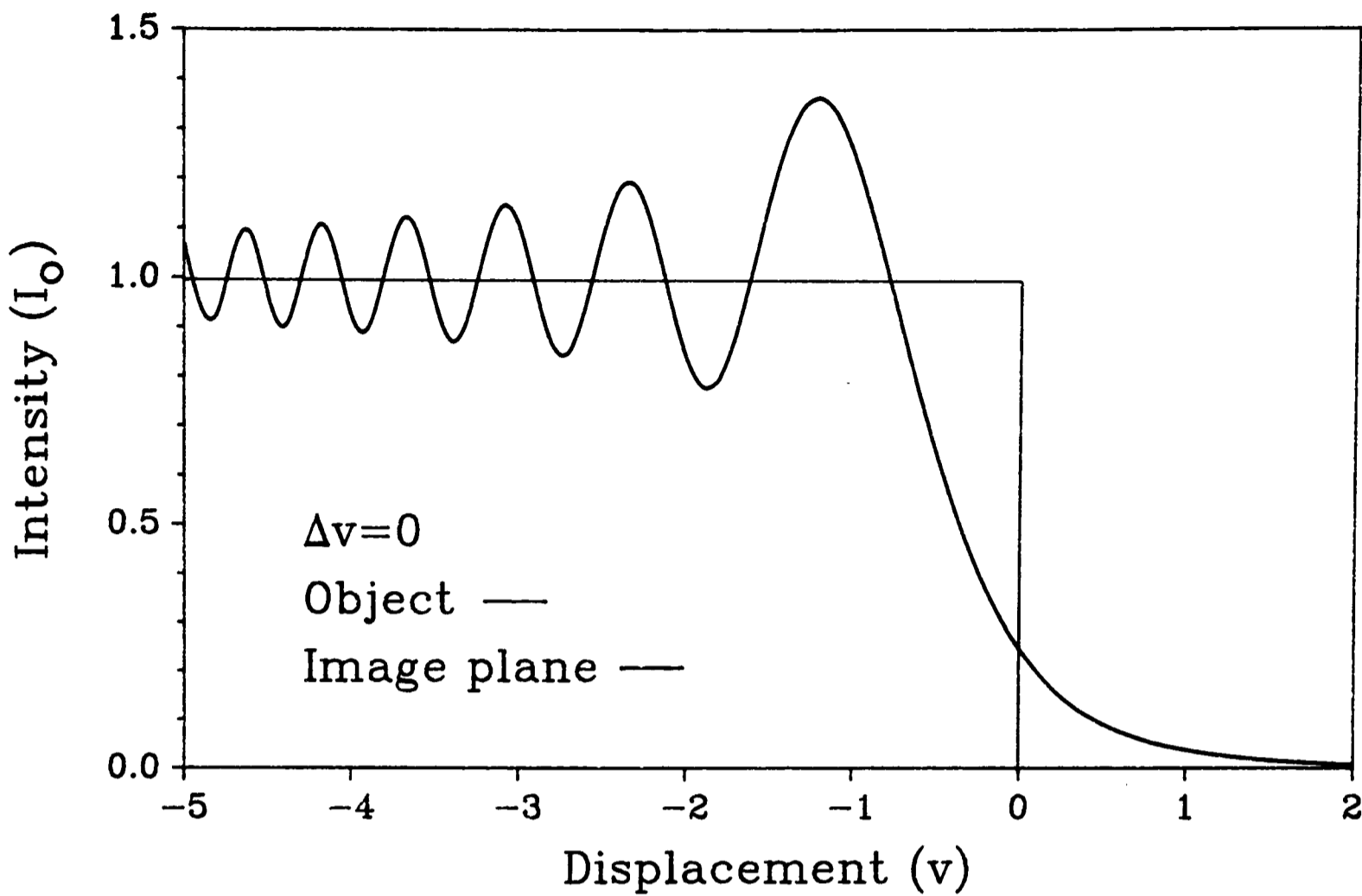


Figure 2.6: Fresnel diffraction resulting from a sharp edge.

Figure 2.7: Fresnel diffraction resulting from a sinusoidal edge.

then features of approximately 120nm could be observed without diffraction and this performance certainly could not be matched even by a confocal light microscope. This is supported by the absence of any diffraction effects in the resists exposed on either the Oxford or the RAL X-ray microscope systems. Cheng [1986] has observed diffraction, in the image of a yolk granule, but in this case a monochromatic illumination source was used to view a particularly particulate specimen.

There will be a problem with Fresnel diffraction, however, when a ‘thick’ specimen is viewed in which small sub-structures are supported in a medium and are therefore not resting on the resist surface. In this case, s may be large and the corresponding value of Δy possibly bigger than the small feature itself. In such a situation, Fresnel diffraction will be a severe and unsurmountable problem, suggesting that the technique of SXCM will only be of use for viewing sub-micron specimens if they are discrete or at least not distributed through a large supporting structure. It is for this reason that the current studies have used individual objects of a few microns size as specimens, such as the *Bacillus cereus* and *Schizosaccharomyces pombe*, which are able to rest on the resist surface prior to exposure.

2.7.3 Dosage statistics

A third effect arises from the statistics of the X-ray dosage received by each area of the resist. For an exposure flux of $E_i \text{ J/cm}^2$, the number of photons absorbed by a small area of the resist, of side $s \text{ cm}$, will be

$$\bar{n} = (E_i/h\nu)As^2 \quad [2.16]$$

where A is the absorbed fraction of radiation, given by

$$A = 1 - e^{-\alpha d} \quad [2.17]$$

for a thickness d of resist, of linear absorption coefficient α . To record details of a size s , the thickness of the resist will have to be approximately s or smaller to minimize the degrading effects of penumbral blurring and Fresnel diffraction. Since the photons arrive at random and independently of each other, the actual dose for each area will be determined by the Poisson distribution;

$$p(n, \bar{n}) = (\bar{n}^n / n!) e^{-\bar{n}} \quad [2.18]$$

Considering the case where, for simplicity, $\bar{n}=16$, and we wish to study a specimen of transmissivity $T=0.5$ such that $\bar{n}=8$ for those areas of resist under the specimen, figure 2.8 shows the probability of exposure for each area of the resist. We can see that there is a sizable overlap between the two regions, indicating areas of the resist which may not be definitely classified as either representing the specimen or not. This problem obviously becomes more acute as \bar{n} decreases, arising from the requirement of higher resolution (ie. small s) or low incident fluxes. The overlap is also increased for specimens of low contrast (small T), in which case, much higher fluxes are required to differentiate between different regions of the specimen. The width of the Poisson distribution is defined by its standard deviation

$$\sigma = \sqrt{\bar{n}} \quad [2.19]$$

and a typical criterion for low error probability is that overlap between the two Poisson distributions should only occur outside the 3σ limit of each distribution. This gives us

$$\bar{n} - T\bar{n} = 3\sigma_{\text{clear}} + 3\sigma_{\text{spec}} \quad [2.20]$$

leading to

$$\bar{n} = 9(1 - T^{1/2})^{-2} \quad [2.21]$$

which requires a flux of

$$E_i = \bar{n} h \nu / \alpha s^3 \quad [2.22]$$

This function is illustrated in figure 2.9 for various specimen transmissivities. The formulae [2.21] and [2.22] indicate that, for example, to obtain a resolution of $s=30\text{nm}$ for a specimen of transmissivity $T=0.5$ at water window wavelengths, we would require

$$\bar{n} = 105 \quad \text{and} \quad E_i \sim 10\text{mJ/cm}^2$$

a figure which has been equalled with the current microscope system. Equation [2.22] also illustrates the inadequacy of using a high contrast test specimen (typically a gold structure for which $T=0$) to evaluate the resolution of a particular X-ray microscope for use with biological samples. It also indicates the importance of limiting the illuminating radiation to within the water window; any contribution from X-rays

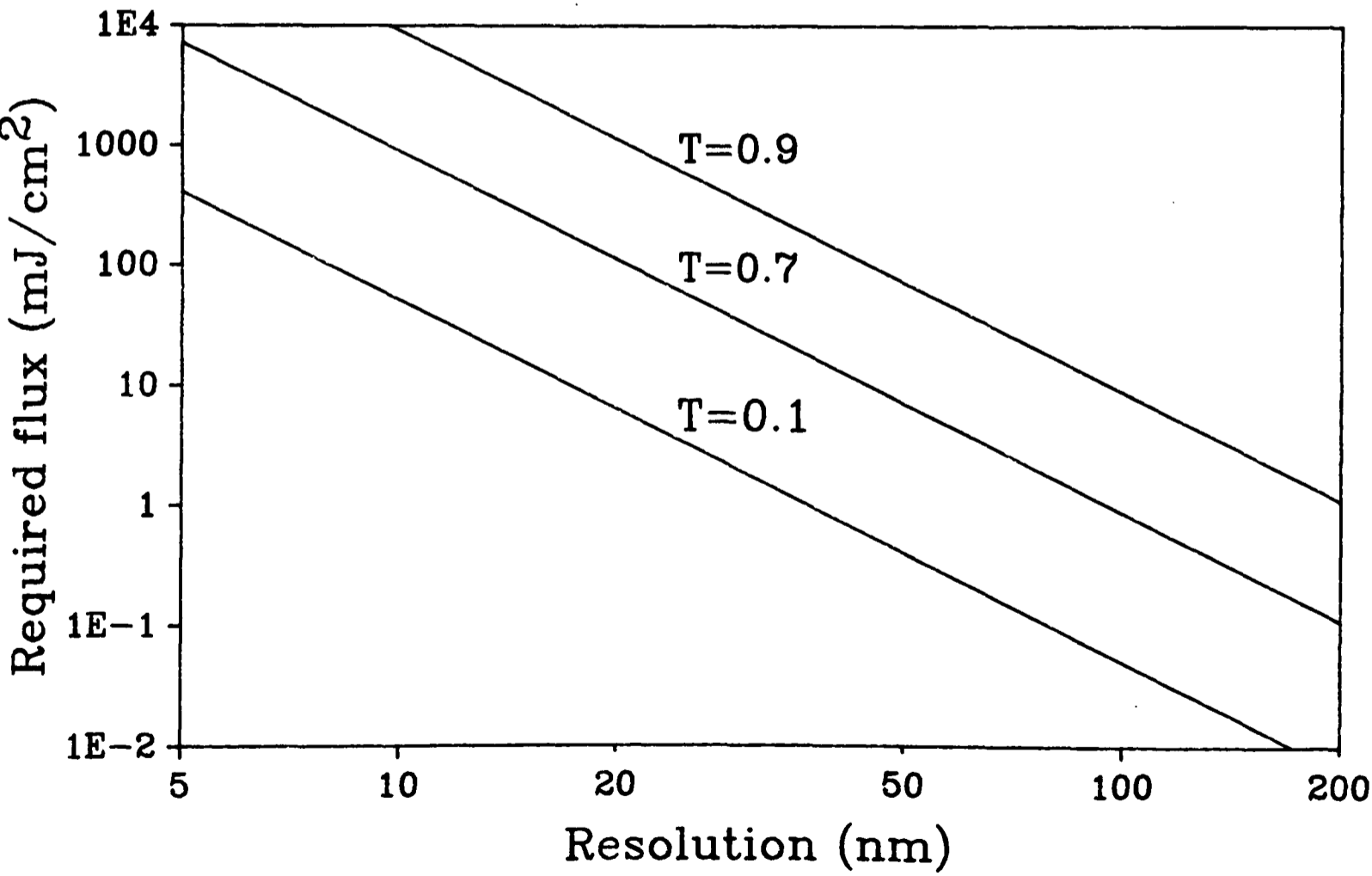
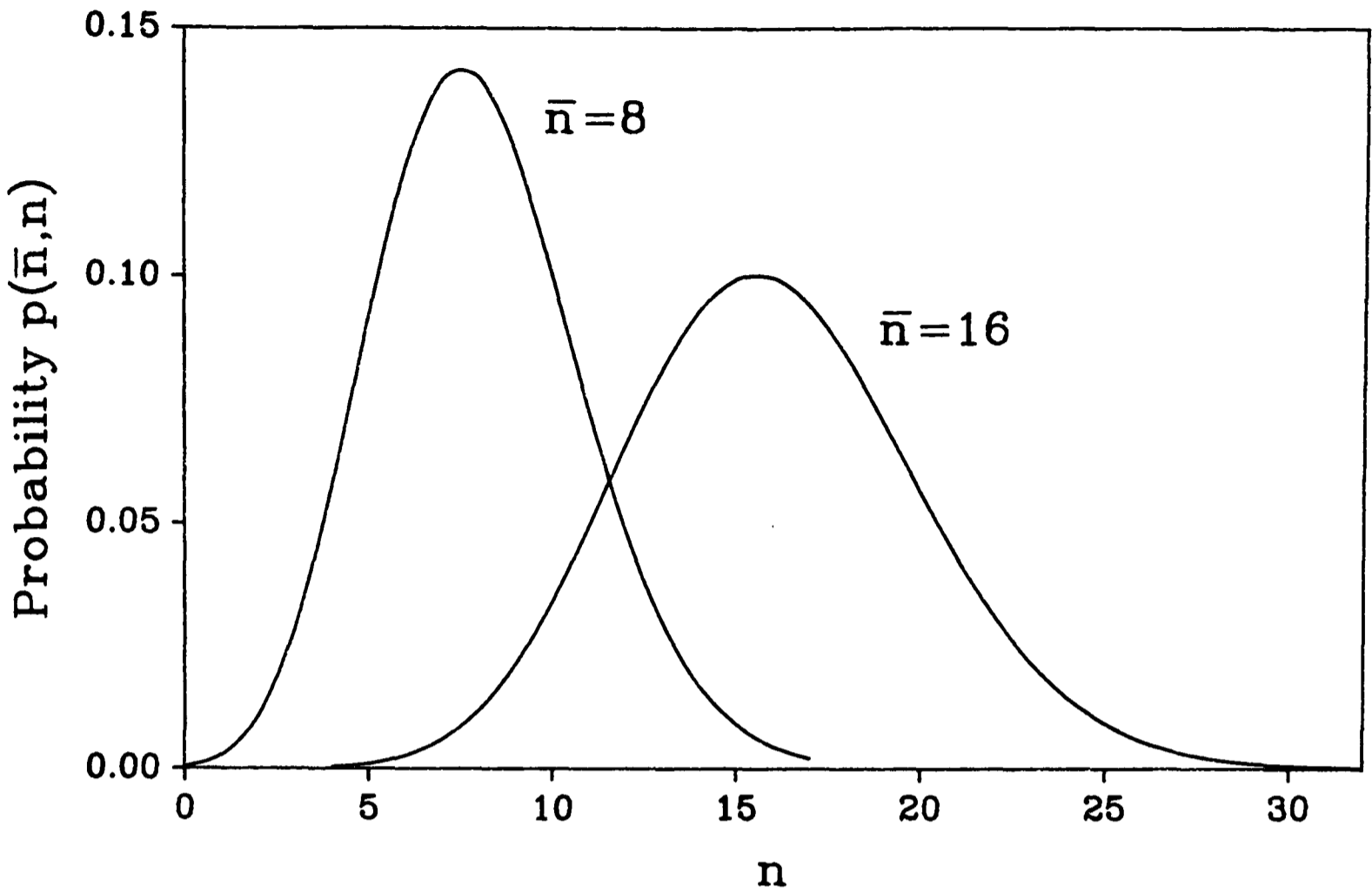


Figure 2.8: Poisson distributions for two values of \bar{n} .

Figure 2.9: The fluxes required to differentiate objects of various transmissivities.

outside this range will decrease the contrast in the final image because of the similar cross-sections for absorption exhibited by carbon and oxygen at these wavelengths.

Figure 2.10 illustrates the contributions made by Fresnel diffraction and dosage statistics to the resolution obtained by the SXCM technique. For the case of Fresnel diffraction, equation [2.15] has been used; to evaluate the limit imposed by dosage statistics, equations [2.21] and [2.22] have been applied with T , the transmission of a particular specimen thickness, evaluated with a linear absorption coefficient of $2 \times 10^4 \text{ cm}^2/\text{g}$ and a density of 1.35 g/cm^3 (ie. a typical protein). The flux incident on the specimen was taken as 10 mJ/cm^2 . The graph indicates that the dosage statistics are only likely to have an appreciable effect on resolution for specimens of less than $\sim 20 \text{ nm}$ thickness, although this value will increase for less protein-dense specimens, whose transmission to water window X-rays will be larger than the relatively dense model used in these calculations.

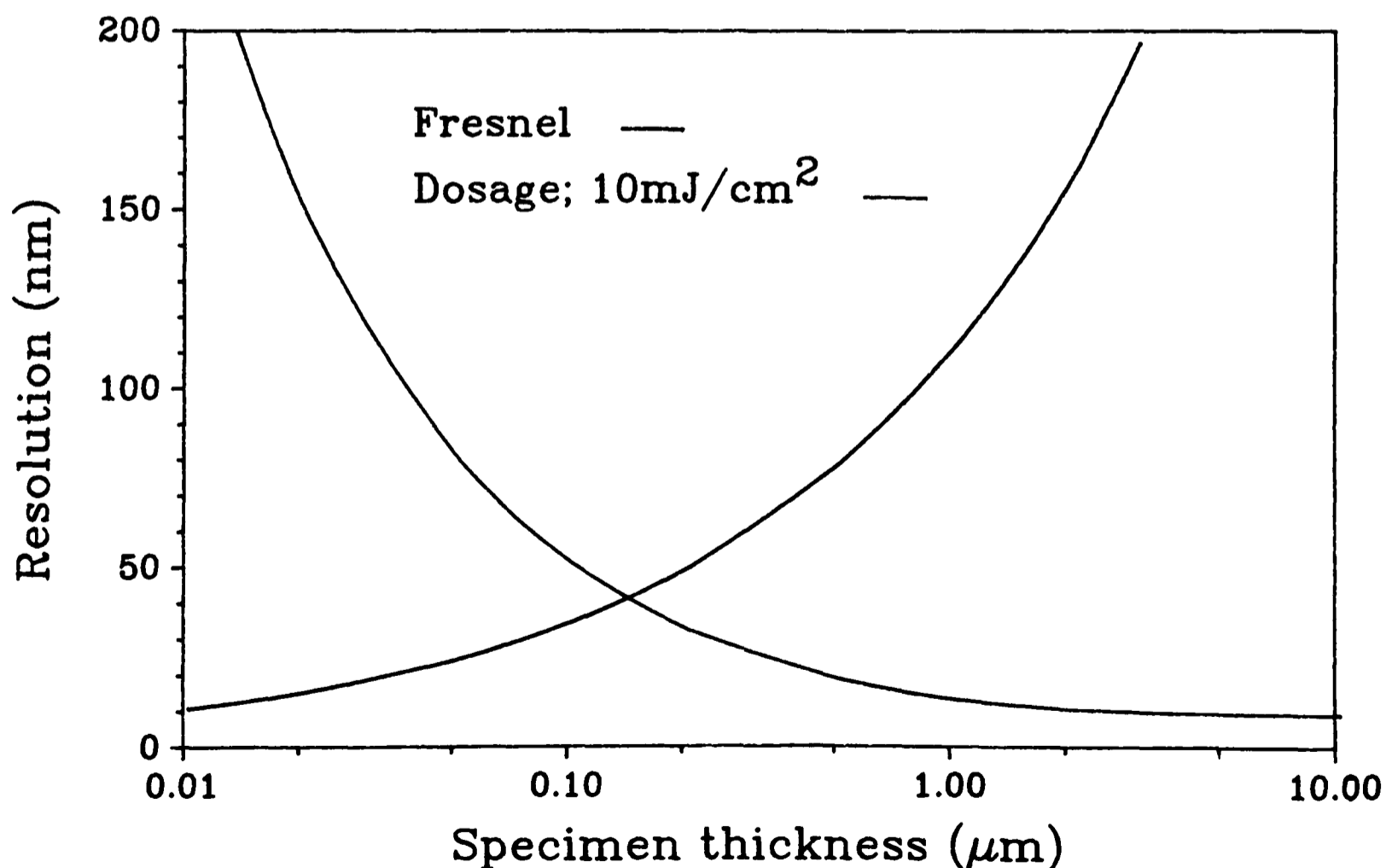


Figure 2.10: The contributions made by Fresnel diffraction and dosage statistics to the resolution obtained in SXCM.

2.7.4 Radiation damage and hydrodynamic motion

As stated previously, one of the main advantages of SXCM using a pulsed plasma source is that an image is recorded within $\sim 20\text{ns}$, before radiation damage can affect the structure of the specimen. The absorption of the X-ray photons in the specimen takes place in $\sim 10^{-17}\text{s}$, causing the liberation of secondary electrons. These are then thermalized in 10^{-13}s resulting in the production of free radical clusters with an initial diameter of $\sim 2\text{nm}$, centred on the original photoabsorption event. These diffuse outwards at a rate of $\sim 10^{-2}\text{mm}^2/\text{s}$ and persist for up to 1ms . Consequently, although some radiation damage will be apparent within 20ns , this will only represent a small fraction of the total damage done by the event, and so we may assume that the radiation damage limit to resolution is not an important factor in the current application.

However, one disadvantage of the short exposure time is that it does not allow a thermal equilibrium to be established between the X-ray energy absorbed and natural heat dissipation. For example, a $1\mu\text{m}$ thick specimen of protein subjected to a flux of only $10\text{mJ}/\text{cm}^2$ will absorb approximately $70\text{J}/\text{g}$ of X-ray radiation, indicating that for the majority of exposures made with the current system, the specimen will probably have been heated, albeit momentarily, to over 100°C . London [1989] has considered this heating effect on an atomic level and a detailed theoretical treatment suggests that for a 20ns pulse, only features of at least 100nm could be successfully imaged. As yet, no practical investigation has been carried out to test these predictions; the images of biological specimens made both at Oxford and RAL do not appear to have been affected by any appreciable degree of hydrodynamic expansion.

2.8 SECONDARY APPLICATIONS

The various methods in which X-ray microscopy has been put into effect have led to several other techniques for obtaining information about the specimen being studied. Attempts at stereo imaging and elemental analysis have had some small measure of success.

2.8.1 Stereo imaging

Experiments have been conducted by Rosser [1985], in which the beam from the Nd:YAG Vulcan laser at the Rutherford Appleton Laboratory was used to create two plasma X-ray sources, separated from each other by a small fixed distance. These simultaneously illuminated a specimen, which was placed a small distance in front of a recording resist. In this way, two overlapping images were recorded on the resist. He concludes that "having both stereo images recorded overlapping is obviously a severe limitation, but with care (and, one suspects, a great deal of computing) it may be possible to develop this technique to extract sections of thick specimens." However it is unlikely that a specimen of even the simplest biological structure would be suitable for such computational treatment. The only realistic arrangement of this method would be to have a specimen to resist distance large enough that the two images did not overlap with each other. Unfortunately, this would lead to a very large decrease in resolution arising from penumbral blurring and Fresnel diffraction (sections 2.7.1 and 2.7.2).

A more realistic approach has been taken by Cheng [1986], in which two images were taken with different angles of incident radiation, on separate recording resists. Although this method will result in a true stereo pair, the fact that the cell has to survive the first of the imaging processes necessitates its preparation and fixing prior to viewing. This nullifies the main advantage of X-ray microscopy over electron microscopy; that no sample preparation is required. In the past when members of the biological community were consulted over the value of stereo imaging, it was found that the achievement of high resolution in final images was considered by far a more important goal.

2.8.2 Elemental mapping

The various absorption edges exhibited by the elements which make up biological specimens may be used to highlight the spatial distribution of a particular element within the specimen (as demonstrated by Kirz [1992] and Suzuki [1992] for example). Two images must be taken of the same sample (with the inherent disadvantages discussed above); firstly with an X-ray illuminating source whose

wavelength falls predominantly just below an absorption edge of the element under investigation, and secondly with a wavelength just above the edge. Assuming that the absorption coefficients of other elements in the specimen do not suffer any large variations in this wavelength range, then the subtraction of the two images will result in a map of the location of the given element. This method obviously requires the X-ray source to have a narrow linewidth and be tunable, and consequently must make use of a synchrotron.

While competing methods such as proton induced X-ray emission (PIXIE) and secondary ionization mass spectroscopy (SIMS) have relatively low resolutions in comparison to optical microscopy, their values are similar to those obtained from the scanning arrangements used to implement this X-ray technique, and they may additionally be used on specimens which have undergone only a moderate degree of preparation. In this respect, the technique currently has little to offer over alternative, well established methods.

2.9 FUTURE PROSPECTS FOR X-RAY MICROSCOPY

As it currently stands, X-ray microscopy is beginning to gain some recognition amongst its would-be users of biologists, botanists, and other workers in the life sciences. In order to progress further, it is these groups who must be consulted as to the direction which must be taken by those who are currently developing soft X-ray microscopes, of whatever type. In the past, biological specimens viewed with X-ray microscopes have largely been chosen as those most amenable to the technique - ie. robust and with naturally high contrast in terms of carbon densities. It is now necessary to address the problems arising from 'non-ideal' specimens and specifically the treatment of material up to the time of observation. For example, workers in the Biochemistry Department at Birmingham University have expressed an interest in using soft X-ray contact microscopy to study electroporation processes which occur when fibroblast cells are subject to small electrical voltages. Such time-resolved studies will require very careful specimen preparation, but this is exactly the type of opportunity offered by soft X-ray microscopy which could not possibly be met by

electron microscopy. The future of X-ray microscopy will depend on its ability to meet the actual requirements of members of the life sciences community, by studying biological systems which are of interest to them, rather than those which make ready subjects for the X-ray microscopy technique.

CHAPTER THREE

THE KrF LASER SYSTEM

3.1	INTRODUCTION
3.2	THE NEW LASER ELECTRICAL CIRCUIT
3.2.1	Operation of the laser electrical circuit
3.3	INITIAL '2 JOULE' DESIGN
3.4	SECOND '2 JOULE' DESIGN
3.5	FINAL '2 JOULE' DESIGN
3.6	THE NEW GAS SYSTEM
3.7	THE NEW ELECTRODE STRUCTURE
3.7.1	Back pre-ionization
3.7.2	Side pre-ionization
3.8	OPTIMIZATION OF THE NEW LASER SYSTEM
3.8.1	Mechanical clamping
3.8.2	Securement by epoxy glue
3.8.3	Structural alteration of the wound electrode
3.8.4	Use of the second electrical circuit design
3.9	OPTIMIZATION OF THE FINAL ELECTRICAL CIRCUIT DESIGN
3.10	GAS OPTIMIZATION
3.11	OSCILLATOR LASER PERFORMANCE
3.12	SUMMARY AND FURTHER DESIGN IMPROVEMENTS

3.1 INTRODUCTION

From the conversion efficiencies obtained with the original '1 Joule' KrF laser system, it was apparent that a sufficiently large X-ray flux for single-shot imaging of a wet biological specimen could not be obtained from the system as it then was. In the initial imaging experiments, at least five shots were required to obtain a satisfactory image of dehydrated diatom specimens. Furthermore, the progression to wet cell imaging would require the use of a 100nm thick Si_3N_4 window, necessary to isolate the specimen from the vacuum of the target chamber. In addition to absorption by this window, the $\sim 1\mu\text{m}$ thickness of water in which the specimen would be resident would further decrease the X-ray flux reaching the PMMA resist. Taking the 'average' value of the mass absorption coefficients for the water window region (2.3 to 4.4nm) as

$1.5 \times 10^4 \text{ cm}^2/\text{g}$ and $0.3 \times 10^4 \text{ cm}^2/\text{g}$ for Si_3N_4 and water, this gives two corresponding attenuation factors of $\sim 40\%$ and $\sim 25\%$ respectively, which combine to reduce the flux reaching the polymer resist by half.

Therefore, it was decided to upgrade the laser system to one which could deliver 2J of laser energy with a plane-plane cavity and some large fraction of this when equipped with an unstable resonator. Measurements of the laser energy were made with a Gentec ED-500 pyro-electric meter. At the same time, both the gas system and the electrical circuit controlling the laser were simplified and re-built in the light of experience gained with the original system. These alterations and improvements are detailed in the following sections, along with an explanation of the operation of the capacitor transfer circuit.

3.2 THE NEW LASER ELECTRICAL CIRCUIT

In order to pump the enlarged gain volume of the new laser with a sufficient energy, the external electrical circuit had to be re-designed to incorporate a larger storage capacitor for the amplifier. In the original '1 Joule' system, the gain volume had been

$$\begin{aligned} V_g &= 86(\text{length}) \times 1.5(\text{width}) \times 2.5(\text{height}) \text{ cm}^3 \\ &= 0.322 \text{ l} \end{aligned}$$

With a storage capacitance of $C_s=100\text{nF}$ and a charging voltage $V_o=55\text{kV}$, the internal peaking capacitors C_p , of total capacitance 36nF , were raised to a potential of

$$\begin{aligned} V_p &= 2V_o C_s / (C_s + C_p) \\ &= 80.9\text{kV} \end{aligned} \tag{3.1}$$

(as shown in section 3.2.1). This led to an energy of

$$\begin{aligned} E &= \frac{1}{2} C_p V_p^2 \\ &= 118\text{J} \end{aligned} \tag{3.2}$$

being transferred to the internal capacitor bank. Thus, assuming breakdown occurred after the full transfer of charge, the gain volume would have been pumped to the extent of 366J/l . To achieve the same density with twice the previous gain volume (in order to achieve an output energy of 2J), with a peaking capacitance of $C_p=65\text{nF}$ in

the new laser electrode structure, a storage capacitance of $C_s=210\text{nF}$ would be required.

It was also decided to simplify the circuit by the replacement of the commercial mid-plane spark gap used to trigger the electrical circuit with a spark gap of a standard Clarendon design. This was supplied with air at ~ 2 atmospheres pressure to enable the gap of approximately 7mm to hold off the 60kV potential difference between the two terminals. The standard laboratory air supply was used for this purpose and only a slow flow rate was required to achieve extremely reliable triggering of the electrical circuit. The elimination of water vapour from the air supply was not found to be necessary, as it had been for the previous mid-plane spark gap, and the presence of oil vapour only resulted in a very slow build up of a brown deposit in the spark gap which did not adversely affect its operation. The spark gap was triggered by a pulser unit built by the Clarendon Electronics Workshop and a commercial spark plug, which could be easily replaced as necessary, was used to initiate the breakdown of the gap.

Finally, the mechanical high voltage switch, designed by Cotton [1990], was removed. This had enabled the oscillator to be run independently of the amplifier, a facility which was not necessary for the new system, since beam alignment could be carried out satisfactorily using the NO_2 attenuator and HeNe alignment lasers.

3.2.1 Operation of the laser electrical circuit

A capacitor transfer circuit was used to run both the oscillator and amplifier lasers; figure 3.1 illustrates the general arrangement of the two units. Each circuit operates independently of the other, and is represented in figure 3.2. The purpose of the circuit is to provide a way of storing energy from the power supply over a period of a few seconds, and then releasing this energy into the laser discharge in as short a time as possible. The storage capacitor C_s is charged to a potential $+V_0$ through resistors R_1 and R_2 (R_2 being made up of a chain of resistors of total value $1\text{M}\Omega$, located inside the power supply), whereupon point A will be at $+V_0$ volts. When this charging cycle is complete, the spark gap SG is triggered, causing point A to fall to earth, and point B to $-V_0$ volts. At this point we have the equivalent electrical circuit illustrated in figure

3.3. Capacitor C_s then discharges through the inductor L_1 to charge the peaking capacitor C_p , which was initially uncharged. The resistor R_1 , which had a value of $27k\Omega$ for both lasers, was chosen to be very large in comparison to the initial resistance of the laser gap G . Capacitor C_p will continue to be charged by the storage capacitor C_s until the potential across it, and hence the laser gap G , is sufficiently large for the laser gap to break down. The voltage at which this occurs will depend on the laser electrode configuration (ie. electrode cross-section and separation), the pressure and formulation of the laser gas mix and the extent of the pre-ionization (described in section 3.7). Up to the point of breakdown, the circuit may be considered as illustrated in figure 3.4. The free oscillation of current in this circuit is described by

$$L_1 \ddot{I} + I/C_s + I/C_p = 0 \quad [3.3]$$

leading to $I = \text{Re}(I_0 e^{i\omega t})$ where $\omega^2 = (C_s + C_p)/L_1 C_s C_p$. We may also write

$$\begin{aligned} V_s &= V_0 - \int I dt / C_s \\ &= L_1 \dot{I} + \int I dt / C_p \end{aligned} \quad [3.4]$$

where V_s is the potential at the point illustrated in figure 3.4. Equating these two;

$$V_0 = L_1 \dot{I} + \int I dt \cdot (C_s + C_p) / C_s C_p \quad [3.5]$$

Thus, at $t=0$, $V_0 = L_1 i\omega I_0$ and so we obtain $I_0 = V_0 / L_1 i\omega$. The voltage across the peaking

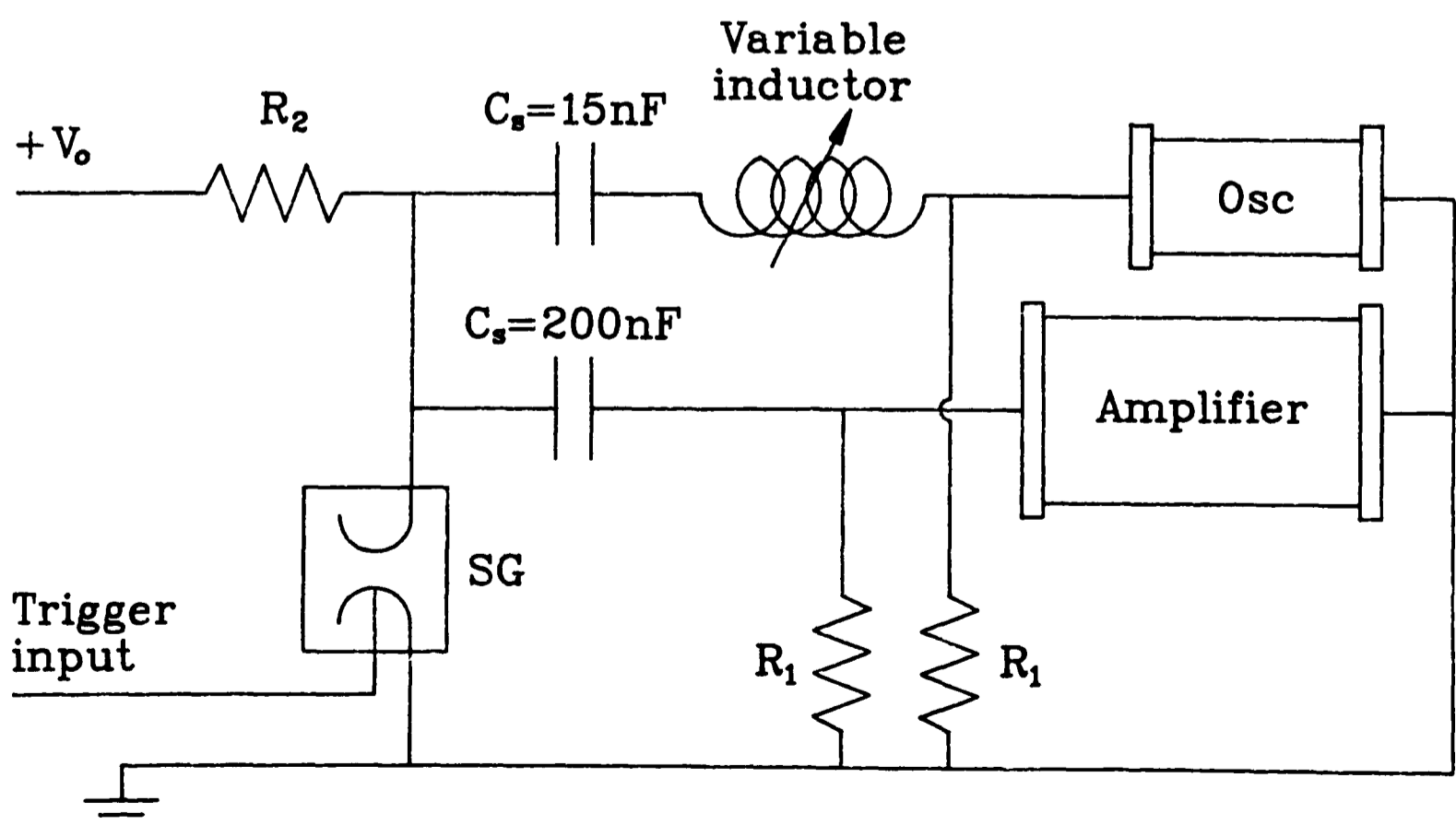


Figure 3.1: The oscillator-amplifier electrical circuit.

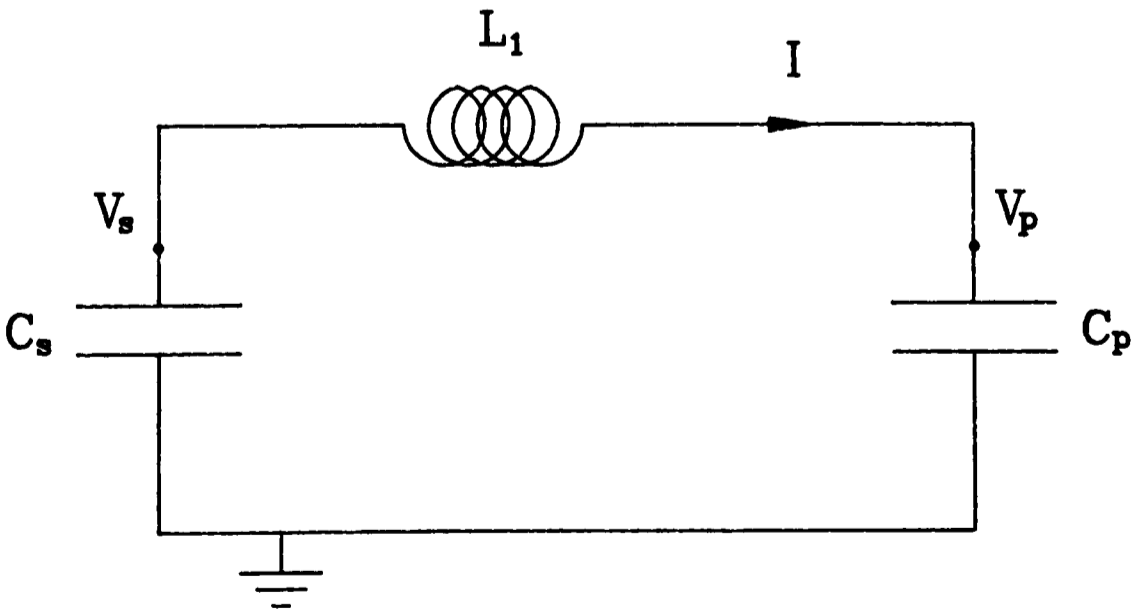
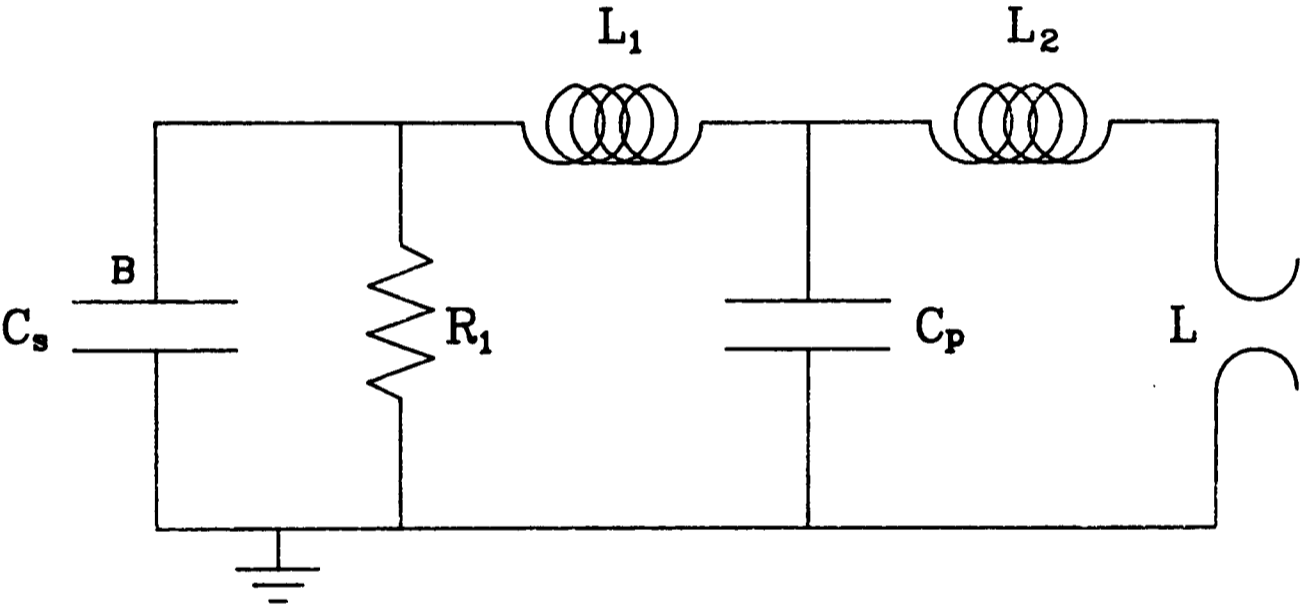
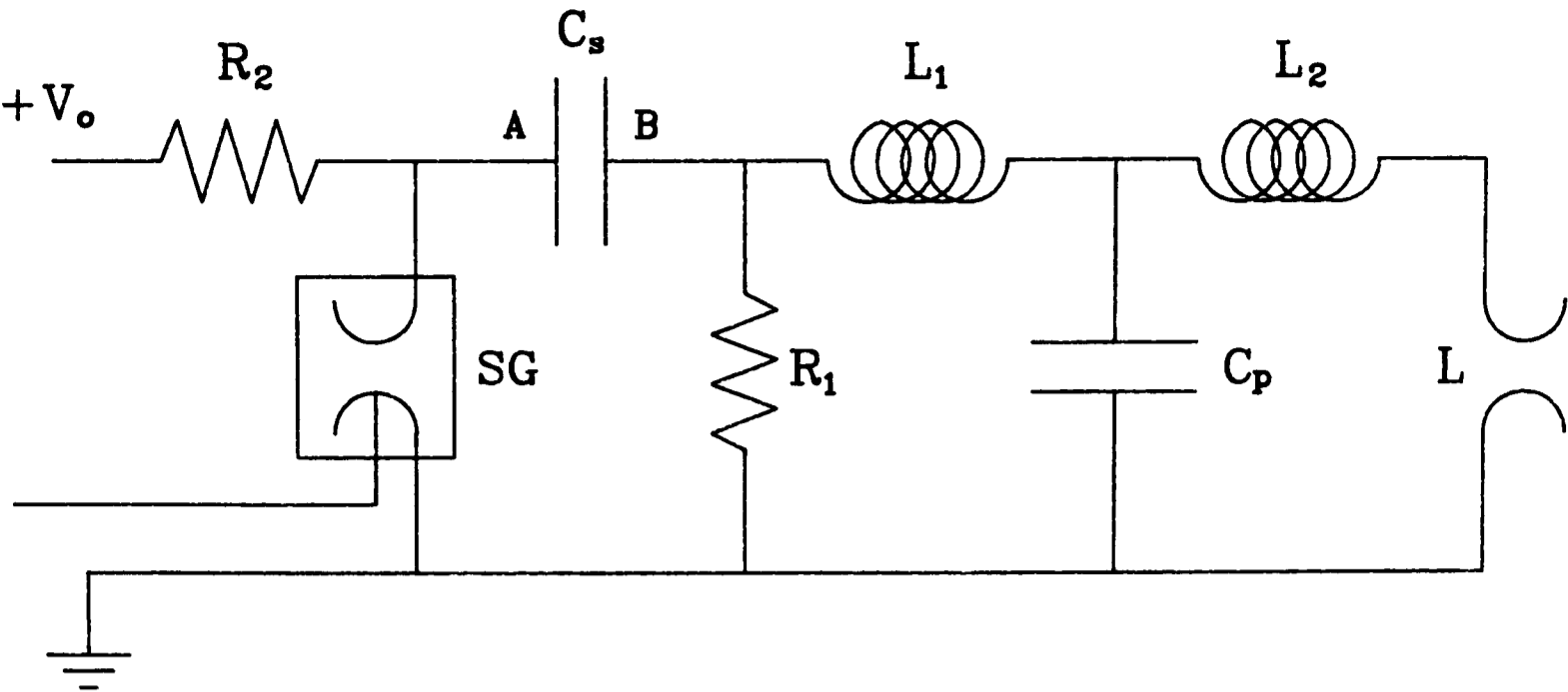


Figure 3.2: The capacitor transfer circuit

Figure 3.3: The equivalent circuit after triggering of the spark gap.

Figure 3.4: Charging of the internal peaking capacitors.

capacitor and hence the laser gap G is then given by

$$\begin{aligned} V_p &= \int Idt/C_p \\ &= (e^{i\omega t_f} - e^{i\omega t_i}).I_0/i\omega C_p \end{aligned} \quad [3.6]$$

At the point when $\omega t_f = \pi$ and assuming $t_i = 0$, we obtain

$$V_p = 2V_o/L_1 C_p \omega^2 \quad [3.7]$$

Therefore, the maximum voltage which may appear across the laser gap is given by

$$V_p = 2V_o C_s / (C_s + C_p) \quad \text{after a time } \tau = \pi \sqrt{L_1 C_s C_p / (C_s + C_p)} \quad [3.8]$$

However, before this situation arises, the laser gap G will break down, and the peaking capacitor C_p will discharge through inductance L_2 into the laser channel.

i) Amplifier structure

In the amplifier module, the final electrical circuit had a storage capacitor C_s of value 200nF, while C_p was composed of 26 parallel sets of two 5nF capacitors in series, giving a total capacitance of 65nF. The inductance of the electrode structure itself is denoted by L_2 , and this was kept to as low a value as possible by situating the peaking capacitors C_p within the laser body. The small inductance L_2 thus obtained ensured that the discharge of the peaking capacitors through the laser gap G had a small rise time. The inductance L_1 was composed of 86 parallel ballast inductors (which are described in section 3.7). The peak voltage which might appear across the laser gap is given by

$$\begin{aligned} V_p &= 2 \times 60 \times 200 / (200 + 65) \text{ kV} \\ &= 90.6 \text{ kV} \end{aligned}$$

For the new '2 Joule' design, it was decided to raise the operating voltage of the laser from the previous value of 55kV to 60kV. This led to the peaking capacitors reaching a slightly greater potential before discharge occurred and consequently, a greater pumping density of the gain volume. The increase to 60kV was permitted by the use of new 100nF capacitors rated to 70kV, and limited by the power supply being used for the laser.

ii) Oscillator structure

The oscillator module had a much smaller storage capacitor, of 15nF, while capacitance C_p consisted of twenty 650pF units, making a total of 13nF. This led to a maximum attainable voltage of

$$\begin{aligned} V_p &= 2 \times 60 \times 15 / (15 + 13) \text{ kV} \\ &= 64.3 \text{ kV.} \end{aligned}$$

The structure was unchanged from the original '1 Joule' laser system and is briefly considered in section 3.11.

3.3 INITIAL '2 JOULE' DESIGN

In the original '1 Joule' laser system, great care had been taken to avoid corona and electrical shorting by the use of silicone rubber compound and perspex sheeting. For the new system, the circuit was designed initially to reside almost entirely in an on-board tank of transformer oil. This greatly reduced the need for perspex sheeting between components of different electrical potentials. The 15nF oscillator storage capacitor of the initial system was retained, while the 100nF amplifier storage capacitor was replaced by one of 238nF (both manufactured by Maxwell Laboratories Inc). However, this arrangement suffered from two major drawbacks:

a) The process of alteration and adaptation of any part of the circuit necessitated the transfer of the oil to a separate container which, linked with the residual oil left on parts of the circuit, led to a gradual contamination of all objects in the immediate area of the laser with transformer oil.

b) The requirement of having to put components such as both storage capacitors and the spark gap in a region which was relatively far away from both laser envelopes led, it soon transpired, to an unacceptably high inductance in the amplifier circuit. This limited the rate at which the potential across the laser gap could rise, resulting in premature instabilities in the discharge, and a low output energy. A fast rise-time would result in more intense pre-ionization, with a smaller time delay between the formation of the pre-ionizing sparks and the laser breakdown. This obviously limits the extent to which the ionized gas may recombine, and thus

encourages a more uniform discharge.

The maximum laser output energy obtained with this circuit was only 429mJ.

3.4 SECOND '2 JOULE' DESIGN

With the importance of obtaining a low inductance in any circuit constructed to supply the laser electrode structure so evident, the idea of enclosing any part of it in a tank of transformer oil was rejected. Furthermore, it was considered that the 238nF storage capacitor would also be a hindrance in achieving a circuit of sufficiently low inductance. This was because the capacitor was of such a size and shape that it had to be laid on its side within the framework of the laser system, thus making the electrical circuit unnecessarily complicated. It was therefore replaced by five capacitors (manufactured by CSI), each of capacitance 35nF, rated to 100kV DC. This arrangement enabled a close positioning of the capacitor terminals to the amplifier high voltage feed-throughs, and the spark gap to be located on top of the capacitors in a readily accessible position. With this arrangement, an output energy of 1.3J was obtained, before a capacitor failure led to the construction of a third, and final, design.

3.5 FINAL '2 JOULE' DESIGN

The procurement of two further CSI capacitors, of capacitance 100nF each, rated to 70kV DC, enabled the construction of a third electrical circuit, of even lower inductance than the previous ones. The relatively large distance between the terminals of each capacitor was used to minimize the size of the discharge circuit loop (as illustrated in figures 3.5 and 3.6). The size of the high voltage plate was greatly reduced in this arrangement, and the oscillator storage capacitor was also brought near to the spark gap, to reduce the amount of corona and the likelihood of external flashovers.

3.6 THE NEW GAS SYSTEM

The original gas system had been constructed to enable the amplifier and oscillator to be run with different gas mixes and at different pressures in an attempt to

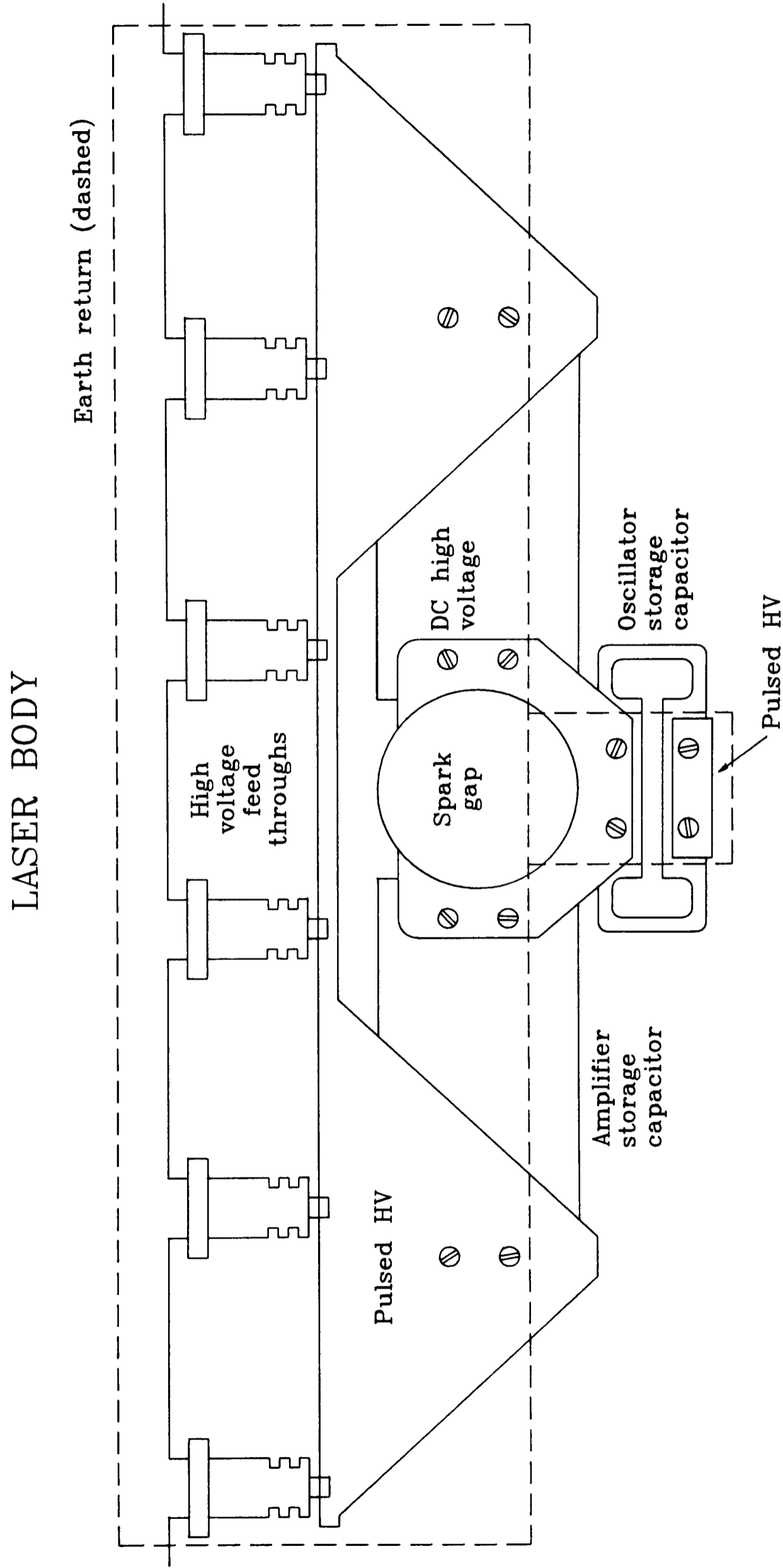


Figure 3.5: Aerial view of the external electrical circuit - final design.

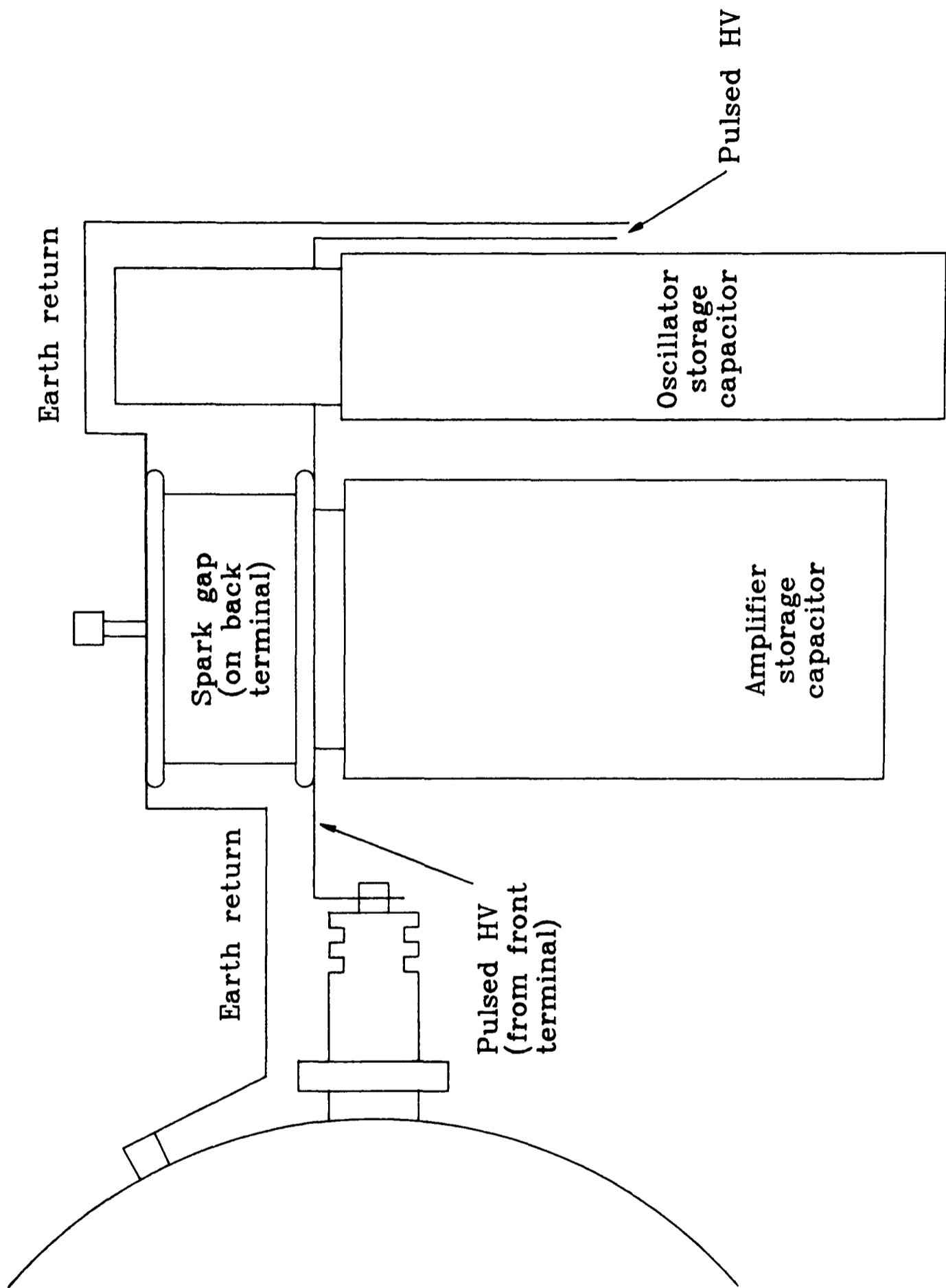


Figure 3.6: End view of the external electrical circuit - final design.

control the relative timing of the two discharges, so as to optimize the output of the oscillator and the divergence of the amplifier beam. However, this prevented the GP2000 gas purifier being used for both lasers, and resulted in the rapid decrease of the laser output energy due to the formation and build-up of impurities within the gas volume. Consequently, the oscillator and amplifier were run with the same gas mix, so that the gas purifier could be used. The new gas system (represented schematically in figure 3.7) was simplified by the removal of this unused facility. The relative timing of the two laser discharges was then controlled by the introduction of a variable inductor in the oscillator laser circuit (as described in section 4.4.1) for both the '1 Joule' and '2 Joule' systems, the value of which enabled the oscillator to reach threshold before, and hence seed, the amplifier. The solenoid valves, which had proved to be unreliable, were also removed and all taps were of the Edwards KF type, with fluorine resistant diaphragms. To further increase the system's transportability, the three connections from the gas system to the GP2000 were mounted on a readily accessible bulkhead, to enable the purifier to be easily disconnected from the main body of the laser and be moved independently of it.

3.7 THE NEW ELECTRODE STRUCTURE

The most important part of the upgrade was the design and construction of a completely new electrode structure for the amplifier laser, with the aim of it being able to deliver 2J of laser radiation. The beam cross-section was increased from the $15 \times 25 \text{ mm}^2$ of the original system to a potential maximum of $30 \times 30 \text{ mm}^2$. To ensure an even discharge in this larger gain volume, both back and side pre-ionization were again employed. Investigations by Cotton [1990] on the original '1 Joule' design indicated that the back pre-ionization had little or no effect on the laser output energy, probably due to the obscuration of the sparks by the wire wound mesh electrode. In the new design, the pre-ionizing sparks were brought to within 7mm of the front face of the mesh electrode in an attempt to overcome this problem. A cross-section of the entire electrode structure (after the various design modifications detailed in the following sections) is given in figure 3.8. A view of the high voltage plate is given in plate 3.1.

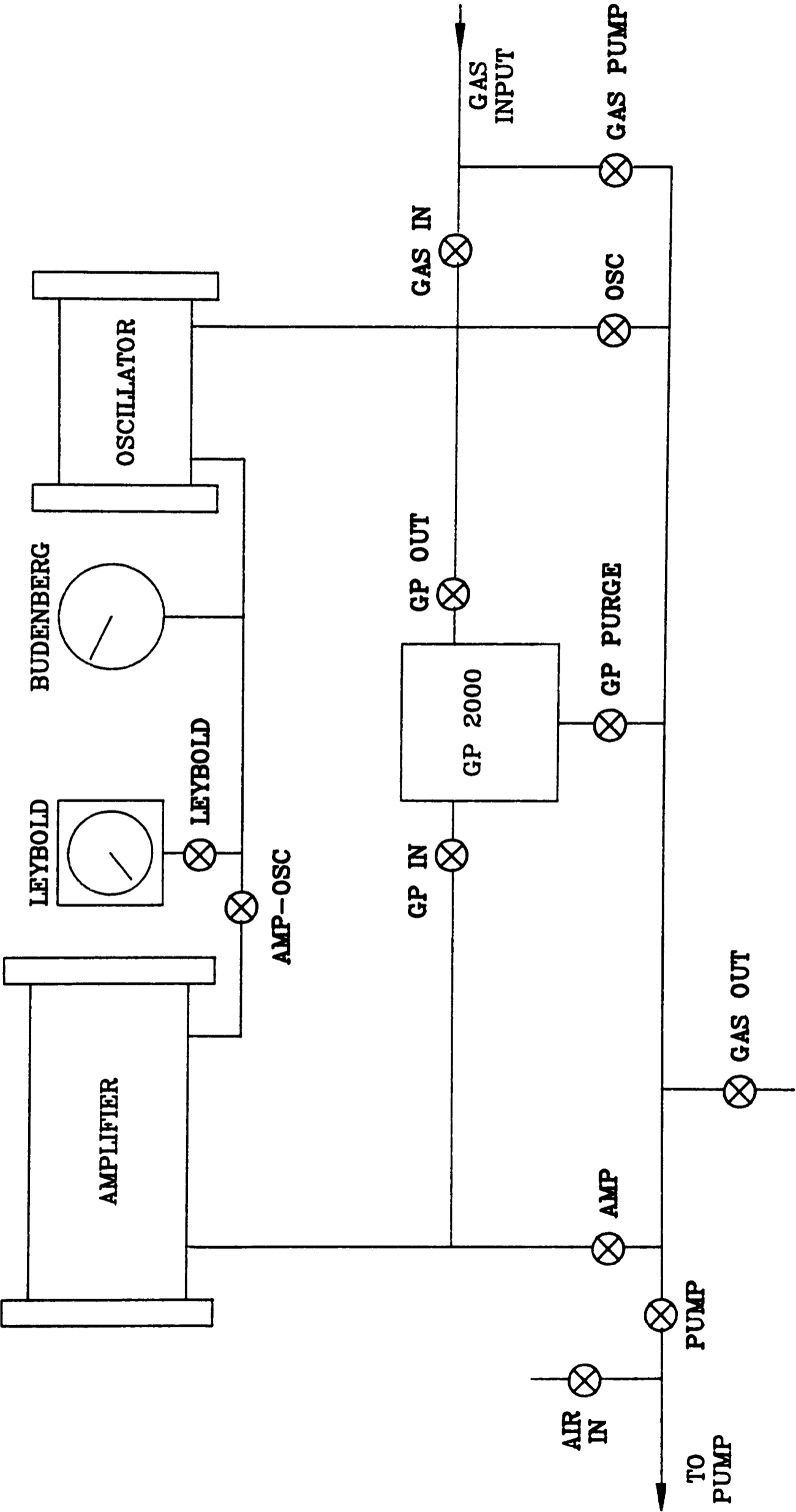


Figure 3.7: The laser gas system.

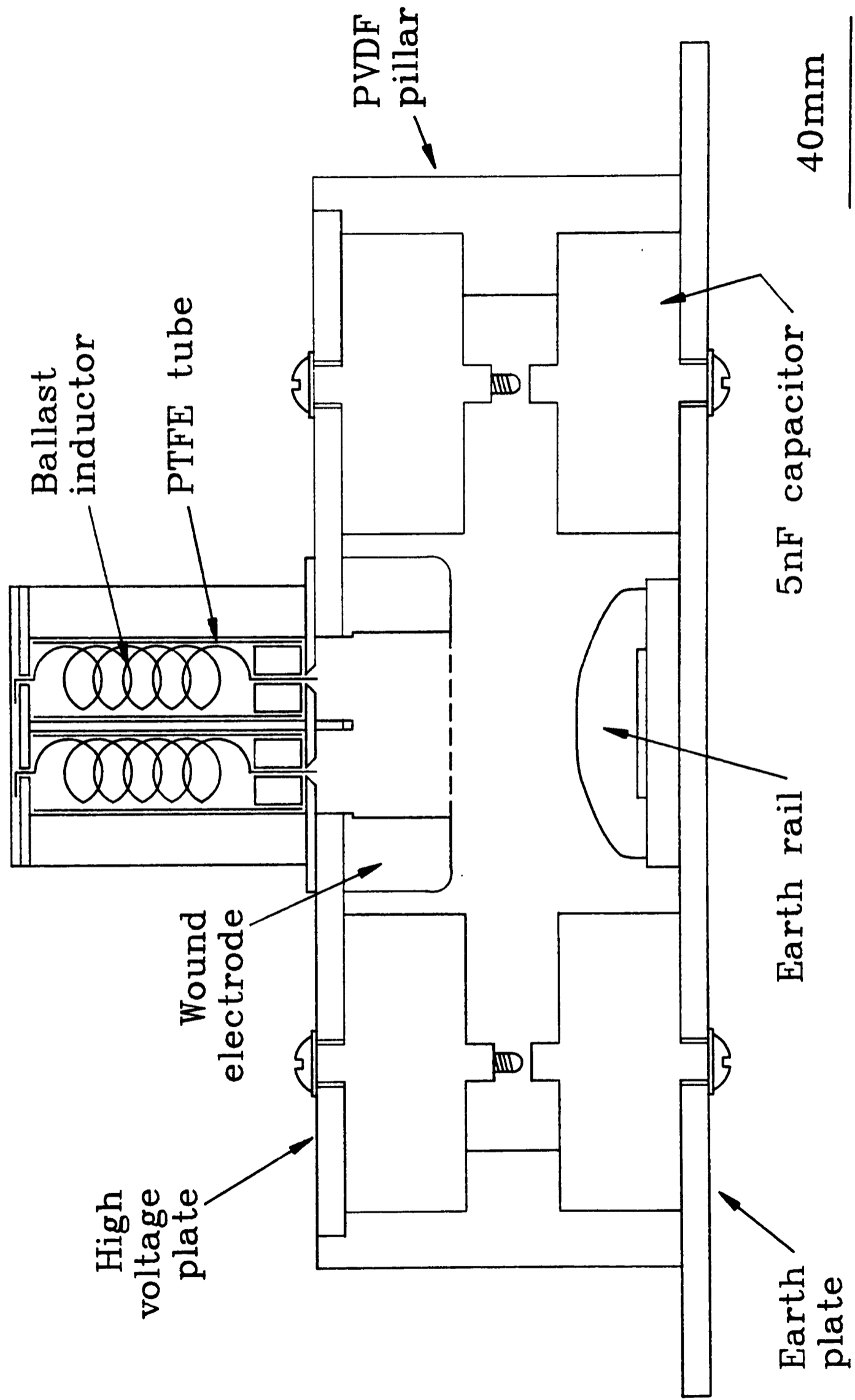


Figure 3.8: Cross section of the laser electrode structure - final design.

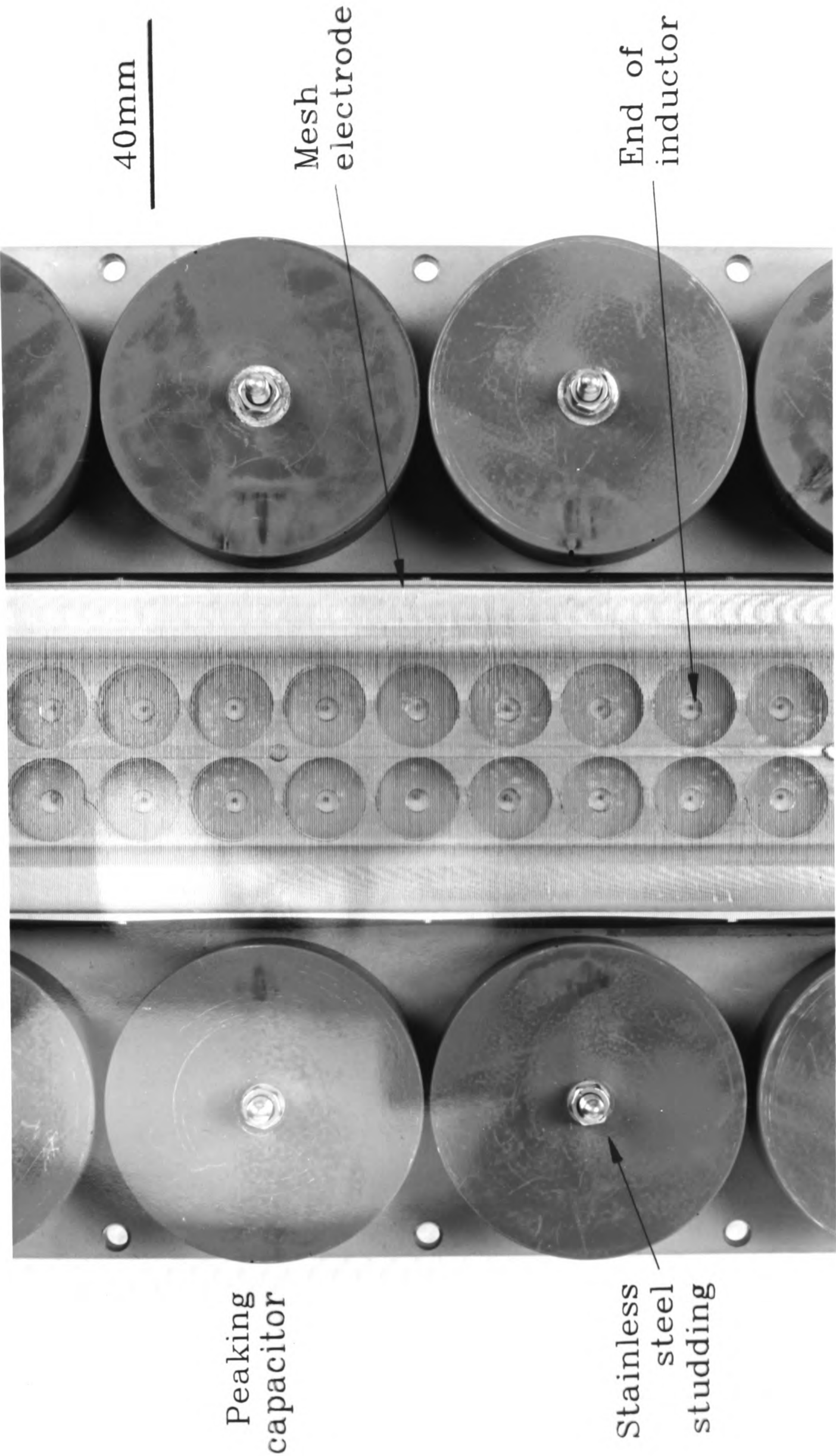


Plate 3.1: The underside of the high voltage plate.



3.7.1 Back pre-ionization

The first contribution to the UV irradiance of the gain volume was provided by back pre-ionization, generated by 86 individual ballast inductors which formed part of the laser electrical circuit. The high voltage feed-throughs from the external storage capacitors passed through the gas envelope and were connected to the top plate of the amplifier electrode structure. Each inductor, housed in an electrically insulating polytetrafluoroethylene (PTFE) tube with end plug, made electrical contact with this plate, and passed through the high voltage plate and wound electrode, such that the end of the inductor resided in a 5mm diameter hole within the wound electrode. (This arrangement, illustrated in figure 3.9a, was subsequently altered as described in section 3.8.3.) As the potential supplied to the top plate increased, breakdown would eventually occur between the end of one inductor and the wound electrode, causing a pre-ionizing spark to illuminate the gain volume below it. As soon as a particular gap had broken down and a current began to pass through the inductor, a back emf of

$$V = L\dot{I} \quad [3.9]$$

would appear across it, opposing any increase in current. In this way, it was ensured that each and every one of the 86 ballast inductors would take part in the circuit, to provide 86 individual pre-ionizing sparks.

3.7.2 Side pre-ionization

The internal peaking capacitance was provided by 52 5nF capacitors, rated to 30kV DC, placed in 26 series pairs between the high voltage and earth plates. No electrical connection was made between the two capacitors of each pair such that a pre-ionizing spark was formed between the two terminals during the charging cycle. (This method of pre-ionization was first investigated by Kearsley [1979].) This provided 26 individual sources of side pre-ionization which evenly illuminated the gain volume in a direction perpendicular to that of the back pre-ionization. Initially, a stainless steel fork was attached to each terminal and a PTFE spacer inserted between the two so that each spark was ~50mm from the centre of the gain volume. As described in section 3.8.3, these forks were subsequently removed and replaced by lengths of studding in

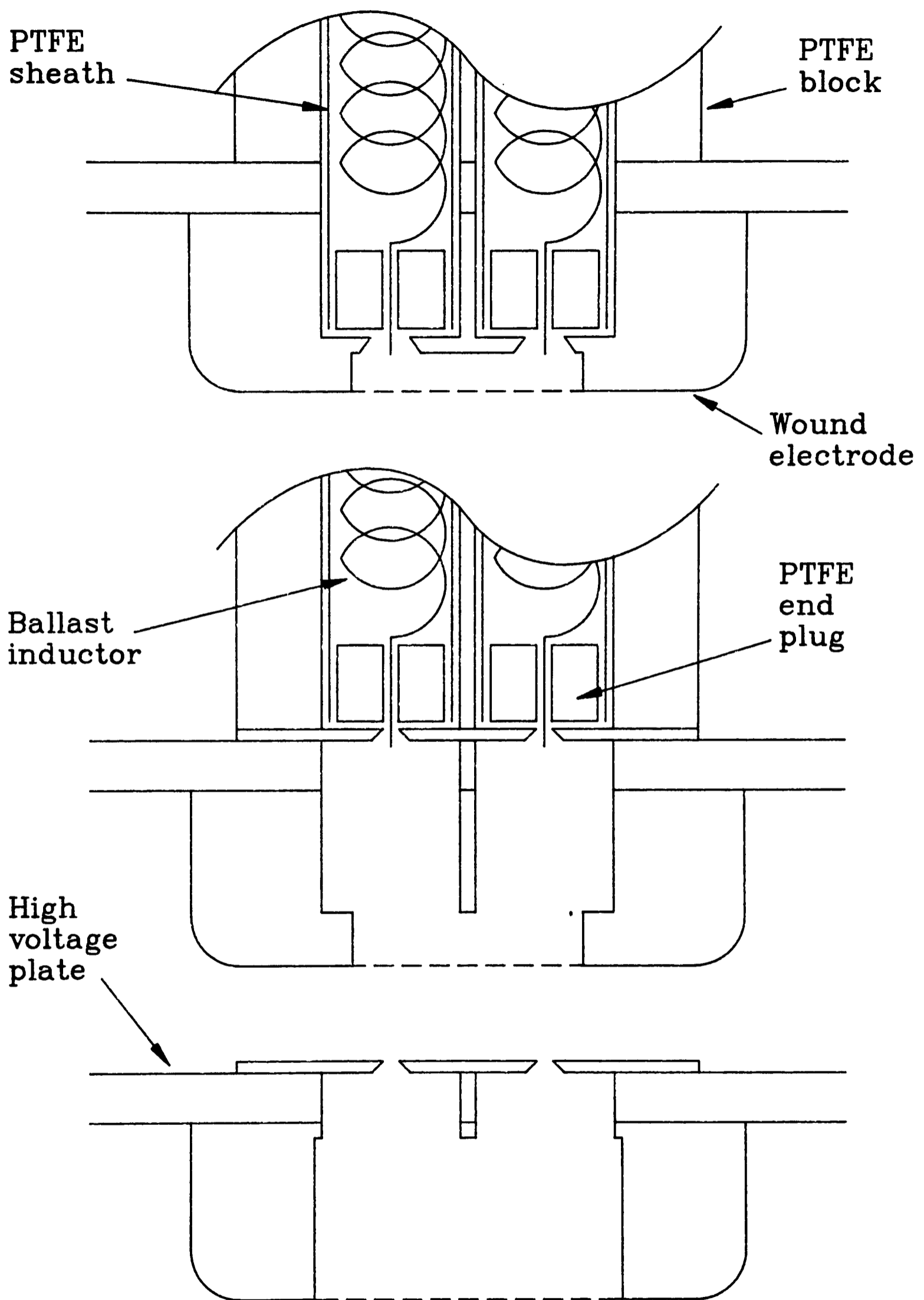


Figure 3.9a: Initial arrangement of the back pre-ionizing inductors.

Figure 3.9b: Modification to achieve more uniform back pre-ionization.

Figure 3.9c: The final arrangement; a clear channel in the mesh electrode.

order to provide a more even illumination of the gain volume.

3.8 OPTIMIZATION OF THE NEW LASER SYSTEM

The final design consideration to be addressed in the new system was the method by which the 0.125mm nickel wire, which was used to wind the mesh electrode, could be secured such that the wires at the front of the electrode would not be disturbed by the removal of the wire at the back of the electrode (between it and the high voltage plate), necessary for the insertion of the ballast inductors to a point just behind the front of the wire winding (as shown in figure 3.9a). The electrode winding was carried out on a lathe which was set at ~ 3 revs/s. As the electrode rotated about its length, it drew wire from a spool through a guide which was secured to the lathe's automatic feed. By keeping the spool under manual tension, the electrode could be wound very uniformly both in terms of tension and wire separation. The feed was set at 56 TPI so that the mesh had an average transmission of 72%. Approximately 400m of nickel wire was required for each winding.

3.8.1 Mechanical clamping

Initially, two grooves were machined along the length of the electrode and the high voltage plate, so as to be adjacent when the two were brought together. Viton cord was laid in both pairs of grooves prior to the electrode being wound with nickel wire. The high voltage plate was then placed on the wound electrode, and the two secured together by means of the four screws at the ends of the plate, which did not pass through the wire. The two were then clamped together, and the remaining screws inserted. Unfortunately, the process of forcing the two components together caused the Viton cord to deform and flatten, such that the tension in the wound nickel wire was largely lost. The subsequent cutting of the wire at the back of the electrode caused a very marked disturbance to the wire at the front.

The entire structure was assembled nevertheless, and inserted into the laser body. As previously, a discharge in 3 atmospheres of helium was run, as a necessary, but not sufficient condition that a good glow discharge would be obtained with a laser

gas mix. At a 55kV supply, very strong hard arcs were seen, discharging between the wound electrode and the earth rail.

In an attempt to overcome these problems, the electrode was re-wound with nickel wire, this time without the Viton cord along its two grooves. Viton cord was placed in the high voltage plate as before, and the two were held together by as few screws as possible, so as not to disturb the nickel wire. Despite the fact that this arrangement of Viton cord resulted in an increase in the tension of the nickel wire when the two components were clamped together, disturbances in the wire at the front of the electrode were again clearly visible, corresponding to the positions of the securing screws. The back pre-ionizing ballast inductors were then removed, and an alternative electrical contact was made between the feed-throughs and the high voltage plate, thus obviating the need to cut through the backs of the wires, and further disturb the front face. The use of this arrangement, in which there was no back pre-ionization, with both 3 atmospheres of helium and a laser KrF mix, again resulted in hard arcs. The markings on the earth rail revealed two interesting effects:

a) There were hard arc marks exactly corresponding to the irregularities in the wire caused by the securing screws.

b) There were periodic, softer markings, exactly corresponding to the positions of side pre-ionization, from the sparks produced across the internal peaking capacitors. (These are shown in plate 3.2.)

These observations illustrated the need for both the back pre-ionization and uniformity in the wire wound electrode.

3.8.2 Securement by epoxy glue

In the light of these observations, it was decided that the only method of obtaining a uniform wound electrode which would remain flat after the back section of the wire had been removed would be to glue it to the high voltage plate. Thus, the electrode was wound for a third time. A fibre carrier (of thickness $\sim 0.1\text{mm}$), cut to the shape of the electrode, was impregnated with an epoxy resin and placed between the electrode and the high voltage plate. The two were then clamped together as the resin

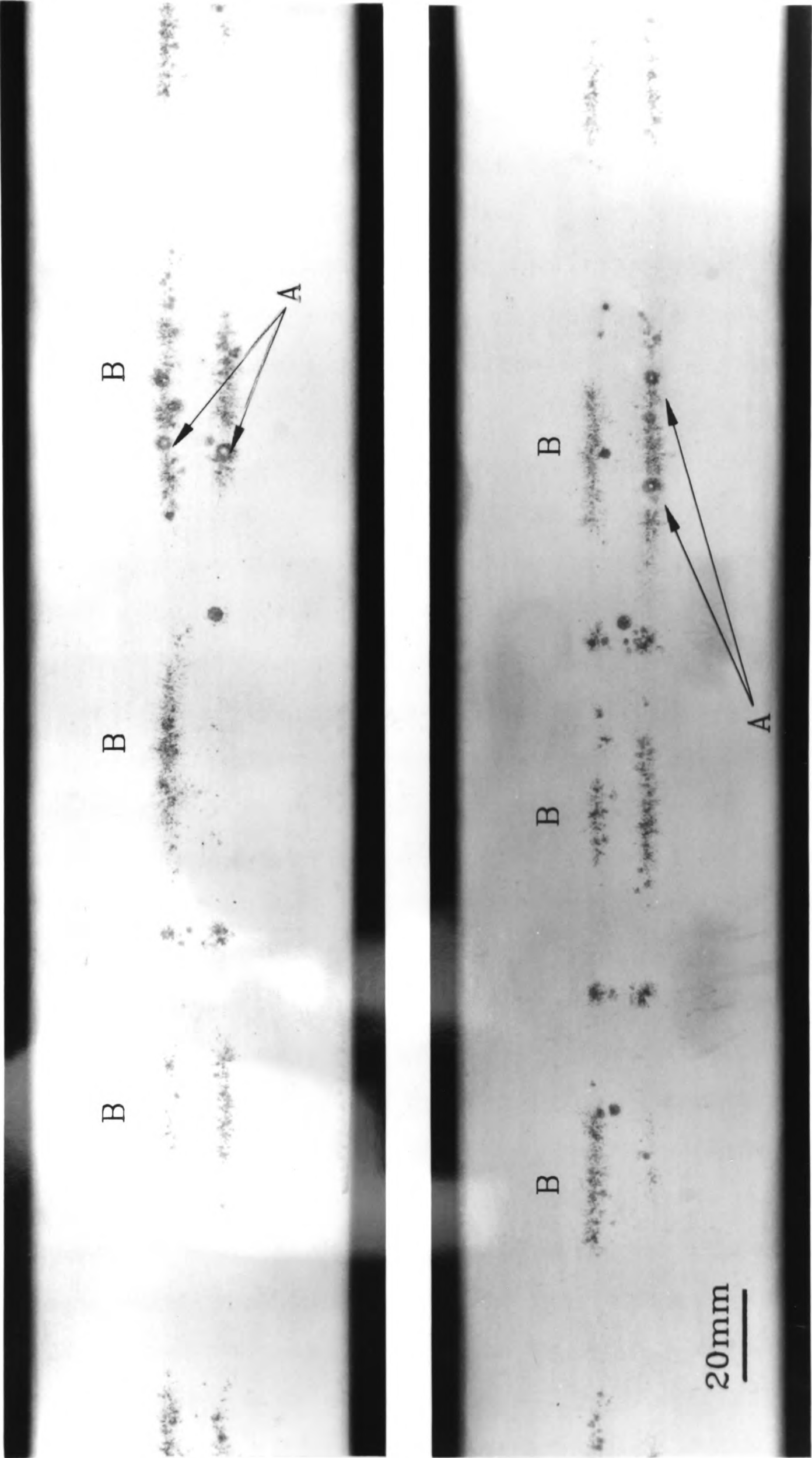
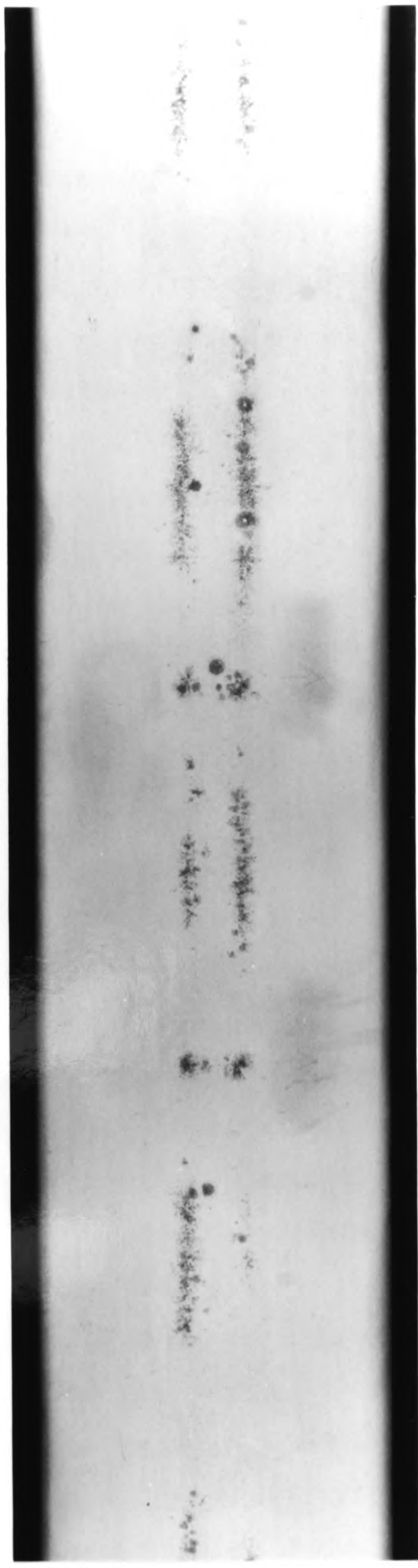
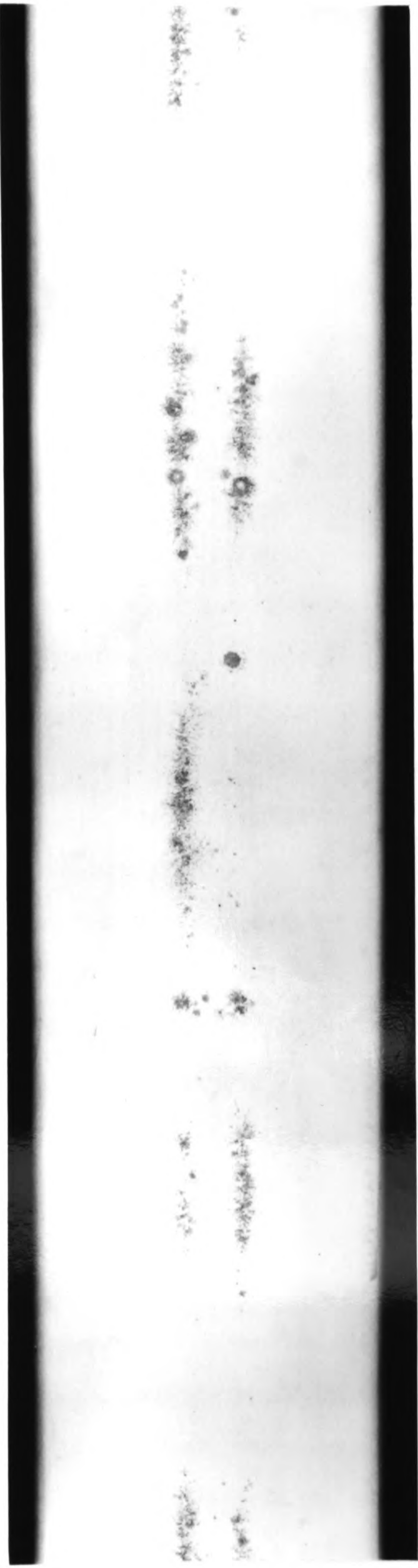


Plate 3.2: Burn marks on the earth rail, arising from irregularities in the mesh electrode and variation in the side pre-ionization.
‘A’ - hard arcing at positions of wire disturbances; ‘B’ - softer arcing at positions corresponding to the peaking capacitors.



set. Evidently, screws were no longer needed to secure the two together, and all that remained was to remove the disks of resin-bonded wire from the holes in which the ballast inductors were to be placed. To achieve this, a cutter was machined from silver steel and hardened by heat treatment (as shown in plate 3.3). This was used to punch out the disks, with no apparent disturbance of the front surface of the wire resulting. The use of epoxy glue in the original design had been avoided since it was thought that such materials would have a detrimental effect on gas lifetime. In practice, this was not found to be the case.

With this construction, the laser was operated under a variety of conditions, with alterations made to the amplifier storage capacitor, side and back pre-ionization, laser gap and gain volume. Although it later transpired that the external circuit ('Initial design') used with it was not of sufficiently low inductance to allow the achievement of an evenly pumped gain volume, observations of the markings on a number of different earth rails suggested that the back pre-ionization was not uniform enough itself to enable an even pumping of the gain volume. Plate 3.4 shows the surface of a 16mm flat rail; only a few hard arcs are present, but there are distinct markings corresponding to the positions of the back pre-ionizing ballast inductors. Unlike in the previous case (plate 3.2), there are no periodic markings corresponding to the positions of the side pre-ionizing sparks.

The pumping density of the amplifier laser (defined as the energy stored in the peaking capacitors, taking into account the increased potential across them as explained in section 3.2.1, divided by the gain volume) was calculated to be 266J/l. The previous '1 Joule' laser had a value of 366J/l, and the oscillator laser was being pumped at 753J/l - more than twice the value of that in the new amplifier. Consequently, it was realized that the hard arcing observed in the new structure was almost certainly due to the fact that the back pre-ionizing sparks were not providing uniform enough irradiation of the gain region. Figure 3.10 illustrates the variation in radiation intensity at the wire surface, assuming a $1/r^2$ dependency, and with the pre-ionizing sparks a distance of 7mm behind the wound wire. A variation in the relative intensity by a factor of two is evident, resulting from the close proximity of

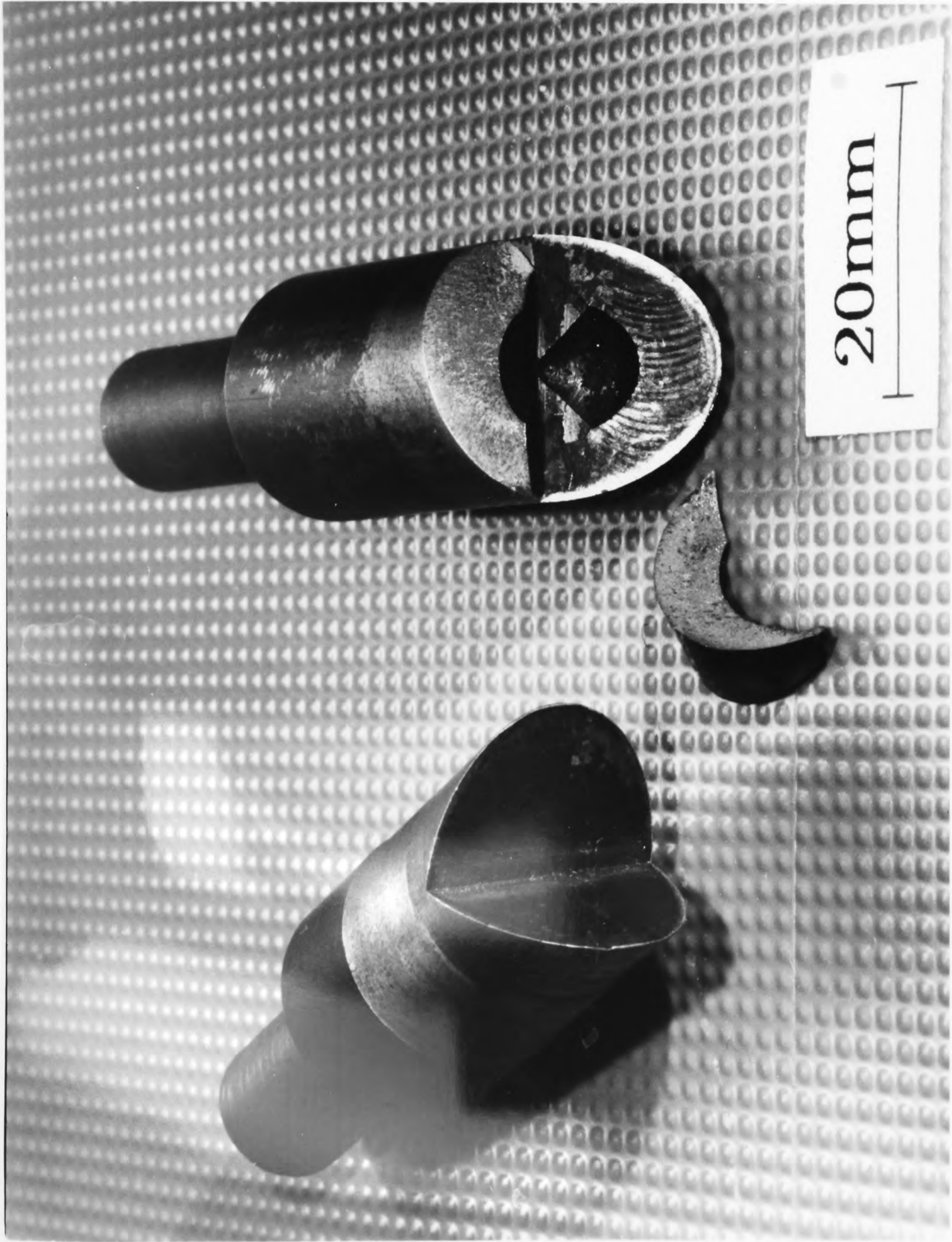
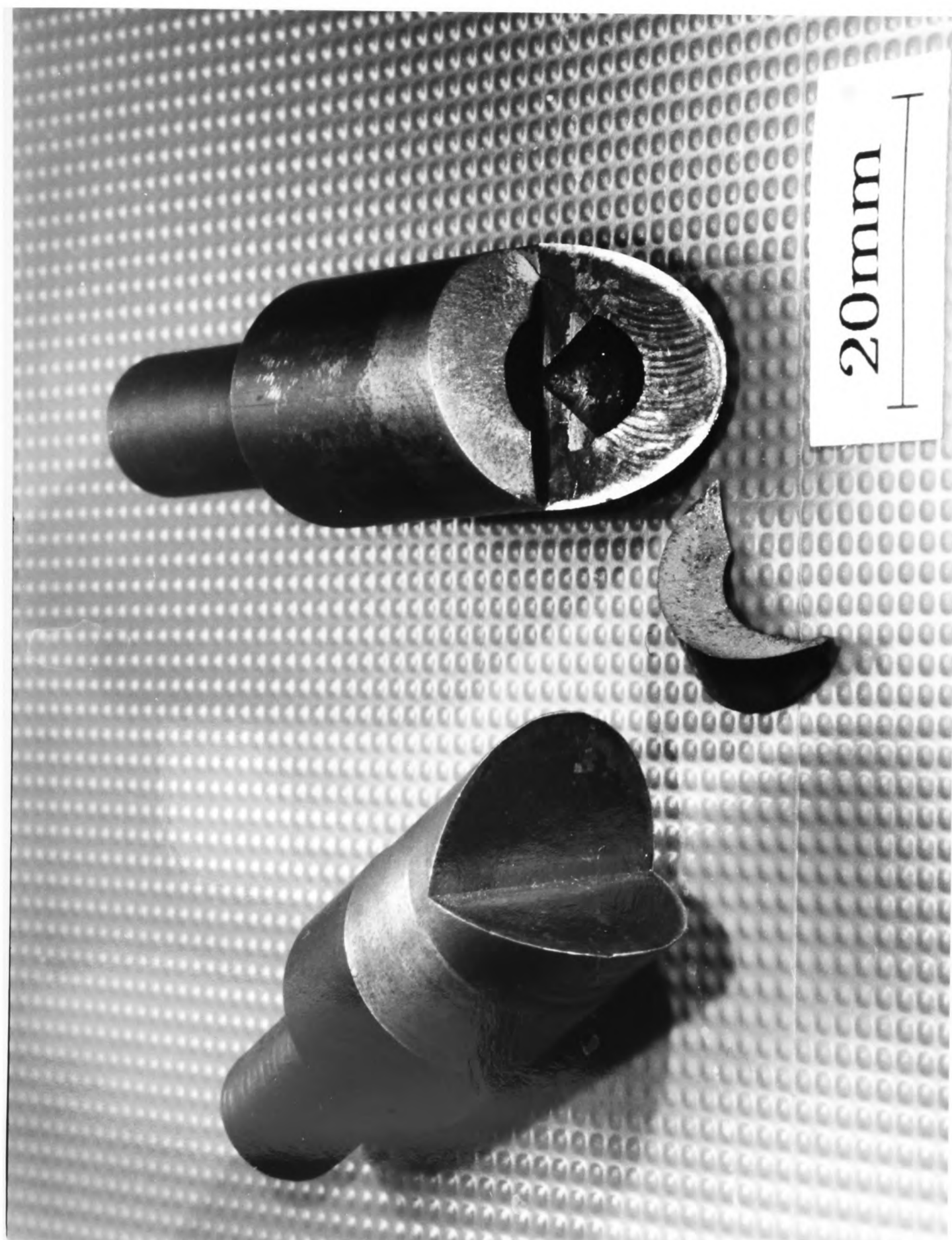
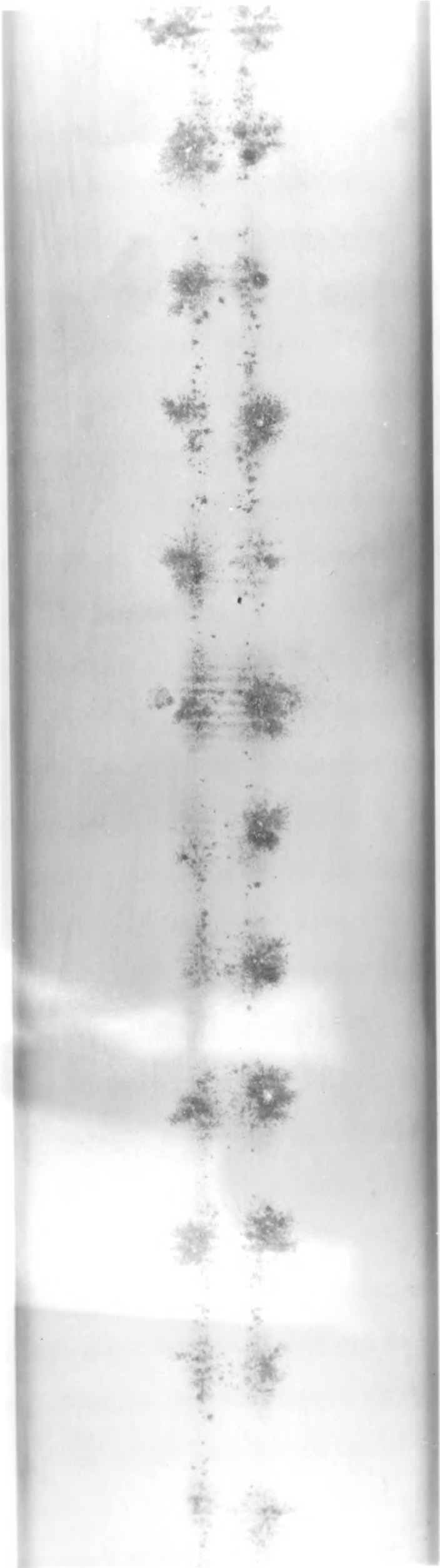


Plate 3.3: The cutter used to remove disks of resin-bonded wire from the mesh electrode. Right; failure resulting from heat treatment.





20mm

Plate 3.4: Burn marks on the earth rail illustrating non-uniformity of the back pre-ionization.



the sparks to the wire in comparison to the area over which illumination is required.

3.8.3 Structural alteration of the wound electrode

To achieve a more uniform illumination of the gain volume, it was decided that the back pre-ionizing sparks would have to be moved back, away from the wound wire surface. To achieve this, the mesh electrode structure was dismantled, and the high voltage electrode bar machined so as to remove the shoulders of the holes in which the ballast inductors had resided (as shown in figure 3.9b). A thin metal plate was placed between the high voltage plate and the PTFE block which held the ballast inductors. Holes of diameter 5mm in this plate allowed the ends of the inductors to protrude some way into the high voltage plate, and provided an electrical path to the wound electrode, such that the pre-ionizing sparks would be formed at the top of the high voltage plate, at a distance of 28mm from the wire surface. This would give a far smaller variation in the illuminating radiation intensity (shown in figure 3.11).

However, when this electrode arrangement was used, hard arcs were evident when the laser was operated at 40kV. Inspection of the earth rail revealed very strong burn marks, once again corresponding to the positions of the back pre-ionizing sparks. The strength of these marks, which indicated a much greater degree of arcing than with the previous arrangement, led to the belief that the cylindrical holes within the wound electrode were in some way acting to channel the UV radiation produced by each spark in an axial direction, into the gain region. The electrode structure was once again disassembled, and the majority of the remaining material in the centre of the mesh electrode removed (figure 3.9c). A 2mm thick layer was left at the top of the resultant channel to retain the structural strength of the electrode, and also to enable the back wires and epoxy to be removed in the same manner as previously - this required a scissor action between the cutting tool and the electrode structure.

The wound electrode structure thus achieved was much closer to that of the design of Hirst [1987b], where flash-boards, which provided the back pre-ionization, resided at the bottom of a channel of depth 30mm, over which the wires were laid. By considering the geometry of this layout, it is evident that any one position on the wire

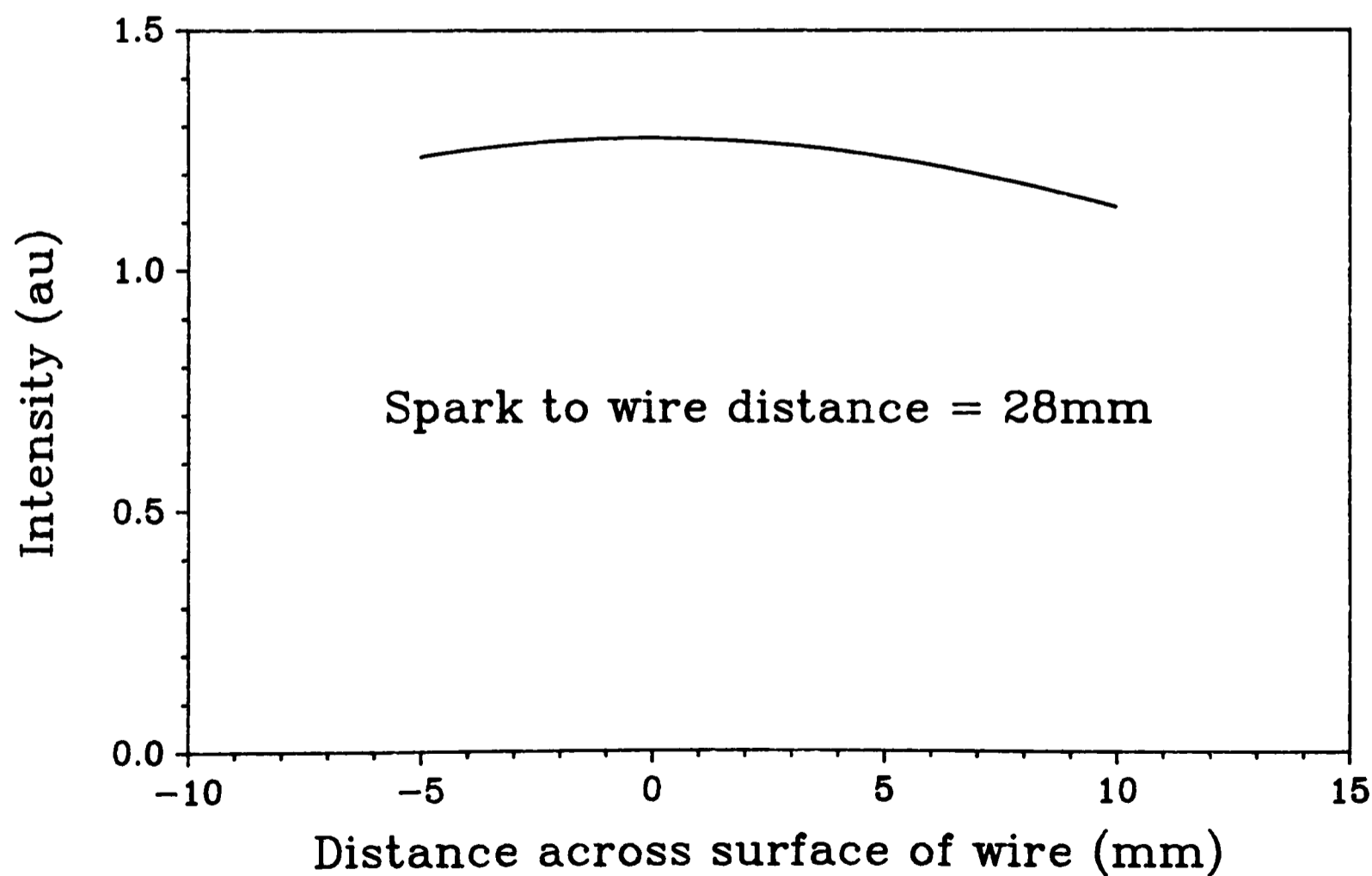
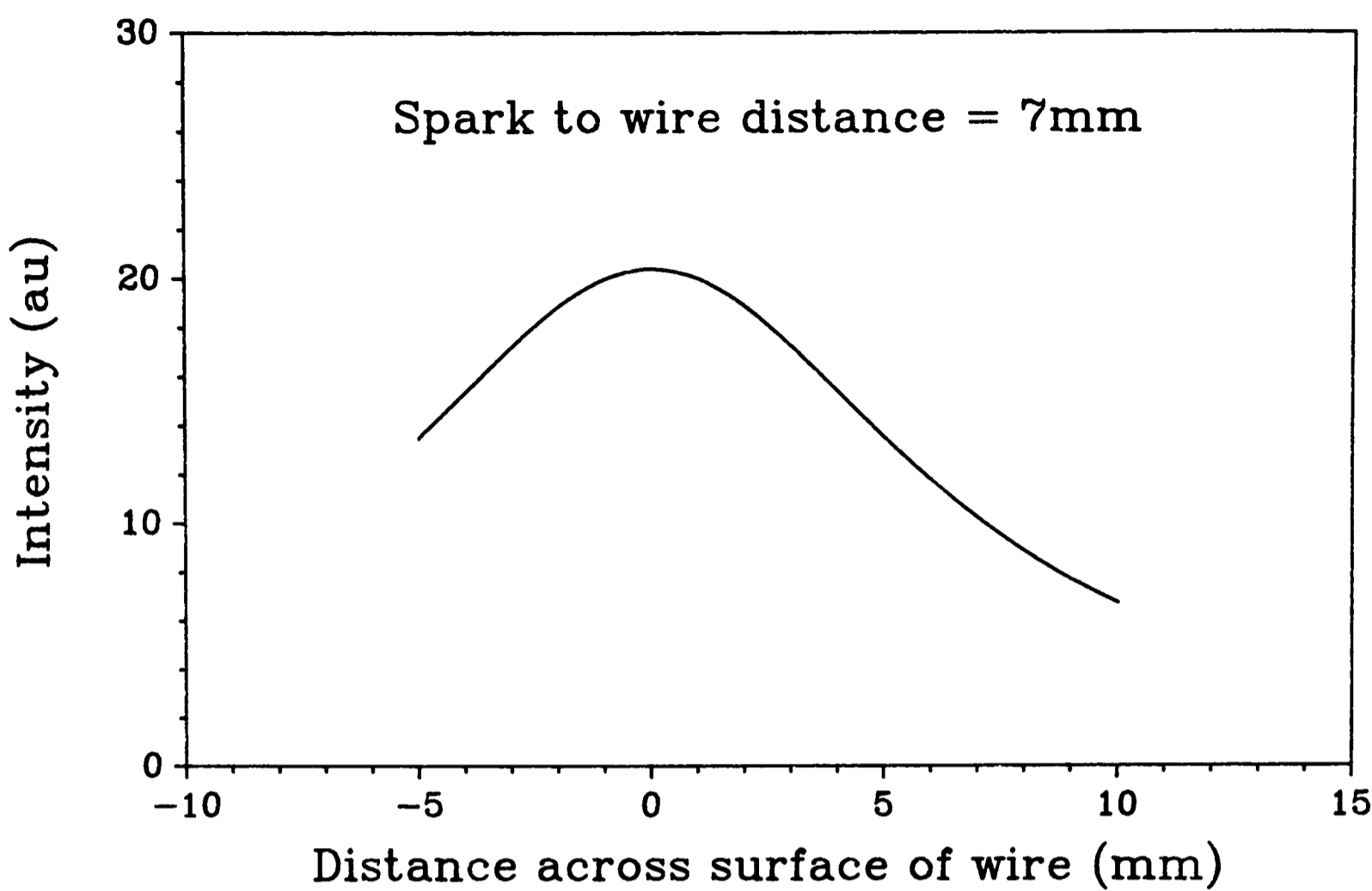


Figure 3.10: The initial variation in pre-ionizing intensity across the gain volume.

Figure 3.11: The decrease in pre-ionizing intensity variation resulting from the optimization of the wound electrode structure.

will be able to 'see' 6 pre-ionizing sparks, in contrast to the original arrangement, in which the majority of the wire surface was only being illuminated by 2 sparks.

With this arrangement, hard arcing was still observed at 50kV in 3 atmospheres of helium. The side pre-ionization was removed, by joining the capacitor pairs with short lengths of studding, to see if this had been causing too great a non-uniformity in the pre-ionization over the region of the gain volume. However, this resulted in many randomly positioned burn marks on the earth rail. The side pre-ionization was therefore re-introduced by leaving a 3mm gap between the end of the studding and the terminal of the earth plate capacitor. In comparison to the original fork arrangement, the pre-ionizing sparks were 20mm further away from the gain volume, and also nearer the earth rail. It was hoped that this would lead to a more uniformly pre-ionised gain volume. The markings observed on a 20mm rail did then indicate that the side pre-ionization was sufficiently uniform over the gain volume.

At this stage, the original '1 Joule' electrode structure was introduced into the laser body. With a storage capacitance of 133nF, an output of only 370mJ was achieved, indicating that the external electrical circuit was of too high an inductance for the laser to operate satisfactorily.

3.8.4 Use of the second electrical circuit design

By this stage, the contribution of the inductance of the total laser discharge circuit as well as that of the actual electrode structure itself was suspected as being partly to blame for the poor performance of the system. Specifically, the earth return path from the electrode to the storage capacitor was studied in the light of the persistent preference for arcing to occur along the top of the gain volume. This was observed with both the initial and second external circuit designs, despite marked differences in their earth return paths. It was suspected that the return path through the top capacitors was not the same as through the bottom capacitors (as viewed with the electrode structure rotated through 90° and inserted in the laser body), because of a possible path through the laser tube support, connected to the iron frame containing the system, which may have been taken. To overcome this difference, copper foil was

placed in the laser tube, so as to ensure good electrical contact between the laser tube and the edges of the earth plate which rested against the tube. In addition, a strip of copper, of thickness 0.13mm and width ~10mm, was placed between the earth rail and the earth plate, so as to cause the discharge gap to be smaller at the bottom than at the top. These two measures resulted both in a general improvement of the discharge, and also the suppression of noticeable arcing along the top of the gain volume. With a 20mm flat earth rail and a discharge gap of 31mm, 1302mJ per laser pulse was obtained with a 'standard' gas mix.

3.9 OPTIMIZATION OF THE FINAL ELECTRICAL CIRCUIT DESIGN

Using this external circuit and the internal structure as previously (ie. a 20mm flat rail and discharge gap of 33mm) a laser energy of 1.4J was obtained immediately. The discharge was observed to be now stronger along the bottom of the gap than along the top, and so the 0.13mm copper foil spacer was replaced by one of 0.05mm aluminium. This still led to a discharge which was stronger along the bottom of the rail, and so the foil was removed. This decreased dependence on the laser frame as a return path to earth supported the view that the new external electrical circuit was of much lower inductance than previously. There was also evidence of shorting from the peaking capacitors to the earth rail and wound electrode. This observation was further evidence of the improvement in the final electrical circuit design over the previous ones. Through its lower inductance, a much faster rise-time would have been obtained, enabling the peaking capacitors to be charged to a higher potential. This would have encouraged the observed shorting to the earth rail and wound electrode, and therefore re-affirmed the need to replace the forks initially fixed to the peaking capacitor terminal with lengths of studding. To overcome this problem, the overall width of the earth rail was greatly reduced and epoxy resin was used to cover the majority of the studding and capacitor terminals so as to discourage this electrical path.

The burn pattern produced by the laser beam still indicated that the earth rail profile was not optimal in that the burn pattern produced consisted of two horizontal bands, corresponding to discharge to the corners of the 20mm wide central flat. This

had been initially machined with a 5° fall-off on either side. To overcome this effect, the earth rail was re-machined with a 10mm central flat and 2.5° fall-off, with the 'edges' of the cross-section rounded off by extensive hand filing, so as to approximate a continuous curve. This resulted in a marked improvement in beam uniformity, and it was then decided that the combination of pre-ionization, mesh electrode and earth rail were as good as might be reasonably expected, and the process of gas optimization was commenced. A beam area of 7.99cm^2 was obtained with the 'standard' gas mix, indicating that an output energy of $\sim 2\text{J}$ could be achieved, assuming an energy extraction of 3J/l as obtained with the '1 Joule' system.

3.10 GAS OPTIMIZATION

Kinetic studies (as carried out by Kearsley [1980]) of the mechanisms of the formation of excimer species indicate that laser output energy will increase with increasing fluorine and krypton concentrations, as well as increasing total pressure (as provided by the helium buffer). However, by increasing these pressures, the gas becomes electrically 'harder', and a greater voltage must be applied across the laser gap before breakdown will occur. Although this will lead to a greater energy deposition into the gain volume, it does have two disadvantages:

a) The breakdown across the gain volume is delayed, thus diminishing the effect of the back pre-ionization.

b) The breakdown will occur at a more slowly varying part of the voltage pulse as it builds up on the mesh electrode (for a given operating potential). This will obviously encourage discharge instabilities as the voltage rise-time increases towards those due to the inductance of the various detrimental electrical paths through the gain volume.

Thus for a given practical system, the optimum gas mixture and pressure must be found empirically - those which give maximum output energy while remaining within the limitations set by the imperfections of the system (ie. finite voltage rise-time, non-uniform pre-ionization and imperfections in the mesh electrode and earth rail). A total of 14 different gas mixtures were tried, and the resulting laser energies

are displayed in figures 3.12 and 3.13 and in table 3.1. From figure 3.12 we see that the lower pressures of fluorine allow higher pressures of krypton to be employed (eg. 160mb of krypton with 4mb of fluorine), while at higher fluorine concentrations, the peak in output energy is achieved at lower krypton concentrations (eg. 140mb of krypton with 7mb of fluorine). The optimal balance between the two components was found to be 140mb of krypton with 6mb of fluorine, which resulted in an output energy of 2.04J. This was increased to 2.24J by the use of anti-reflection coatings on the output windows of the laser tube, giving an energy extraction of 3.3J/l, compared to the value of 2.9J/l obtained in the ‘1 Joule’ system. The importance of the back pre-ionization in this electrode structure is apparent in that the optimum gas mixture for the ‘1 Joule’ structure, for which the back pre-ionization was regarded as not having any effect on the gain volume, was 5mb of fluorine and 120mb of krypton; a much electrically ‘softer’ gas mix than could be used satisfactorily in the ‘2 Joule’ structure.

Pressure (mb)	Kr	120	140	160	180
	F ₂				
	4		1.84	1.87	1.57
	5	1.83	1.97	1.89	1.86
	6	1.89	2.04	1.95	1.74
	7	1.93	1.99	1.81	

Table 3.1: Laser output energy (in joules) for the various gas mixes tested.

As expected, the output energy increased with increasing voltage (as shown in figure 3.14) and increasing pressure (figure 3.15). The variation with pressure for the hardest gas mixture used is also shown, as it indicates a decrease at high pressures. At 4 bar total pressure, the gas was too ‘hard’ for the system to operate satisfactorily. As the pressure was decreased the output energy increased as the discharge improved, but as the pressure was further decreased, the energy then decreased as normally expected. It may also be seen that the energy for the ‘best’ gas mixture leveled off at the 4 bar working pressure, indicating that this is indeed close to the optimal for this particular system at this pressure. The variation for the softest gas mix tested (4mb of fluorine

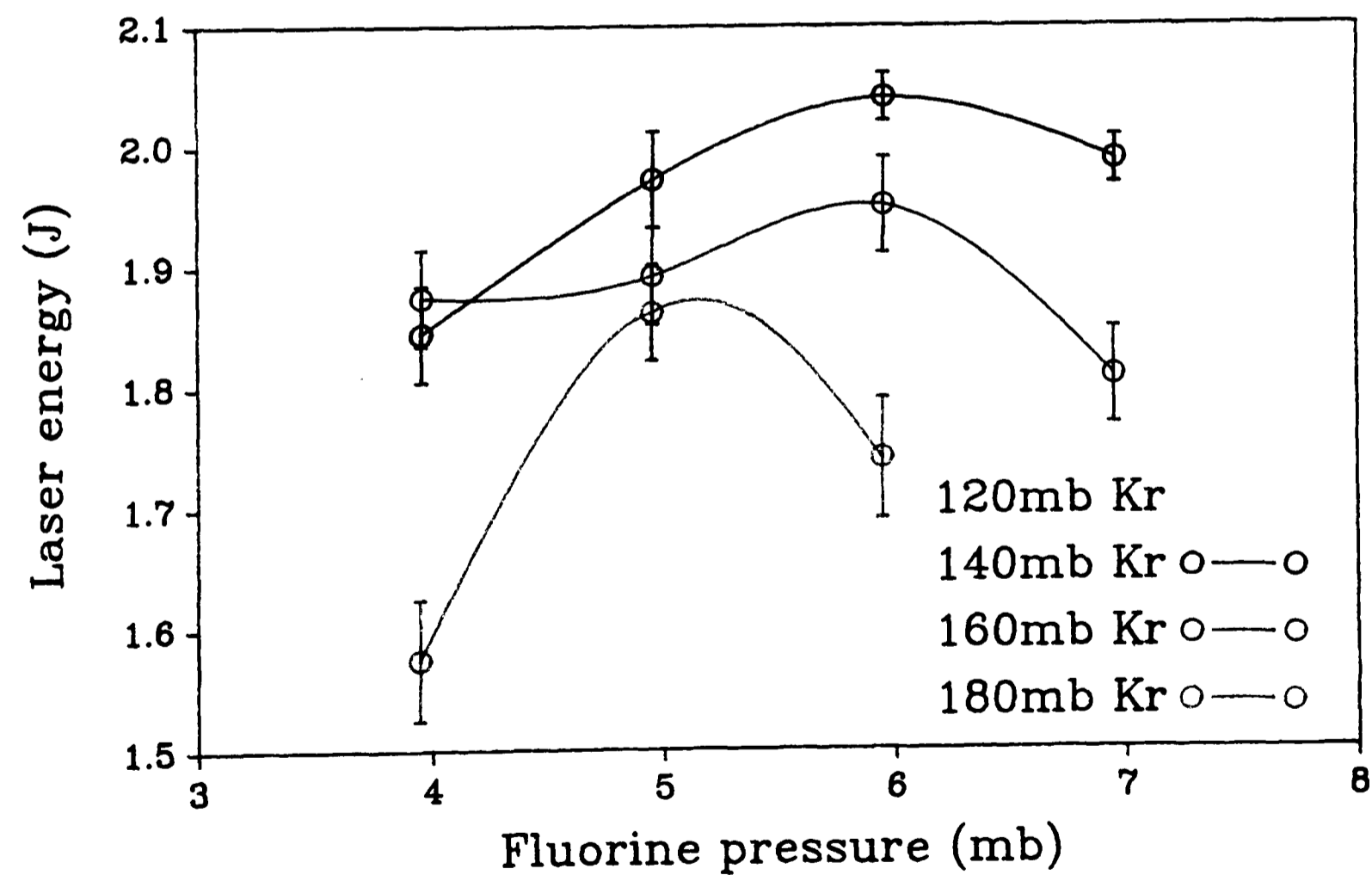
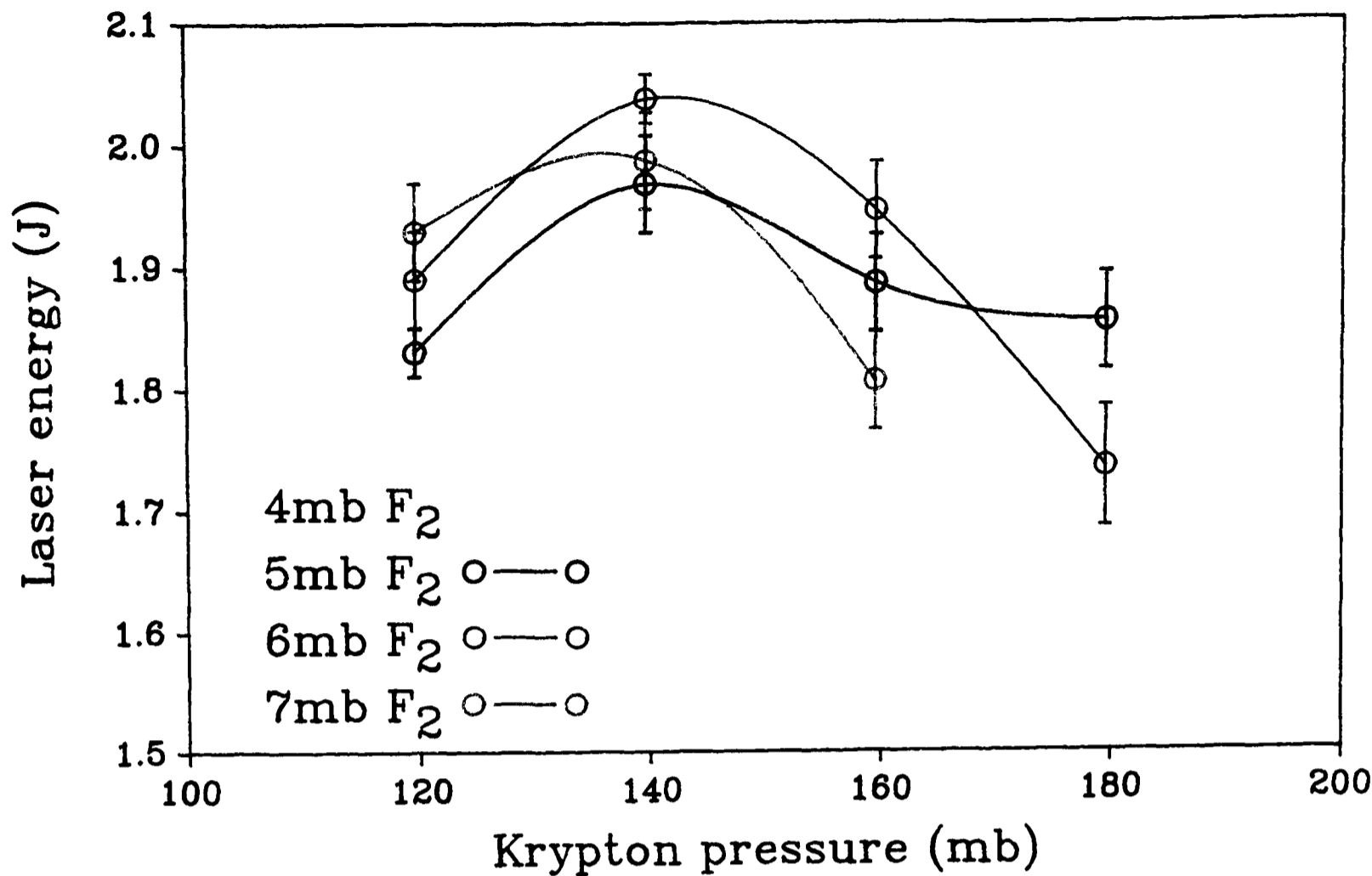


Figure 3.12: The variation in the amplifier output energy as a function of krypton partial pressure.

Figure 3.13: The variation in the amplifier output energy as a function of fluorine partial pressure.

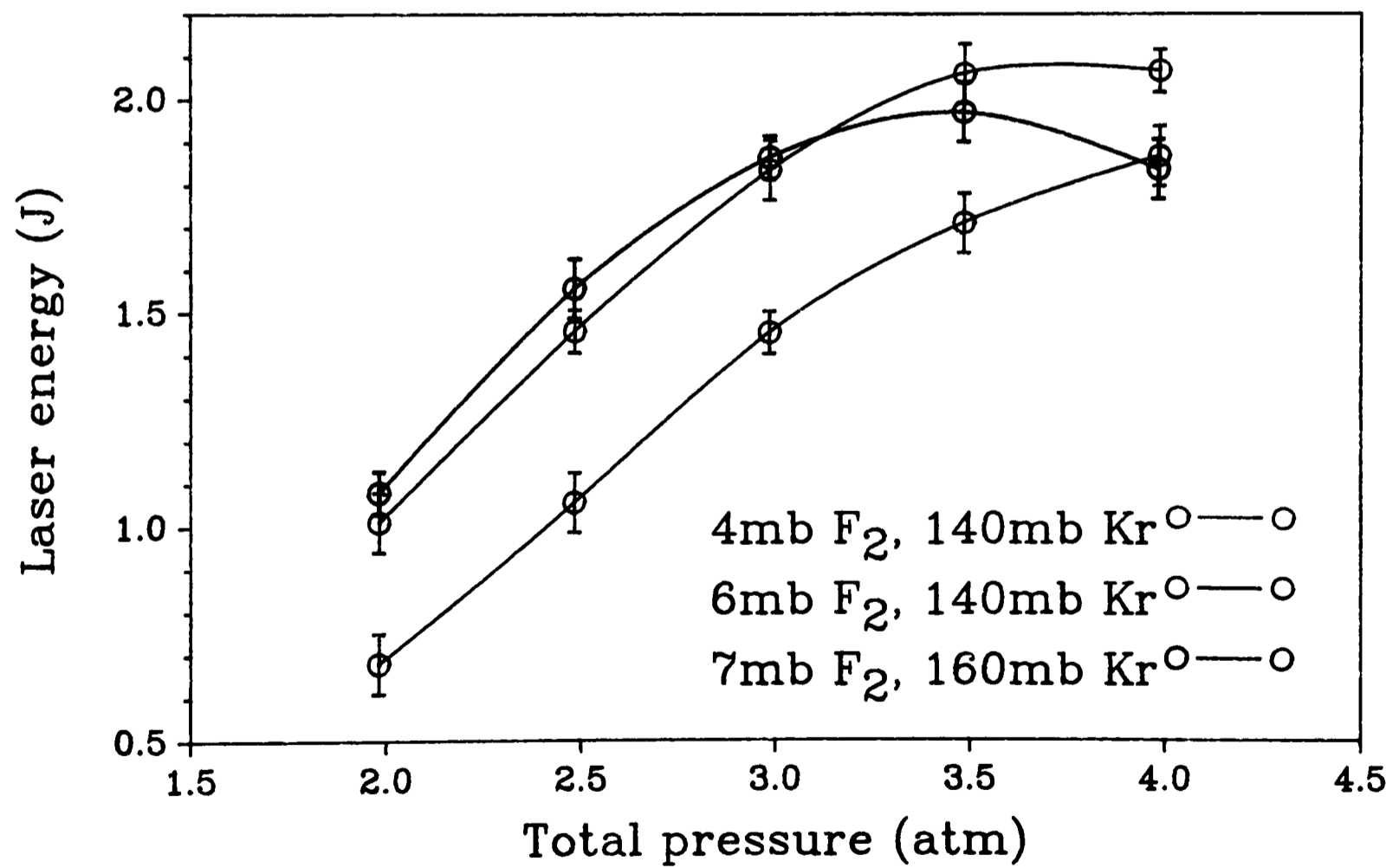
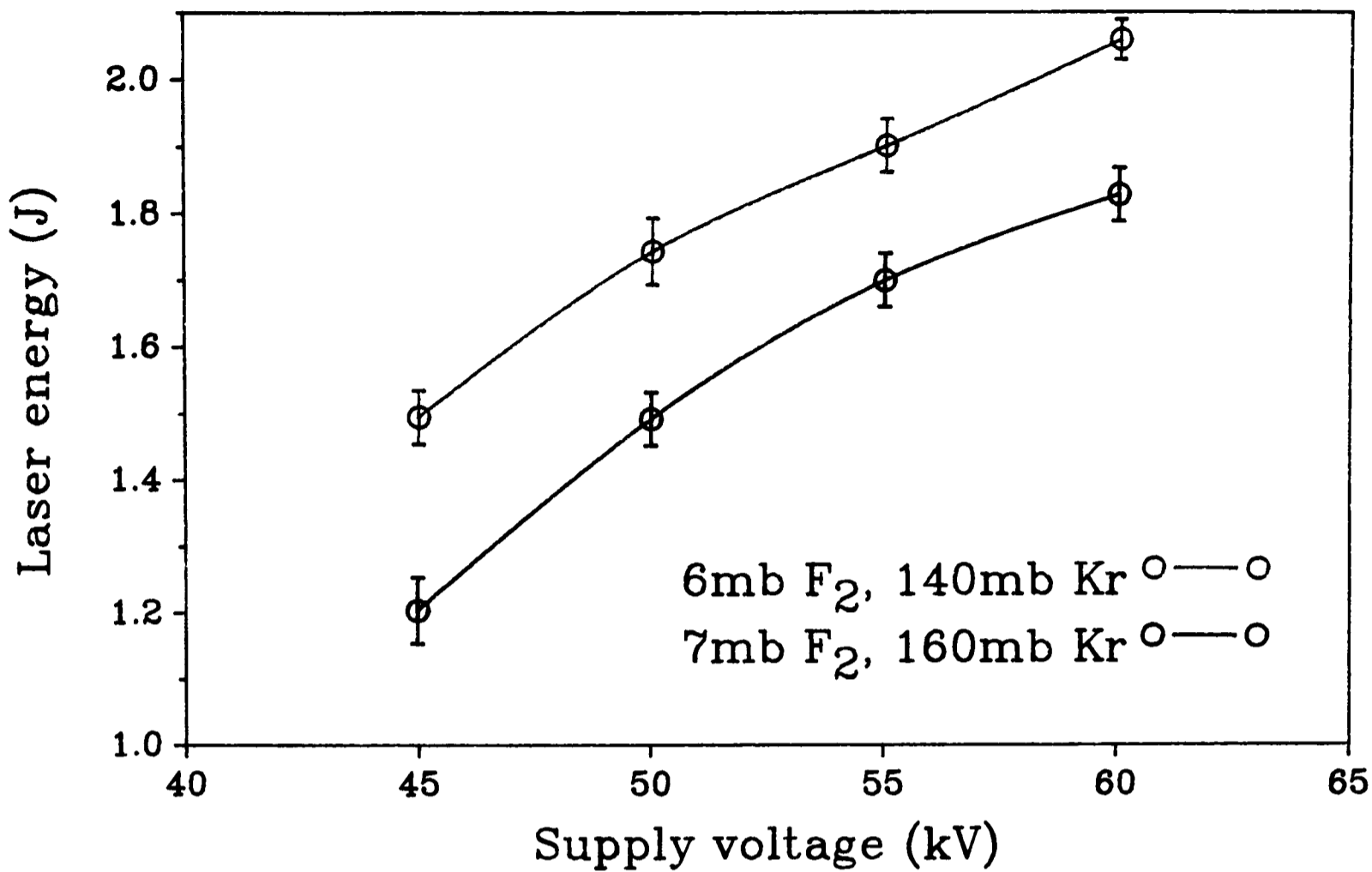


Figure 3.14: The variation in the amplifier output energy as a function of the supply voltage for two typical gas mixes.

Figure 3.15: The variation in the amplifier output energy as a function of total laser gas pressure for the optimal, hardest and softest gas mixes.

and 140mb of krypton) indicates that more energy would be obtained at a higher pressure, since this mixture could become harder without adversely affecting the discharge uniformity. The limit of 4 bar was set by the maximum working pressure of the laser tube.

3.11 OSCILLATOR LASER PERFORMANCE

The electrode structure of the oscillator laser was unchanged from the previous system. Far simpler than the amplifier, only side pre-ionization was employed as the gain volume was much smaller, at 7mm by 19mm in area and 22.5cm in length. A cross section of the structure is given in figure 3.16. Since it was the performance of the amplifier which was of the greatest importance in terms of output energy, optimization was not carried out for the oscillator. Rather, it was operated under the same gaseous conditions as the amplifier so that the gas purifier could be used for both lasers, with the knowledge that the improvements in output energy and beam quality obtained by injection seeding would be largely independent of the oscillator energy. Using a plane-plane cavity for the oscillator, an energy of 80mJ was obtained initially. This was increased to 121mJ by a small amount of electrode profiling and improvement of electrical contact between the earth plate of the electrode structure and the laser tube in a manner similar to that used for the amplifier. Gas optimization for the oscillator was carried out by Cotton [1990], who obtained 110mJ with a plane-plane cavity and a gas mixture of 9mb of fluorine and 80mb of krypton; the improvements in electrical contact, as above, enabled the oscillator to exceed this output with a gas mixture which was far from the optimum for this particular laser (ie. that dictated by the performance of the amplifier structure).

3.12 SUMMARY AND FURTHER DESIGN IMPROVEMENTS

In obtaining an output of 2.24J with a plane-plane cavity from the amplifier laser, the design aim of the new electrode structure was obviously met and exceeded. However, this only resulted from significant alterations to the back and side pre-ionization from that generated by the original structure. The importance of an external

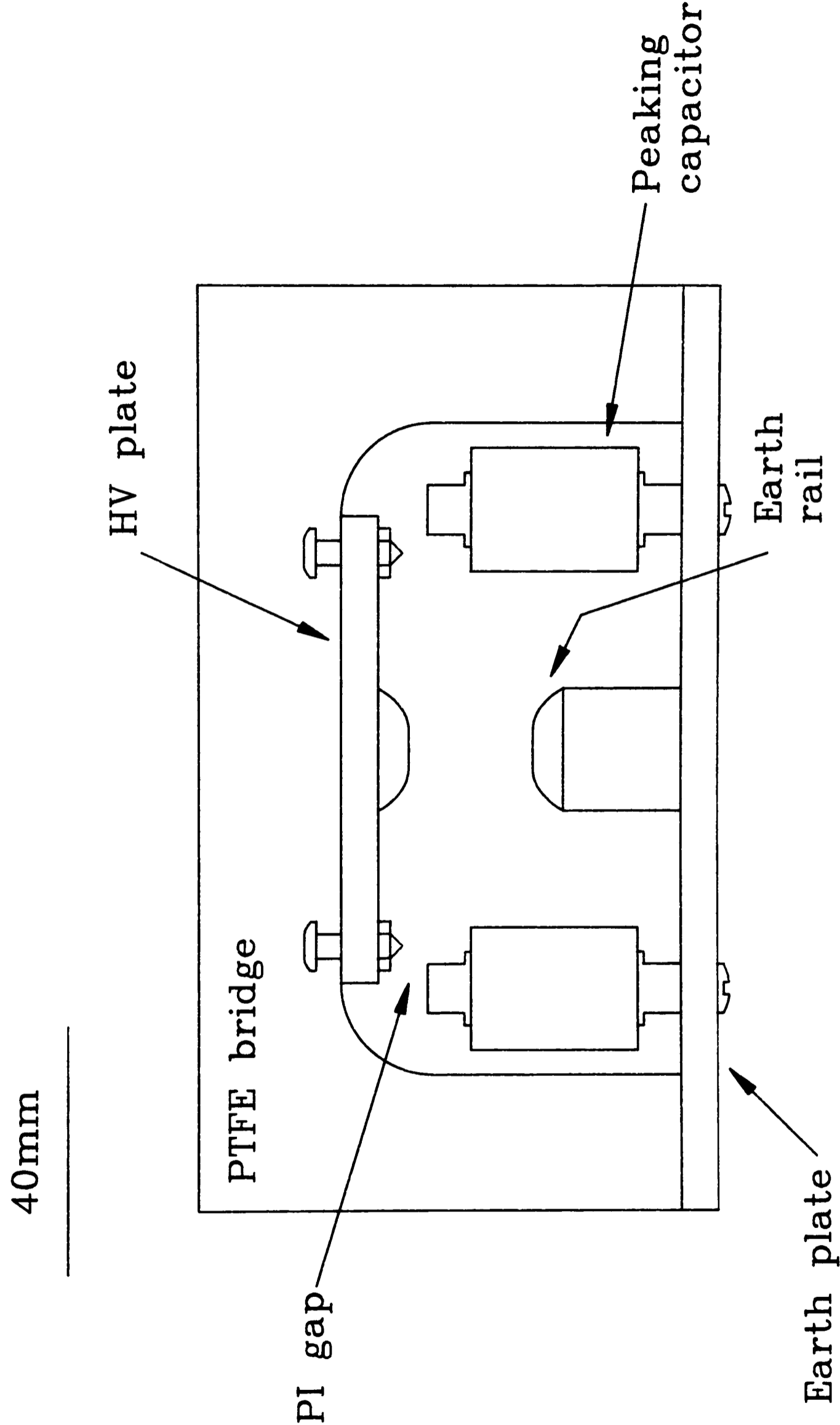


Figure 3.16: A cross section of the oscillator electrode structure.

electrical circuit of very low inductance was also reconfirmed, as was the need for good electrical contact between the electrode's earth plate and the walls of the laser tube. Unlike in the earlier '1 Joule' laser used by Cotton [1990], it was also evident that the back pre-ionization played an important role in encouraging a uniform discharge. Therefore, a new high voltage plate and electrode was commissioned from the Clarendon Workshop in which the 86 holes through which the ballast inductors had initially protruded were replaced by a single channel, of width 40mm and length 860mm. The pre-ionising sparks would still be formed between the ends of the ballast inductors and the thin plate placed on top of the high voltage plate, but would now have a totally unobstructed view of the gain volume. The structure was wound with nickel wire and glued together (and is shown in plate 3.5), but unfortunately, time did not permit this structure to be tested. Such an improvement in the pre-ionization would, it was hoped, enable harder gas mixes to be used in the system without leading to discharge instabilities, resulting in larger output energies.



Plate 3.5: Improved design of the wound electrode structure.



CHAPTER FOUR

THE OPTICAL RESONATOR

4.1	INTRODUCTION
4.2	UNSTABLE OPTICAL RESONATORS
4.2.1	Magnifying and demagnifying beams
4.2.2	The Fresnel Number
4.2.3	Conditions for operation
4.3	INJECTION SEEDING
4.4	RELATIVE TIMING MEASUREMENTS
4.4.1	Results
4.5	OPTIMIZATION OF THE CONFOCAL CAVITIES
4.6	ENERGY DEPENDENCE ON CAVITY
4.7	DIVERGENCE DEPENDENCE ON CAVITY
4.7.1	Results
4.8	SUMMARY

4.1 INTRODUCTION

As discussed in chapter 2, the only current method by which an X-ray flux of sufficient strength to be of practical use in SXCM may be generated is to produce a pulsed plasma source. In the present application, a laser generated plasma (LGP) is used since this is the most convenient type, although Z-pinches may also be suitable and have been employed as the illuminating source in some X-ray microscopes (for example, as described by Schmahl [1992]). The water window wavelengths correspond to approximately 5×10^6 K, and in order to produce a plasma of this temperature by focusing a laser beam onto a metal target, an irradiance of at least 10^{12} W/cm^2 is required (as explained in section 5.2). Using a low energy laser system (for example, $E \sim 2 \text{ J}$ in the present application), the irradiance must be even higher, and a value of $\sim 10^{13} \text{ W/cm}^2$ must be attained.

If we assume that a laser energy of $E = 1.5 \text{ J}$ may be delivered to the target in a time $\tau = 20 \text{ ns}$ FWHM, then to achieve an irradiance of $I = 10^{13} \text{ W/cm}^2$, it must be focused to a circle of diameter

$$d = 2\sqrt{E/\pi\tau I} \quad [4.1]$$

$$\sim 31\mu\text{m}$$

The full angle divergence of a laser beam produced by a simple plane-plane cavity is dependent on the diameter of the cavity mirrors D , and the effective path length of the pulse inside the cavity, and is given by

$$\theta = D/c\tau \quad [4.2]$$

For the laser system used in this chapter, $D \sim 3\text{cm}$, giving $\theta \sim 5\text{mrad}$. Such a beam could be focused to an area of diameter d by a lens of focal length f , where

$$d \sim f\theta \quad [4.3]$$

The present system employs an aspheric lens of $f=9\text{cm}$, which would result in $d=450\mu\text{m}$. This would give rise to an irradiance of only $I=2.6 \times 10^{10}\text{W/cm}^2$, which would not be sufficient to generate a suitable plasma.

The diffraction limit for a beam of diameter D and wavelength λ is given by

$$\theta \sim \lambda/D \quad [4.4]$$

$$= 8\mu\text{rad}$$

in the case of $\lambda=248\text{nm}$ and $D=3\text{cm}$ as previously. Such a beam could be focused to a spot of size $a=0.7\mu\text{m}$ by an aberration free lens of focal length 9cm , which would lead to an irradiance sufficiently large to excite the required plasma. In order to reduce the divergence of the laser beam to a value nearer this diffraction limit, an unstable cavity was employed. The theory of unstable cavities was first considered by Siegman [1965].

4.2 UNSTABLE OPTICAL RESONATORS

We consider initially an open resonator of two mirrors, M_1 and M_2 , a distance L apart (as shown in figure 4.1). For the resonator to be stable, we require that a specific ray, starting at some arbitrary position and angle within the system, remains inside some finite boundary as it is repeatedly reflected between the two mirrors, so that it contributes to a reproducible amplitude distribution within the cavity. The resonator stability condition does not require that the ray returns to the same position and angle on every round trip, but only that it does so after some, possibly large, number of

reflections.

We use conventional paraxial matrix theory to analyse the resonator geometries; starting at the point X of figure 4.1, the matrix for a complete round trip is

$$\mathbf{M} = \mathbf{M}_L \mathbf{M}_2 \mathbf{M}_L \mathbf{M}_1 \quad [4.5]$$

where

$$\mathbf{M}_L = \begin{bmatrix} 1 & L \\ 0 & 1 \end{bmatrix} \quad \text{and} \quad \mathbf{M}_1 = \begin{bmatrix} 1 & 0 \\ -2/R_1 & 1 \end{bmatrix}$$

with R_1 and R_2 the radii of curvature of the two mirrors. This leads to

$$\mathbf{M} = \begin{bmatrix} 1 + (4L^2/R_1R_2) - (4L/R_1) - (2L/R_2) & 2L - (2L^2/R_2) \\ (4L/R_1R_2) - (2/R_1) - (2/R_2) & 1 - (2L/R_2) \end{bmatrix}$$

$$= \begin{bmatrix} A & B \\ C & D \end{bmatrix} \quad [4.6]$$

From this expression for \mathbf{M} , we may find the eigenvectors, \mathbf{r} , and eigenvalues, μ , as defined by the equation

$$\mathbf{M}\mathbf{r} = \mu\mathbf{r} \quad [4.7]$$

Writing $m = \frac{1}{2}(A+D)$ for convenience and noting that $AD-BC=1$ (which is true for all conventional optical ray matrices), we obtain two such eigenvalues;

$$\mu_1, \mu_2 = m \pm \sqrt{m^2 - 1} \quad [4.8]$$

and two corresponding eigenvectors \mathbf{r}_1 and \mathbf{r}_2

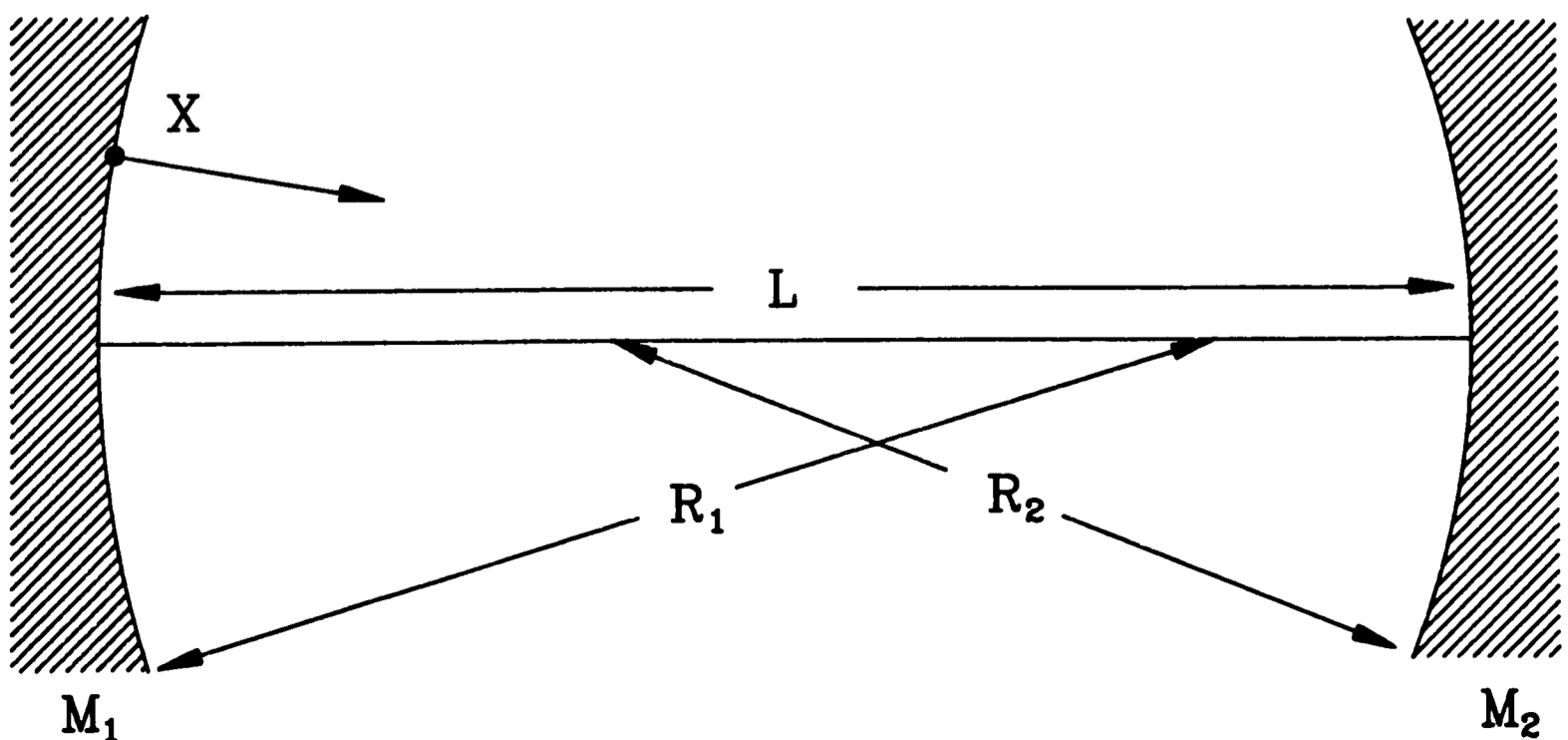


Figure 4.1: The requirements for stability of a laser cavity.

$$\mathbf{M}\mathbf{r}_1 = \mu_1\mathbf{r}_1 \quad \text{and} \quad \mathbf{M}\mathbf{r}_2 = \mu_2\mathbf{r}_2 \quad [4.9]$$

We now wish to monitor the progress of some arbitrary ray, \mathbf{r}_0 , launched into the system, as it is repeatedly reflected between the two mirrors. An important property of the eigenvectors \mathbf{r}_1 and \mathbf{r}_2 is that any such arbitrary ray may be written as

$$\mathbf{r}_0 = k_1\mathbf{r}_1 + k_2\mathbf{r}_2 \quad [4.10]$$

where k_1 and k_2 are two constant coefficients. Using this form for \mathbf{r}_0 , the ray generated after n round trips of the optical cavity may be immediately written as

$$\begin{aligned} \mathbf{r}_n &= \mathbf{M}^n \mathbf{r}_0 \\ &= k_1 \mu_1^n \mathbf{r}_1 + k_2 \mu_2^n \mathbf{r}_2 \end{aligned} \quad [4.11]$$

The designation of a particular cavity as being either stable or unstable is then dictated entirely by the value of the parameter m . The behaviour of a ray launched into a stable cavity is very different from that of a ray in an unstable arrangement, and in practice, the two types of cavity are used with a wide range of gain media to produce lasers which exhibit quite different output characteristics.

a) Stable resonators. If $m^2 < 1$ then we may put

$$\mu_1, \mu_2 = e^{\pm i\theta} \quad \text{where} \quad m = \cos(\theta) \quad [4.12]$$

such that

$$\mathbf{r}_n = \mathbf{r}_0 \cos(n\theta) + \mathbf{s}_0 \sin(n\theta) \quad [4.13]$$

where $\mathbf{s}_0 = i(k_1\mathbf{r}_1 - k_2\mathbf{r}_2)$. In this situation, the position of a ray in a particular transverse plane within the cavity will oscillate back and forth around the optical axis with a range of displacement determined solely by the initial values of \mathbf{r}_0 and \mathbf{s}_0 . Since the ray remains totally enclosed within the cavity, this type of resonator is described as 'stable'.

b) Unstable resonators. If $m^2 > 1$ we then find that

$$\begin{aligned} \mu_1, \mu_2 &= e^{\pm \theta} \\ &= M, 1/M \quad \text{where} \quad m = \cosh(\theta) \end{aligned} \quad [4.14]$$

which gives

$$\mathbf{r}_n = \mathbf{r}_0 \cosh(n\theta) + \mathbf{s}_0 \sinh(n\theta) \quad [4.15]$$

where in this case $\mathbf{s}_0 = (k_1\mathbf{r}_1 - k_2\mathbf{r}_2)$. This solution leads to the formation of two classes of ray in a laser system employing an unstable cavity; one with a displacement which

increases exponentially by a factor $M=e^{\theta}$ on each round trip, and one with a displacement which decreases by the factor M on each round trip. The behaviour of these two classes of ray is described further in section 4.2.1.

The stability condition, dictated by the parameter $m=\frac{1}{2}(A+D)$, may be written in terms of L , R_1 and R_2 ;

$$0 < (1 - L/R_1)(1 - L/R_2) < 1 \quad [4.16]$$

In an unstable resonator, this condition is not met, and in the arrangement used for the present laser specifically, the two mirrors are arranged to be confocal;

$$\begin{aligned} L &= f_1 + f_2 \\ \text{or } R_1 + R_2 &= 2L \end{aligned} \quad [4.17]$$

as shown in figure 4.2. Then,

$$(1 - L/R_1)(1 - L/R_2) = - (R_1 - R_2)^2 / 4R_1R_2 \quad [4.18]$$

Figure 4.3 illustrates the stabilities of the various possible optical arrangements, where $g_n=1-L/R_n$ has been used. By choosing one concave and one convex mirror (ie. $R_1>0$ and $R_2<0$), the expression [4.18] becomes greater than nought, leading to a ‘positive branch’ arrangement, which gives a collimated output and avoids an intra-cavity focus. For a cavity of two concave mirrors, described as ‘negative branch’, the intensity of radiation at the common focus can lead to a power density large enough to cause a dielectric breakdown of laser medium (as observed by James [1979]), and corresponding loss in flux from reflection and absorption at the plasma. For a system of much lower energy, this negative branch arrangement has been used to enable intra-cavity spatial filtering to be carried out, thus reducing the divergence of the output beam [Gobbi 1984, 1985].

An important parameter of such an unstable cavity is the magnification, M , defined by equation [4.14], which gives the increase or decrease in the beam diameter after each round trip. Considering a ray which leaves the surface of mirror M_1 in the confocal direction, such that it is parallel to the optical axis after reflection at M_2 (as shown in figure 4.2), we immediately have the magnification as (from figure 4.4);

$$\begin{aligned} y/x &= \left| \frac{1}{2}R_2 / \frac{1}{2}R_1 \right| \\ M &= |R_2/R_1| \end{aligned} \quad [4.19]$$

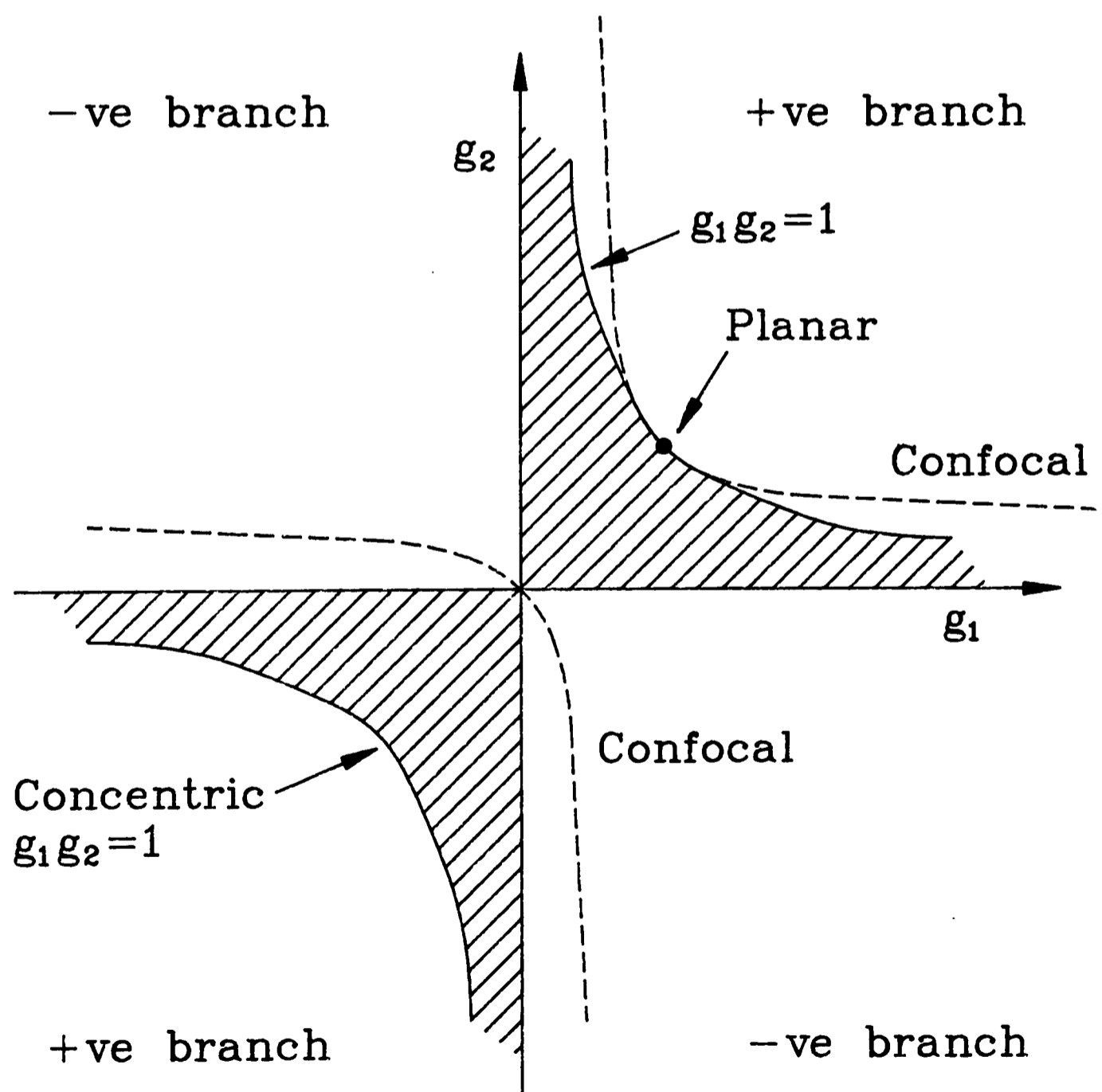
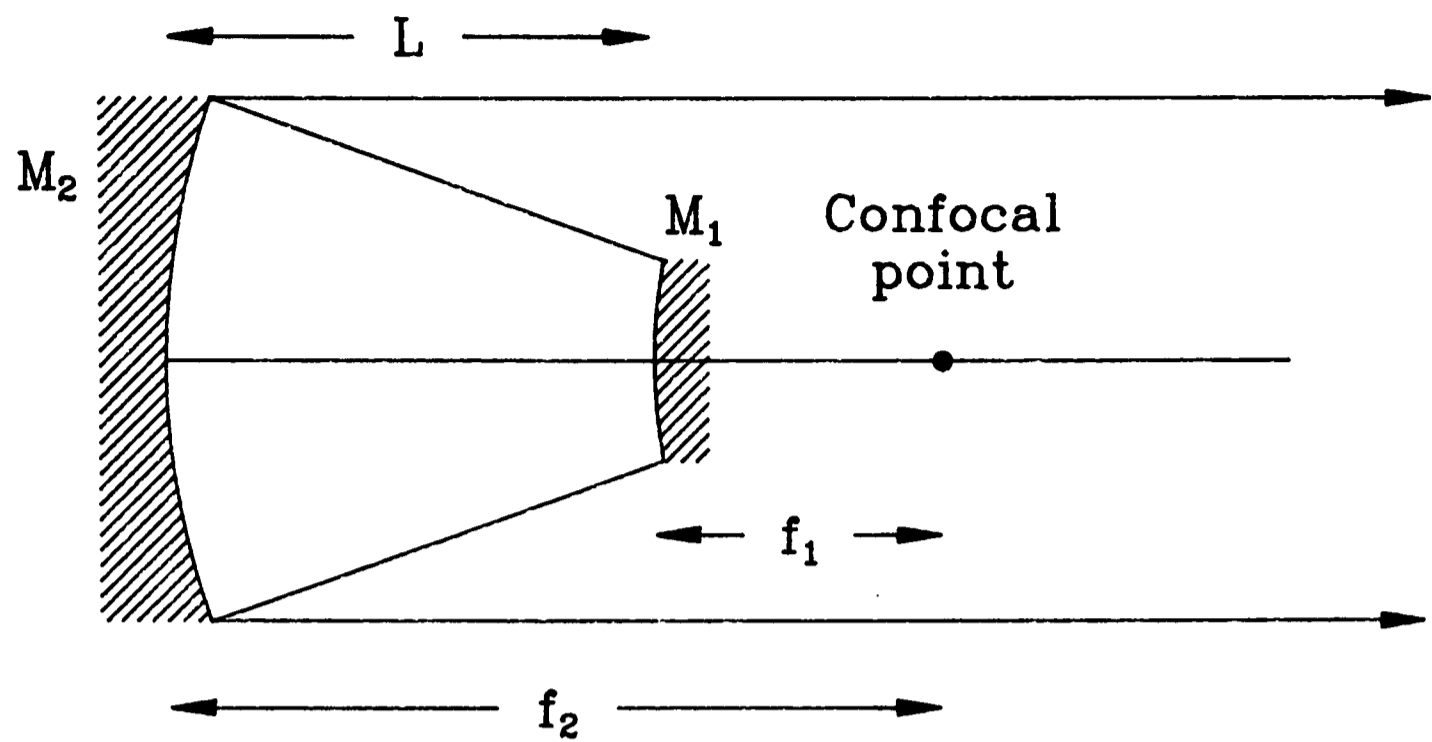


Figure 4.2: The collimated output of an unstable resonator.

Figure 4.3: Conditions required for cavity stability (represented by the shaded area).

which may also be obtained from equation [4.14]. The area of the beam which then passes M_1 , to form the laser output, is therefore $4(y^2 - x^2)$. Consequently, the fractional loss per round trip is

$$4(y^2 - x^2)/4y^2 = 1 - 1/M^2 \quad [4.20]$$

This geometrical loss (or ‘diffraction loss’ as it is sometimes misleadingly called) forms the laser output. In a ‘conventional’ laser system, this loss would be regarded as highly undesirable, and would be minimized by the use of a stable resonator, in which case one of the cavity mirrors is made to be partially transmitting to allow some fraction of the flux incident on it to form the laser output.

For an unstable cavity, a high degree of spatial coherence over the large area of the beam is achieved by way of the manner in which it evolves; an initially small region of coherence on the optical axis is rapidly expanded to cover the whole aperture as the beam propagates. Correspondingly, it is the central flat portion of the beam which comes to fill the entire resonator after a few round trips leading to a uniformly intense (‘top hat’) output.

4.2.1 Magnifying and demagnifying beams

In an unseeded resonator, laser action arises from localized spontaneous emission which occurs in the gain region. Before the onset of lasing, radiation from a large number of these ‘nuclei’ travel between the two mirrors which make up the unstable resonator. We consider the path of a particular beam in figure 4.5. From this, we see that there are two classes of propagating wave. One, which travels from A to B, is expanded by the magnification M on each round trip, and is called the magnifying beam. The second, travelling from B to A, is reduced by the factor M on each round trip, and is consequently called the demagnifying beam. From expression [4.6] for M and the confocal condition [4.17], the passage of the magnifying beam may be described by

$$\mathbf{M} \begin{bmatrix} d \\ 0 \end{bmatrix} = M \begin{bmatrix} d \\ 0 \end{bmatrix} \quad [4.21]$$

and the demagnifying beam by

$$\mathbf{M}' \begin{bmatrix} d \\ 0 \end{bmatrix} = 1/M \begin{bmatrix} d \\ 0 \end{bmatrix} \quad [4.22]$$

where \mathbf{M}' is the matrix for a ray originating from mirror M_2 rather than M_1 . In the first case, the magnification is M as defined by equation [4.14] and in the second, $1/M$ as expected.

The magnifying beam will rapidly reach a steady state situation where, on each round trip, a fraction $(1-1/M^2)$ will pass the smaller diameter mirror M_1 to form the laser output, while the remaining $1/M^2$ fraction will be reflected by M_1 to continue the amplification process. This is then a self-reproducing wave.

The demagnifying beam does not reach a steady state condition; it will continue to be demagnified until it becomes diffraction limited. Then, the focusing effect of the mirrors will be equalled by the beam divergence, and the beam will be converted into one which is subsequently magnified.

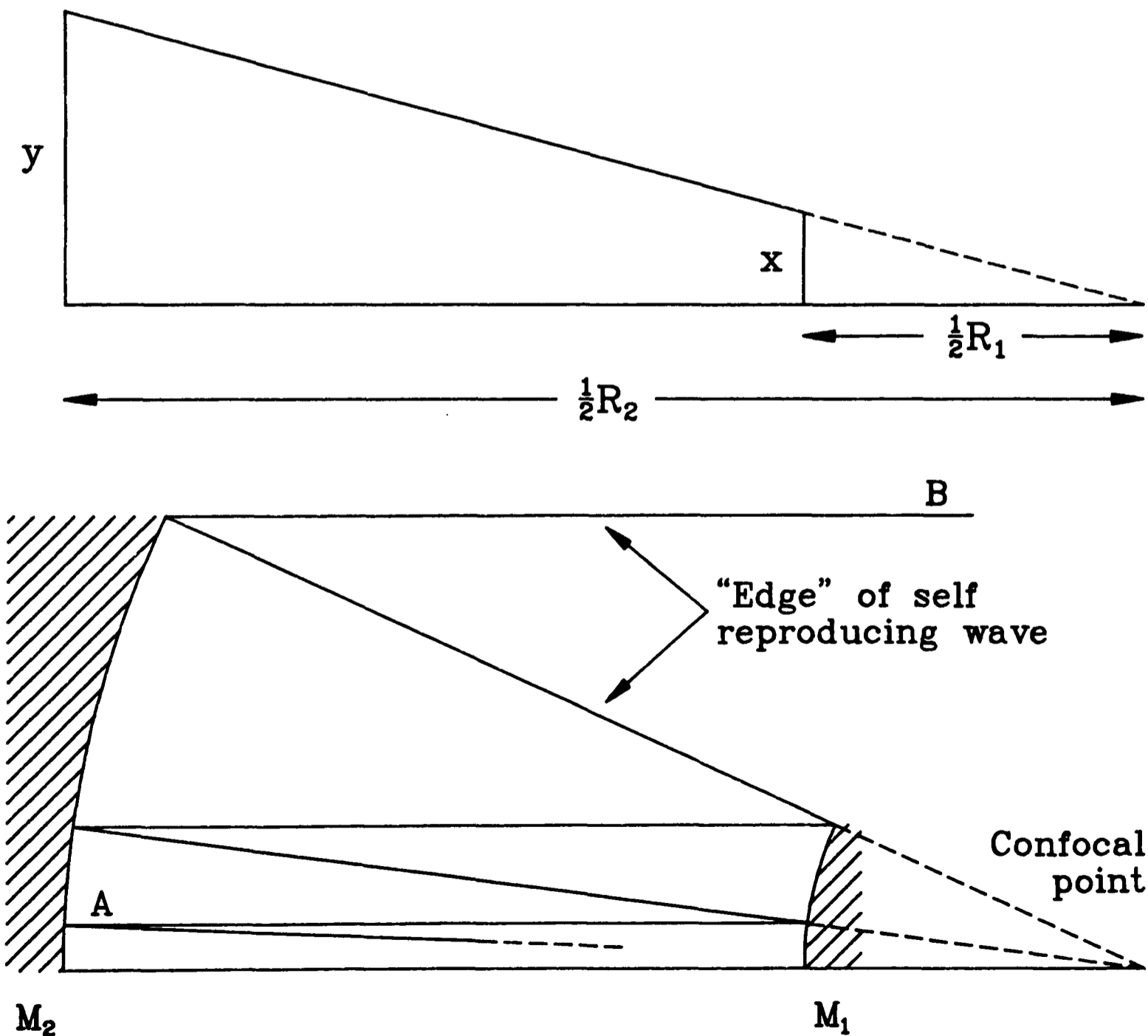


Figure 4.4: The magnification of an optical cavity.

Figure 4.5: Propagation of the magnifying and demagnifying beams.

4.2.2 The Fresnel Number

For a conventional stable resonator, the Fresnel number, N_f , is defined as the number of Fresnel zones subtended by one mirror as seen from the centre of the other. That is to say, it represents the difference in distance, measured in half wavelengths, between the centres of the two mirrors and the distance between the centre of one mirror and the edge of the other. For a cavity of length L and mirror radius a , this immediately gives

$$N_f \frac{\lambda}{2} = -L + \sqrt{L^2 + a^2}$$

$$N_f \sim a^2/L\lambda \quad [4.23]$$

assuming that $L \gg a$. It is commonly used as a measure of the divergence of a beam resulting from such a cavity. The diffraction limit is given by

$$\theta_{d1} = \lambda/2a \quad [4.24]$$

while the geometry of the cavity gives

$$\theta_g = a/L \quad [4.25]$$

and so we may note that

$$\theta_g/\theta_{d1} = 2N_f \quad [4.26]$$

In the case of a confocal unstable resonator however, the outgoing wave is planar and passes a curved output mirror. Here, we define an equivalent Fresnel number, N_{eq} , as the extra distance, measured in half wavelengths, travelled by the outermost part of the outgoing wave which strikes the output mirror, in comparison to that which strikes the centre of the mirror. So, from geometrical considerations,

$$N_{eq} = a_1^2/\lambda R_1 = a_1^2(M - 1)/2L\lambda \quad [4.27]$$

where $2L=R_2-R_1$ is the cavity round trip distance for a negative branch cavity and the output mirror has radius a_1 . Comparing equations [4.23] and [4.27] we note that

$$N_{eq} = \frac{1}{2}(M - 1)N_{f1} \quad [4.28]$$

where N_{f1} is the conventional Fresnel number for the first mirror M_1 . It is the equivalent Fresnel number which is important when considering unstable cavities; for a sharp-edged output mirror, for example, a small part of the reflected (magnifying beam) will be diffracted by the sharp mirror edges as it returns to the cavity region, to

form a demagnifying beam. For integral values of N_{eq} , this will be in phase with the rest of the beam and will enhance the magnifying beam, thus increasing the output coupling. With a half integral value of N_{eq} , the loss is correspondingly reduced. This dependence of loss on the value of N_{eq} has been confirmed experimentally by Freiberg [1972], having been first identified by Fox [1964]. This phenomenon is eliminated in systems with a 'soft' edged mirror, and also in the present laser system which uses a square output coupler, causing the value of N_{eq} to vary along different mirror diameters.

Siegman [1967] introduces a different equivalent Fresnel number, defined as the number of Fresnel zones subtended by mirror M_2 as observed from the virtual centre (here, the confocal point) behind M_1 . This gives us

$$\begin{aligned} N_{eq} &= a_2^2 / \lambda R_2 \\ &= N_{f2}(M - 1) / 2M \end{aligned} \quad [4.29]$$

4.2.3 Conditions for operation

For a diffraction limited beam to result from a given combination of confocal mirrors and gain region characteristics, three conditions must be met. To investigate these, we consider two parameters of the system; the number of round trips which are required for a beam to reach a diameter large enough for it to contribute to the laser output, and also, the effective gain coefficient of the cavity.

From the geometry of the cavity, we see that the maximum divergence that a beam may have is

$$\theta_{max} = a_2 / f_2 \quad [4.30]$$

where mirror M_2 has a focal length of f_2 and radius a_2 . Any beam with a greater divergence than this would not be completely reflected by M_1 , as part of it would pass outside its area and would therefore play no further part in the amplification process¹⁾. The diffraction limited divergence is

¹⁾ In practice, a_2 is taken as the radius of the gain volume cross section as it is this which is the limiting aperture.

$$\theta_{d1} = \lambda/2a_2 \quad [4.31]$$

Starting with a narrow beam having a diameter d_{\min} and the maximum divergence θ_{\max} , after p round trips of the cavity, its diameter is increased to

$$d_p = M^p d_{\min} \quad [4.32]$$

and hence, its divergence decreased to

$$\theta_p = M^{-p} \theta_{\max} \quad [4.33]$$

such that, to obtain θ_{\min} , the required number of round trips is

$$p = \ln(N_{eq})/\ln(M) \quad [4.34]$$

where $N_{eq}=2a_2^2/\lambda f_2$ is the equivalent Fresnel number²⁾. Part of the beam will emerge from the resonator after one further round trip, so that we may put the number of round trips required to achieve a diffraction limited output from an initial highly divergent beam, as

$$\begin{aligned} n &= p + 1 \\ &= 1 + \ln(N_{eq})/\ln(M) \end{aligned} \quad [4.35]$$

Up to this point, the beam will have been completely enclosed within the gain region, experiencing no geometrical losses, and therefore will be of greater intensity than any other beam, which will have suffered such losses.

For a flux, F , passing through a gain medium, we have, by definition;

$$F(l) = F(0)e^{\alpha l} \quad [4.36]$$

where α is the gain coefficient of the medium and l is the distance travelled. If we consider the flux after one pass through the present confocal system, we see that this becomes

$$\begin{aligned} F(L) &= \{F(0)/M^2\}e^{\alpha L_g} \\ &= F(0)e^{\alpha_{eff}L} \end{aligned} \quad [4.37]$$

such that we have an effective gain coefficient for the whole cavity of

²⁾ Note that this is not the same as either of the equivalent Fresnel numbers of section 4.2.2, which were introduced for the consideration of cavity losses. This equivalent Fresnel number pertains to the formation of diffraction limited beams, and is equal to the magnification M required for the formation of a diffraction limited beam from the minimum number of passes through the cavity (ie $n=2$ from equation [4.35]).

$$\alpha_{\text{eff}} = \{\alpha L_g - 2\ln(M)\}/L \quad [4.38]$$

where L_g is the gain length, and L is the mirror separation. We may now consider the three conditions mentioned previously which are required for a diffraction limited output.

a) There must be gain in the system for at least the time, τ_g , required by the beam to reach a diffraction limited mode such that it may contribute to the output beam. Immediately, this gives

$$\tau_g > \{1 + \ln(N_{\text{eq}})/\ln(M)\}.2L/c \quad [4.39]$$

b) The diffraction limit should be reached before saturation occurs. It can be shown that the time taken for a spontaneous nucleus to reach saturation is given by

$$\tau_{\text{sat}} = A/c\alpha_{\text{eff}} \quad [4.40]$$

[Letokhov 1968] where A is a slowly varying dimensionless quantity which depends on characteristics of the laser cavity and the lasing wavelength, λ . For excimer systems, A usually has a value of between 40 and 50. If this time is less than that taken to achieve a diffraction limited divergence, then such a beam emerging from the cavity would be of no greater intensity than one which had been able to reach saturation without being diffraction limited. In this case, the large cross section modes will deplete the energy in the medium and result in a poor quality output beam. This gives us the condition that

$$\begin{aligned} A/c\alpha_{\text{eff}} &> \{2 + \ln(N_{\text{eq}})/\ln(M)\}.2L/c \\ \alpha &< \{1 + A/2\ln(N_{\text{eq}}M)\}.\ln(M)/L_g \end{aligned} \quad [4.41]$$

c) Finally, the threshold for lasing (ie. the situation where the gain of the amplifying medium compensates for losses in the laser, such as output coupling) must be reached before the population inversion ends. The power radiated per unit volume into the solid angle 4π by spontaneous emission from the upper level is $N^*A_{21}h\nu$, where A_{21} is the Einstein A coefficient for the laser transition, N^* is the number density of species in the excited state and we have neglected any population in the ground state, as we are at liberty to do in the case of a KrF system where there is no bound ground state. Considering a small thickness, dz , of the medium, a contribution of

$$dI = N^* A_{21} h\nu (\Omega/4\pi) dz \quad [4.42]$$

where

$$\Omega = \pi \lambda^2 / 4 a_1^2 \quad [4.43]$$

[Jianwen 1990] will be made to the total intensity I , which is travelling through the medium with a solid angle Ω . Incorporating the amplification by stimulated emission, this gives an expression for the intensity of the beam after n round trips of the cavity arising solely from a nucleus of spontaneous emission;

$$\begin{aligned} dI_n &= (1/2)^{2n} (1/M^2)^n N^* A_{21} h\nu (\Omega/4\pi) e^{(2nL_g - z)} dz \\ I_n &= (1/2)^{2n} (1/M^2)^n N^* A_{21} h\nu (\Omega/4\pi) \int_0^{2nL_g} e^{(2nL_g - z)} dz \\ &= (1/2)^{2n} (1/M^2)^n N^* A_{21} h\nu (\Omega/4\pi\alpha) (e^{2nL_g\alpha} - 1) \end{aligned} \quad [4.44]$$

where the factor of $(1/M^2)^n$ represents the decrease arising from the magnification of the beam and $(1/2)^{2n}$ the loss from the 50% reflective spot on the beam splitter (described in section 4.3). A suitable condition for laser oscillation is that this final intensity should be greater than the saturation intensity, I_s , of the transition. This is the intensity which will deplete the upper level at a rate equal to that caused by the spontaneous lifetime. This saturation intensity is given by

$$I_s = h\nu / \sigma \tau_{21} \quad [4.45]$$

Then,

$$h\nu / \sigma \tau_{21} < (1/2)^{2n} (1/M^2)^n N^* A_{21} h\nu (\Omega/4\pi\alpha) e^{2nL_g\alpha} \quad [4.46]$$

Since $\alpha = \sigma N^*$ and $A_{21} \sim 1/\tau_{21}$, we have

$$2^{2n} + M^{2n} < (\Omega/4\pi) e^{2nL_g\alpha} \quad [4.47]$$

The factor A of equation [4.40] may be shown to be $A = (L/L_g) \ln(4\pi/\Omega)$, such that

$$\alpha > A/c\tau_g + \ln(M)/L_g + \ln(2)/L_g \quad [4.48]$$

where τ_g is the time for which there is gain.

These three conditions have not taken into account a number of other considerations, such as the time dependence of the gain coefficient, saturation of the inversion, and any inhomogeneities in the gain volume. These may strongly affect the output characteristics of the laser, although they do not invalidate the conditions

described above which may be seen as necessary but not sufficient for its desired operation.

For the optical cavity which was subsequently found to give the highest quality beam in terms of energy and divergence, these three conditions become;

$$\text{Amplifier: } \tau_g > 31\text{ns}, \alpha < 10.2/\text{m} \text{ and } \alpha > 9.6/\text{m}$$

$$\text{Oscillator: } \tau_g > 21\text{ns}, \alpha < 71.4/\text{m} \text{ and } \alpha > 45.0/\text{m}$$

The condition for τ_g was not met in either laser, although the technique of injection seeding (described in section 4.3) greatly relaxed the requirement made of this parameter for the amplifier. It is also unlikely that the gain coefficient in the oscillator laser would have exceeded $\sim 20/\text{m}$; Hirst [1987a] for example notes a range of values from $5/\text{m}$ to $27/\text{m}$ measured by a number of other workers under a wide variety of experimental arrangements. The failure to meet these conditions, brought about by the limitations imposed by the physical geometry of the laser system, would have been one of the reasons that led to the output beam not being of diffraction limited divergence.

From the discussion, it can be seen that resonators with a large magnification M are desirable, in that the time required to achieve saturation and a diffraction limited output is minimized. However, this must be balanced against the factor of $1/M^2$ which represents the fraction of the energy which is coupled back into the cavity. If M is increased to too large a value, a decrease in the total output energy of the laser will result.

It is also apparent that the beam divergence decreases by a factor M on each round trip of the resonator, such that the latter part of the beam will be of the lowest divergence. This arises as a result of the gradual build up of the beam from a nucleus of spontaneous emission. To overcome this limitation, the technique of injection seeding has been employed, which allows the relaxation of conditions [4.39], [4.41] and [4.48].

Shaw [1983] has shown that for a KrF laser operated under similar conditions to those of the present device with plane-plane cavity, the optimum reflectivity of the output coupler for maximum beam energy is between 5 and 10%, with a totally reflecting rear mirror. During the development of the laser system, a plane-plane cavity was used, with a fully reflecting back mirror and an uncoated silica flat as the

output coupler. This reflected ~4% of the beam from each face, resulting in a total reflection of ~8% as required.

4.3 INJECTION SEEDING

We may consider the time t taken for a beam of initial intensity I_e to be amplified to an intensity of I_s . Immediately,

$$I_s = I_e e^{\alpha_{\text{eff}} l} \quad \text{where } l = ct$$

$$t = \frac{L}{c} \ln(I_s/I_e) \{ \alpha L_g - \ln(M) \}^{-1} \quad [4.49]$$

This suggests that the time required to reach a saturated beam may be reduced by increasing the initial intensity I_e to a value above that of the background spontaneous emission. This is achieved by the use of a master, or oscillator laser, radiation from which is used to seed the slave, or amplifier laser. The oscillator need only be of a low output energy, as the injected signal has only to compete with the spontaneous emission in the amplifier. Furthermore, if it also has a mode structure similar to that of the lowest loss amplifier mode, then there will no longer be any requirement concerning the minimum number of oscillations which must be performed in the amplifier cavity before threshold may be reached.

This technique of seeding enables a diffraction limited beam to be attained more rapidly, allowing a lower magnification to be used in the amplifier, resulting in a larger output energy. The optimum timing for the enhancement of energy and decrease in divergence occurs when the oscillator beam is injected such that the radiation from its trailing edge (ie. lowest divergence part) irradiates the amplifier gain region just at the time when lasing action is about to commence. The relative timing of the two lasers was controlled in such a way as to achieve this (described in section 4.4).

The injection seeding geometry is shown schematically in figure 4.6. A coupled confocal cavity arrangement was used, with M_3 a convex mirror common to both the oscillator and amplifier resonators. All three mirrors were coated to have a reflectivity of ~100% at 248nm. To allow the rapid positioning of the mirrors along the optical axes of the lasers, aluminium bars of cross section 1"x1.5" were rigidly mounted directly to the end flanges of both lasers. The mirrors, in suitable mounts, were then

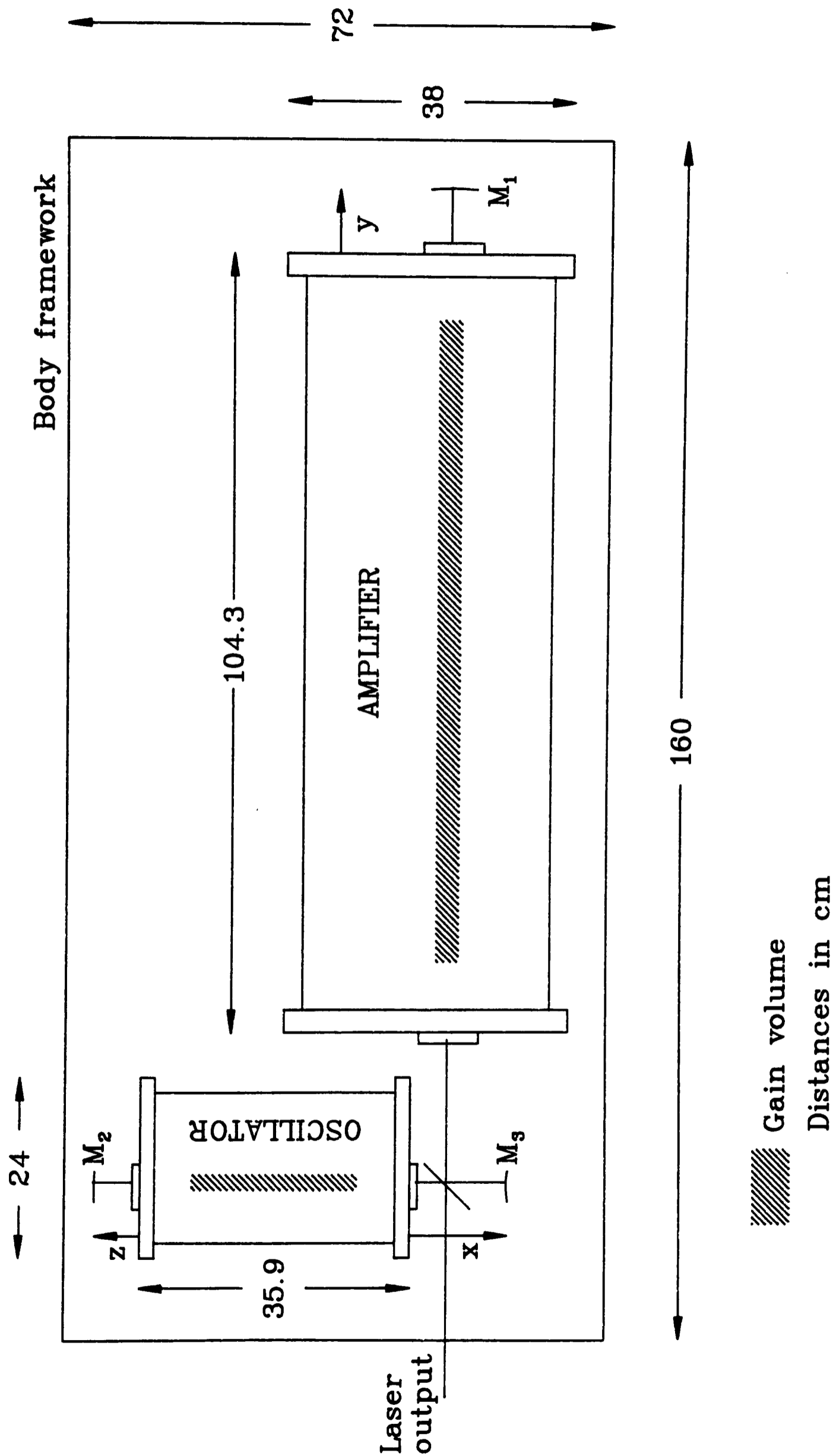


Figure 4.6: Plan view of the laser system.

secured to the rails. In this way, the position of each mirror in the direction of the laser axes could be easily adjusted as required during the investigation of different confocal arrangements, described in section 4.5.

The amplifier cavity was completed by means of a beam splitter, which also coupled radiation from the oscillator into the amplifier. It was constructed from a quartz substrate, of dimensions $50 \times 40 \times 3 \text{ mm}^3$, with a maximum wavefront distortion of $\lambda/10$, and an anti-reflection coating for 248nm on both sides. At the centre of one face, a $3 \times 4 \text{ mm}^2$ 50% reflective spot was deposited such that when the beam splitter was in position in the laser system, the reflective spot lay on the optical axis of both lasers. With this arrangement, the output beam of the oscillator was only affected by the presence of the 50% reflective spot, which coupled an effective area of

$$3 \times 4 \sin(45^\circ) \text{ mm}^2 = 3 \times 2.8 \text{ mm}^2$$

of its beam into the amplifier. For a simple single confocal cavity, the size of the output beam is simply that of M_3 , the convex mirror, multiplied by the cavity magnification M (assuming a gain region large enough to accommodate this). In the present arrangement however, the effective size of the mirror M_3 is dictated by its position relative to the beam splitter. Considering the geometry of the arrangement, it is apparent that the output beam will be of size

$$D = 3 \text{ mm} \cdot f_1 / (f_3 + x - 4.3) \quad [4.50]$$

where f_1 and f_3 are the focal lengths of mirrors M_1 and M_3 and all distances are in centimetres. The quantity $(f_3 + x - 4.3) \text{ cm}$ simply represents the distance of the beam splitter, of effective side $\sim 3 \text{ mm}$ (as above) from the confocal point of the cavity. This dependence of D on x , f_1 and f_3 was verified experimentally for the various cavities employed.

4.4 RELATIVE TIMING MEASUREMENTS

Initially, two independent plane-plane cavities were used to investigate the relative timing of the two lasers. Each beam was steered onto a photodiode, which had a response time of below 1ns. The difference in path length between the two beams, as measured from the output couplers, was less than 2cm, which would correspond to a

time of $\sim 70\text{ps}$, and the amplifier beam was passed through an attenuating NO_2 cell so as to make the signal from each laser approximately equal in magnitude.

4.4.1 Results

It was found that the oscillator laser pulse preceded that of the amplifier by 37.6ns , this resulting from the smaller time constant, LC , for the oscillator circuit. The time between the pulses was then reduced by the use of a variable inductor which was inserted into the oscillator electrical circuit. From equation [3.8], the characteristic rise-time, τ , of either circuit was shown to be

$$\tau = \pi \sqrt{L_1 C_s C_p / (C_s + C_p)} \quad [4.51]$$

and so by increasing the value of L_1 , τ could be increased. The variable inductor was made from a number of rings of copper wire mounted on a perspex post such that the output to the oscillator could be taken after a specific number of turns, n . The inductance of n turns would then be given by

$$L_n = k_1 n^2 \quad [4.52]$$

and the characteristic rise-time of the circuit consequently

$$\tau = k_2 \sqrt{L_{\text{osc}} + L_n} \quad [4.53]$$

where L_{osc} is the inductance of the original circuit. Assuming that $L_n \gg L_{\text{osc}}$, we have

$$\tau = k_3 n \quad [4.54]$$

where k_1 , k_2 and k_3 are constants, and so a linear variation of timing with number of inductor turns, and this was indeed found to be the case, as shown in figure 4.7. By varying the number of turns, n , from 0 to 13, the time difference between the pulses, defined here as that between the first peak of each signal, could be varied from 37.6ns to 5.4ns (figure 4.8). Thus, the addition of each turn caused the pulse separation to decrease by 2.55ns . For a given inductance, the jitter in the pulse separation between successive shots was found to be no more than $\pm 2\text{ns}$.

The FWHM of the oscillator pulse was measured to be 10ns , and that of the amplifier to be 24ns . For both pulses the periodic contribution to the output arising from a beam travelling between the two cavity mirrors is clearly visible in figure 4.8

and corresponds to the cavity round trip time $t=2L/c$. (The output beam arising from the coupled confocal arrangement was also monitored, and it was found, as expected, that its FWHM had decreased, to 20ns; this would have resulted from the greater loss experienced by the beam in the confocal cavity arrangement.)

The output energy of the oscillator laser, equipped with the plane-plane cavity was also measured as the number of inductor turns was varied from 0 to 13 and the values obtained are illustrated in figure 4.9. As expected, there was a decrease in the laser energy with increasing inductance, although the reduction (of about 8%) was much smaller than might have been expected considering the increase in inductance which had been introduced into the oscillator discharge circuit. The variation in energy alone was therefore noted as not being large enough to have any significant consequences on either the output energy or beam divergence of the amplifier when seeded by the oscillator, in that the injected intensity would be greater than that of any amplified spontaneous emission for all of the relative timings used in the current studies.

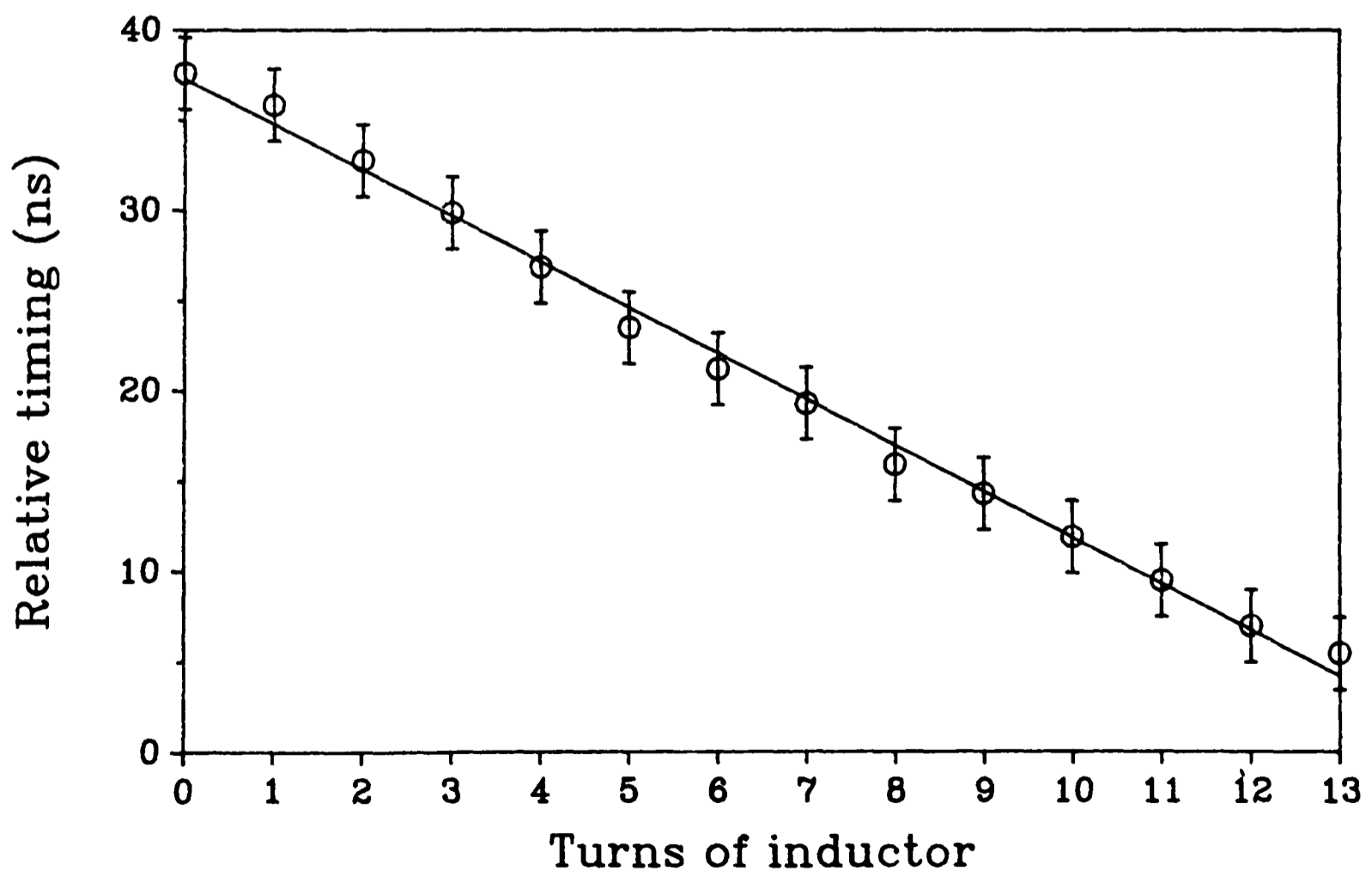


Figure 4.7: The relative timing of the oscillator and amplifier as a function of the number of inductor turns in the oscillator electrical circuit.

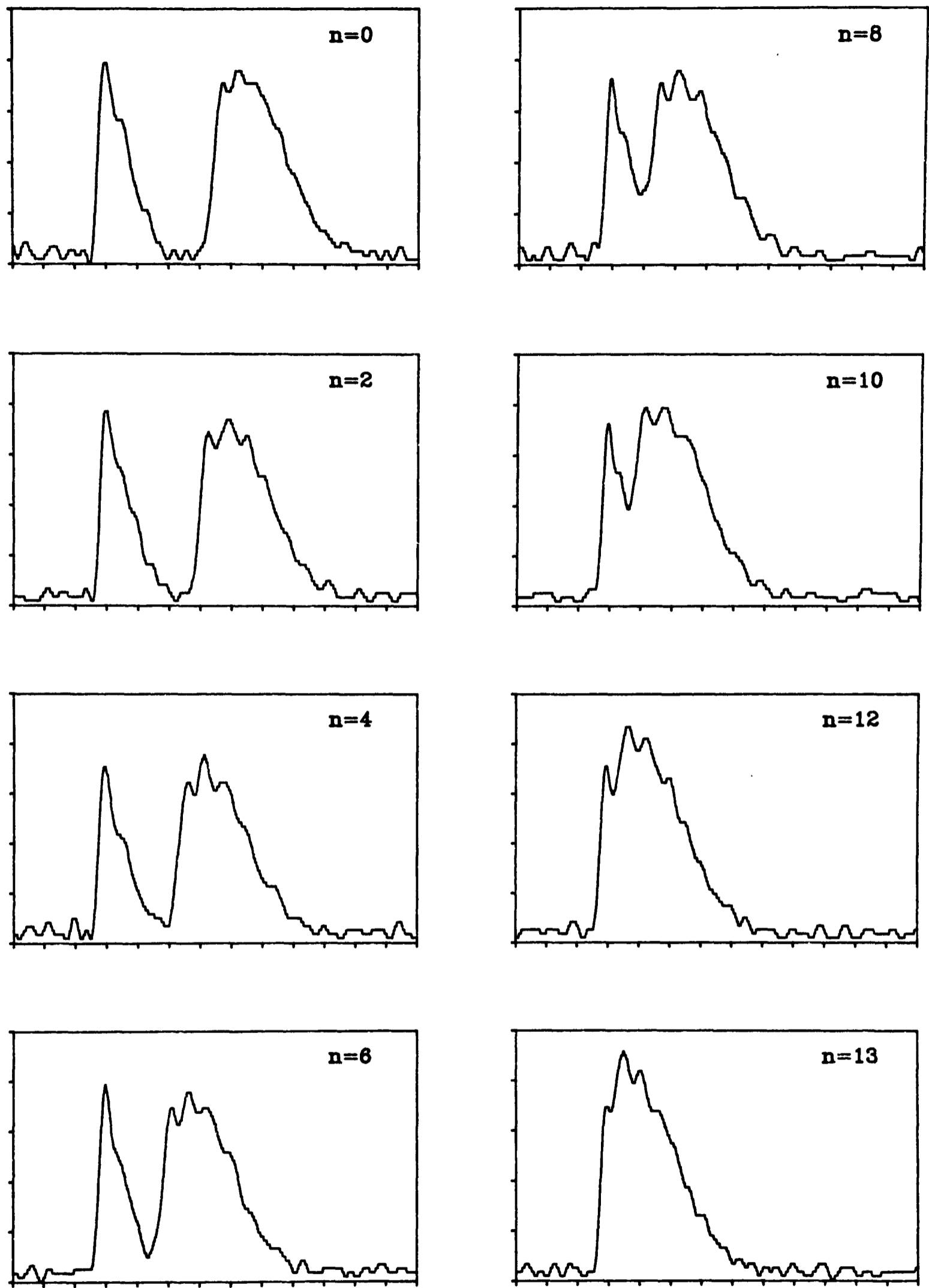


Figure 4.8: An illustration of the variation in timing between the two output beams as a function of the number of inductor turns in the oscillator electrical circuit. Each horizontal division represents 10ns.

4.5 OPTIMIZATION OF THE CONFOCAL CAVITIES

Although, for a given set of gain region conditions, a plane-plane cavity would have given the largest laser energy output, the current application required the use of a confocal cavity, as explained in section 4.1. Such an optical arrangement leads to a decrease in the total energy output of the laser however, and the improvement in beam divergence obtained must be balanced against the total beam energy.

In the initial '1 Joule laser' system, only a very brief optimization process was carried out. The original choice of $f_1=135\text{cm}$, $f_2=54\text{cm}$ and $f_3=-9\text{cm}$, such that $M_a=15$ (the magnification of the amplifier cavity) and $M_o=6$ (the magnification of the oscillator cavity), was found to be unsatisfactory in that an output energy of only 350mJ was obtained. To increase the fraction of radiation being coupled back to the amplifier, its magnification was decreased. Mirrors of $f_1=150\text{cm}$, $f_2=100\text{cm}$ and $f_3=-15\text{cm}$ were chosen to obtain $M_a=10$ and $M_o=6.7$, with this choice being dictated by the immediate availability of components within the laboratory. This led to an output energy of 650mJ.

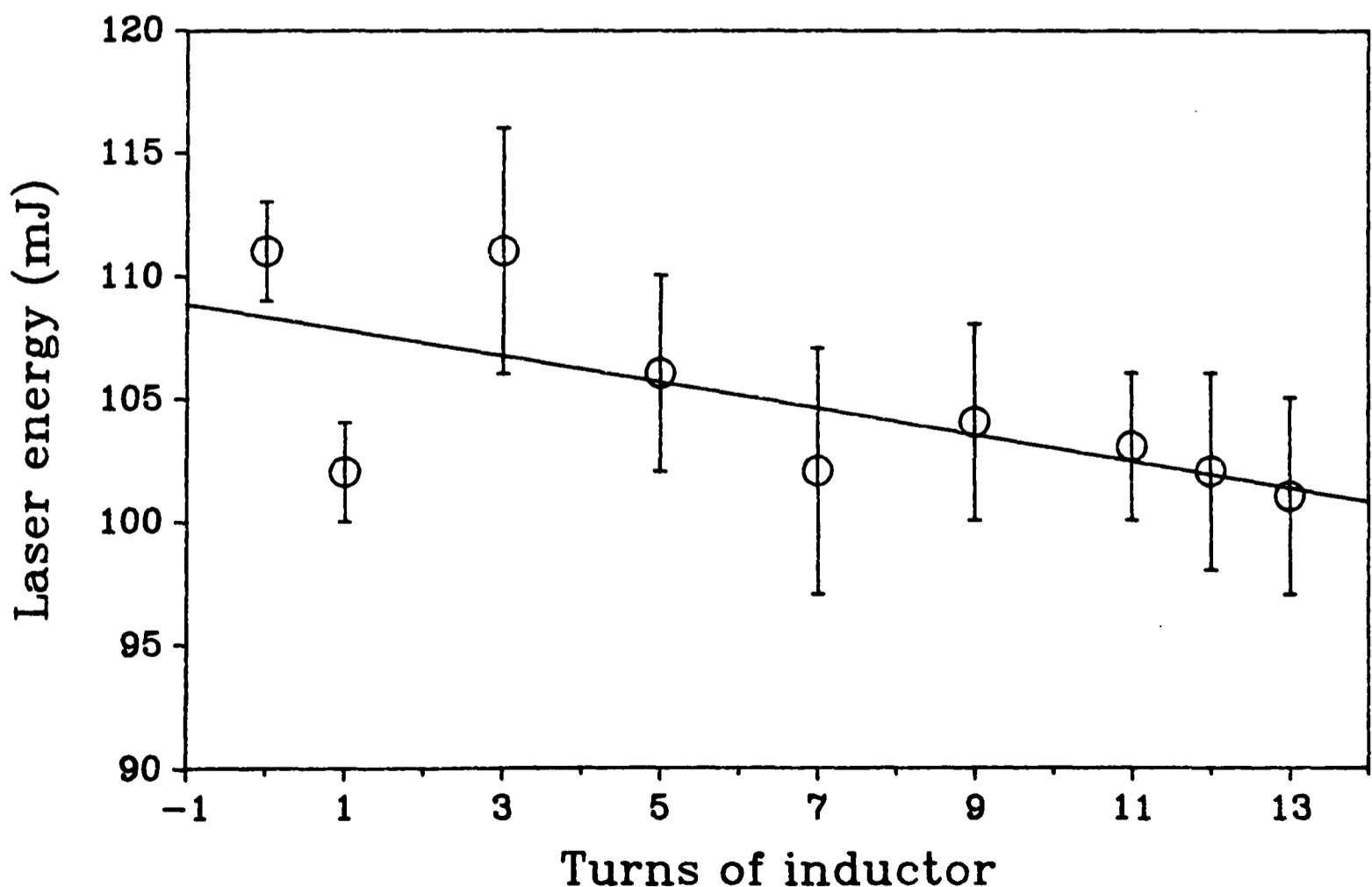


Figure 4.9: The oscillator output energy, with a plane-plane cavity, as a function of the number of inductor turns in its circuit.

For the upgraded laser system, a more detailed investigation into the effect of the magnification on the output energy and beam divergence was carried out. The requirements of mirror quality were also considered, since those of the ‘1 Joule’ system were of unknown, and probably poor, tolerance. The mirrors used to study the effects of confocal cavity arrangement on the output energy and beam divergence are shown in table 4.1 and the different cavity arrangements in table 4.2.

f (cm)	Diameter	Quality	Mirror	
150	5cm	?	M ₁	Used in ‘1J’ system
150	5cm	$\lambda/10$	M ₁	
135	5cm	$\lambda/10$	M ₁	Original system
100	2"	?	M ₂	Used in ‘1J’ system
69.5	1"	$\lambda/10$	M ₂	
54	1"	$\lambda/10$	M ₂	Original system
-20	1cm	$\lambda/10$	M ₃	
-15	1"	Poor	M ₃	Used in ‘1J’ system
-12.4	1cm	$\lambda/10$	M ₃	
-9	0.5"	$\lambda/10$	M ₃	Original system
-6	1cm	$\lambda/10$	M ₃	

Table 4.1: Mirrors used in the optimization of the confocal cavities.

4.6 ENERGY DEPENDENCE ON CAVITY

For each of the confocal cavities, the output energy was measured as the relative timing between the two lasers was adjusted by the use of the variable inductor. The energy output of a plane-plane cavity for the amplifier was found to be 2.24J, decreasing at a rate of only 0.165J/hour as a result of the use of the GP2000 gas purification system. The values obtained from the confocal cavities were adjusted to take into account this decrease in performance.

In each case a peak in the enhancement obtained by seeding was found to occur at a relative timing of between 10 and 20ns. This is at variance with the findings of Cotton [1990], where the enhancement was seen to saturate at ~30ns for the M_a=10.0, M_o=6.7 cavity, but similar to those of McCown [1988] for a plane-plane cavity. Table

4.3 gives the salient performance characteristics for each arrangement and the variations with timing are given in figures 4.10 to 4.21.

The output beam size (as considered in section 4.3) was maintained at $20 \times 20 \text{ mm}^2$ for all the cavities, where permitted by the layout of the apparatus. In this way, the dependence of the output energy and beam divergence on the cavity magnification would not be affected by the finite area of the gain region or variation in the beam size. From table 4.3, we can see that the unseeded energy decreased with increasing magnification as expected, as the fractional loss per round trip of $1 - 1/M_a^2$ increased. The requirements set down by equations [4.39], [4.41] and [4.48] are also shown for each cavity. McKee [1988] and Maruyama [1992] measured the total energy output of cavities with various magnifications between 5 and 25 to find a similar decrease with increasing magnification. The energies obtained from the unseeded amplifier laser as a fraction of that obtained by a plane-plane cavity are plotted in

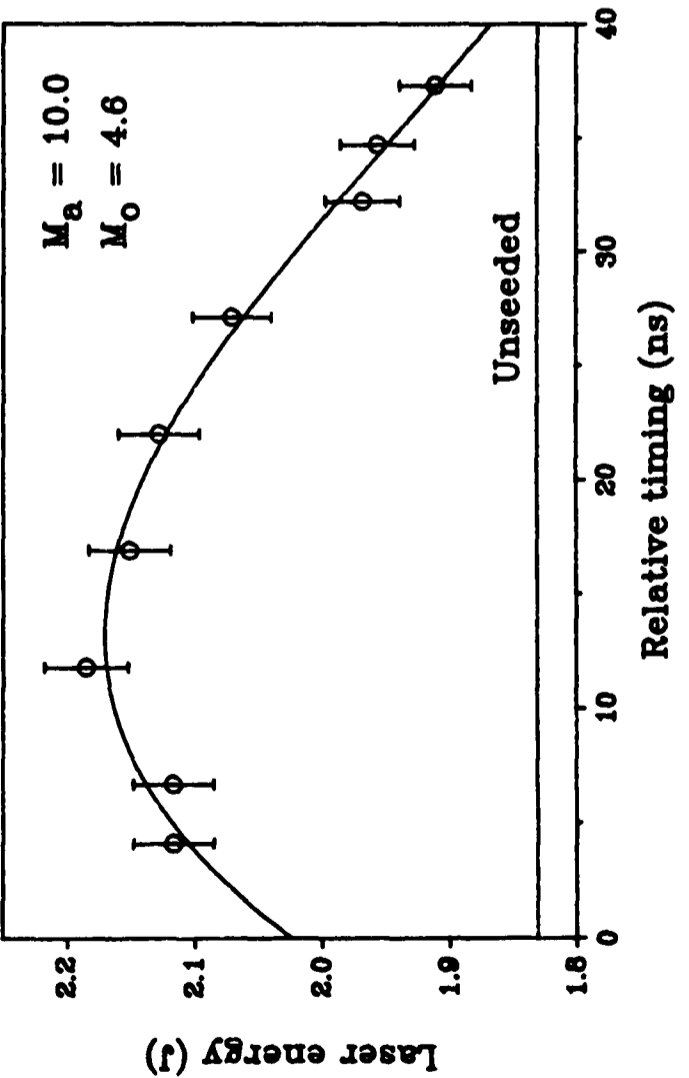
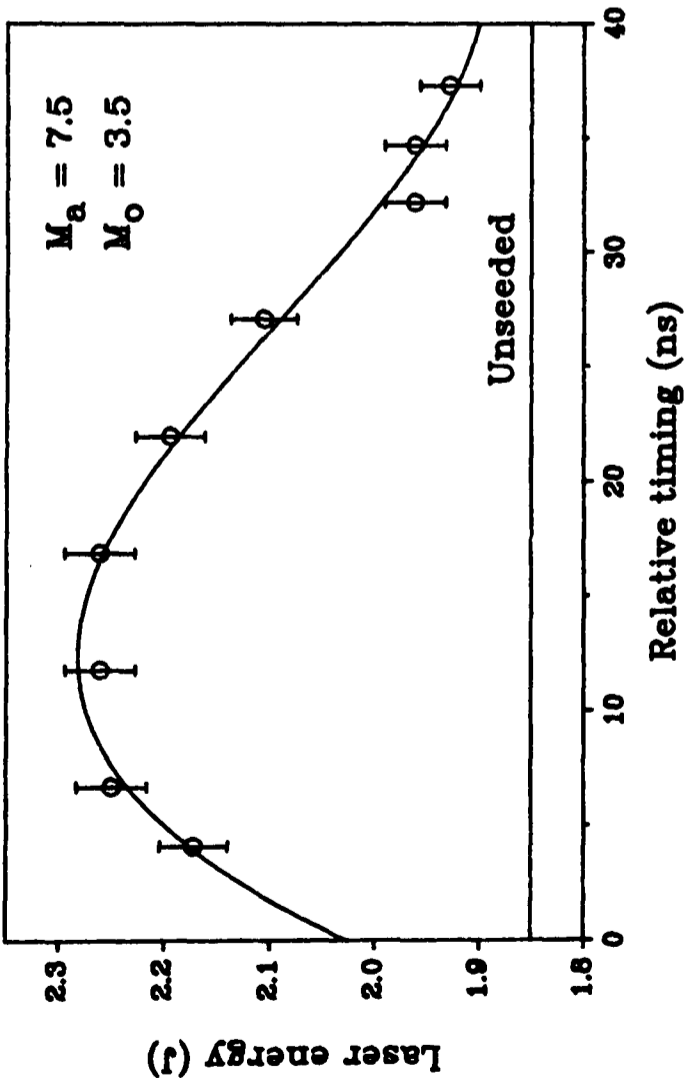
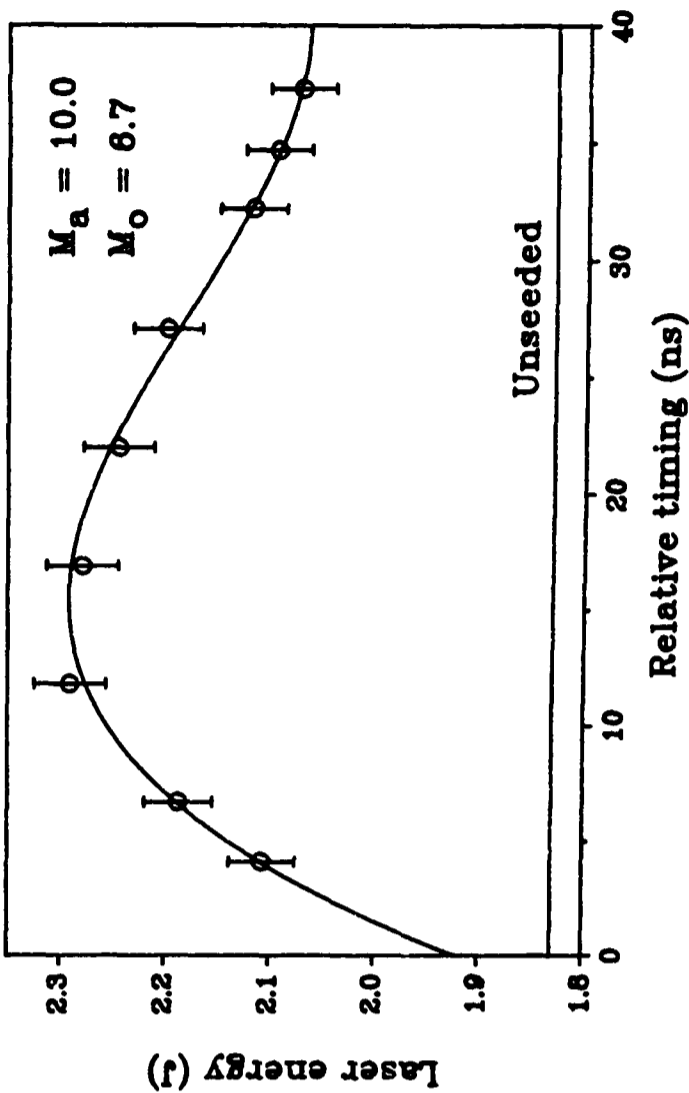
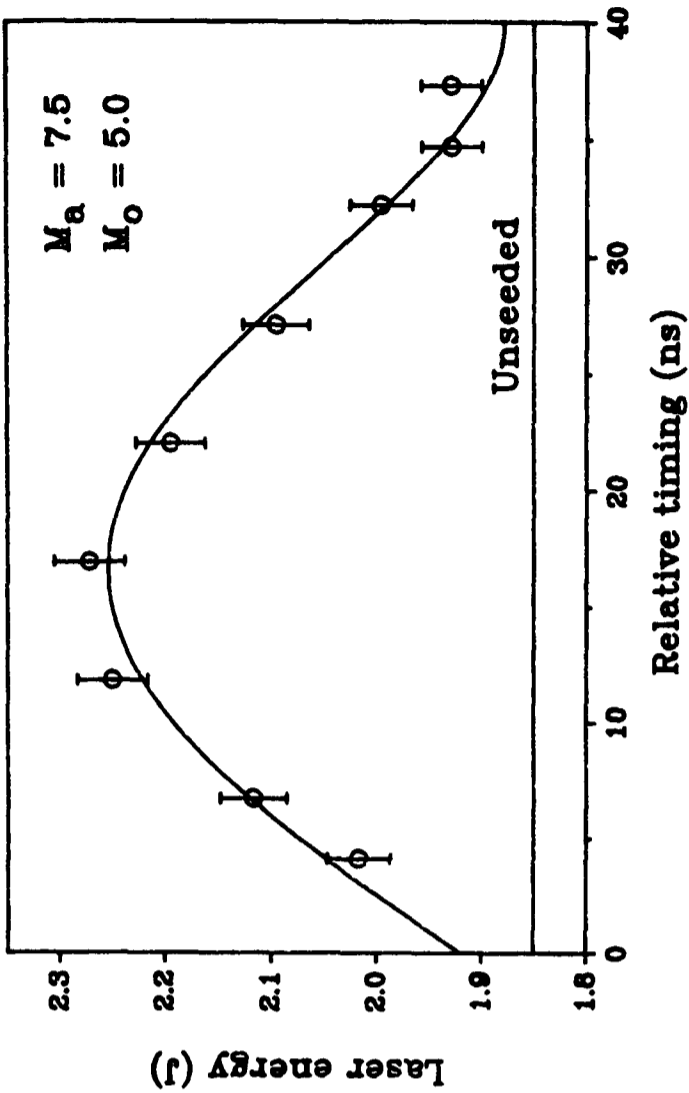
f_1 (cm)	f_2 (cm)	f_3 (cm)	M_a	M_o	x (cm)	y (cm)	z (cm)	Beam size
150	69.5	-20.0	7.5	3.5	6.8	4.1	6.8	20
150	100	-20.0	7.5	5.0	6.8	4.1	37.3	20
150	69.5	-15	10.0	4.6	11.8	4.1	6.8	20
150	100	-15 ^a	10.0	6.7	11.8	4.1	37.3	20
150	69.5	-12.4	12.1	5.6	14.4	4.1	6.8	20
150	100	-12.4	12.1	8.1	14.4	4.1	37.3	20
150	69.5	-9.0	16.7	7.7	17.8	4.1	6.8	20
150	100	-9.0	16.7	11.1	17.8	4.1	37.3	20
150	69.5	-6.0	25.0	11.6	20.8	4.1	6.8	20
150	100	-6.0	25.0	16.7	20.8	4.1	37.3	20
135	54.0	-9.0 ^b	15.0	6.0	5.0	1.9	4.1	42 ^c
135	54.0	-6.0	22.5	9.0	8.0	1.9	4.1	42 ^c

^a Mirrors used in the working '1 Joule' system

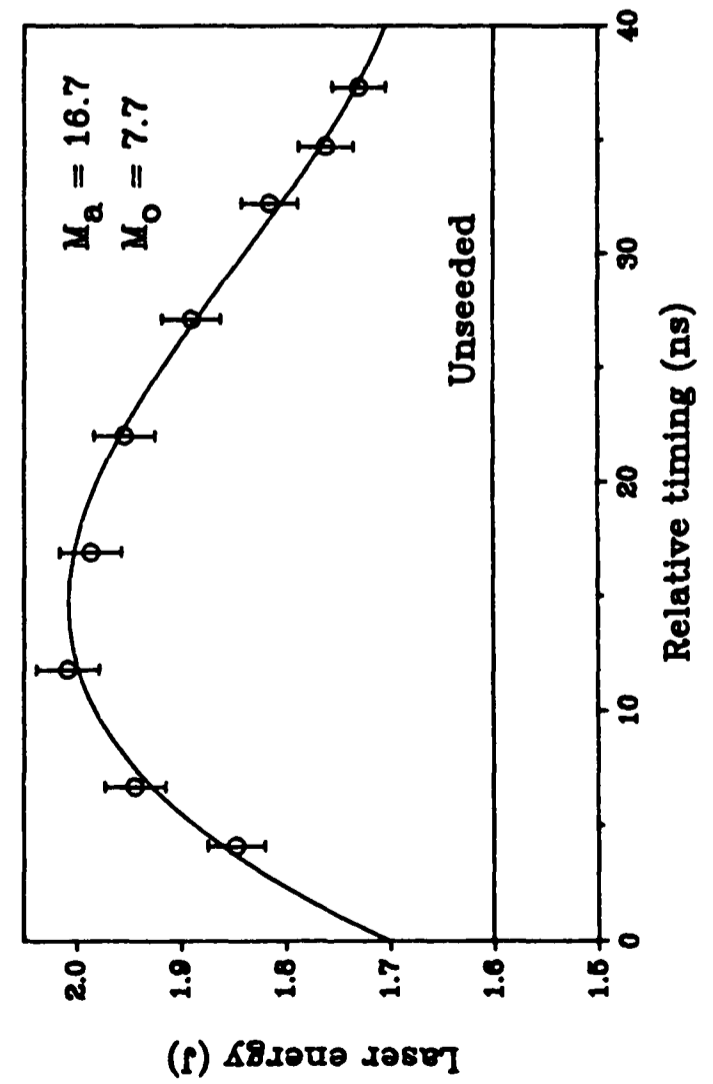
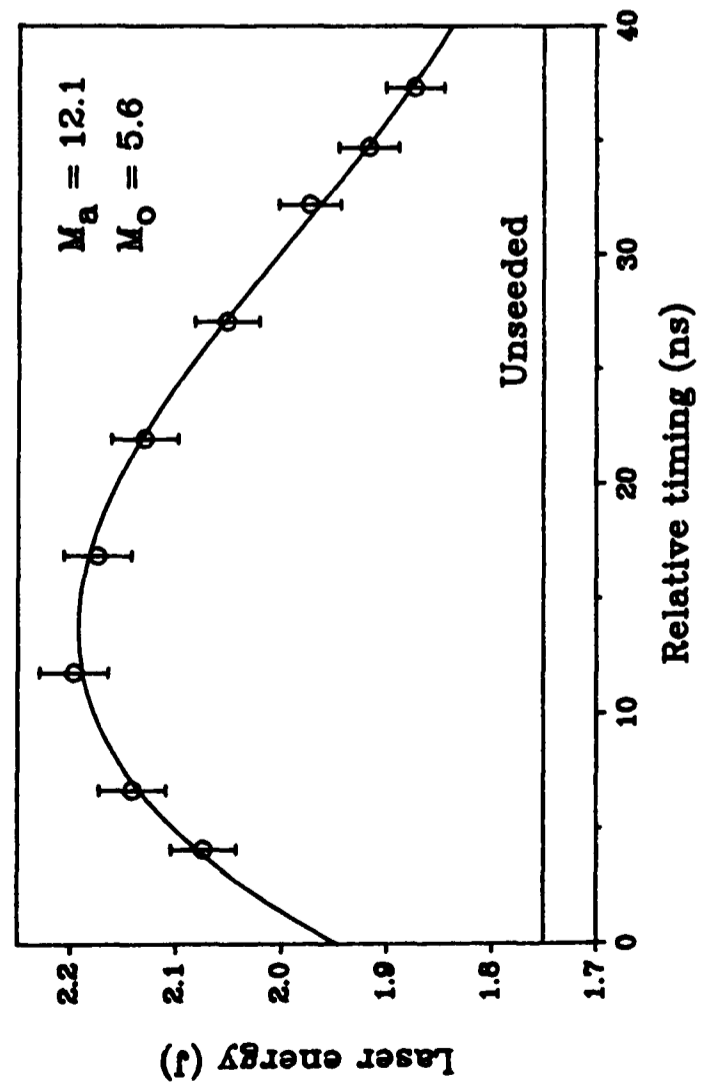
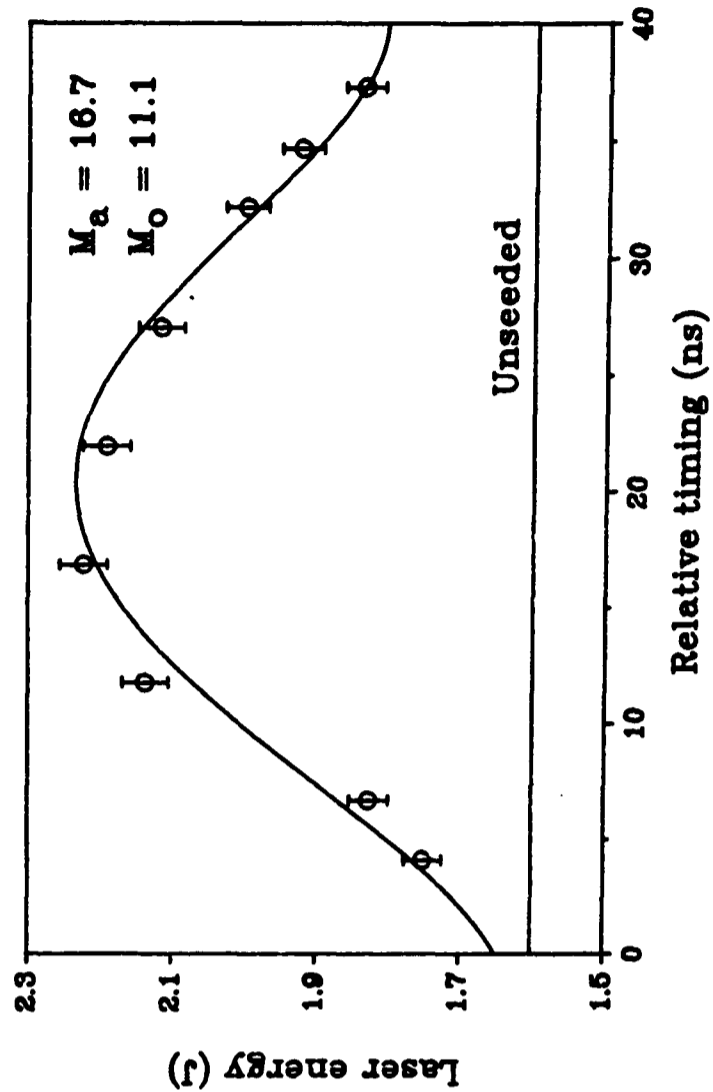
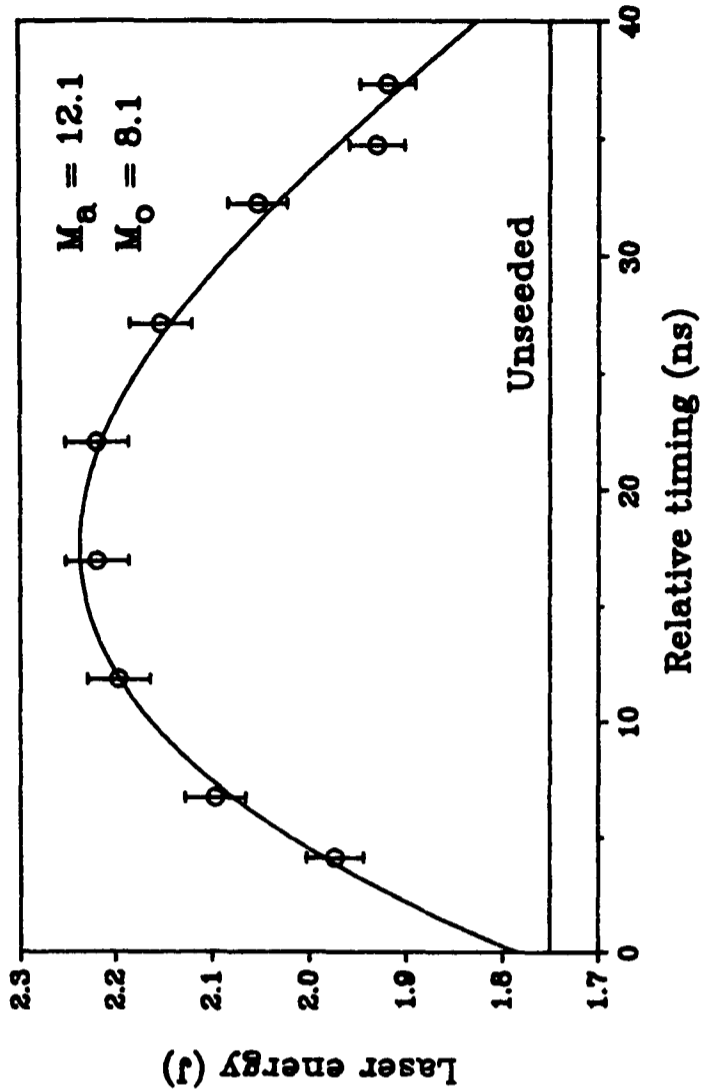
^b Initial mirrors for the '1 Joule' system

^c Limited by the gain area to $32 \times 30 \text{ mm}^2$

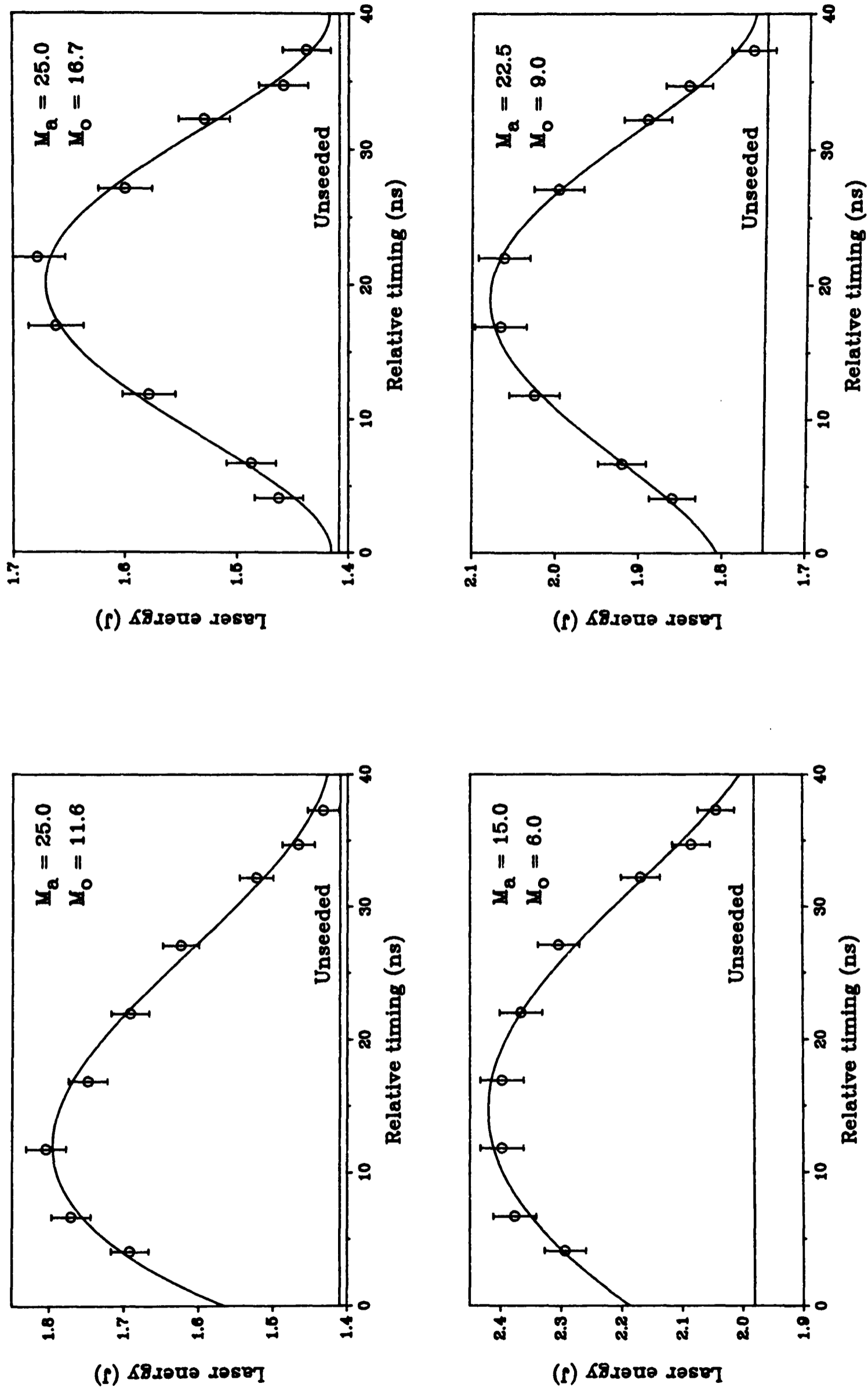
Table 4.2: Parameters of the various optical cavity arrangements investigated.



Figures 4.10 to 4.13: The energy dependence on seeding delay for the various cavities used.



Figures 4.14 to 4.17: The energy dependence on seeding delay for the various cavities used.



Figures 4.18 to 4.21: The energy dependence on seeding delay for the various cavities used.

figure 4.22, along with those of McKee [1988] and Maruyama [1992]. The measurements made with the present system and those of McKee [1988] suggest that a further decrease in the amplifier magnification would in fact lead to a decrease in the output energy. This would be the result of too high a fraction of the magnifying beam being returned to the gain medium, necessarily at the expense of the output beam, in a situation where a sufficient amount of feedback would already have been supplied by a higher magnification cavity.

In the case of the $M_a=15$, $M_o=6$ and $M_a=22.5$, $M_o=9$ arrangements, the close proximity of mirror M_3 to the beam splitter led to an output beam which covered the full gain area generated by the electrode structure, leading to the observed high output energy. For the original ‘1 Joule’ system, this optical arrangement was not satisfactory (as explained in section 4.5) and it is assumed that this was because of the smaller gain area for this laser (ie. $15 \times 25 \text{mm}^2$) which would have already been fully utilized by the smaller magnification $f_1=150$, $f_2=100$, $f_3=-15$ optical system which was subsequently employed.

M_a	M_o	$E_a(\text{J})$	$E_a(\text{J})$ (peak)	% gain	τ_a (ns)	τ_o (ns)	α_a (/m)	α_o (/m)
7.5	3.5	1.85	2.26	22	36.8	19.7	<7.4, >8.2	<24, >26
7.5	5.0	1.85	2.27	23	36.8	24.7	<7.4, >8.2	<47, >38
10.0	4.6	1.83	2.18	19	34.5	18.3	<8.4, >8.8	<31, >29
10.0	6.7	1.83	2.28	25	34.5	23.1	<8.4, >8.8	<56, >41
12.1	5.6	1.75	2.20	25	33.2	17.5	<9.1, >9.1	<36, >30
12.1	8.1	1.75	2.22	27	33.2	22.2	<9.1, >9.1	<62, >42
16.7	7.7	1.60	2.01	26	31.2	16.3	<10.2, >9.6	<43, >33
16.7	11.1	1.60	2.22	39	31.2	20.8	<10.2, >9.6	<71, >45
25.0	11.6	1.41	1.80	28	29.1	14.9	<11.5, >10.2	<52, >36
25.0	16.7	1.41	1.68	19	29.1	19.3	<11.5, >10.2	<82, >48
15.0	6.0	1.98	2.40	21	31.5	13.8	<8.8, >9.1	<30, >26
22.5	9.0	1.75	2.07	18	29.2	12.6	<10.1, >9.6	<38, >29

Table 4.3: Unseeded and peak seeded energies obtained from the confocal cavities. τ_a and τ_o evaluated from [4.39] and the limits imposed on α from [4.41] and [4.48].

For a given amplifier magnification, the seeded output energy appeared to have only a small dependence on the oscillator magnification.

4.7 DIVERGENCE DEPENDENCE ON CAVITY

The divergence of the laser beam arising from each optical arrangement was measured by focusing the beam using an $f=2\text{m}$ lens, after a great deal of attenuation (achieved by the use of an NO_2 cell) onto a CCD based Exitech 256 beam profiler. The profiler and the controlling computer were situated outside the screened laser room, as illustrated in figure 4.23 as the large amount of electrical noise generated by the discharge circuit interfered with the triggering of the unit. The laser beam was steered through a port in the wall of the screened room by means of a coated flat. The profiler was optically triggered by light from the laser spark gap and two UG5 filters were placed immediately in front of the detector to prevent any visible light from reaching the CCD.

The output beam of a confocal cavity will, by the nature of its formation, approximate to a top hat function in terms of intensity. Assuming a square beam with no phase curvature, this will be focused by a lens of focal length f to a pattern of intensity

$$I(X,Y) = I(0)\text{sinc}^2(\alpha)\text{sinc}^2(\beta) \quad [4.55]$$

which is simply the Fourier transform of the top hat function, where

$$X = f.\sin(\theta), \quad Y = f.\sin(\varphi) \\ \alpha = (kD/2)\sin(\theta) \quad \text{and} \quad \beta = (kD/2)\sin(\varphi) \quad [4.56]$$

for a beam of side D and wavenumber $k=2\pi/\lambda$. This characteristic sinc^2 function has a FWHM given by³⁾ $\alpha=2.8$. Correspondingly, the FWHM in the focal plane of the lens will be

$$\text{FWHM} = 2f\alpha/kD \quad [4.57]$$

In the current application, this becomes

³⁾ For comparison, a circular top hat function of diameter D would be focused to an Airy disk of FWHM $\alpha=3.2$. A Gaussian beam of FWHM D would be focused to a Gaussian spot of $\alpha=2.8$.

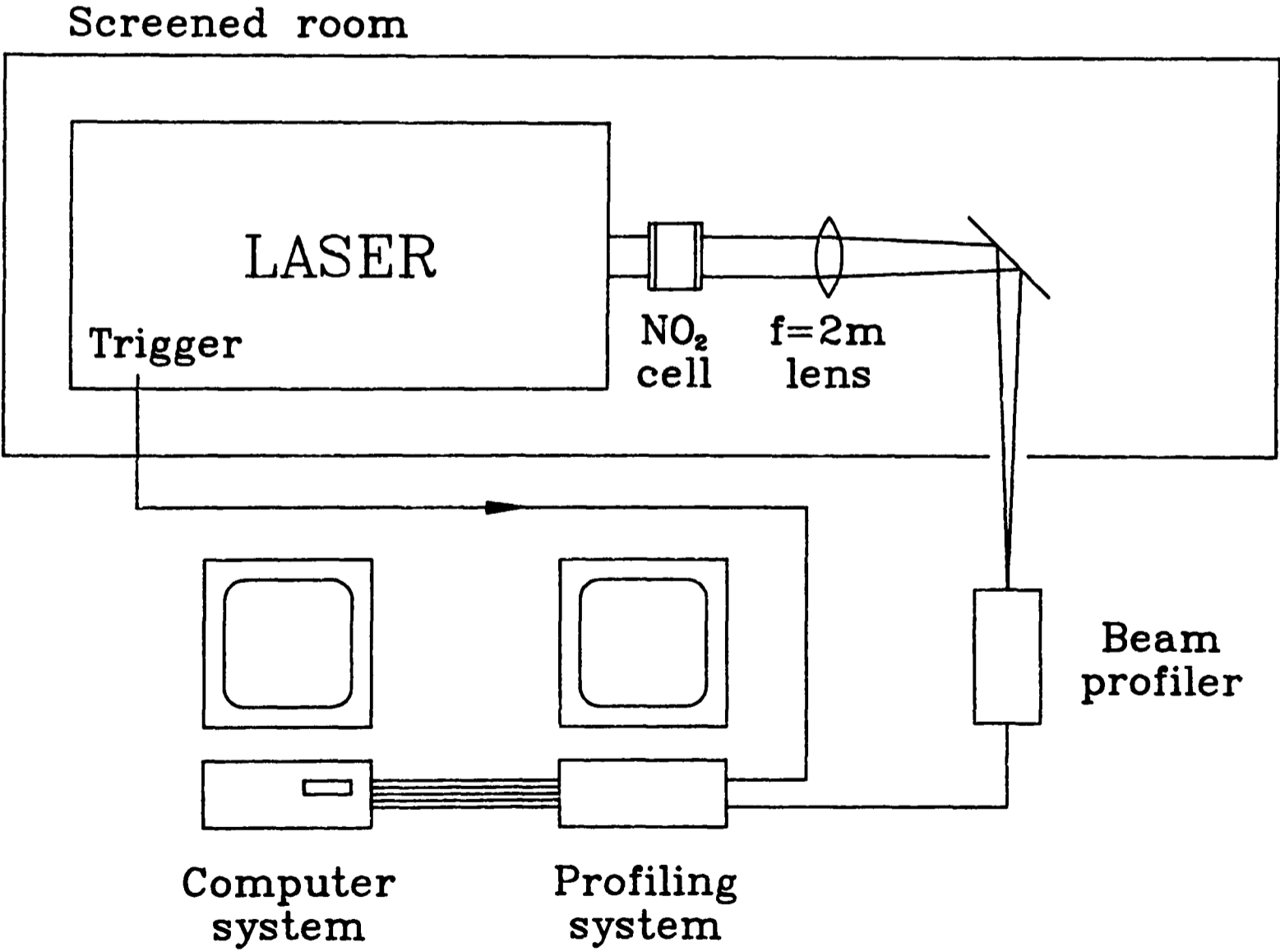
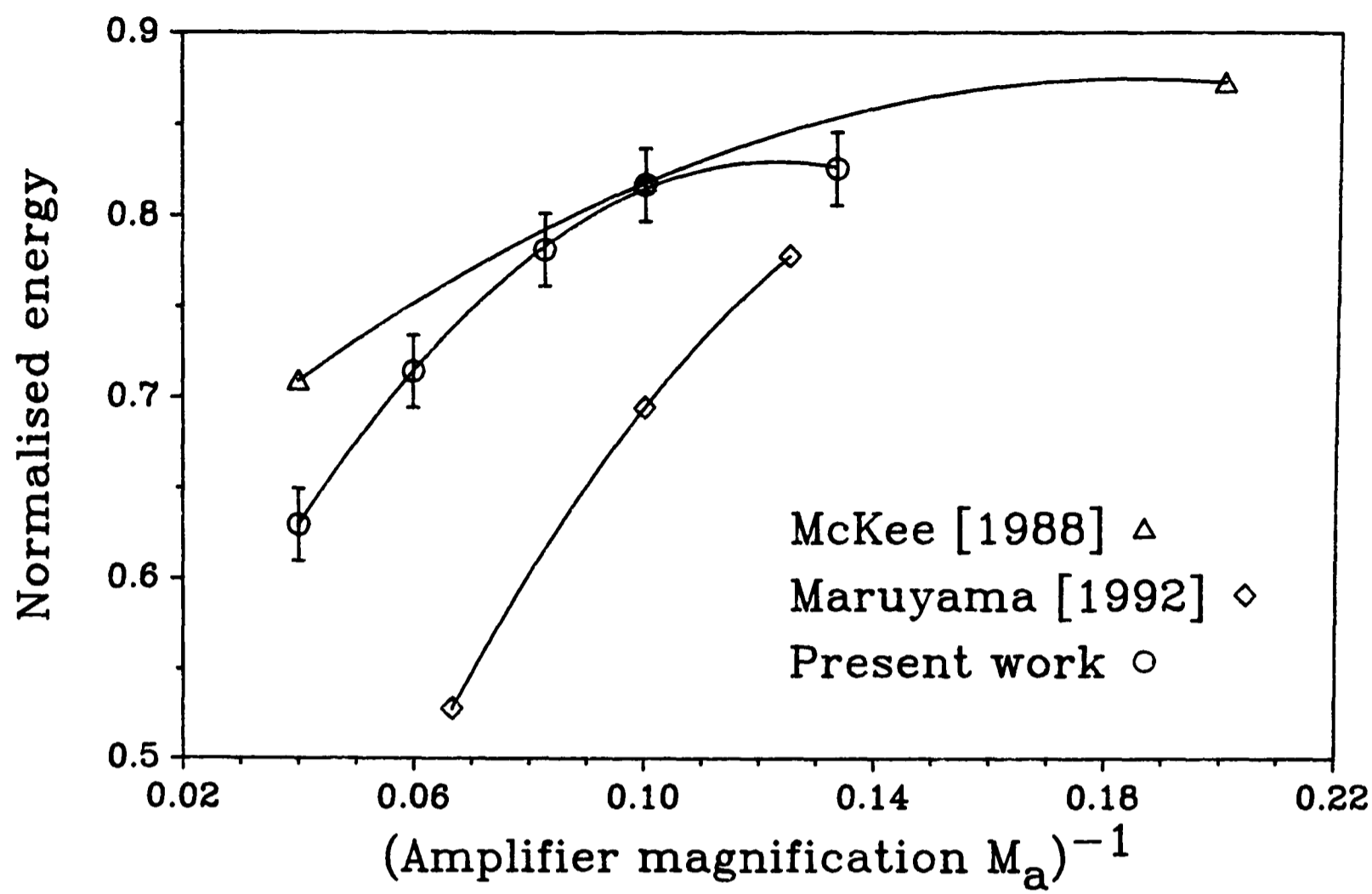


Figure 4.22: Output energies as a fraction of the plane-plane oscillator energy obtained from the various unstable cavities.

Figure 4.23: The arrangement for measuring the intensity of the beam in the focal plane of a 2m lens.

$$\begin{aligned}\text{FWHM} &= 0.89 f\lambda/D \\ &= 0.442\mu\text{m}/D\end{aligned}$$

with D measured in metres. In the case of $D=0.02\text{m}$ for example, we obtain a diffraction limited ‘spot size’ of $22\mu\text{m}$, corresponding to a beam divergence of $11\mu\text{rad}$.

We may use this figure to estimate the accuracy with which the beam profiler had to be placed with regard to the focus of the lens in order to correctly measure the beam waist. Assuming that the beam propagation could be described by

$$w^2 = w_0^2(1 + [\lambda z/\pi w_0^2]^2) \quad [4.58]$$

along the z axis, where the beam waist has a diameter of w_0 and w is the beam diameter at a distance z from the waist, we may write

$$z = (\pi w_0^2/\lambda) \sqrt{(w/w_0)^2 - 1} \quad [4.59]$$

Putting $w_0=22\mu\text{m}$, we see that the beam diameter increases by 10% after a distance $z=1.3\text{mm}$. For a twice diffraction limited beam (ie. $w_0=44\mu\text{m}$), this figure increases to 5mm . Care was therefore taken during the measurements to ensure that the beam profiler was correctly positioned along the axis of the propagating laser beam so as to measure the minimum of the beam width.

For each of the twelve cavities described in table 4.2, five profiles were taken at relative seeding times of 4.1, 16.9, 27.1 and 37.3ns in addition to that of the unseeded amplifier. These represented the shortest and longest possible delays and also values for direct comparison with the results of Cotton [1990]. The 150cm mirror used was that of the working ‘1 Joule’ system; ie. of unknown quality. The cavity of $f_1=150$, $f_2=69.5$, $f_3=-6$ was then repeated using the $\lambda/10$ 150cm mirror, such that all three mirrors were of $\lambda/10$ quality, and the results compared with those from the first cavity.

4.7.1 Results

In all cases, the profile measured at the focus of the lens was approximately sinc^2 in shape, although subsidiary maxima (which would have been one twentieth the magnitude of the main peak) were not discernible. For each cavity and each relative

timing, the measured divergence of the resultant beam was averaged over a number of laser shots; the results⁴⁾ are presented in table 4.4. The divergences arising from the unseeded amplifier are illustrated in figure 4.24. It was immediately apparent that the divergence of the unseeded amplifier alone was much better than that of the ‘1 Joule’ laser even when this had been seeded by the oscillator. In this latter case, a FWHM of 138 μ m was obtained in the focal plane of the 2m lens, while in the former, the average for all of the thirteen unseeded cavities was 76 μ m. Even when attenuated with 60mb of NO₂ over a path length of 5cm (which absorbed ~85% of the beam’s energy), the electric field produced by such a beam at the focus of the 2m lens was sufficiently high to cause the dielectric breakdown of air.

M _a	M _o	No seeding	Seeding delay (ns)			
			4.1	16.9	27.1	37.3
7.5	3.5	51.7	67.4	61.8	61.3	51.6
7.5	5.0	51.2	61.4	57.6	51.4	47.3
10.0	4.6	46.6	47.3	37.0	37.7	38.7
10.0	6.7	42.3	47.5	50.7	45.0	43.6
12.1	5.6	46.8	45.5	43.5	42.1	38.1
12.1	8.1	47.2	46.4	34.7	34.5	29.4
16.7	7.7	40.3	43.4	40.3	38.3	33.3
16.7	11.1	35.6	33.5	29.4	31.1	29.1
25.0	11.6 ^a	32.1	35.6	42.1	34.1	31.6
25.0	11.6 ^b	33.2	34.1	34.7	35.9	30.8
25.0	16.7	34.5	39.6	41.1	34.8	33.1
15.0	6.0	53.4	35.9	32.1	27.8	30.9
22.5	9.0	40.9	36.3	37.6	36.1	36.3

^a M₁ of unknown quality
^b M₁ of $\lambda/10$ quality

Table 4.4: Beam divergencies in μ rad, for the different cavities and timings.

⁴⁾ A Pascal program was written to analyse each frame from the Exitech 256 beam profiler. This counted the number of pixels, each of area 244 μ m², whose value was equal to or greater than half the maximum pixel value of that frame. This gave a ‘FWHM area’ which was converted to the equivalent ‘FWHM divergence’.

As expected, there was a decrease in the divergence as the amplifier magnification increased. McKee [1988] found a similar trend using magnifications of 5, 10 and 25 as shown in figure 4.25. Unfortunately, the beam size produced by the laser system studied in this paper was not given, and therefore the diffraction limit is unknown. The unexpected increase in the beam divergence obtained with a magnification of 25 may have been the result of too low a feedback from the convex mirror, which would have been only 0.16% in this case, compared to 1% for the $M=10$ arrangement. For such a high gain system, this would not have greatly affected the total output energy, but may have permitted the evolution of higher divergence modes. The divergences measured by Maruyama [1992] are also plotted; the beam size in the case was $20 \times 26 \text{ mm}^2$.

It was also noted that for low amplifier magnifications, the presence of late (ie. 4.1ns) seeding from the oscillator was in fact detrimental to the amplifier beam divergence. For these low amplifier magnifications, the effect of early (ie. 37.3ns) seeding was noticeably more beneficial than for those cavities with a high amplifier magnification (eg. $M_a=25$) where the effects of seeding were less pronounced.

These observations may be understood by considering the buildup of propagating beams within the cavity as explained in section 4.2.1. As the value of M_a increases, so the time required to reach a diffraction limited beam decreases since the beam divergence is decreased by a factor M_a on each round trip. Thus, a high M_a cavity will produce a diffraction limited beam relatively quickly even without the aid of seeding, while a low M_a cavity will benefit more from seeding.

The detrimental effect of late seeding is especially evident where there is a low oscillator magnification M_o . Here, the the maximum angle a beam may make with the laser axis and still be reflected by the enclosing mirrors (θ_{\max} for the oscillator of equation [4.30]) will be particularly large, enabling the laser beam to have an initially large divergence. If this early part of the beam is used to seed the amplifier it may act to increase the amplifier beam divergence to a value above that which it would have attained if unseeded.

It might also be expected that, for a given value of the amplifier magnification,

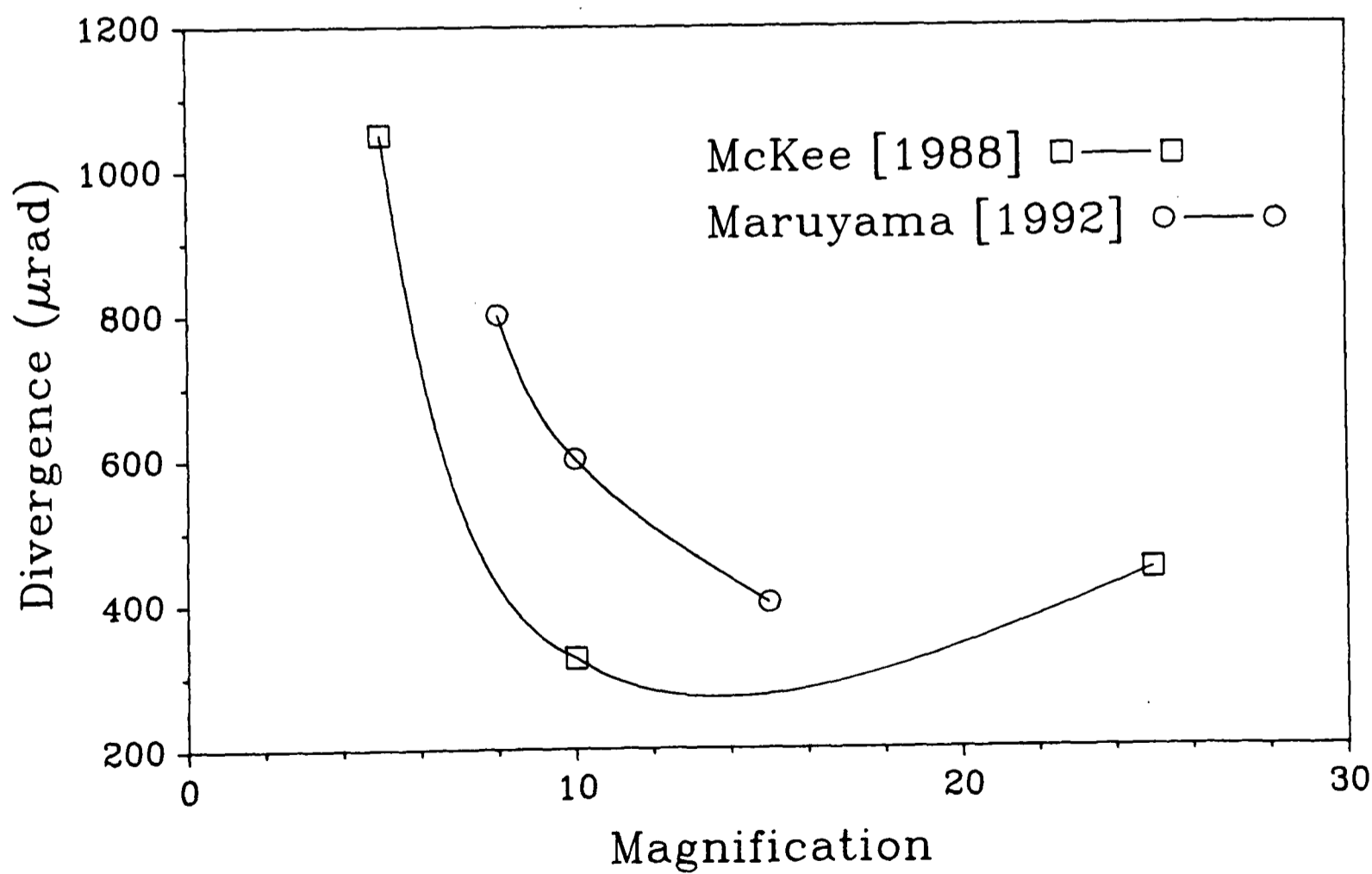
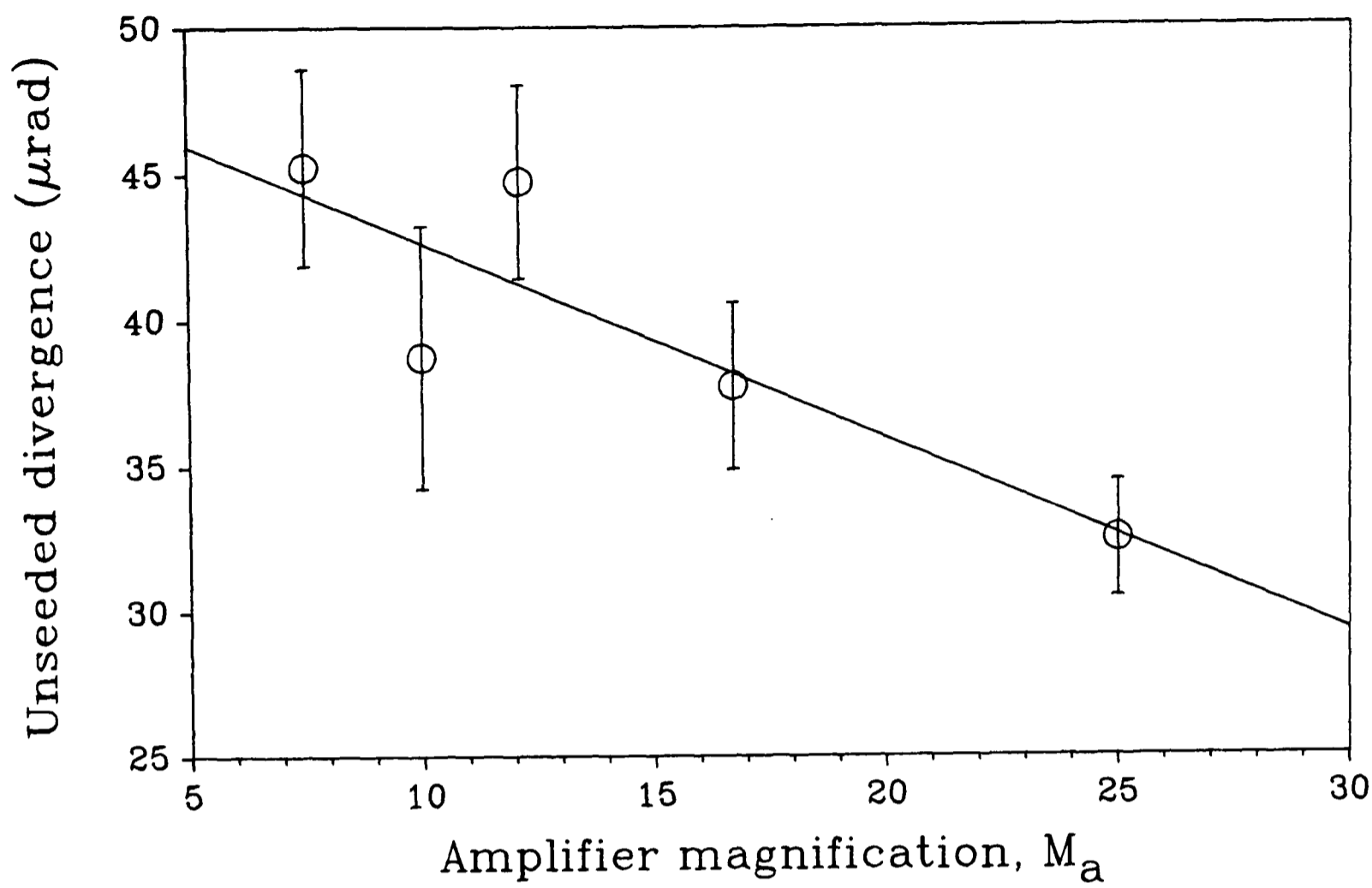


Figure 4.24: Divergences obtained from the various unseeded cavity arrangements.

Figure 4.25: Divergences obtained from unseeded cavities by McKee [1988] and Maruyama [1992].

M_a , the seeding of the amplifier would become more beneficial as M_o increases. As already mentioned, the beam divergence of the oscillator at a given time after the discharge will be smaller for larger cavity magnifications. Thus, for a given seeding time (eg. 27.1ns) an oscillator with a larger M_o will inject a beam with a smaller divergence than will one with a smaller M_o , leading to a larger improvement in beam divergence. Some evidence of this effect was observed. Comparing the intensities obtained with the $f_1=150$, $f_2=69.5$, $f_3=-15$ cavity with the 150cm lens of unknown quality with that obtained when the 150cm lens of $\lambda/10$ quality was used, no significant variation is apparent, indicating that the original mirror may have been of $\lambda/10$ quality already or alternatively that the quality of this mirror did not have any effect on the divergence of the output beam.

4.8 SUMMARY

From the experiments described in this chapter, it is apparent that the highest intensity at the focus of the 2m lens was obtained by the use of the $M_a=16.7$, $M_o=11.1$ cavity at a relative timing of 16.9ns. This profile had a FWHM of $58\mu\text{m}$ with 20% of the total beam energy falling within this diameter⁵⁾, leading to an intensity at focus of $8.4 \times 10^{11} \text{W/cm}^2$ in the absence of the attenuating NO_2 cell. By the use of the $f=9\text{cm}$ lens employed for the production of X-rays, the focal spot size would have been reduced to $2.6\mu\text{m}$ and the intensity increased to $4.1 \times 10^{14} \text{W/cm}^2$. Figure 4.26 illustrates the intensity profiles obtained with this system and the previous '1 Joule' laser; the area of each graph is in proportion to the square root of the beam energy. From this we may see that a gain in the peak intensity by a factor of 4.5 has been achieved over the previous system.

The fact that the profile FWHMs of the $32 \times 27 \text{mm}^2$ beams were similar to those of the $20 \times 20 \text{mm}^2$ beams arising from cavities of the same amplifier magnifications seems to indicate that there is some limiting factor which dictates the minimum

⁵⁾ A second Pascal program was written to calculate from each frame generated by the Exitech 256 beam profiler the fraction of the energy which fell within the FWHM area.

output beam divergence, such as inhomogeneities in the gain medium, imperfections in optical components and alignment errors. It may also have been the case that reflections of the expanding beam, as it travelled from mirror M_3 to M_1 , from components of the electrode structure such as the earth rail, may have led to the evolution of higher divergence modes. This would not have been a problem for the beams of side 20mm as these could be wholly accommodated by the gain area generated by the laser system.

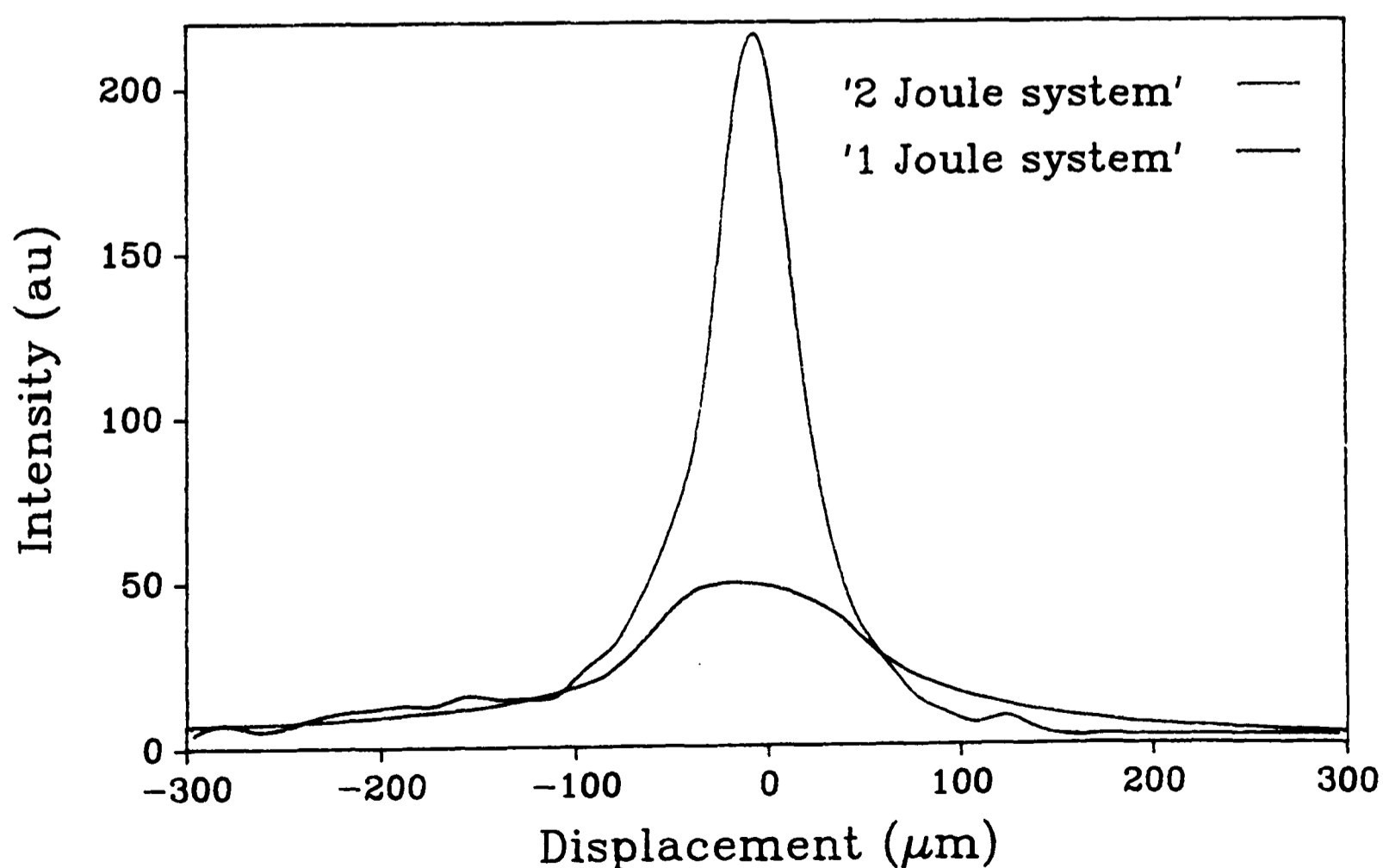


Figure 4.26: A comparison of the intensities in the focal plane obtained with the original and upgraded laser systems.

CHAPTER FIVE

LASER GENERATED PLASMAS

5.1	INTRODUCTION
	5.1.1 Laser intensity on target
5.2	BLACK BODY RADIATION
5.3	PLASMA FORMATION
	5.3.1 The conversion layer
	5.3.2 The re-emission zone
	5.3.3 Energy transfer within the plasma
5.4	SPECTRAL DEPENDENCE ON Z
5.5	THE TARGET DELIVERY SYSTEM
5.6	TARGET ALIGNMENT
5.7	VARIATION OF X-RAY EMISSION WITH FOCAL POSITION
5.8	VARIATION OF X-RAY EMISSION WITH SEEDING DELAY
5.9	PLASMA EMISSION SPECTRA
	5.9.1 Target debris
	5.9.2 Resolution
	5.9.3 Results
5.10	ANGULAR DISTRIBUTION OF EMISSION
5.11	CALCULATION OF CONVERSION EFFICIENCY
5.12	MEASURED CONVERSION EFFICIENCIES
5.13	VARIATION OF YIELD WITH LASER ENERGY
5.14	PINHOLE CAMERA IMAGES OF THE PLASMAS
	5.14.1 Results
	5.14.2 Estimation of conversion efficiency
5.15	APPLICATION OF ELECTRIC FIELDS TO THE PLASMA REGION
5.16	CONCLUSIONS

5.1 INTRODUCTION

As explained in chapter 2, the soft X-ray microscope constructed at the Clarendon Laboratory makes use of a laser generated plasma source to obtain very high intensity short pulses of radiation in the water window region of the spectrum. Interest in both the theoretical and practical aspects of laser generated plasmas has increased recently, partly because of the source requirements of SXCM, but mainly in association

with inertial containment fusion (ICF) experiments where the very large pressures resulting from extremely high intensity, focused laser beams are used to force hydrogen, deuterium and tritium rich matter together in an attempt to initiate a fusion reaction. Consequently, much practical work has been carried out to study the processes by which plasmas are generated and the effects of laser intensity, wavelength, duration and other parameters on their behaviour. The current work, however, has been limited to investigating those aspects considered to be of importance for the attainment of a source suitable for SXCM.

In this chapter, a brief description of the plasma processes occurring in a laser generated plasma is followed by details of the experiments carried out with the present laser system and target chamber.

5.1.1 Laser intensity on target

From the experiments detailed in chapter 4, it was found that the optimal confocal cavity arrangement enabled the laser to produce 2.22J of energy in 20ns FWHM in a beam of divergence 2.5 times that of the diffraction limit. For these measurements, the beam size had been maintained at $20 \times 20 \text{mm}^2$ so that direct comparisons could be made between the divergences and energies arising from the different cavities. However, for the operation of the microscope, it was important to deliver as much energy as possible to the wire target in order to obtain a large X-ray flux for the illumination of the specimen, and so this cavity arrangement of $M_a=16.7$ and $M_o=11.1$ was adjusted to give an output beam size of $30 \times 30 \text{mm}^2$. The relative timing between the amplifier and oscillator lasers was changed to nine inductor turns, corresponding to a time delay of $\sim 15 \text{ns}$, this being the value which gave the largest output energy from the seeded amplifier. As may be seen from table 4.4, this would have had little effect on the divergence of the output beam.

This larger area output beam had a total energy greater than that of the $20 \times 20 \text{mm}^2$ beam by a factor of 1.21. Losses arising from the transmission of the beam through the entrance window of the target chamber and the focusing lens were unfortunately appreciable, and an incident energy of $\sim 1.4 \text{J}$ on target was achieved for

all experiments in this chapter unless otherwise stated. Nevertheless, this was greater by a factor of 3.5 than that obtained with the previous '1 Joule' system.

This larger area beam was analysed with the Exitech beam profiler (previously described in section 4.7). With an incident energy of 1.4J and using the f=9cm aspheric focusing lens, the measurements made with the beam profiler indicated that an intensity on the target wire of $1.25 \times 10^{14} \text{W/cm}^2$ was obtained.

5.2 BLACK BODY RADIATION

We firstly consider the radiation spectrum emitted from a small hole in the side of a perfect black body cavity at a temperature T. The spectral radiant excitance M_λ is given by Planck's formula;

$$M_\lambda = 2\pi hc^2 (e^{hc/\lambda kT} - 1)^{-1} / \lambda^5 \quad [5.1]$$

This function has a maximum at a wavelength which is defined by

$$1 - e^{-hc/\lambda kT} = hc/5\lambda kT \quad [5.2]$$

From this, we see that to obtain a spectral output which peaks in the water window region (ie. 2.3 to 4.4nm), the black body must be raised to a temperature of $T \sim 10^6 \text{K}$.

The total power radiated per unit area by the black body is given by

$$M = \int_0^\infty M_\lambda d\lambda = \sigma T^4 \quad [5.3]$$

which is the Stefan-Boltzman law, where $\sigma = 5.67 \times 10^{-8} \text{W/m}^2 \text{K}^4$. This shows that at a temperature of 10^6K , a radiant power of $5.67 \times 10^{12} \text{W/cm}^2$ is emitted, illustrating the need for an extremely powerful heating source, both to reach the required temperature, and then to sustain this temperature against these very large radiation losses.

Although Sigel [1987] has used laser-heated gold cavities in an attempt to generate perfect high temperature black body radiation, the majority of studies of relevance to SXCM have investigated plasmas generated by focusing a laser beam onto the front surface of a relatively large (compared to the focal spot diameter), near planar target. The radiation spectrum produced in this manner deviates considerably from that of a true black body, but has the advantage of being easier to realize experimentally.

5.3 PLASMA FORMATION

When an electromagnetic wave of intensity I falls onto a material, the amplitude of the electric field generated at the surface is given by

$$E_0 = \sqrt{2I/c\epsilon_0} \quad [5.4]$$

If the incident radiation is formed from a focused laser beam of suitably small divergence, I may be as large as 10^{14}W/cm^2 , leading to an electric field strength of $\sim 3 \times 10^{10} \text{V/m}$. This causes the material within the vicinity of the focus to be ionized, and a plasma is rapidly formed at its surface. The subsequent action of the laser radiation incident on this plasma leads to the formation of a number of distinct zones within the plasma and target material.

The plasma may be modelled in one of two ways; either by considering the behaviour of individual particles in velocity-position space as a function of time, or by making use of macroscopic properties, such as density and average particle velocity. These are termed the kinetic and fluid approaches. The former allows for the numerical treatment of a system by the computational modelling of the behaviour of a large number (eg. 10^6) of particles, subject to the effects of the incident laser beam. Although this method has been very successful in predicting observed plasma behaviour, it is the fluid model which we will employ in order to describe the physical processes which occur in the formation of a laser generated plasma.

The leading edge of the focused laser beam vaporizes and ionizes material from the surface of the target, creating a low temperature expanding plasma. This then absorbs the remainder of the laser pulse, causing its temperature to increase to $\sim 10^6 \text{K}$. A dynamic equilibrium plasma flow is established within $\sim 20 \text{ps}$, as heat is transported through the plasma to vaporize more target material, which replenishes the plasma lost owing to hydrodynamic expansion into the vacuum. Fabbro [1985] suggests the following formula for τ , the time taken to achieve a steady state flow for an incident beam of intensity I and wavelength λ falling onto a target of average atomic number Z and atomic weight A ;

$$\tau \sim 7 \times 10^{-3} I \lambda^4 (A/2Z)^{3/2} \text{ s} \quad [5.5]$$

where τ , I and λ are in SI units. This gives $\tau \sim 25\text{ps}$ for an irradiance of 10^{14}W/cm^2 , $\lambda = 248\text{nm}$ and $A/2Z = 1$. The same author gives the ablation rate, \dot{m} , as

$$\dot{m} = 1.5 \times 10^{-8} I^{1/3} \lambda^{-4/3} (A/2Z)^{2/3} \text{ kg/m}^2\text{s} \quad [5.6]$$

So, for example, with a tungsten target of density $\rho = 1.93 \times 10^4 \text{ kg/m}^3$ and a beam of intensity $I = 10^{14} \text{ W/cm}^2$, the depth of material ablated by a pulse of duration $\tau = 20\text{ns}$ will be

$$\dot{m}\tau/\rho = 10\mu\text{m} \quad [5.7]$$

X-rays are emitted mainly from the region of the plasma which is at the highest temperature; under the experimental arrangements used for the measurements carried out in this chapter, this region was found to be approximately $100\mu\text{m}$ in size. Emission occurs into the 2π solid angle in front of the target, and the duration is dictated by the length of the laser pulse; this may be longer than, the same as, or shorter than the incident beam, although in the current arrangement, the X-ray emission was found to follow the incident laser beam.

In the steady state condition, the plasma may be divided into two distinct regions; the under-dense plasma (or conversion layer) and the over-dense plasma (or re-emission zone). Within the target material itself, there is a shocked region which advances into the unperturbed solid. The situation is represented schematically in figures 5.1 and 5.2. The division of the expanding plasma into these two regions is dictated by their interaction with the incident laser beam. In the low density conversion layer, free electrons may gain energy by directly absorbing photons of the laser beam in an inverse Bremsstrahlung process. This form of absorption will predominate if a plasma with a relatively high density in the conversion layer is generated, as would result, for example, from the use of a long duration laser pulse. The boundary with the re-emission zone is defined by the location of the critical electron density, $n_c = \omega^2 m_e \epsilon_0 / e^2$. In the case of $\lambda = 248\text{nm}$ radiation, n_c has a value of $1.8 \times 10^{28} / \text{m}^3$, which is about 10^3 times lower than the electron density in solids. At this critical density, plasma electrons gain energy from the incident beam by means of resonant absorption. Beyond this boundary, the laser radiation is unable to directly propagate through the re-emission zone, and the small fraction of the beam which has

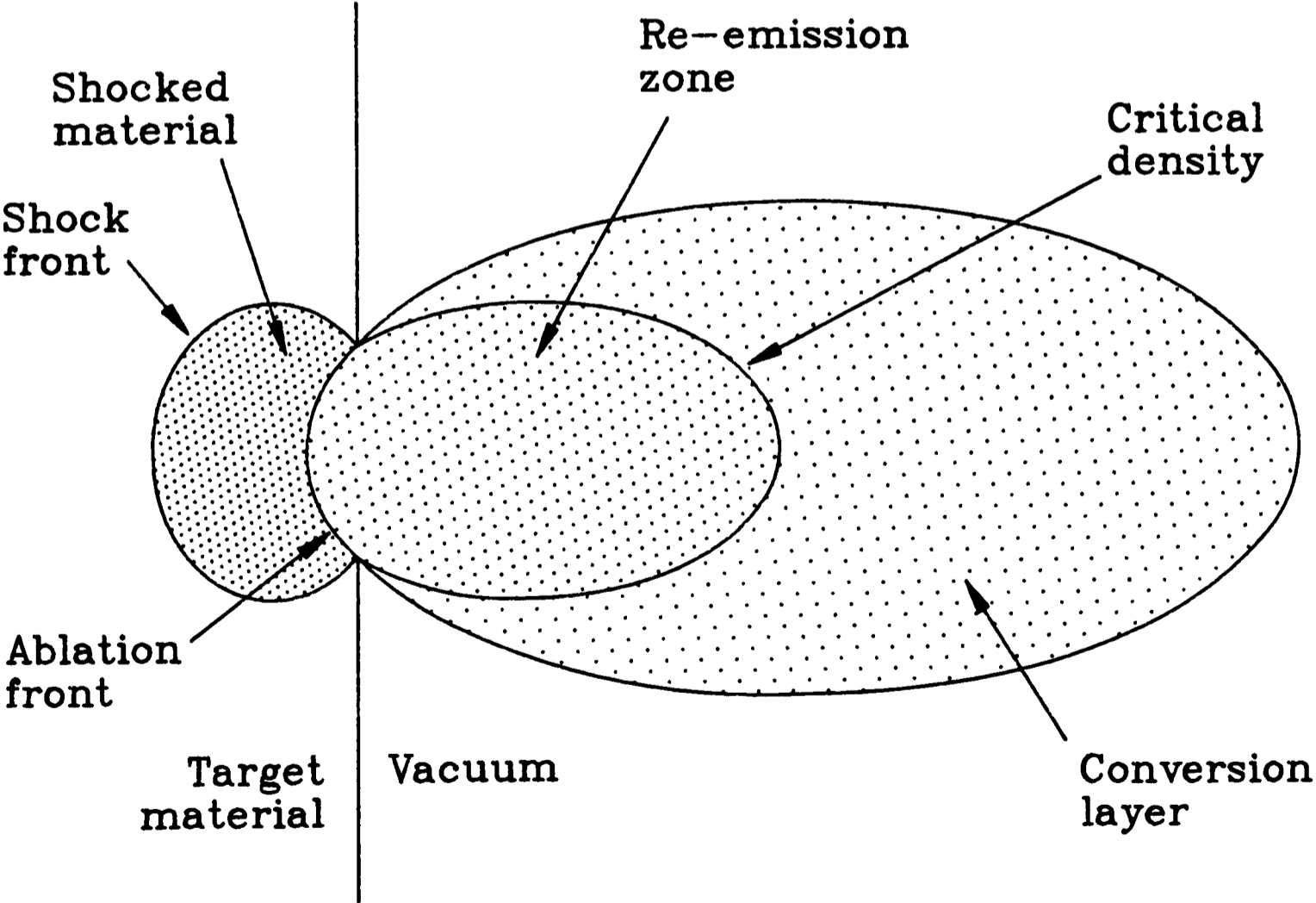
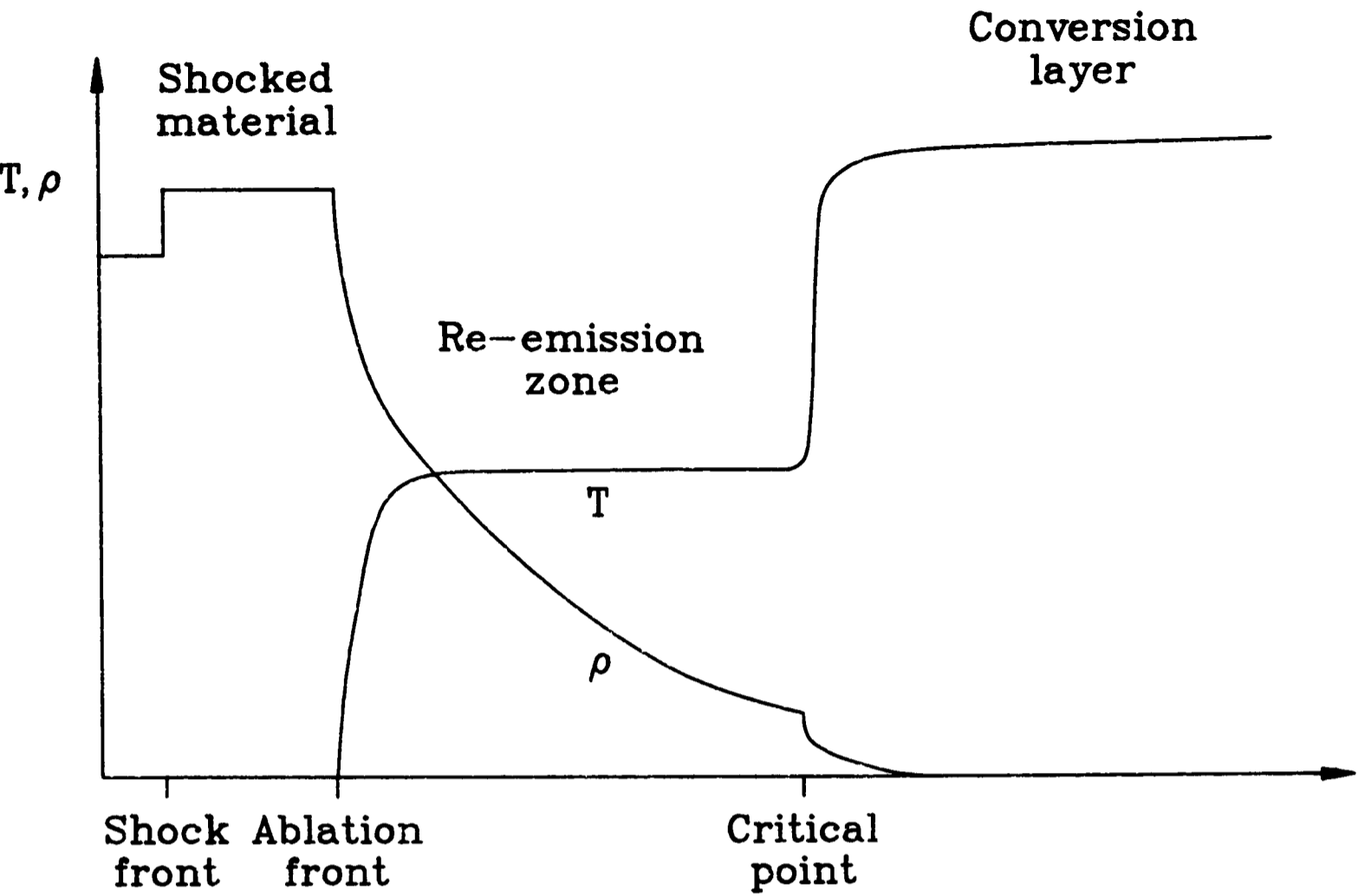


Figure 5.1: The variation in density and temperature within the plasma region.
Figure 5.2: A schematic representation of the laser generated plasma.

not been absorbed by either process will be reflected back through the conversion layer.

The atoms ablated from the target material are ionized to form multiply charged species by collisional excitation with the thermal electrons generated within the plasma. For low Z target materials, all but the last one or two electrons will be removed from the atoms, while for higher Z elements, the plasma temperature reached will not be large enough to fully ionize the atoms and many-electron line spectra are produced. A broad continuum is generated, with a high frequency cut-off, as these highly charged ions capture free electrons. Characteristic X-ray lines are then emitted as transitions occur between the various energy levels of the ion, and a background continuum is also generated as plasma electrons undergo Bremsstrahlung processes. This radiative emission cools the plasma, although a fraction emitted by the conversion layer is absorbed in the dense material of the re-emission zone. This part is emitted again to be absorbed, in part, by deeper layers of the zone, thereby leading to an energy transport through the zone to the ablation surface.

As the plasma expands into the vacuum, the associated recoil momentum generates a shock wave in the target material which may be several Mbar in magnitude. The shock is large enough to cause melting of the material (in the case of a metal target), and, aided by the reflection of the wave from the rear surface of the target, it is this effect which results in the large craters (of several hundred microns diameter), generated by each laser pulse. The energy transfer to the shock wave is small, because of the high density of the target material, and is therefore neglected in the following considerations.

5.3.1 The conversion layer

The outermost part of the plasma, which has the lowest physical density and an electron density lower than the critical electron density, n_c , is called the conversion layer, or corona. It has the highest temperature of all zones, and is optically thin to the emitted thermal X-rays. Consequently, it radiates equally towards the vacuum and towards the target. Thermal diffusion is most efficient in this region, so that it has a nearly uniform temperature over its volume. Shorter laser wavelengths are able to

penetrate the plasma to a greater extent than longer wavelengths so that absorption then takes place in a relatively large volume, leading to a lower plasma temperature and more efficient absorption of the laser radiation. For short laser radiation wavelengths, energy transport by the plasma electrons also becomes less important, and the temperature gradients are consequently shallower. At longer laser radiation wavelengths, the critical electron density is smaller, and hence the penetration depth becomes shallower. In that case, the laser energy is deposited in a smaller volume, so that a higher temperature is reached. Electron heat transport may be insufficient to prevent the formation of large temperature gradients, and convective heat losses may start to become significant. This leads to a reduction in energy absorption and the resulting decrease in conversion efficiency that is indeed observed when lasers of a longer wavelength (for example, the $1.06\mu\text{m}$ obtained from a Nd:YAG) are used to generate plasmas.

In the conversion layer, energy is transferred to the plasma by inverse Bremsstrahlung, also known as collisional absorption. In this process, an electron gains energy by colliding with a photon, and this may be the main mechanism for energy transfer between the laser radiation and the plasma, depending on factors such as the length of the incident laser pulse. The absorption coefficient, a , for this process has been shown to vary as

$$a \propto n_e n_i (Z/\omega)^2 \sqrt{1/T^3} \quad [5.8]$$

by Hughes [1979], where n_i is the ion density, n_e the electron density, Z the ionic charge, T the plasma temperature and ω the laser frequency. The density dependence of absorption indicates that much of the absorption will occur in the immediate vicinity of the critical electron density. For a fully ionized plasma, we have

$$n_e n_i = \omega_p^4 m_e^2 \epsilon_0^2 / Z e^4 \quad [5.9]$$

where ω_p is the plasma frequency. At the critical density, $\omega_p = \omega$ so that

$$a \propto \omega^2 Z \sqrt{1/T^3} \quad [5.10]$$

which illustrates an increased absorption for small λ , low T and large Z .

At very high laser irradiances, the electron motion is dictated by the associated

electric field rather than by its own temperature. Then,

$$v_e = eE/m_e\omega \quad [5.11]$$

with

$$v_e \gg v_{th} = \sqrt{3kT/m_e} \quad [5.12]$$

In this situation,

$$\begin{aligned} a &\propto n_e n_i \omega Z^2 / E^3 \\ &\propto \omega^5 Z / E^3 \end{aligned} \quad [5.13]$$

However, in order to achieve the condition of $v_e \gg v_{th}$, an irradiance of $I \sim 10^{15} \text{ W/cm}^2$ is required, which suggests that in the present application this non-linear effect does not come into play.

5.3.2 The re-emission zone

The re-emission zone is optically thick to its own thermal emission, and emits near black body radiation through the conversion layer into the vacuum beyond the plasma. It is heated by X-rays from the conversion layer and by electron heat transport. The laser radiation also contributes energy to this region by the process of resonant absorption, which occurs at the critical electron density, where $\omega_p = \omega$. The electric field of the laser radiation produces a charge separation as the electrons of the plasma oscillate along the plasma density gradient. At the critical surface, this charge separation oscillates with the plasma frequency (by definition), and is able to resonantly excite a plasma wave, thereby transferring energy to the plasma. This transfer is mainly to hot electrons, and is independent of the plasma temperature and the wavelength and intensity of the laser radiation. Hence, the process is most important for long wavelength, high temperature and high intensity schemes, since the degree of collisional absorption decreases in these limits.

5.3.3 Energy transfer within the plasma

Aside from the transfer of laser energy to the plasma, there are several processes by which energy is passed between the conversion layer and the re-emission zone. In

order to maximize the total X-ray emission from the plasma, a low temperature in the conversion layer is required, as this leads to a larger absorption of the incident laser radiation. This requires an efficient thermal transfer process from the conversion layer to the re-emission zone to avoid over-heating, and also to maximize the rate of ablation from the target surface.

The transfer of energy through the plasma towards the ablating surface is effected by electron thermal transport and X-ray radiation, while the return flow takes the form of kinetic energy and work done in expanding the plasma. There is negligible energy transfer in the outward direction by X-rays, since the conversion layer is optically thin to the radiation emitted by the re-emission zone.

The electron thermal transport was originally described by Spitzer [1953], who treated the plasma electrons as a fluid and applied the heat diffusion equation

$$n_e C \frac{\partial T}{\partial t} = -\nabla \cdot \underline{S} \quad [5.14]$$

where n_e is the electron density, C is the plasma heat capacity and \underline{S} is the heat flux. This quantity is defined by

$$\underline{S} = -\kappa \nabla T \quad [5.15]$$

where κ is the plasma thermal conductivity. Eliminating \underline{S} , we find

$$\frac{\partial T}{\partial t} = \chi \nabla^2 T \quad [5.16]$$

where $\chi = \kappa / C n_e$ is the thermal diffusion coefficient. Kinetic theory relates κ and v_{th} via the formula [Present 1958]

$$\kappa = \frac{1}{3} \lambda_e v_{th} \rho C \quad [5.17]$$

where v_{th} is the average electron velocity, ρ the gas density and λ_e is the electron mean free path. This latter parameter depends on the electron temperature, ion density and ionic charge according to

$$\lambda_e \propto T^2 / n_i Z^2 \quad [5.18]$$

as shown by Nicholas [1982] so that

$$\chi \propto T^{5/2} / n_i n_e Z^2 \quad [5.19]$$

where we have used

$$v_{th} = \sqrt{3kT/m_e} \quad [5.20]$$

This indicates that the thermal diffusion will be most efficient for high temperature, low density regions, suggesting an almost constant temperature within the conversion layer.

Any electron thermal diffusion will result in a localized charge depletion, whose electric field encourages a return current. This counteracts the heat flux, leading to the modifications suggested by Spitzer [1962];

$$\underline{S} = -\kappa \underline{\nabla} T - \beta \underline{E} \quad [5.21]$$

$$\underline{j} = \sigma \underline{E} + \alpha \underline{\nabla} T \quad [5.22]$$

where \underline{j} is the current density and σ is the electrical conductivity. The coefficients α and β are related by the formula

$$\beta = \alpha T + 5\kappa T / 2e\sigma \quad [5.23]$$

5.4 SPECTRAL DEPENDENCE ON Z

As described previously, the spectra emitted by a laser generated plasma will consist of a broad continuum, of a general black body nature, in addition to a number of line features which are characteristic of the target material being used. The positions of these lines are determined by the expression

$$E_n = 13.6\text{eV}[(Z - \sigma_n)/n]^2 \quad [5.24]$$

for the shell of principal quantum number n . The effect of shielding of the nuclear charge by the inner electrons is represented by σ_n . In terms of wavelength,

$$\lambda_n = 91.2\text{nm}[n/(Z - \sigma_n)]^2 \quad [5.25]$$

Emission lines will arise either from transitions between loosely bound electrons and the highly bound lower shell levels, or alternatively, by the capture of free electrons by highly excited ions. For levels of $n \geq 2$ there will also be an appreciable degree of fine structure splitting, given by

$$\Delta E_{nl} = 580hc(Z - \sigma_n)^4 / n^3 l(l + 1) \quad [5.26]$$

where l is the orbital quantum number of the level.

In the case of low Z elements such as beryllium and carbon, it is transitions to the K shell levels (ie. $n=1$) which cause the observed line spectra. As Z is increased, the K shell line moves to a shorter wavelength as the K electrons become more tightly

bound to the nucleus. For aluminium ($Z=13$), radiation arises from transitions down to the L shell in preference to the K shell, whose level would lead to radiation of 0.80nm. As Z is increased further, it is the M, N and O shells which give rise to radiation within the X-ray range. Figure 5.3 shows the inner shell energy levels of the various elements. The $1/n^3$ dependence of the fine structure splitting causes the different wavelengths of these levels to merge into a semi-continuum as Doppler broadening becomes larger than the line separation.

For a given set of plasma conditions characterized by, for example, temperature

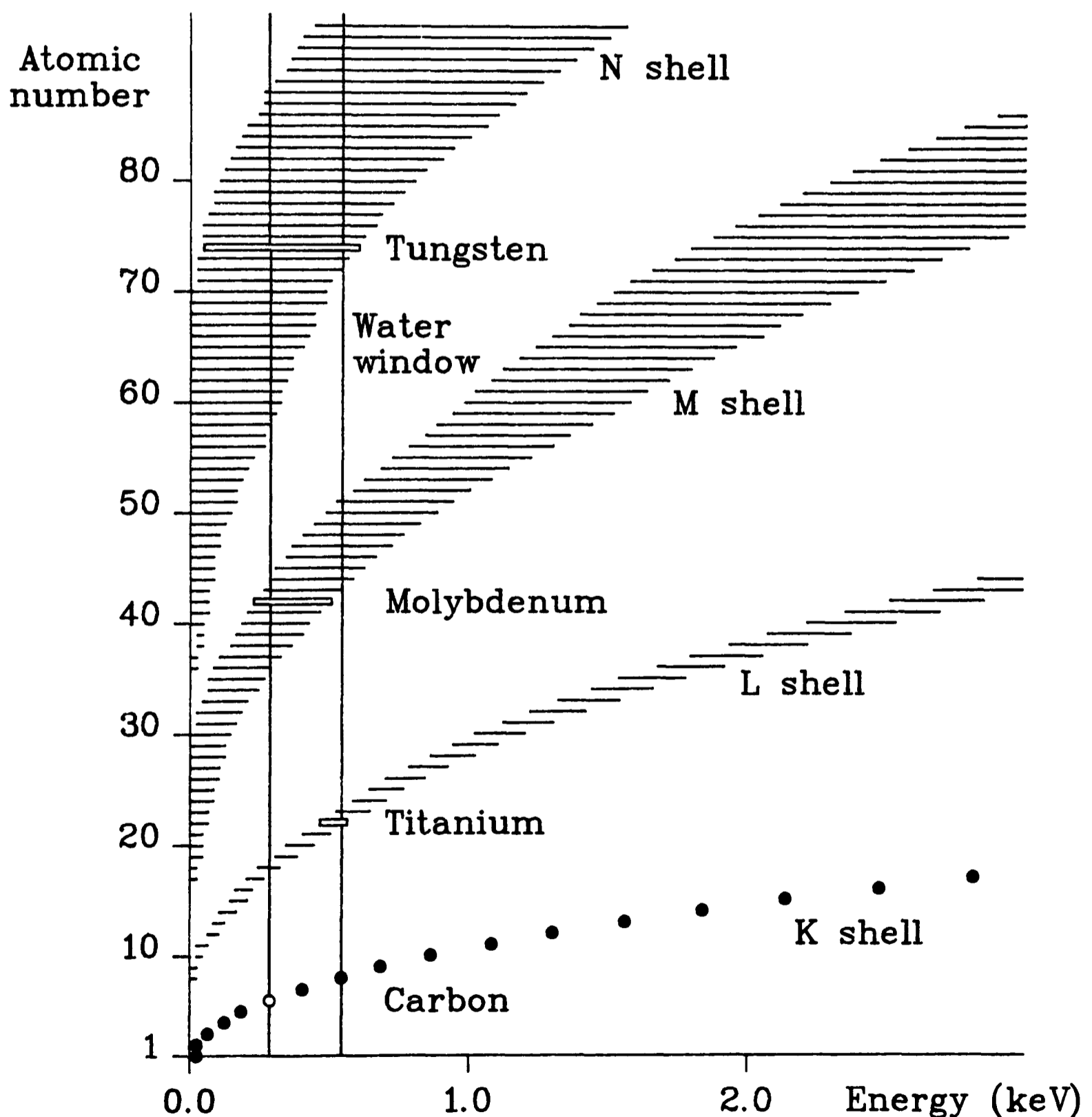


Figure 5.3: X-ray inner shell energy levels of the various elements, illustrating the suitability of C, Ti, Mo and W for soft X-ray generation.

and density (as dictated by the laser used to generate the plasma), the emission into a certain spectral range, such as the water window or alternatively all soft X-rays, will be dictated by the number of ionic species emitting in that spectral range. Alaterre [1986] has shown that the most intense lines for ions with an ionization energy E_i (pertaining to the electrons in the outermost shell) are associated with transitions in the energy range of $\sim 0.6E_i$ to E_i . Coupled with the fact that E_i varies smoothly within a given shell but changes abruptly from one shell to another, and that for a given shell, E_i varies only slowly with atomic number Z , this indicates that for a given spectral range of emission, there will be a limited number of values of Z for which emission from a given shell is likely to take place. This leads us to expect a variation in conversion efficiency with atomic number which shows several peaks, corresponding to emission from the various electron shells, and this is indeed observed (for example, by Mochizuki [1986] and Popil [1987]). Only if a sufficiently large energy range is considered, then as a very rough guide, the conversion efficiency from incident laser energy to emitted X-rays, η , may be said to vary in proportion to $Z^{1/2}$.

In the present application, a peak of emission within the water window range is required. Suitable elements for this are carbon ($Z=6$, K shell), titanium ($Z=22$, L shell), molybdenum ($Z=42$, M shell) and tungsten ($Z=74$, N and O shells). These are highlighted in figure 5.3 and investigated in sections 5.7, 5.9, 5.10, 5.12 and 5.14. Gold ($Z=79$, N and O shells) would also be appropriate for the generation of soft X-rays, but has not been studied here because of expense. Yttrium ($Z=39$, M shell) has been used by other workers [Tomie 1993] despite problems arising from the rapid formation of an oxide layer on the material's surface.

5.5 THE TARGET DELIVERY SYSTEM

The target positioning mechanism which was supplied with the target chamber (constructed at the Rutherford Appleton Laboratory in 1987) consisted of an xyz translation stage, driven by three orthogonal screw motors which enabled a straight section of target material, of $\sim 5\text{cm}$ length, to be positioned at the laser focus. After each shot of the laser, the target was moved along its length so as to bring a new area

to the laser focus. This was necessary because of the formation in the target material of craters of several hundred microns in size. Plate 5.1 shows SEM pictures of such craters produced in titanium and molybdenum target wires; in both cases, evidence of localized melting of the target material is apparent. This system had several inconvenient drawbacks:

a) If the wire was not exactly perpendicular to the laser axis then its movement by one of the three screw motors would result in a change in its longitudinal and lateral position with respect to the laser focus.

b) Because of the limited length of the wire which could be accommodated in each holder, only a few shots could be made on each target wire.

c) The method of securing the wire to the wire holder (viz. glueing the target into a metal holder) was time consuming and difficult.

To overcome these problems, a new target delivery system was constructed which enabled a 30cm length of wire to be used. The system, illustrated in figure 5.4, was mounted on the same translation stage on which the previous wire holder had been secured. A stepper motor was used to draw the wire, held under tension by means of a weight, over a grooved capstan. In this way, once the entire assembly had been correctly positioned, a fresh area of target material could be brought along by a small turn of the stepper motor, such that its position with respect to the laser focus was unchanged (limited to the constancy of the wire thickness). This enabled over 100 shots to be made from each wire sample and made the process of target wire preparation considerably more easy. Such is the improvement over the initial method that the chamber in TA4 at the Rutherford Appleton Laboratory (which is used with the Vulcan laser system) has been equipped with a copy of the design.

The amount of material ejected from the wire target, resulting from the melting caused by the shock wave generated in the target, was quite considerable as can be seen from plate 5.1. It was found that, for example, a 100nm thick Si_3N_4 window placed on the chamber wall (a distance of $\sim 30\text{cm}$ from the plasma) was broken by the debris generated by only one laser shot. For those measurements which required the use of such delicate windows (ie. the recording of plasma spectra and the use of



Plate 5.1: The craters generated in titanium and molybdenum target wires.
(Magnifications: 130 and 150).



vanadium-coated Si_3N_4 windows to filter the X-ray photodiode), it was necessary to use a foil target. In these cases, capstans to accommodate foil ribbons of 0.7mm width and $20\mu\text{m}$ thickness were used. Since only a few microns of material is actually ablated during the generation of a plasma (as considered in section 5.3), this change should not have significantly reduced the magnitude of the soft X-ray flux obtained by the process, while greatly reducing the amount of debris created. That debris which did result would have been ejected along the laser axis away from the plasma since such thin foils were punctured by the laser beam; for wire targets, the material was ejected

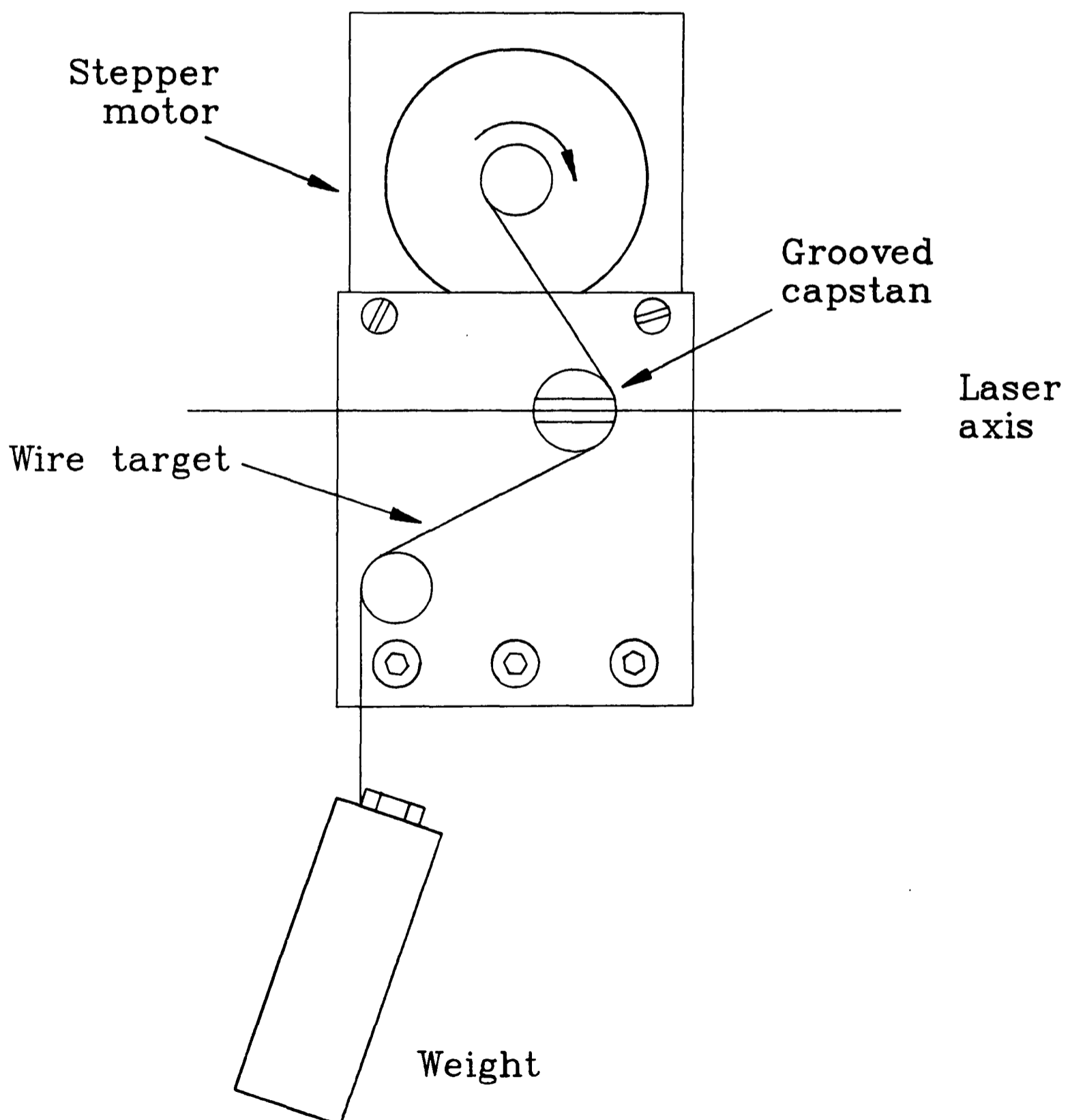


Figure 5.4: The target delivery system.

backwards, towards the incoming laser beam, by the shock wave reflected from the back of the target.

5.6 TARGET ALIGNMENT

The alignment mechanism originally used with the chamber consisted of a HeNe laser whose beam, made divergent by the use of a concave lens, was passed over the target wire and then allowed to fall onto a white screen such that a geometrical magnification of ~ 100 was achieved. In this way a target position resolution of $20\mu\text{m}$ was claimed, despite the very severe diffraction effects which degraded the image of the wire on the screen.

In order to make the target alignment as straightforward an operation as the target delivery, this HeNe based system was replaced by a commercially purchased 'reading telescope'. This was secured to the chamber and the target wire was viewed from vertically above by means of reflection from a plane mirror. By focusing on the target wire itself at the position of incidence of the KrF laser, a resolution of $40\mu\text{m}$ was immediately obtained without the diffraction effects which had made the previous arrangement so difficult to operate.

A 3mm diameter hole in the grooved capstan enabled the wire to be positioned laterally with respect to the laser axis by the use of the HeNe alignment beam which was arranged to be coaxial with the KrF laser. Finer positioning was achieved by the observation of the craters produced in the wire by each laser shot, using the reading telescope. Its longitudinal position, of course, could not be ascertained by means of the HeNe laser and for this, the strongly attenuated KrF beam was employed. The wire was positioned so that it cast a shadow of a certain width on the back window of the chamber and its position was noted from the alignment telescope. The wire was then moved along the KrF laser axis through the focus and beyond to reach a position where it gave a shadow of the same width as before, and its position again noted. The location of the KrF focus was then nominally deemed to be the halfway point between these two positions.

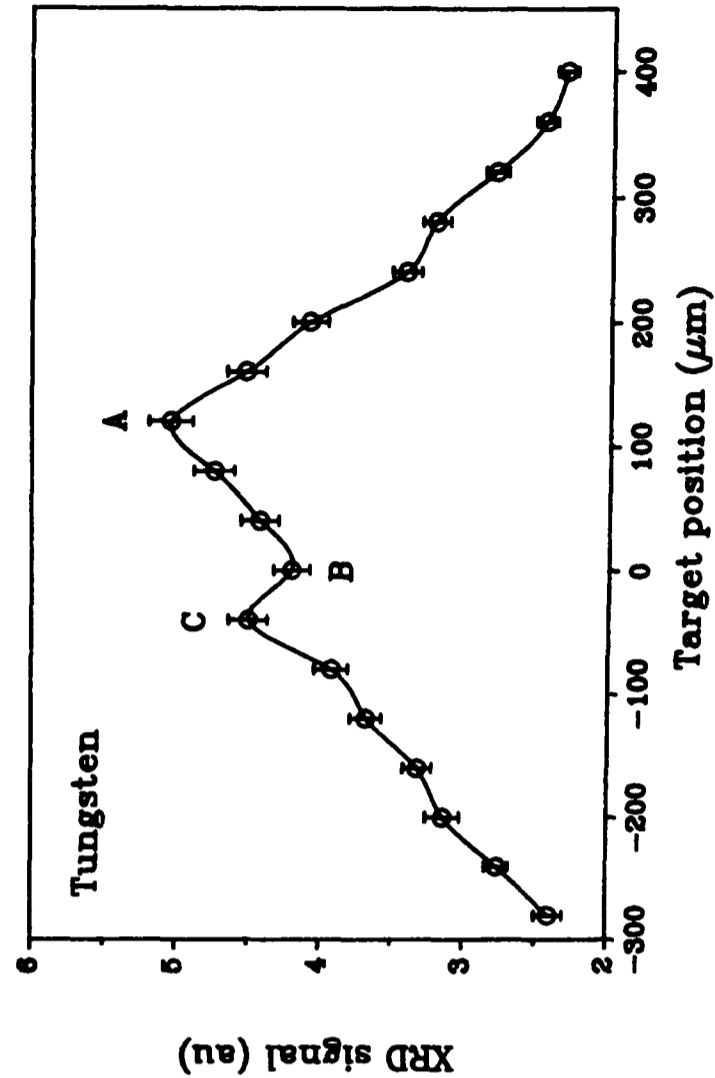
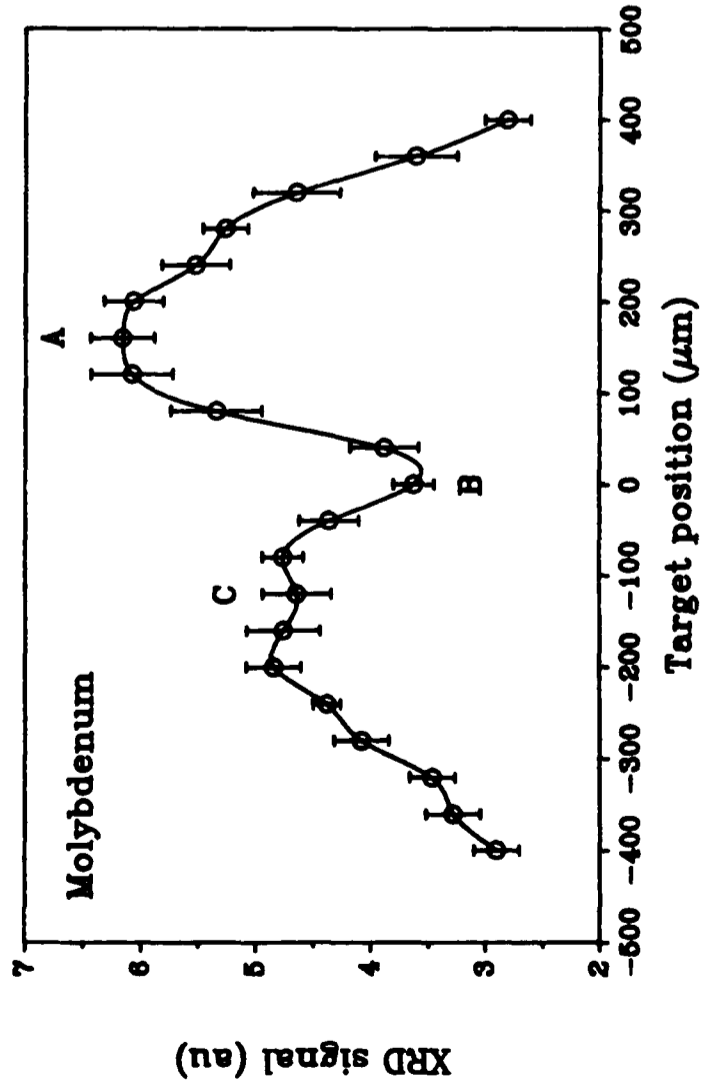
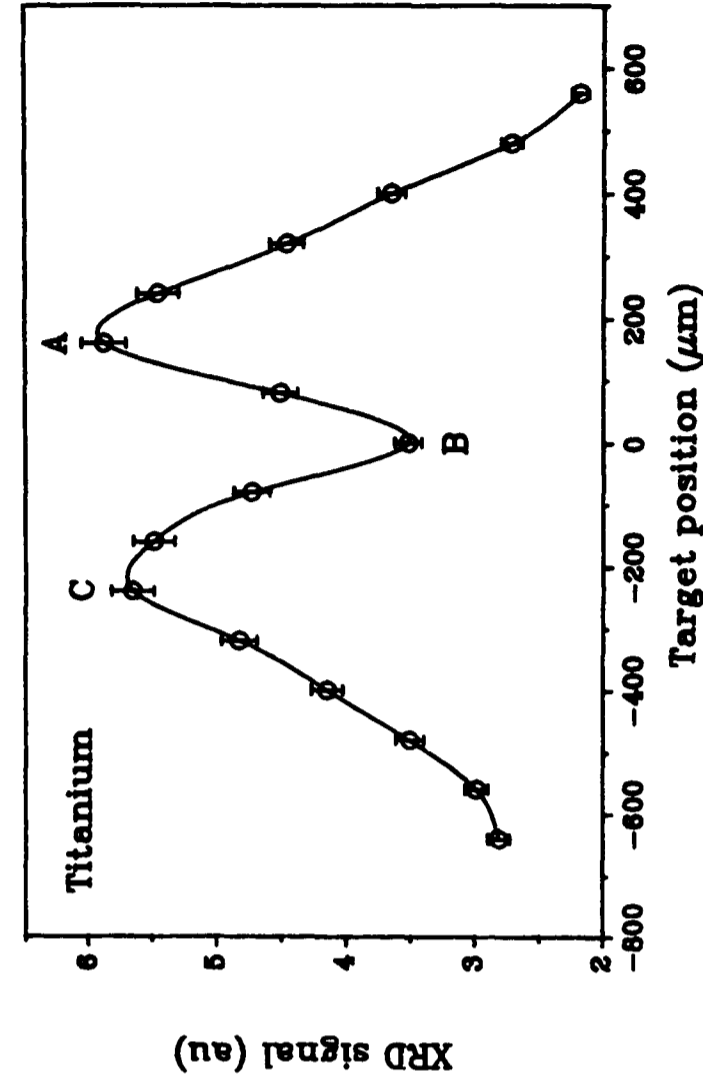
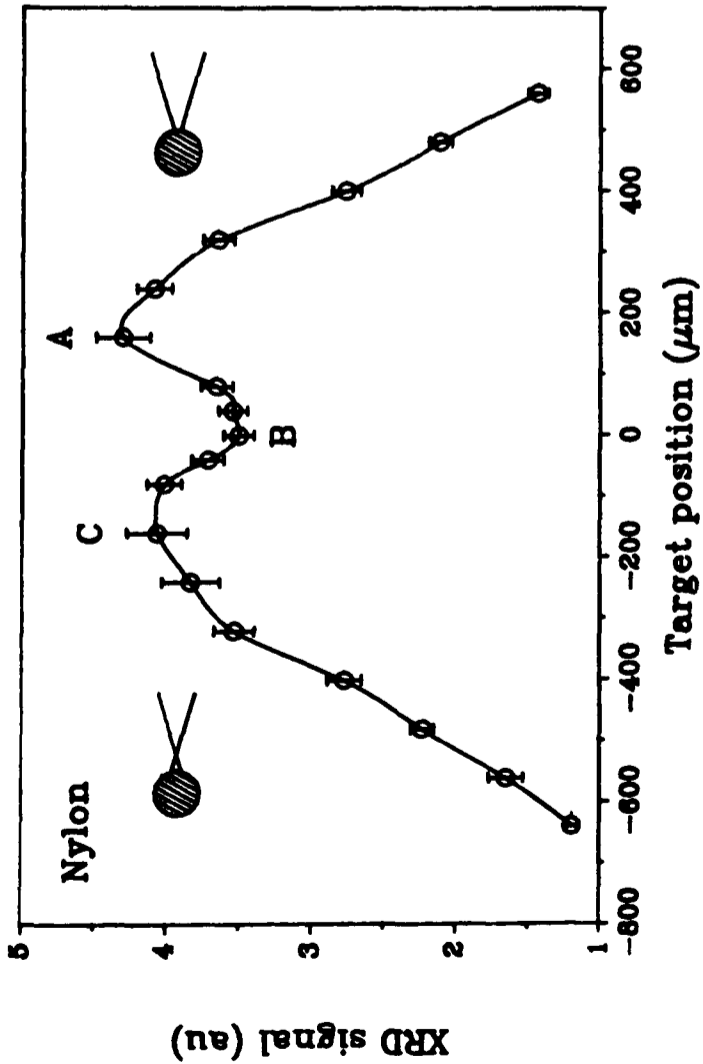
5.7 VARIATION OF X-RAY EMISSION WITH FOCAL POSITION

To obtain the greatest flux at a particular angle to the axis of the incident laser beam, it was found that the position of the front face of the wire target with respect to the location of the beam focus had to be accurately controlled. To assess the importance of the target position, a 'focal scan' was made for each target material being investigated (carbon in the form of a nylon-66 wire, titanium, molybdenum and tungsten). Although it would have been interesting to measure the signal obtained at a range of angular positions, only one (at 60° to the laser axis) was chosen, as this was the angle at which the vacuum feed-through presented the specimen holder for X-ray illumination during biological imaging experiments. As such, it represented the parameter which was of ultimate importance in the operation of the X-ray microscope.

The variations in signal measured are presented in figures 5.5 to 5.8, and for all four target materials, a large dip in the X-ray photodiode signal was observed at the position of the laser focus. O'Neill [1987] measured a similar feature when studying X-ray emission at 1keV from a copper target irradiated with 0.3J of radiation at 248nm in 20ns, with a peak intensity of approximately $2 \times 10^{14} \text{W/cm}^2$. Michette [1988a] has also performed a series of focal scans to measure the water window X-rays emitted from carbon, aluminium and copper targets when illuminated by 0.5J of $1.064 \mu\text{m}$ radiation in 8ns at an intensity of $\sim 2 \times 10^{12} \text{W/cm}^2$. In this case the width of the trough was $\sim 5\text{mm}$ and a signal was measured over a very large range of focal positions. Other workers (for example Gerritsen [1986] and Nagel [1984]) have also performed focal scans, but without observing this type of variation, probably because of the much larger step sizes employed, which were in excess of $200 \mu\text{m}$. There are several possible causes of this decrease in the signal when the target was at the position of focus:

a) A decrease in the fraction of the laser energy absorbed by the plasma because of Brillouin scattering (as suggested by Michette [1988a], supported by an observed coincident peak in the measured infrared backscatter).

b) A possible shift in the spectra of the emitted X-rays to higher energies which, while not necessarily leading to a decrease in the total emitted X-ray flux, might have given a smaller signal from the X-ray diode because of the spectral



Figures 5.5 to 5.8: Variation in XRD signal with focal position for nylon, titanium, molybdenum and tungsten targets.

response of the detector system.

c) Variation in the angular distribution of emitted X-rays, as described by the parameters n and k in section 5.10 (and observed by Rogoyski [1989]).

d) An actual decrease in the overall conversion efficiency arising from the production of a higher temperature plasma than at positions of pre- and post-focus. Such a plasma would experience larger radiative heat losses and hence give lower conversion efficiencies to X-ray radiation. This would result from the plasma expanding into a region of high laser radiation intensity in comparison to a lower intensity experienced for a pre-focus target position. This is supported by the lower peak observed in the post-focus position in comparison to the pre-focus, where a lower plasma temperature would have been generated.

Finally, it was noted that the FWHM of the emission variations decreased with increasing atomic number, so that the accuracy with which the wire target had to be positioned increased from carbon to tungsten. This variation arises because of the increase in intensity required to reach the threshold for soft X-ray production with increasing atomic number, Z .

5.8 VARIATION OF X-RAY EMISSION WITH SEEDING DELAY

Since the timing delay between the oscillator and amplifier lasers affected both the laser output energy and beam divergence (as measured in sections 4.6 and 4.7), the variation in the flux emitted at 60° to the laser axis was measured for a molybdenum wire target as the number of inductor hoops in the oscillator electrical circuit was varied from nought to the maximum of 13, corresponding to a change in the delay between the oscillator and amplifier lasers from 37.6ns to 5.4ns. The results are presented in figure 5.9, from which it may be seen that a maximum in the emission was recorded at nine hoops, corresponding to a delay of ~ 15 ns. From the results of sections 4.6 and 4.7, we may see that this timing roughly corresponds to the maximum in the laser output energy as well as the minimum beam divergence.

5.9 PLASMA EMISSION SPECTRA

Although the soft X-rays emitted by various laser generated plasmas have been spectrally analysed several times by previous workers, it was felt that in none of these studies did the parameters such as laser wavelength, duration or intensity match closely enough those of the current system to enable their results to be used in the calculations undertaken in sections 5.12 and 5.13. Daido [1992] for example has measured the spectrum emitted by a mylar target (polyethylene terephthalate, $[C_{10}H_8O_4]_x$), irradiated by a 50ps KrF laser pulse, of energy 130mJ at an intensity of 10^{14}W/cm^2 with a transmission grating similar to that used here. Various lines arising from O^{6+} , C^{4+} and C^{5+} species were observed. Eidmann [1986] investigated the spectra emitted by a number of elements, including carbon, titanium, molybdenum and tungsten, with a transmission grating made of free-standing gold bars of period 500nm. In this case however, a frequency doubled Nd:YAG laser was used ($\lambda=530\text{nm}$, $\tau=3\text{ns}$) to obtain an intensity of $3 \times 10^{13} \text{W/cm}^2$ with 7J of energy on target. The resolution obtained by this arrangement was only sufficient to identify one broad peak of emission

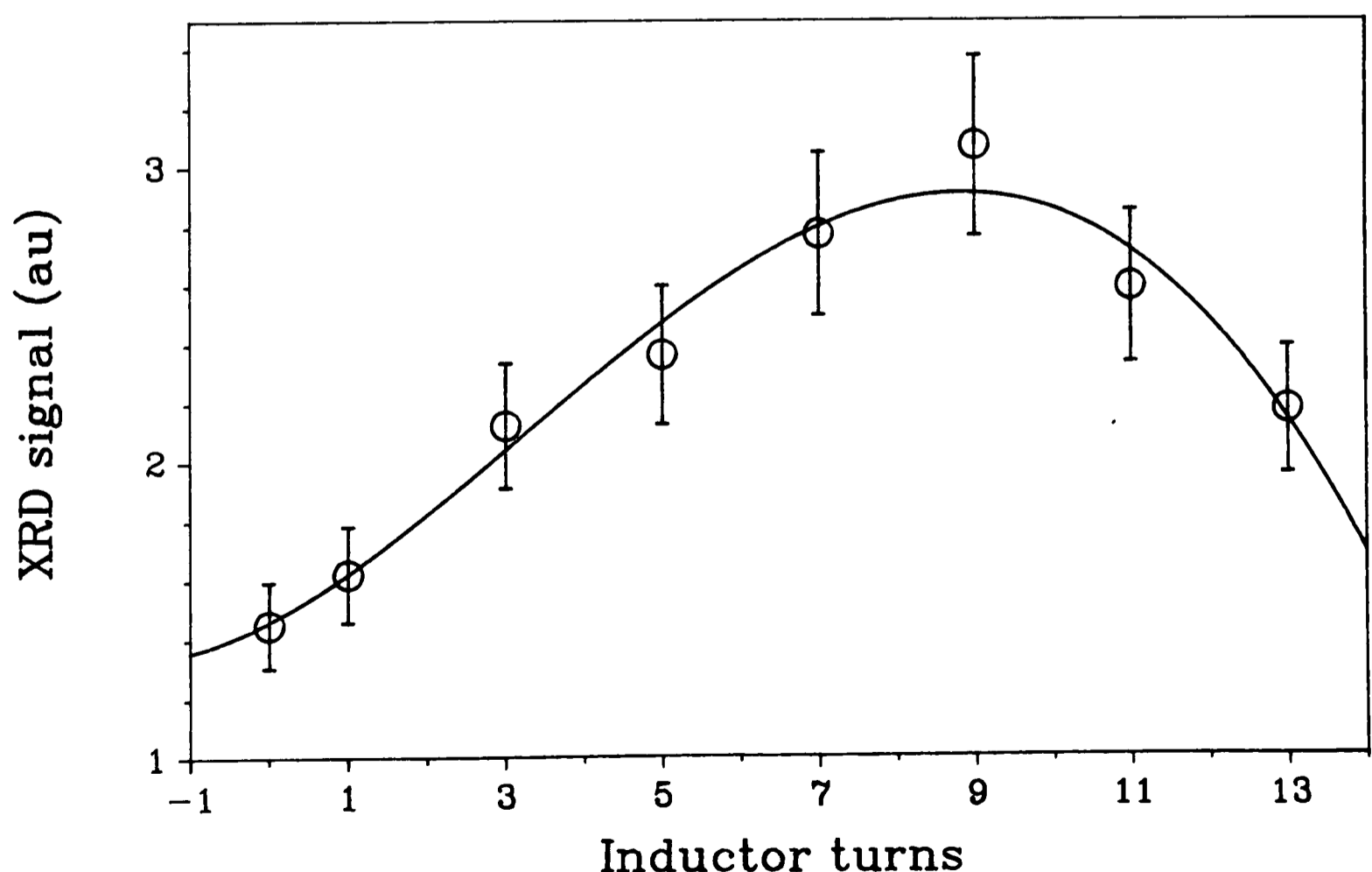


Figure 5.9: Variation in signal with number of inductor turns in oscillator circuit.

arising from transitions to any particular shell.

It was therefore decided to measure the emission spectra of the plasmas generated by each of the four target materials under those conditions which were to be used for biological imaging. A transmission grating was used, made to order at King's College London; this consisted of a series of electron beam written carbon lines, of period 167nm, supported on a 50nm thick window of Si_3N_4 which was coated with 50nm of aluminium. The overall grating dimensions were $50\mu\text{m}$ by $50\mu\text{m}$ and filters of 100nm of Si_3N_4 coated with 50nm of aluminium were used to reduce the amount of UV reaching the film, in an attempt to prevent fogging by longer wavelength components. The grating was placed at a distance of 13cm from the plasma and the spectra were recorded on Kodak 104-02 film, placed 22cm behind the grating. This had the same spectral response as the more widely used type 101-07 (as characterized by Henke [1984]), but was only one quarter as sensitive, enabling it to be handled under a red safelight. The exposed film was developed at 20°C in a 1+1 dilution of Kodak D19 stock developer in accordance with the procedure suggested by Henke [1984].

Unfortunately, the use of a transmission grating did not give as satisfactory results as would have been obtained with a grazing incidence reflection grating, although it was easier to realize experimentally. Problems were encountered with zeroth order and UV fogging and also from the very small degree of dispersion provided by the grating. However, it was felt that the additional trouble and expense of using a reflection grating would not have been justified in that a detailed spectroscopic analysis was not of paramount importance to the operation of the X-ray microscope.

5.9.1 Target debris

Despite using thin foil targets in preference to wires, there was still a problem of debris being emitted in the direction of the grating, which was both delicate and expensive. In an attempt to minimize the risk of damage to the grating, the target chamber was filled with 40mb of helium during the recording of some of the spectra. This should have greatly reduced the number and velocity of particles reaching the grating while only slightly attenuating the soft X-rays. The transmission of 40mb of

helium over the 35cm path length to the film is given in figure 5.10.

5.9.2 Resolution

There were three factors arising from the geometry of the arrangement which affected the resolution obtained in the recorded spectra; the finite source size, the grating dimension (since the incident X-rays were not planar) and the movement of the target between laser shots. These are represented schematically in figure 5.11. Simple geometry shows that they have the following effects on resolution;

$$\text{Finite source size: } \Delta\lambda \sim sd/nl_1 = 0.1\text{nm} \quad [5.27]$$

$$\text{Grating dimension: } \Delta\lambda \sim pd/nl_1 = 0.06\text{nm} \quad [5.28]$$

$$\text{Plasma movement: } \Delta\lambda \sim rd.\sin 60^\circ/nl_1 = 0.03\text{nm} \quad [5.29]$$

The resolution of the grating itself is given by

$$\Delta\lambda = \lambda^2/Nd\sin\theta$$

$$\sim \lambda/Nn = 0.01\text{nm} \quad [5.30]$$

where $N=300$ is the number of lines in the grating, of period $d=167\text{nm}$ and $n=1$ is the

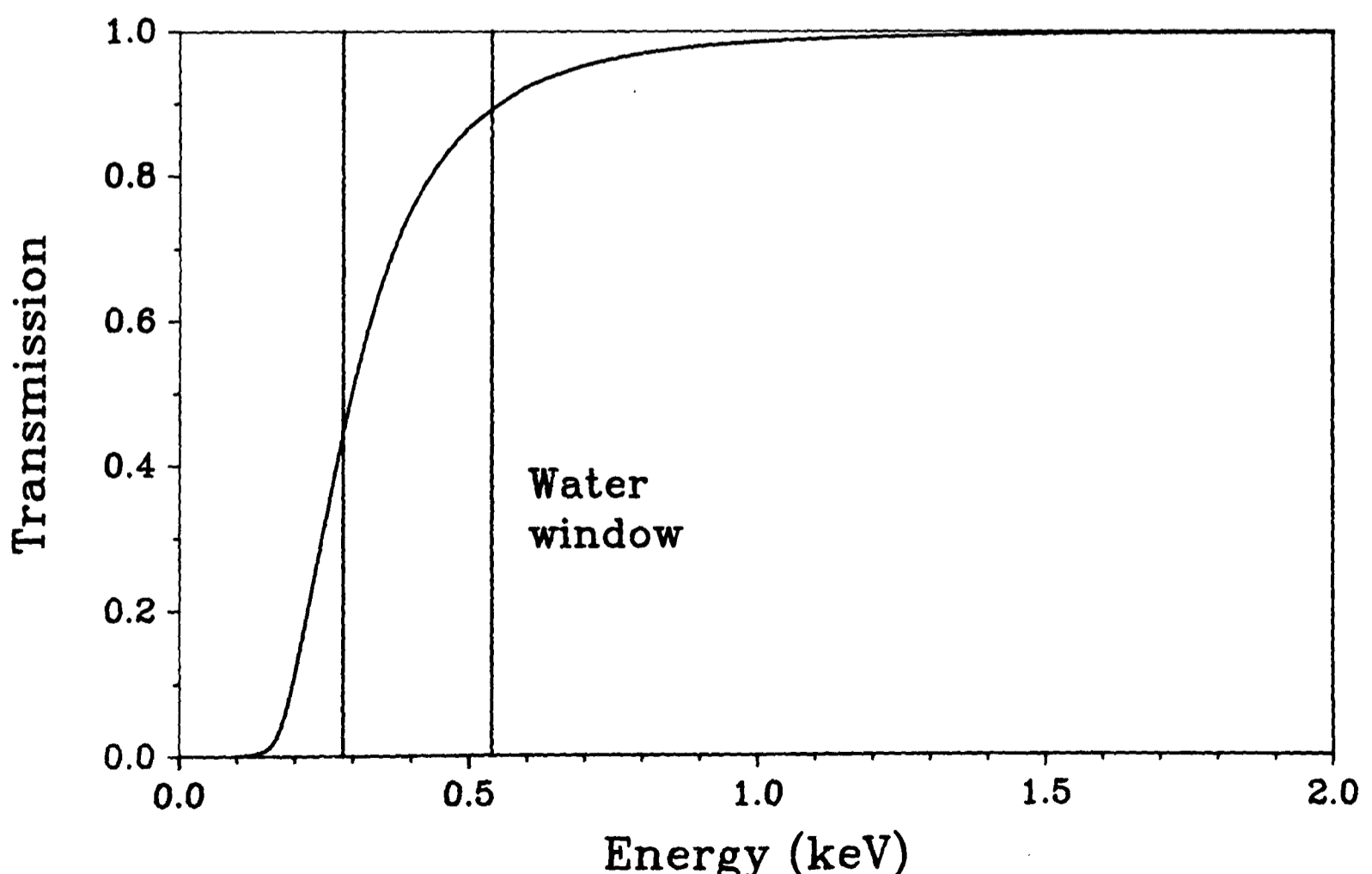


Figure 5.10: The transmission of 40mb of helium over a length of 35cm.

diffraction order. These various contributions to the resolution obtained by the use of the grating combine to give a total limit of $\sim 0.12\text{nm}$.

5.9.3 Results

The spectra recorded by the X-ray film were read out using an auto-densitometer with a step size of $5\mu\text{m}$. A background measurement was also made to enable compensation to be made for any general fogging arising from larger wavelength components and also the zeroth order. The resultant profiles were converted to optical densities and then to intensities from the calibrations made by Henke [1984]. Corrections were then made for the various filter factors arising from the use of helium or aluminium coated Si_3N_4 windows in addition to the calculated efficiency of the grating. The resultant profiles are given in figures 5.12 to 5.15. The small peaks observed in the spectra at $\sim 3.1\text{nm}$ are the result of the discontinuity in the transmission of Si_3N_4 at this wavelength, arising from the nitrogen absorption edge. There is also a problem, particularly noticeable for the titanium spectrum, of a significant background contribution to the profile from UV wavelengths, probably arising from direct reflection of the incident laser beam onto the diffraction grating. From plate 5.2, it can clearly be seen that some long wavelength components have

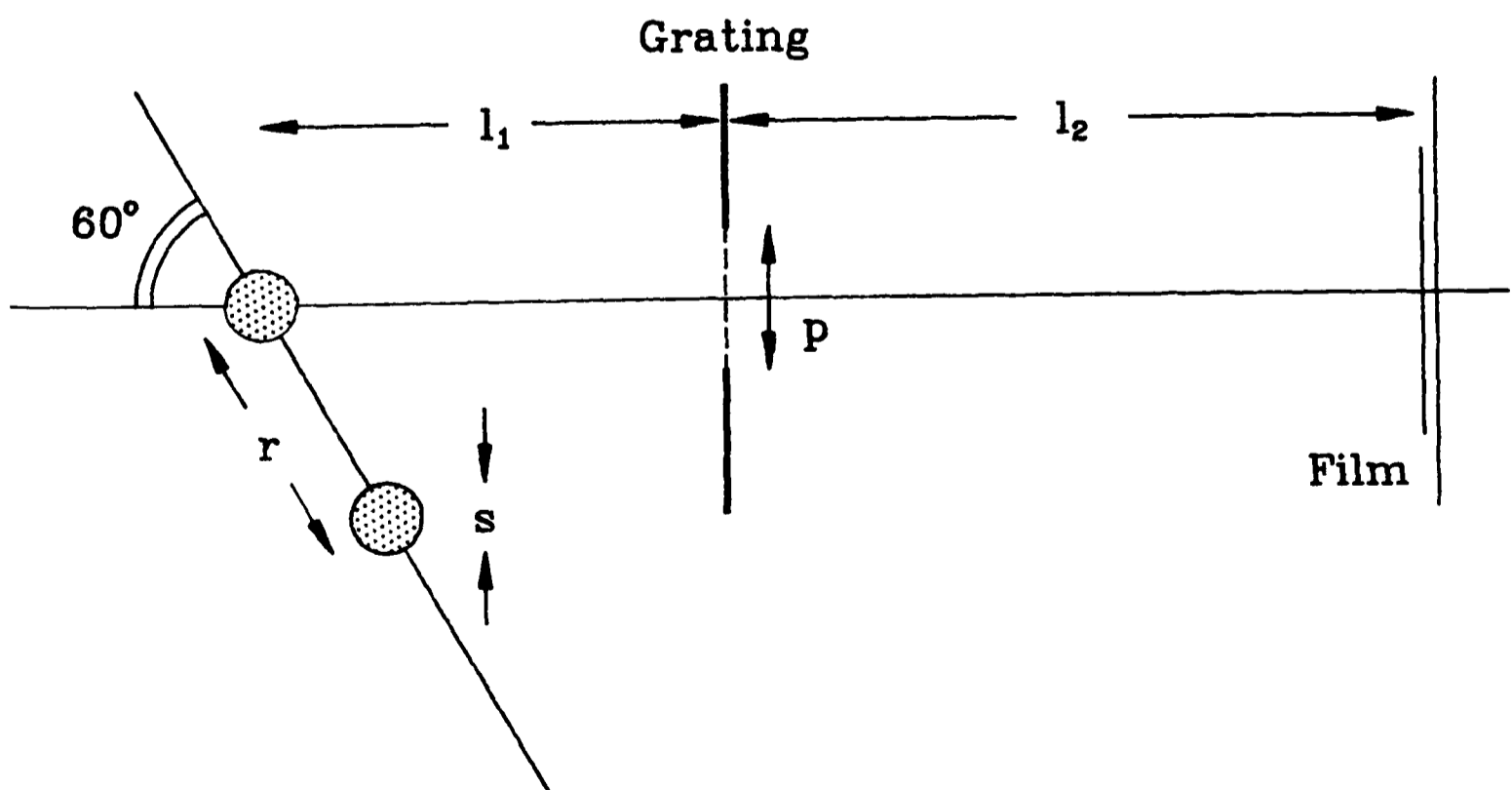
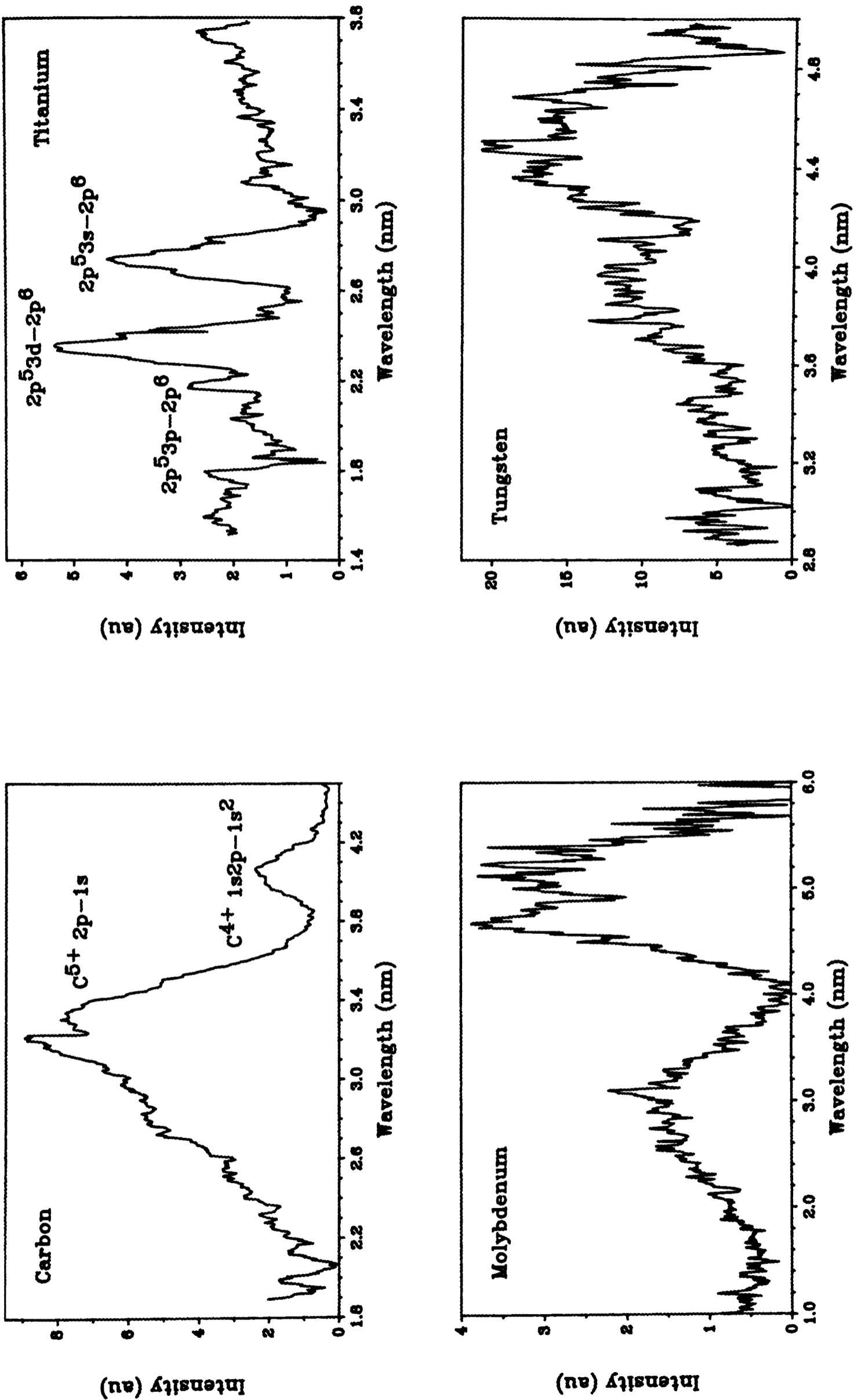


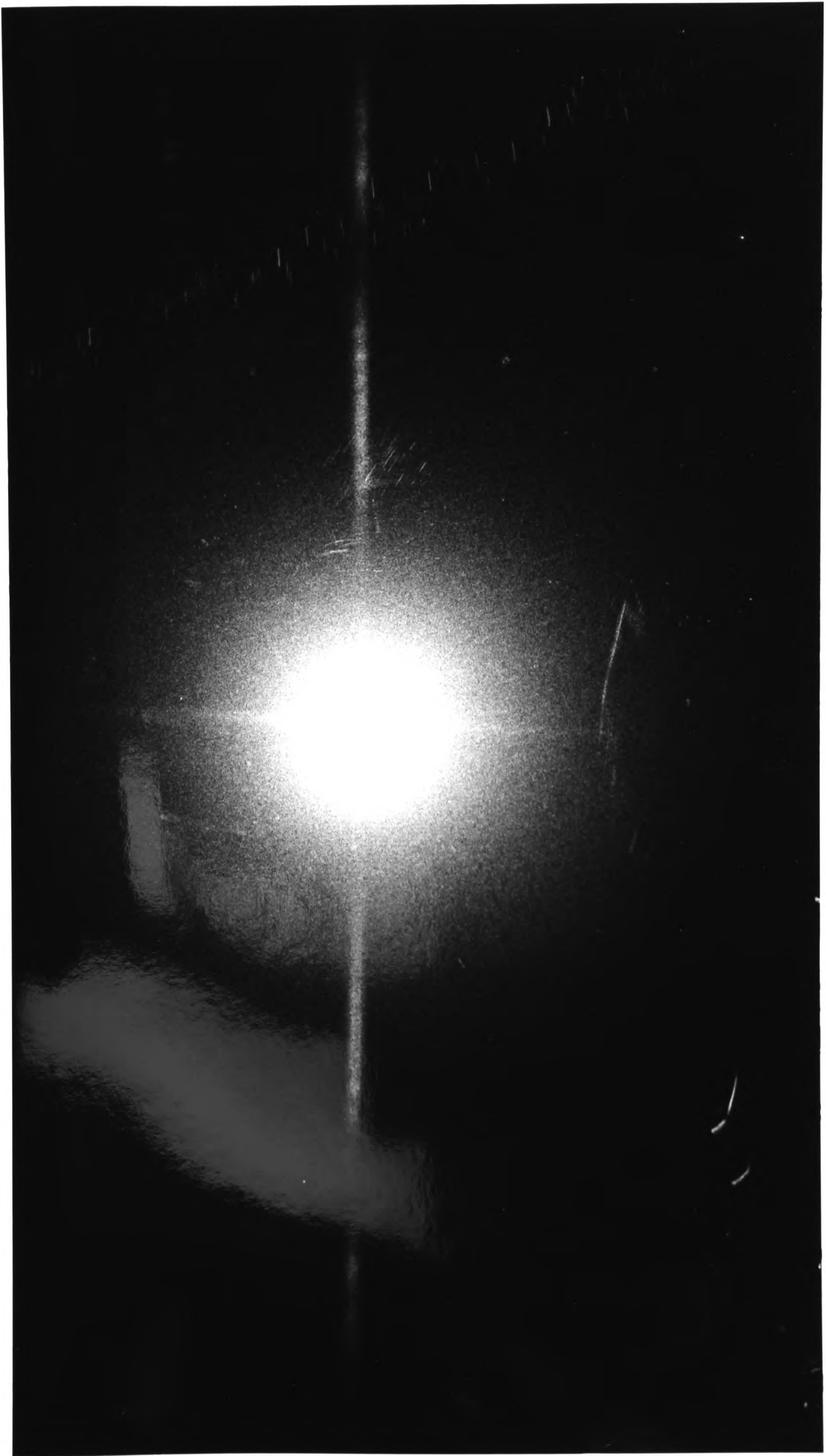
Figure 5.11: Schematic representation of the transmission grating arrangement.



Figures 5.12 to 5.15: The spectra emitted by nylon, titanium, molybdenum and tungsten targets.



Plate 5.2: The spectrum emitted by the molybdenum plasma as recorded by the transmission grating.
Magnification from film = 15.



been diffracted by the grating, perpendicular to the X-ray line, as it acted as a partially transmitting aperture of size $50\mu\text{m}$; correspondingly, there will have been a contribution to the intensity measured along the X-ray spectrum from this diffracted UV. Spectra taken on the RAL system, using a laser of wavelength $1.053\mu\text{m}$ with a similar grating showed no such contributions from UV components.

a) Carbon. Here, the principal emission arises from the C^{4+} transition $1s2p-1s^2$ at 4.07nm and the C^{5+} transition $2p-1s$ at 3.37nm . The broad fall-off to shorter wavelengths is composed of the unresolved lines in this latter series, $np-1s$, which converges to 2.53nm . The spectrum obtained here is similar to that measured by Zeng [1991] using a free-standing gold bar grating of size $50\mu\text{m}$ and period $1\mu\text{m}$, although in this case, the grouping of the $np-1s$ lines for $n \geq 3$ was resolved from that of $2p-1s$.

b) Titanium. The two largest peaks observed here are from the Ti^{12+} $2p^53s-2p^6$ transitions at 2.66nm and $2p^53d-2p^6$ at 2.34nm . Also visible is the much less intense $2p^53p-2p^6$ transition at 2.10nm . The series limit for these lines is at 1.58nm although as mentioned previously, the shorter wavelength signal is probably the result of UV contributions.

c) Molybdenum. For this element, the L shell electrons lie at $\sim 2.7\text{keV}$ and so are unlikely to be excited in the present arrangement. Therefore, it would seem likely that the broad peak at $\sim 2.8\text{nm}$ was the result of free-bound transitions to the lower M shell levels such as a $3s$ vacancy, while the lower energy peaks at $\sim 5\text{nm}$ might arise either from similar transitions to a $3d$ level or from the various possible transitions between the N and M shells.

d) Tungsten. The spectrum recorded with a tungsten target shows two broad peaks at $\sim 3.9\text{nm}$ and $\sim 4.5\text{nm}$ which arise from transitions to vacancies in the N shell from either O shell or completely ionized electrons in a system analogous to that of molybdenum but based on the N rather than M shell.

5.10 ANGULAR DISTRIBUTION OF EMISSION

For a small aperture in the side of a black body cavity, the radiance has an angular variation of

$$I(\theta) = I(0)\cos\theta \quad [5.31]$$

where θ is the angle between the direction of observation and the normal to the cavity. Such a source is described as Lambertian; it has an area but no depth. A laser generated plasma usually appears as an extended source, with emission from in front of the initial target surface. This leads to a variation in the irradiance of

$$I(\theta) = I(0)\cos^n\theta \quad [5.32]$$

The value of n typically varies from ~ 0.3 to ~ 3.0 , depending on the experimental arrangement employed. In particular, it has been found that the position of the target relative to the laser focus has a marked effect on its value. Using a tungsten wire target, Rogoyski [1989] observed a gradual increase in n from ~ 0.8 to ~ 2.1 as the target was brought from $200\mu\text{m}$ pre-focus to the position of focus. This high degree of directionality along the axis of the incident laser beam may have been due to the absorption of some X-rays by the cooling, laterally expanding plasma. As the target was moved to the post-focus position, a sharp drop in n was observed, to a value of ~ 0.4 , indicating a more isotropic emission distribution. In this case, the plasma expanded into the focus of the oncoming laser pulse such that it experienced a high irradiance at the optical axis but a much lower one away from this region. This may be seen to suggest a more spherical region of X-ray emission, which would lead to the observed angular variation of intensity.

In the current experiment, it was found that the intensity of emitted X-rays did not fall to zero at $\theta=90^\circ$ as predicted by equation [5.32]. This was because it was possible to ‘see’ the expanding plasma in front of the wire target from a position beyond the tangent, where the line of sight was not obscured by the target itself. In these circumstances, the angular distribution may be modelled in one of two ways:

a) Using a straight line fit; $I(\theta)=\alpha(m\theta+c)$. This enables the predicted flux to fall to zero at some angle greater than 90° . However, for more isotropic emissions, this would suggest a non-zero flux at very large angles, tending to ∞ for a perfectly isotropic distribution.

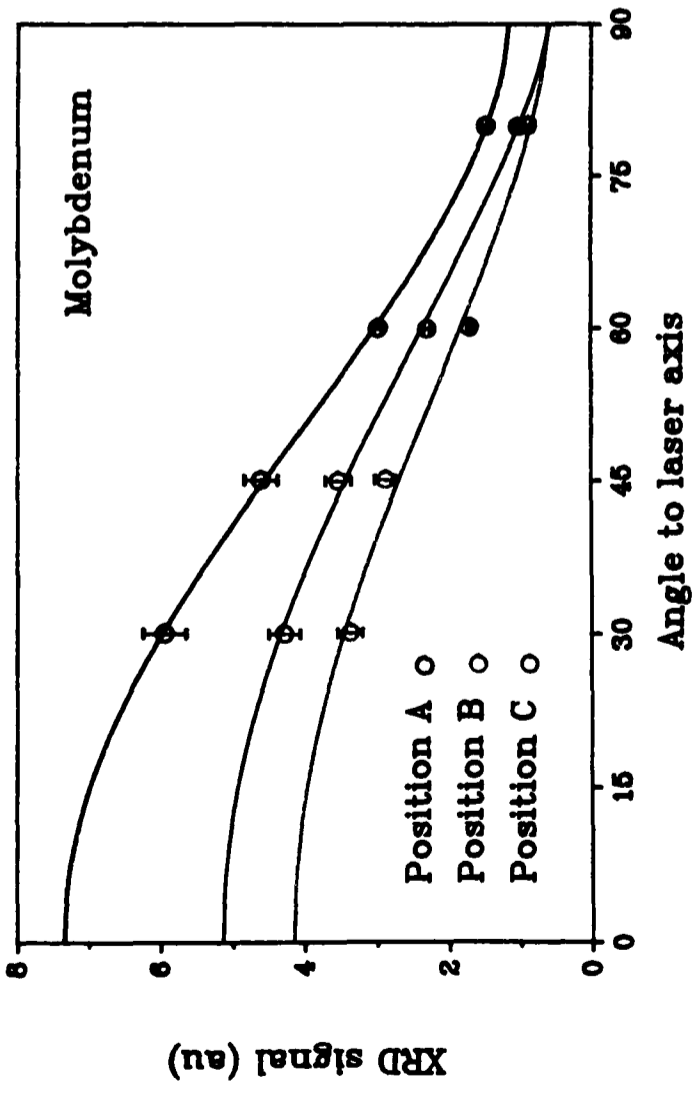
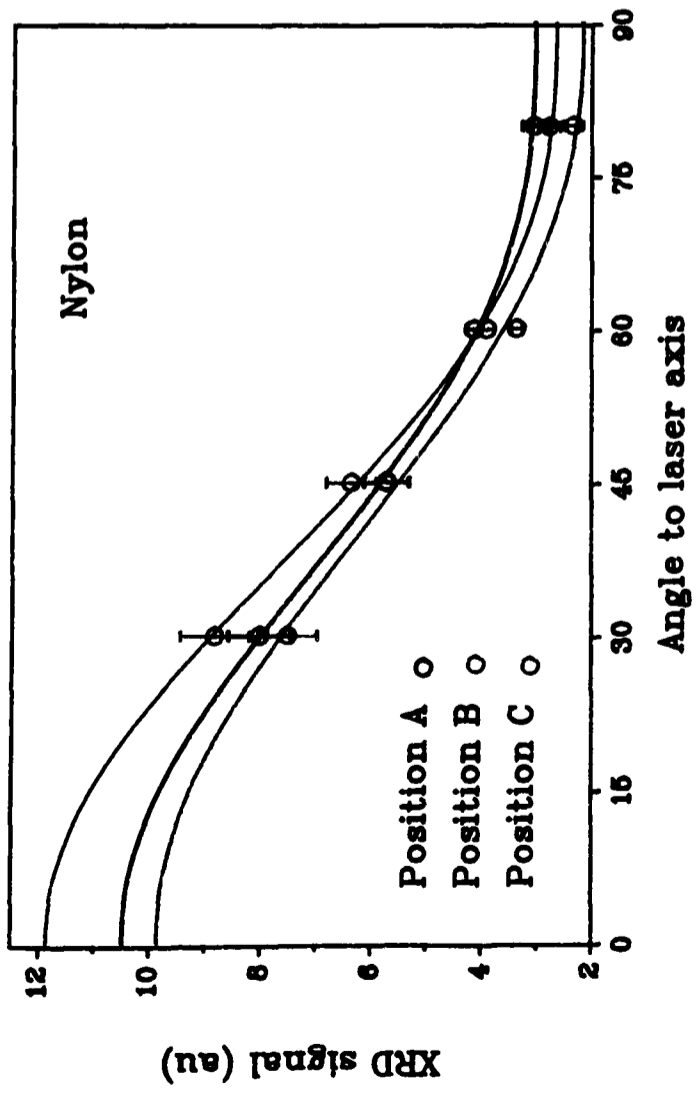
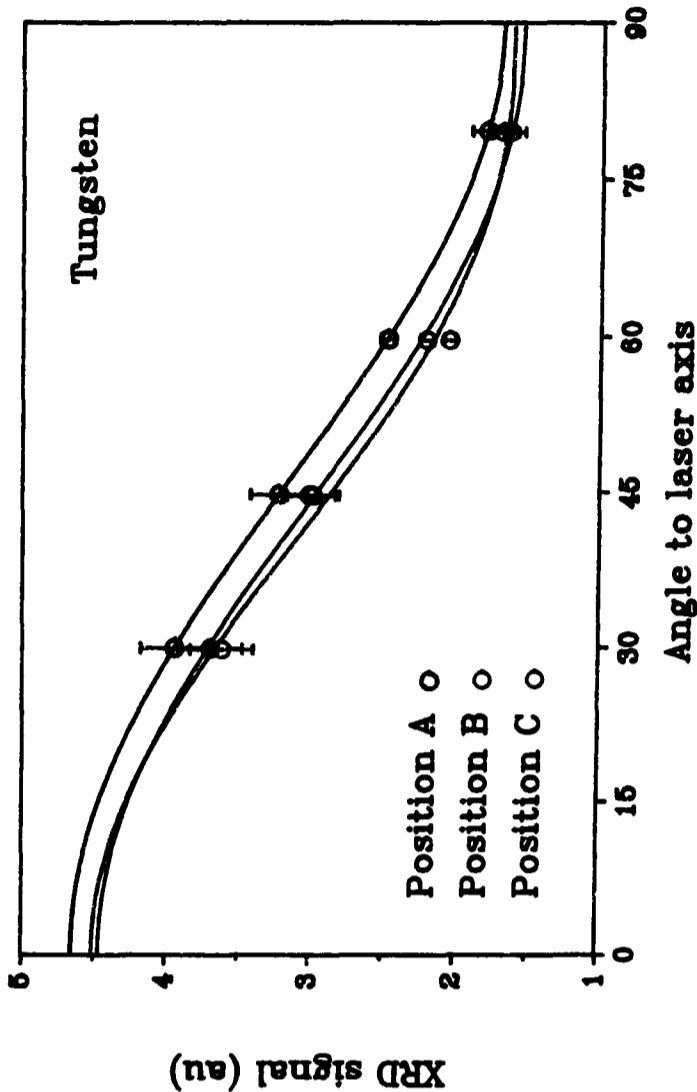
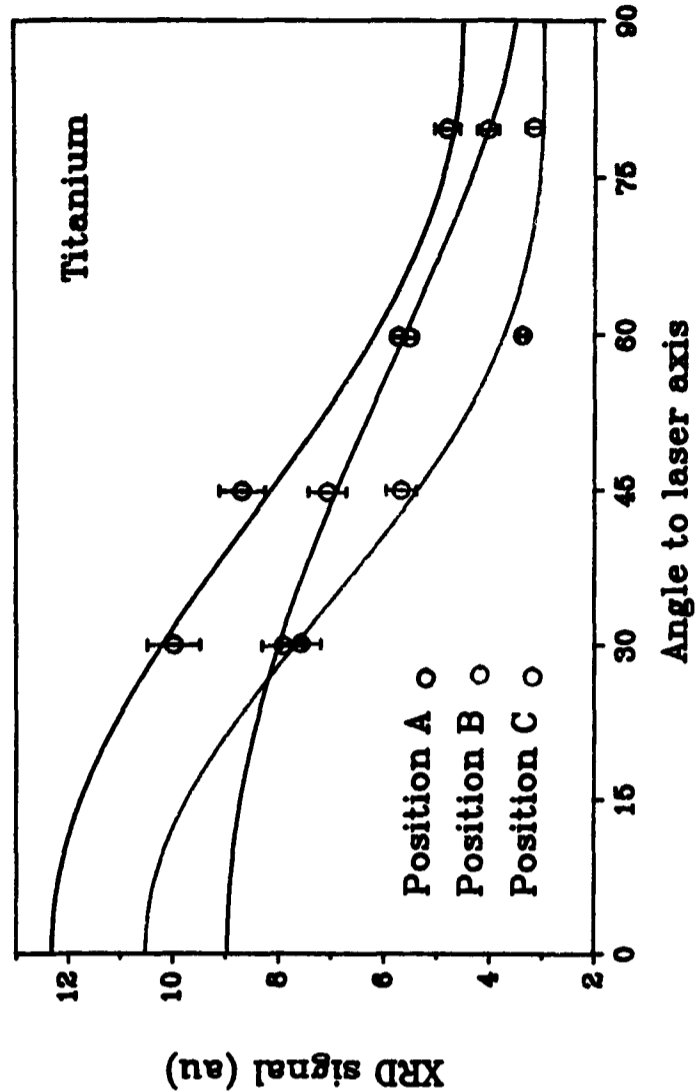
b) Using a ‘hybrid cosine’ fit of $I(\theta)=\alpha(k+\cos^n\theta)$. This in turn suffers from not predicting a zero flux at any angle.

It was decided to use this second model, as it most closely described the results of the measurements made with the current system. In calculating the conversion efficiencies using this function, integration was only made over the 'forward' 2π steradians, to overcome the problem of the model not giving a zero value at $\theta > 90^\circ$.

Only a limited investigation into the angular variation of X-ray emission was made, since the effect was not directly relevant to the operation of the X-ray microscope, for which the size of the vacuum feed-through and the position of the 9cm focusing lens restricted the angle at which specimens could be presented for illumination to 60° . However, future arrangements of the microscope might allow this angle to be decreased and the increase in flux to be gained by such an alteration was of interest. Consequently, the flux was measured at a range of angles, limited by the lens holder and the need for a clear line of sight past the target to enable the telescope to be used for accurate positioning. Measurements were made at three target positions; at focus and at the two peaks on either side, as these would show evidence of variations in the parameter n most easily, while also permitting the plasma to be investigated under the conditions in which the microscope would generally be operated for maximum specimen illumination (that is, position A of figures 5.5 to 5.8).

The measurements made are presented in figures 5.16 to 5.19 and values obtained¹⁾ for the parameters n , α and k in table 5.1. Although an increasingly isotropic emission was expected on moving the target from point A to B to C, as would be apparent from a decrease in the parameter n , this was only observed to be the case for the molybdenum target. Carbon and titanium also showed an overall decrease from positions A to C despite values at position B which did not follow the overall trend. With a tungsten target, the emission actually became slightly less isotropic at the post-focal position. Other than that carried out by Rogoyski [1989], work on the angular distribution of X-ray emission has not considered the effect of focal position on the value of n . Turcu [1987] used the 100J KrF Sprite laser at RAL at an intensity of

¹⁾ These were calculated by means of minimizing the expression $\{y_s - \alpha[\cos^n(\theta_s) + k]\}^2$ summed over the four data points for each focal position; $s=1$ to 4.



Figures 5.16 to 5.19: Angular distribution of X-ray emission from nylon, titanium, molybdenum and tungsten targets.

10^{13}W/cm^2 on a carbon rod and found a value of $n=2.75$ for water window X-rays at the position of maximum X-ray emission in an arrangement which most closely resembles the current work. It may be noted that this value for the parameter n is in very close agreement with that measured at position C.

	Position A			Position B			Position C		
	n	α	k	n	α	k	n	α	k
Carbon	2.86	7.50	.424	2.44	7.74	.296	2.74	9.26	.303
Titanium	2.20	7.87	.588	3.31	7.60	.408	1.37	5.49	.663
Molybdenum	1.73	6.20	.202	1.54	3.56	.202	1.36	4.56	.150
Tungsten	1.91	2.97	.584	2.41	2.90	.574	2.07	2.92	.545

Table 5.1: The measured angular distribution parameters.

It is suspected that the problem associated with the photodiodes used in this part of the experiment (described in section 5.12) may have resulted in these unexpected observations. This was particularly problematical for these angular dependence measurements for which a calibration curve had to be used to equate the signals obtained from the photodiodes RAL1 and RHBNC1. As was the case in the measurement of the flux as a function of the target position in relation to the laser focus, any possible variation in the spectral content of the emitted X-rays with angular position was not investigated and may, to some extent, have affected the accuracy of the measurements made. However, it is apparent that for the focal position A, the flux obtained at 30° to the laser axis was significantly larger than that obtained at 60° .

5.11 CALCULATION OF CONVERSION EFFICIENCY

The calculation of the total amount of X-rays produced by any one ‘shot’ of laser energy incident on a particular wire target needed careful consideration in order to produce an accurate and meaningful value. Calculations made by previous workers (for example by Kühnle [1988]) have frequently made several assumptions in order to simplify the process, such as average values for diode response, filter transmission, etc.

over a range of wavelengths. These simplifications have not been repeated; rather, a numerical approach has been taken for those parts of the calculation where required.

The measuring device used was one of a number of 100PIN125 photodiodes, (manufactured by Quantrad) with an integral silicon entrance window of thickness $0.25\mu\text{m}$. The calibration curve for the diode and window, relating incident energy to output charge as a function of incident photon energy, was supplied by the manufacturer, and is given in figure 5.20. This illustrates a factor of almost 5 in the variation of response within the water window region alone.

In addition to the silicon entrance window, a supplementary filter was also used when measurements were being made. This was either a 3mm diameter vanadium filter of thickness $0.5\mu\text{m}$, supported on a mylar grid which had a geometrical transmission of 40% for X-rays independent of wavelength, or a 100nm thick Si_3N_4 window, of side 1.5mm, onto which $0.5\mu\text{m}$ of vanadium had been evaporated. The transmission as a function of photon energy for each is given in figures 5.21 and 5.22. The output of the diode detector was placed across a load of $R=50\Omega$, and the resultant voltage measured

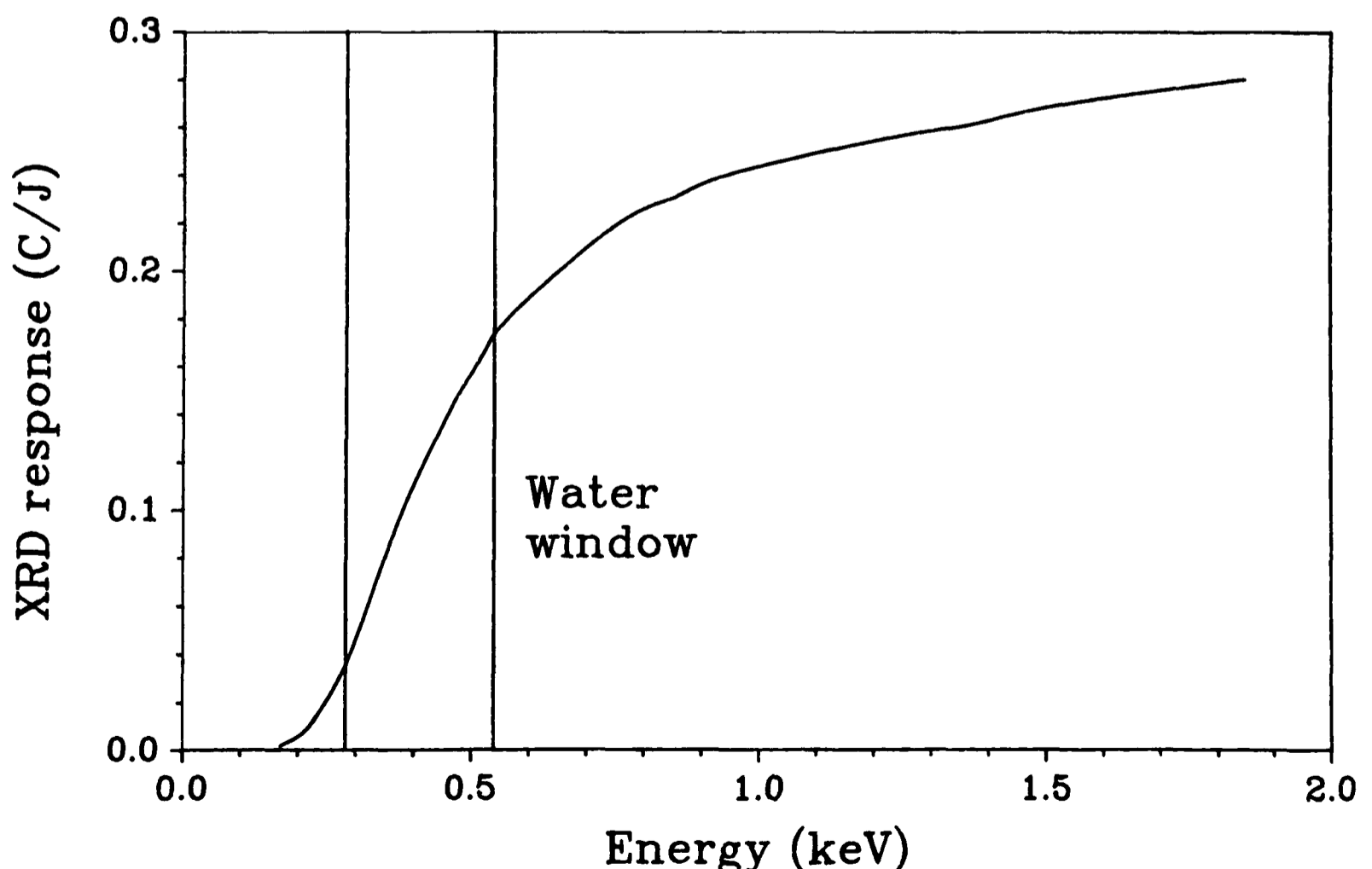


Figure 5.20: The response of the PIN X-ray photodiodes (from manufacturer's data).

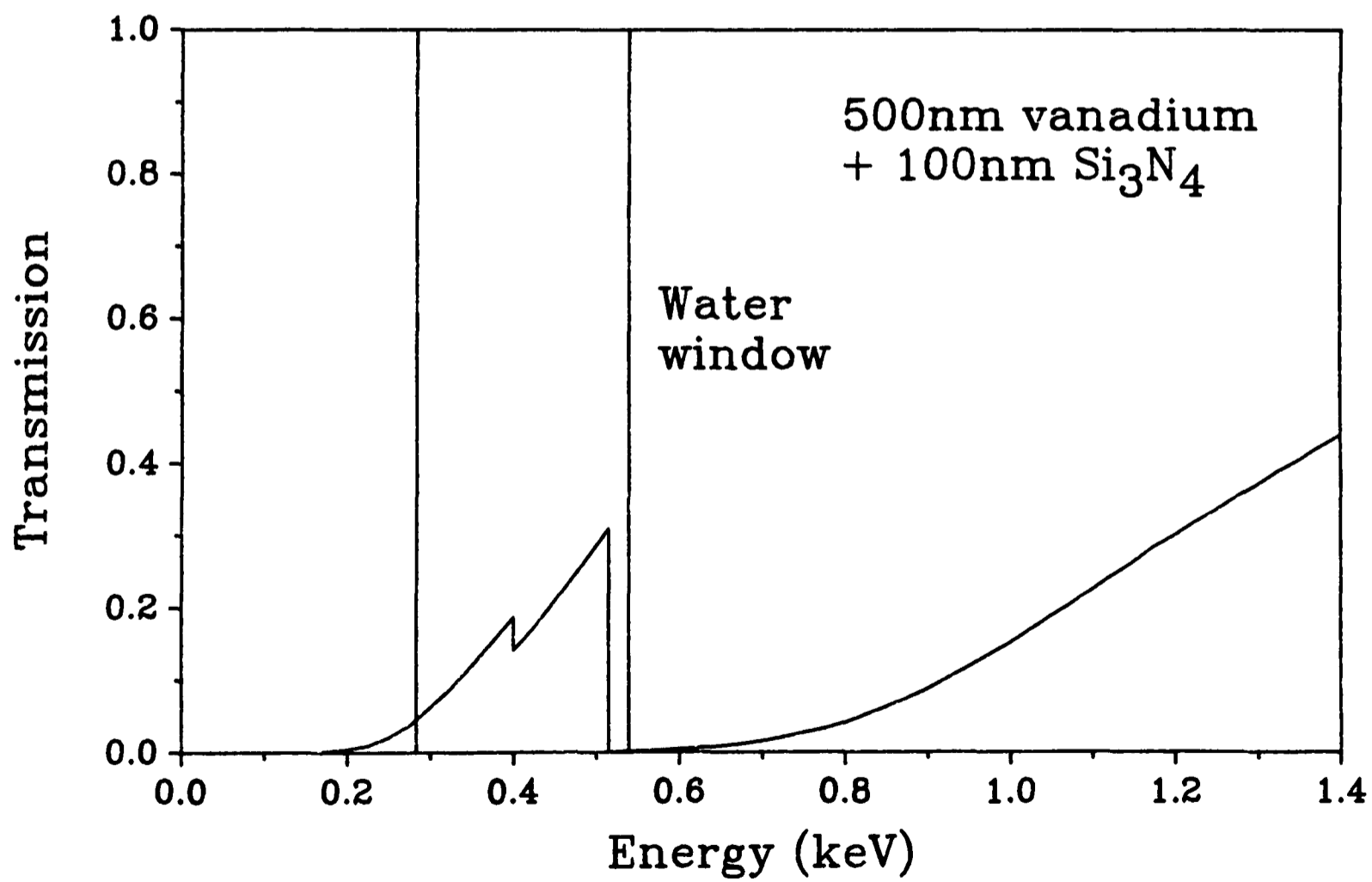
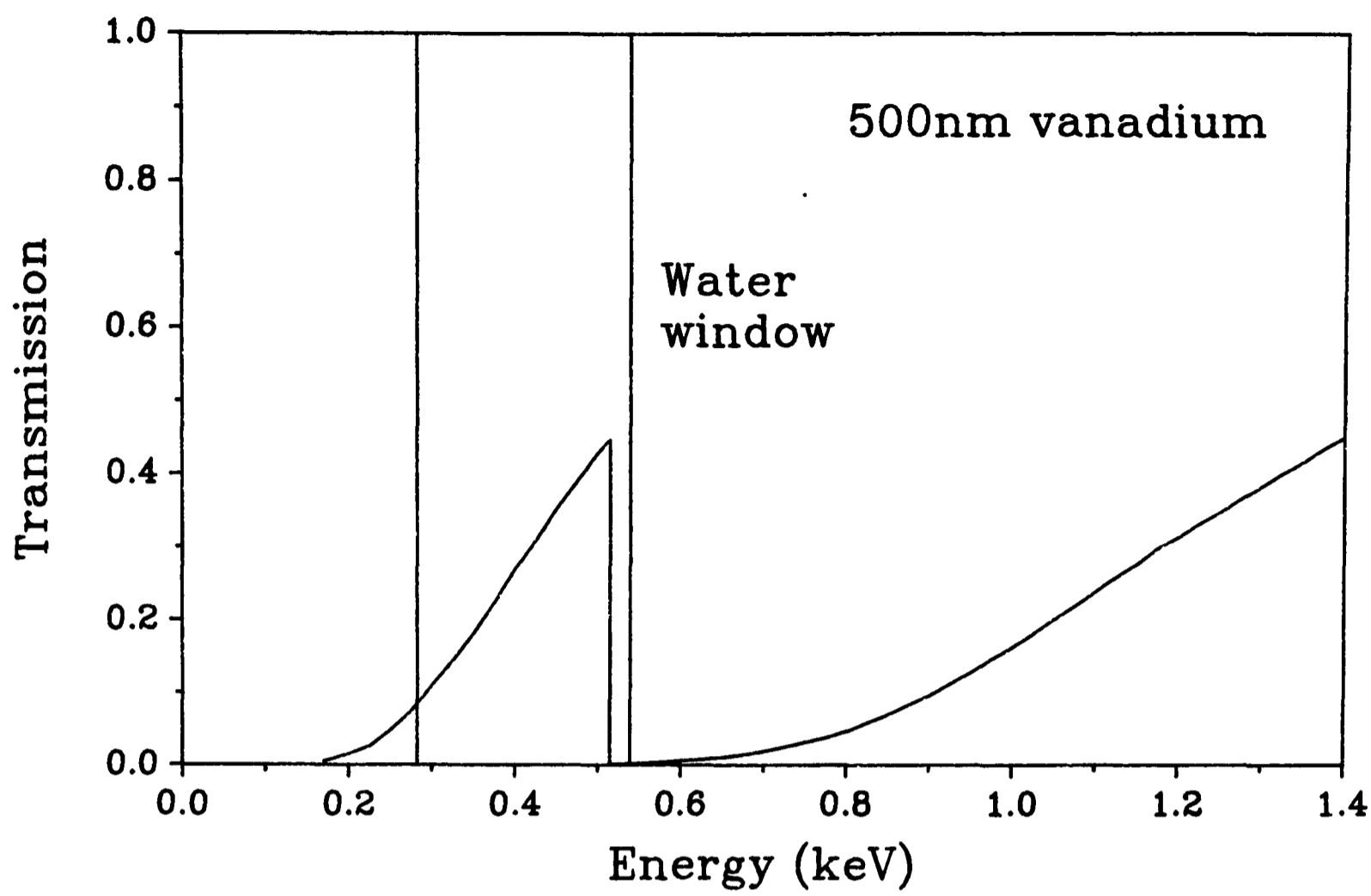


Figure 5.21: Transmission of the mylar-supported 0.5 μ m vanadium filter.

Figure 5.22: Transmission of the 0.5 μ m vanadium on 0.1 μ m Si₃N₄ filter.

with a 2440 Tektronix digital storage oscilloscope. This had a built-in function which allowed the area of the voltage-time trace to be automatically evaluated and displayed. For any particular measurement, a number of readings were taken to arrive at a mean value of the trace area, in units of volt.seconds. We denote this by A_{vt} . A filter, of diameter d mm, was placed in front of the diode, which was then positioned in the target chamber such that:

- a) It was on axis with the laser generated plasma.
- b) The angle between its axis and that of the laser was θ .
- c) The front of the filter was a distance s mm from the wire target.

From these parameters, it was necessary to calculate the total amount of X-rays emitted by the plasma within the water window. We begin with the variation in the X-ray spectral intensity per unit solid angle as a function of photon energy; $S(E) \text{ sr}^{-1}$ as measured in section 5.9. Initially, this is simply a shape function of arbitrary magnitude. We wish to use the measurement obtained from the photodiode to give this function an absolute scale, such that when integrated over the region of the water window, the actual X-ray energy emitted by the plasma source will result.

We must also take into account the fact that the emitted X-rays might not be isotropic in distribution. As explained in section 5.10, we have chosen a $(k+\cos^n\theta)$ variation in intensity, where θ is the angle from the normal to the wire target (ie. the axis of the laser) to the axis of the photodiode, and k is some constant. Setting $n=0$ will then result in an isotropic distribution if required.

Initially, we consider what our measured value of A_{vt} represents. It results from a charge produced by the photodiode of

$$Q_d = A_{vt}/R \quad [5.33]$$

The X-ray flux which reaches the diode will be a product of the X-ray spectral intensity $S(E) \text{ sr}^{-1}$, the filter transmission function $F(E)$, with geometrical transmission $T\%$ if applicable, and the angular variation, $\alpha(k+\cos^n\theta)$, where α is a constant. If we multiply by the diode response $D(E)$ coulombs per joule and integrate over all energies, then we will obtain the charge that would have resulted had our initial choice of X-ray spectral intensity been such that it matched the actual spectral

intensity of the plasma source;

$$Q_{\text{abs}} = \int_0^{\infty} S(E)F(E).(T/100).\alpha(k+\cos^n\theta).D(E) dE.\pi(d/2s)^2 \quad [5.34]$$

where $\pi(d/2s)^2$ is the angle subtended by the supplementary filter. The actual measured charge, of Q_d coulombs, indicates that $S(E) \text{ sr}^{-1}$ is too large by a factor

$$\begin{aligned} Q_{\text{abs}}/Q_d &= (R/A_{\text{vt}}).\pi(d/2s)^2.(T/100).\alpha(k+\cos^n\theta)\int_0^{\infty} S(E)F(E)D(E)dE \\ &= M \end{aligned} \quad [5.35]$$

We consequently have the actual spectral intensity of the laser generated plasma as $S(E)M^{-1} \text{ sr}^{-1}$. All that remains is to evaluate the amount of X-rays generated which fell within the water window. The angular dependence of the emitted X-rays leads to the factor

$$\int_0^{2\pi} d\varphi \int_0^{\pi/2} \alpha \sin\theta.(k+\cos^n\theta)d\theta = 2\pi\alpha[k+(n+1)^{-1}] \quad [5.36]$$

so that the required energy is

$$E_{\text{ww}} = M^{-1} \int_{0.28}^{0.54} S(E)dE.2\pi\alpha[k+(n+1)^{-1}] \quad [5.37]$$

If the laser energy incident on target is given by E_i joules, then this indicates a conversion efficiency to water window X-rays of

$$\eta (\%) = 8 \times 10^4 s^2 A_{\text{vt}} [k+(n+1)^{-1}] I / E_i T (k+\cos^n\theta) R d^2 \quad [5.38]$$

where

$$I = \int_{0.28}^{0.54} S(E)dE / \int_0^{\infty} S(E)F(E)D(E)dE \quad [5.39]$$

The ‘integral ratio’ I here accounts for the spectral dependencies of the photodiode, filter and plasma emission. In practice, the $0 \rightarrow \infty$ limits of the lower integral were reduced such that only the range over which $S(E)F(E)D(E)$ was non-zero was covered. Figure 5.23 illustrates this function for a molybdenum target and mylar-supported $0.5\mu\text{m}$ vanadium filter. The relevant spectral intensities, photodiode response and mass absorption coefficients were entered into a Lotus 123 spreadsheet, and the required integrals evaluated numerically. Table 5.2 gives values for I , the ratio of the two integrals of equation [5.39] for the four target materials used and the two types of filtering employed.

	0.5μm vanadium	0.5μm V + 0.1μm Si ₃ N ₄
Carbon	31.9	53.1
Titanium	35.4	58.5
Molybdenum	38.1	63.5
Tungsten	86.1	145.9

Table 5.2: The integral ratios, I, used to calculate the water window conversion efficiencies.

5.12 MEASURED CONVERSION EFFICIENCIES

Once the spectra and angular distribution of X-ray emission generated by this particular system had been measured, the conversion efficiency from incident laser energy to water window X-rays could be calculated from each charge delivered by the X-ray photodiodes located in the target chamber. Unfortunately, however, the absolute and spectral responses of the five photodiodes used did not appear to be the same for each unit, contrary to the calibration data provided with each by the supplier

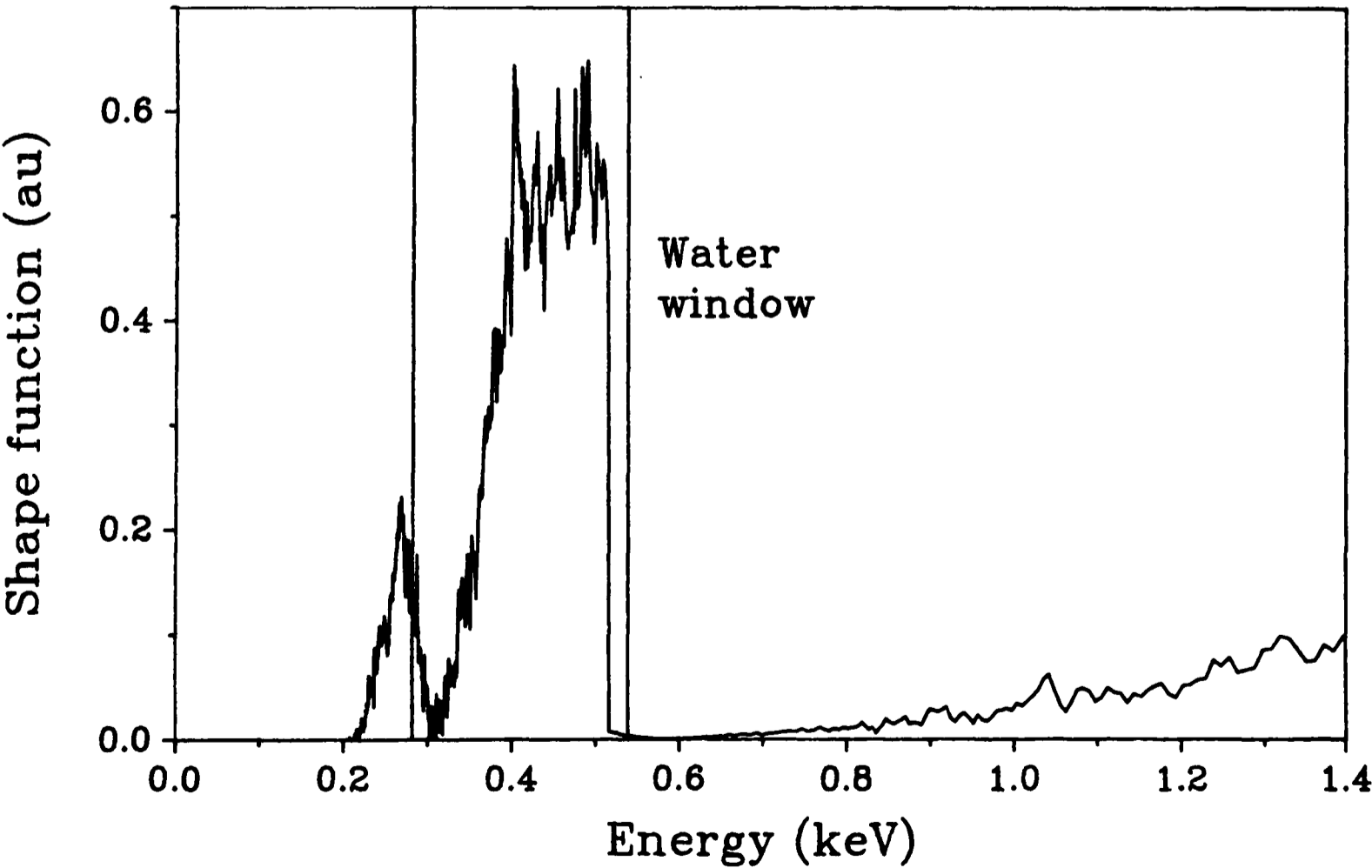


Figure 5.23: The product of the molybdenum spectrum, vanadium filter transmission and the X-ray photodiode response.

which suggested that all of the photodiodes would have identical characteristics. Most noticeably, the magnitude of the signals from the five photodiodes, labelled as RAL1, RAL2, RHBNC1, RHBNC2 and OXF, seemed to have a fixed ratio of approximately 4:1:3:1:1 to each other for all of the four target materials used. Furthermore, the replacement of the $0.5\mu\text{m}$ vanadium filter supported on a 40% transmissive mylar grid by a 100nm thick Si_3N_4 window which had been coated with $0.5\mu\text{m}$ of vanadium, resulted in an increase by a factor of approximately 4 in the calculated conversion efficiency for a particular target. This suggested that either

- a) The older mylar-supported vanadium filters had been contaminated in some way (possibly by oxidation) thus reducing their transparency to soft X-rays, or
- b) The spectral response of the photodiodes was not the same as that suggested by the manufacturer.

(An additional possibility, that there was a significant UV contribution to the signal, was ruled out by placing a thin section of fused silica in front of the photodiode. This would have permitted only UV components to reach the detector, and when this was done, no signal was recorded.)

To obtain a set of conversion efficiencies which were at least self-consistent, measurements were made with the photodiodes labelled RAL1 and RHBNC1, both using the mylar-supported $0.5\mu\text{m}$ vanadium filters and also the vanadium-coated Si_3N_4 windows (which could only be used with foil targets). All measurements were made at 60° to the laser axis with an energy of $\sim 1.4\text{J}$ on target; the focal position of the target was in each case that which gave the maximum flux (ie. position A in figures 5.5 to 5.8). Using the formula of [5.38], the spectra as measured in section 5.9 and assuming isotropic X-ray emission (ie. $n=0$ and $k=0$), the efficiencies for water window X-ray generation were measured for all four target materials being investigated. The results are presented in table 5.3.

Figures in brackets are values predicted for certain configurations which were not (or could not be) realized in practice. It is immediately apparent from the results obtained with the RHBNC1 photodiode that there is a significant decrease in the conversion efficiencies obtained from thin foil targets in comparison to wire targets. As

shown in section 5.3, this is not as would be expected from the theory proposed by Fabbro [1985]. However, it is interesting to note that the greatest decreases observed were with the 12.5 μ m titanium foil and the 12 μ m mylar foil, whereas much smaller decreases resulted from the use of the molybdenum and tungsten foils, both of which were 40 μ m thick. In the latter case, the foil was only just punctured by one laser shot and it was found that the vanadium-coated Si₃N₄ window used to filter the photodiode was broken after an average of about 10 shots even when placed ~26cm from the plasma. These observations suggest that, although only the first few micrometres of the target material may have been contributing to the generation of the plasma as suggested by Fabbro [1985], the presence of an impenetrable mass behind this thin layer did in some way act to eject the plasma forwards into the incident laser beam. When a thin foil was used which was punctured during the plasma generation process, as was especially the case for the titanium and mylar foils, the plasma may have been driven back towards the target by the pressure generated by the hydrodynamic expansion into the vacuum, causing emitted X-rays to be partially obscured and possibly leading to X-ray emission along the forward direction of the incident laser beam. Zeng [1991] also measured a decrease in conversion efficiency when using progressively thinner copper foil targets, although in this case, the dependence on

Material	RAL1 + V	RAL1 + V, Si ₃ N ₄	RHBNC1 + V
Nylon wire	1.39±0.01	[6.38±0.17]	0.484±0.005
Mylar foil	[0.362±0.007]	1.66±0.03	0.127±0.002
Ti wire	2.00±0.04	[9.28±0.26]	0.801±0.015
Ti foil	[0.644±0.020]	2.99±0.04	0.258±0.004
Mo wire	4.16±0.07	[16.8±0.6]	1.45±0.03
Mo foil	[2.82±0.09]	11.4±0.2	0.983±0.019
W wire	8.23±0.24	[32.0±0.9]	2.41±0.07
W foil	[5.91±0.17]	23.0±0.7	1.73±0.05

Table 5.3: Percentage conversion efficiencies of laser energy to water window X-rays.

target thickness was apparently much weaker than that indicated here.

The factors arising from the variation in angular distribution of the emitted radiation are given in table 5.4, from which it may be seen that this variation has only a small effect on the results of the calculation in practice; in effect, the flux emitted at 60° may be regarded as an ‘average’ for the full angular range. For a straight line fit of $I(\theta)=\alpha(m\theta+c)$, this factor becomes $(m+c)/(m\theta+c)$; for the straight line fit suggested by Cotton [1990] for carbon and tungsten, values of 1.09 and 1.02 are obtained, again illustrating the relative unimportance of this factor in the calculation of conversion efficiencies.

	Position A	Position B	Position C
Carbon	1.22	1.22	1.26
Titanium	1.12	1.26	1.03
Molybdenum	1.13	1.09	1.06
Tungsten	1.09	1.14	1.11

Table 5.4: Correction factors from the variation in angular distribution of emission.

As suggested in section 5.4, the conversion efficiency of laser energy into X-ray radiation varies very approximately as $\eta\propto Z^{1/2}$ for a sufficiently large energy range. To calculate the total amount of X-rays generated rather than just those in the water window, the limits of the integral in the numerator of equation [5.38] were changed to cover the whole of the soft X-ray energy range, resulting in a new set of integral ratios, as given in table 5.5.

Using these values and the factors arising from the angular distributions of emission given in table 5.4, the corresponding efficiencies were calculated for the four target materials from the measured values obtained with the RAL1 photodiode and mylar-supported vanadium filter for a wire target and, for comparison, the predicted values for the RAL1 photodiode and Si₃N₄ supported vanadium filter with a wire target. These are presented in table 5.6 and figure 5.24, and in table 5.7, a comparison

is made with the efficiencies measured by other workers under conditions approximately similar to those used in the current work.

	0.5μm vanadium	0.5μm V + 0.1μm Si ₃ N ₄
Carbon	34.8	57.9
Titanium	43.7	72.3
Molybdenum	85.0	141.8
Tungsten	116.9	198.1

Table 5.5: The integral ratios, I, used to calculate the total soft X-ray conversion efficiencies.

5.13 VARIATION OF YIELD WITH LASER ENERGY

In an attempt to discover the cause of the unexpectedly low conversion efficiencies indicated by the X-ray photodiodes when used with the mylar-supported vanadium filters, the yield obtained from a tungsten wire was measured as the incident laser energy was varied. Initially, the NO₂ cell was used to control the energy on target, but it was immediately found that the energy transmitted by the cell increased with each laser shot. This was probably caused by the temporary dissociation of the NO₂ into NO and O*, neither of which absorbs at 248nm. It was also noted that this bleaching was reversible, which would have resulted from the slow recombination of the NO and O* to re-form NO₂. Figure 5.25 illustrates the energy transmitted by the NO₂ cell used in the current experiment when filled to a pressure of 50mb. Transmission through the empty cell was 1.3J and the path length through the

Material	RAL1 + V	RAL1 + V,Si ₃ N ₄
Nylon wire	1.85±0.01	[8.49±0.23]
Ti wire	2.77±0.06	[12.8±0.4]
Mo wire	10.5±0.2	[42.4±1.5]
W wire	12.2±0.4	[47.4±1.3]

Table 5.6: Percentage conversion efficiencies of laser energy to all soft X-rays.

absorbing gas was 50mm. Two measurements were taken during the recombination period to indicate the rate at which the cell regained its opacity to radiation at 248nm.

To overcome this problem, a number of coated silica flats were used to attenuate the laser beam so that the energy on target varied from 1.4J to 54mJ. The RAL1 and RHBNC1 photodiodes were used with nominally identical mylar-supported 0.5 μ m vanadium filters to measure the emitted water window X-ray flux and the conversion efficiencies obtained are shown in figure 5.26. The presence of a plateau in the efficiency is similar to that found for some other target materials (for example, as

Target material	Laser λ (nm)	Intensity (W/cm ²)	Energy range (eV)	η (%)	Reference
Carbon	248	5x10 ¹²	100-1100	4	Popil [1987]
	248	5x10 ¹²	10-850	6	Fedosejevs [1987]
	532	7x10 ¹²	250-800	4	Gerritsen [1986]
	532	3x10 ¹³	50-1240	4	Eidmann [1986]
	248	1x10 ¹²	282-539	8	Present work
Titanium	248	5x10 ¹²	100-1100	12	Popil [1987]
	248	5x10 ¹²	10-850	16	Fedosejevs [1987]
	532	7x10 ¹²	250-800	10	Gerritsen [1986]
	532	2x10 ¹⁴	>100	23	Mead [1981]
	532	3x10 ¹³	50-1240	26	Eidmann [1986]
	532	1x10 ¹⁴	100-1560	38	Mochizuki [1986]
	260	2x10 ¹⁴	250-2500	21	Alaterre [1986]
	248	1x10 ¹⁴	282-539	13	Present work
	248	5x10 ¹²	100-1100	16	Popil [1987]
Molybdenum	532	7x10 ¹²	250-800	8	Gerritsen [1986]
	532	3x10 ¹³	50-1240	31	Eidmann [1986]
	532	1x10 ¹⁴	100-1560	69	Mochizuki [1986]
	260	2x10 ¹⁴	250-2500	34	Alaterre [1986]
	248	1x10 ¹⁴	282-539	42	Present work
	532	3x10 ¹³	50-1240	35	Eidmann [1986]
Tungsten	248	1x10 ¹⁴	282-539	47	Present work

Table 5.7: Comparison of conversion efficiencies obtained here with those from other laser systems.

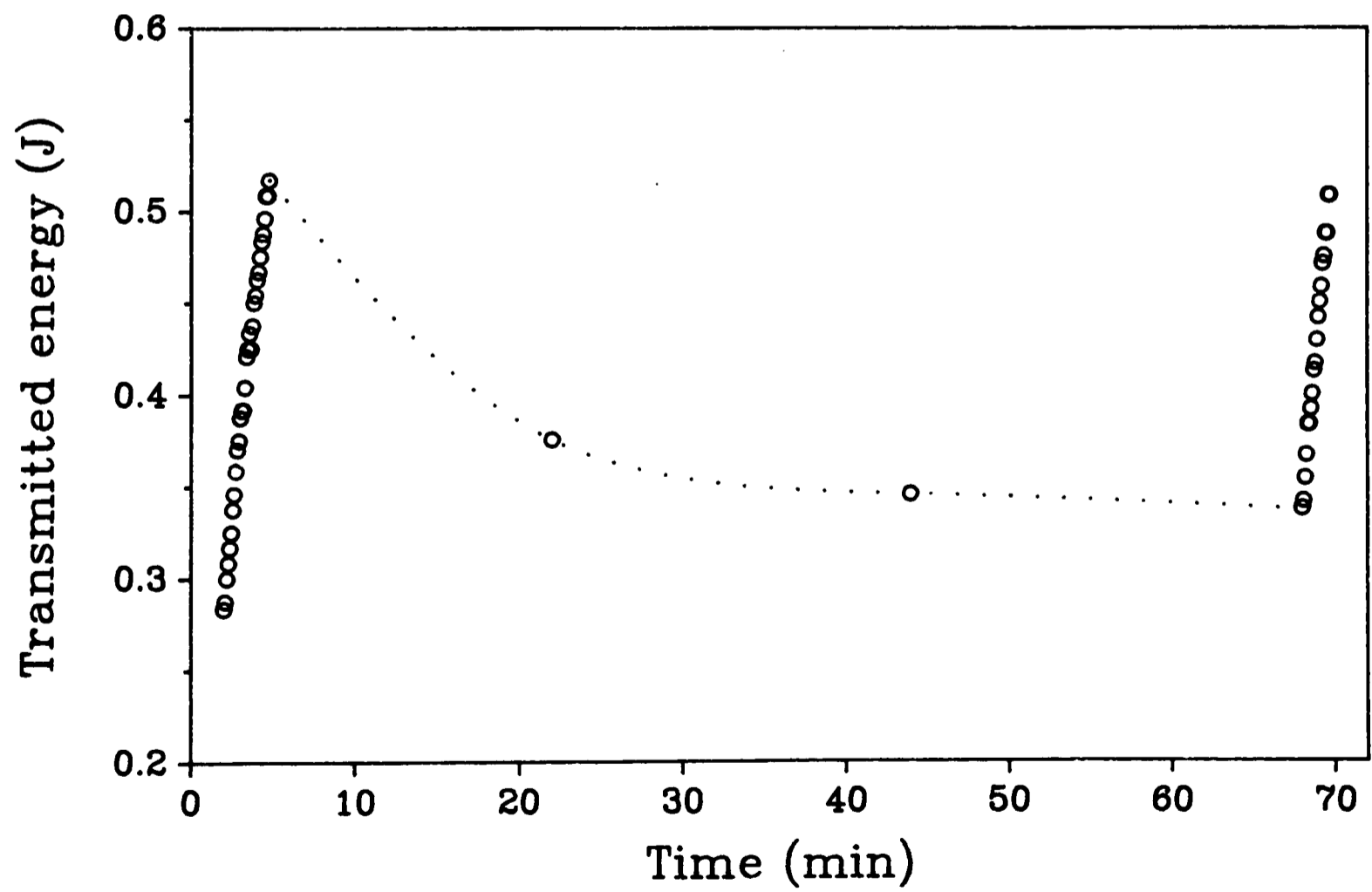
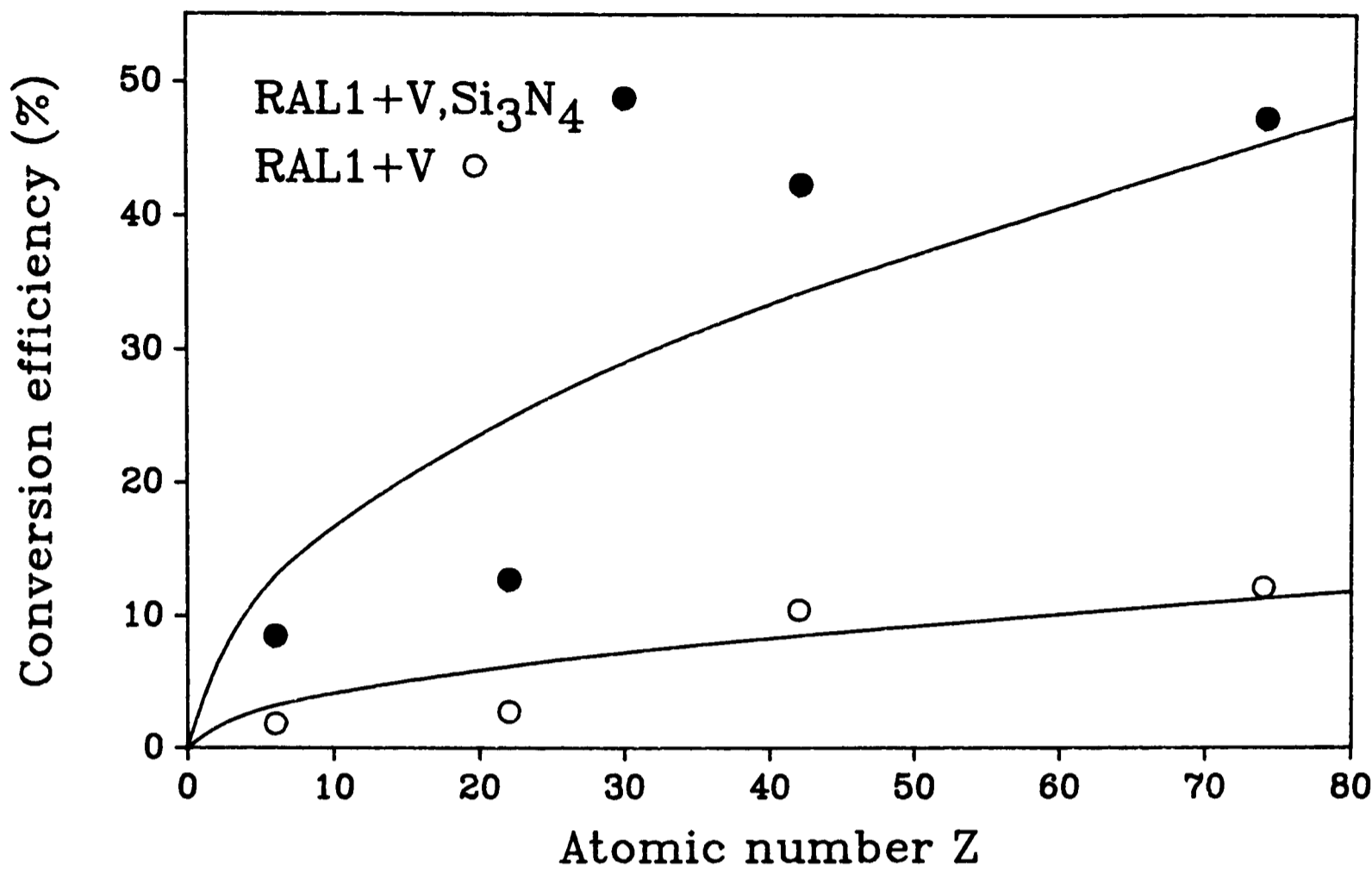


Figure 5.24: The total conversion efficiencies obtained for the four target materials.
Figure 5.25: Laser energy transmitted through the NO₂ cell.

shown by Nagel [1984]), although the increase at energies of over $\sim 1\text{J}$ has not previously been observed. It was felt that the shape of the curve may have been affected by the silica flats used to attenuate the beam; being of unknown quality, they may have adversely affected its divergence and consequently caused a decrease in the efficiency by way of an increase in the focal spot diameter. By this stage, however, it was realized that the problem of low conversion efficiencies was probably the result of the operation of the photodiodes, and their variation with incident energy was not further investigated.

5.14 PINHOLE CAMERA IMAGES OF THE PLASMAS

As indicated in section 2.7.1, the size of the emitting plasma will have an effect on the resolution obtained by the SXCM process by way of penumbral blurring. To evaluate the importance of this effect, the plasmas generated by the four target materials used in the current application were imaged with a pinhole camera under various conditions, but principally those which gave the maximum X-ray yield at 60°

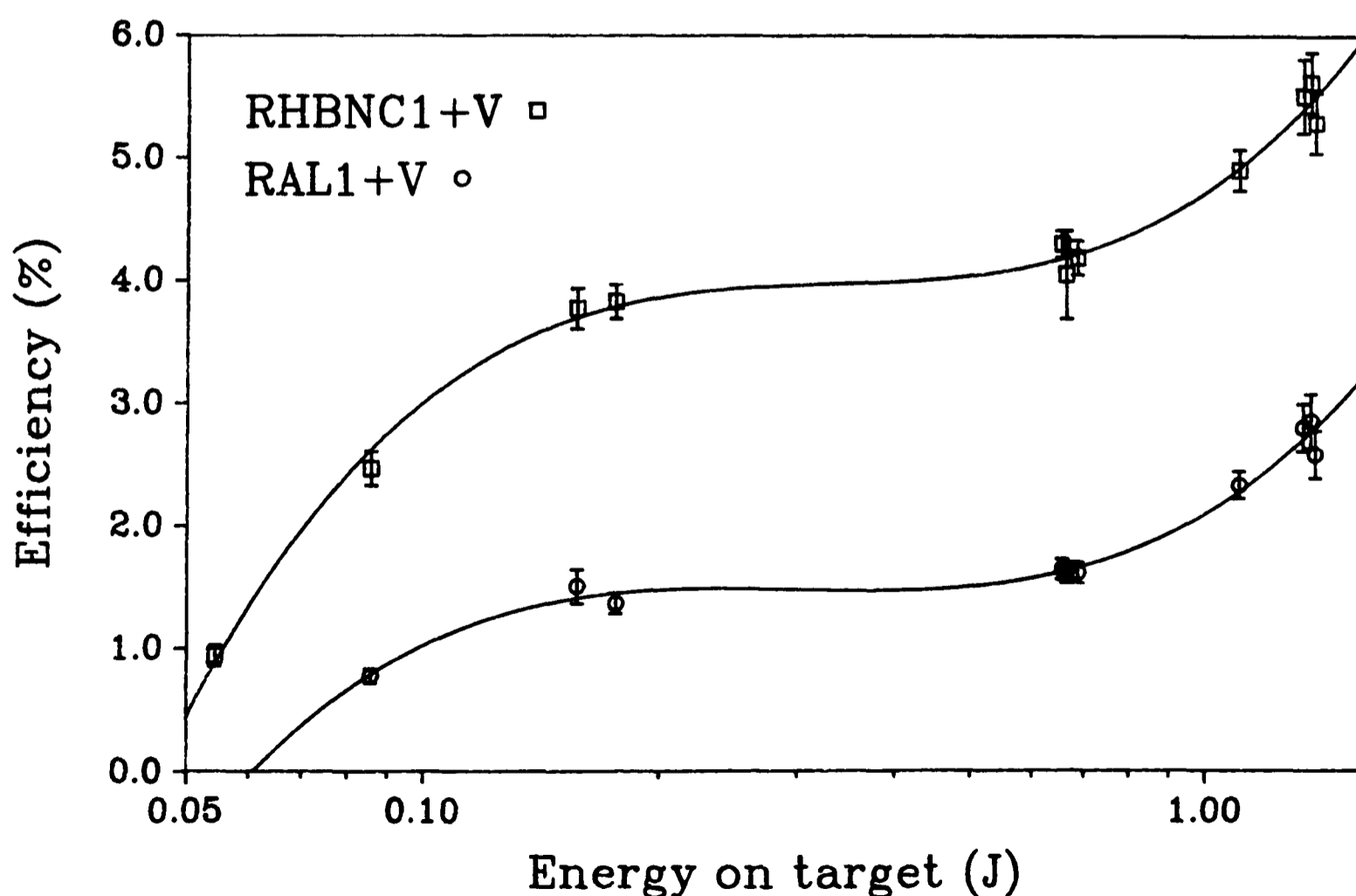


Figure 5.26: Variation in efficiency with incident energy for a tungsten target.

to the laser axis (ie. those which were used for the imaging of biological specimens).

A specially designed 'snoot' was made which could be attached to one of the ports in the target chamber wall and which allowed ~ 10 mm of lateral movement within the port, enabling the axis of the pinhole camera to be aligned with the laser generated plasma. One of the chamber port flanges was used as a film back and attached to the end face of the snoot. A smaller extension tube was fitted to the other end, into which one of a number of brass pinhole holders could be screwed. These are shown in plates 5.3 and 5.4 and the arrangement represented schematically in figure 5.27. Three holders were made; one for use in alignment, one fitted with a $12.5\mu\text{m}$ diameter pinhole and the third with a pinhole and 100nm thick Si_3N_4 window which had been coated with 200nm of aluminium. This latter arrangement transmitted $\sim 30\%$ of the incident water window X-rays but totally eliminated any UV component to which the X-ray film was sensitive. The film used was Kodak type 104-02; as for the recording of the emission spectra, this was developed in accordance with the procedure described by Henke [1984]. For all imaging experiments, the plasma to pinhole distance was 13mm and the pinhole to film distance 327mm, so that a magnification of 25 was obtained.

5.14.1 Results

Pictures of the plasmas obtained from mylar, titanium, molybdenum and tungsten targets, both with and without UV filtering, are shown in plates 5.5 and 5.6. The focal position of the target in each case was that which gave the maximum X-ray flux at 60° to the laser axis. The scratches visible in the pictures are in fact lines of exposure on the film arising from surface abrasions to the emulsion. The film was particularly susceptible to this problem as it did not have the usual protective coating applied to most photographic films since this would have absorbed the soft X-rays. The number of laser shots for each exposure varied from 45 for the mylar plasma (which unfortunately led to some background fogging) to 1 with the tungsten so that each image had approximately the same overall exposure of water window radiation. As expected, comparison between the images taken with and without UV filtering indicates that the region of the plasma which emitted soft X-rays was smaller than the

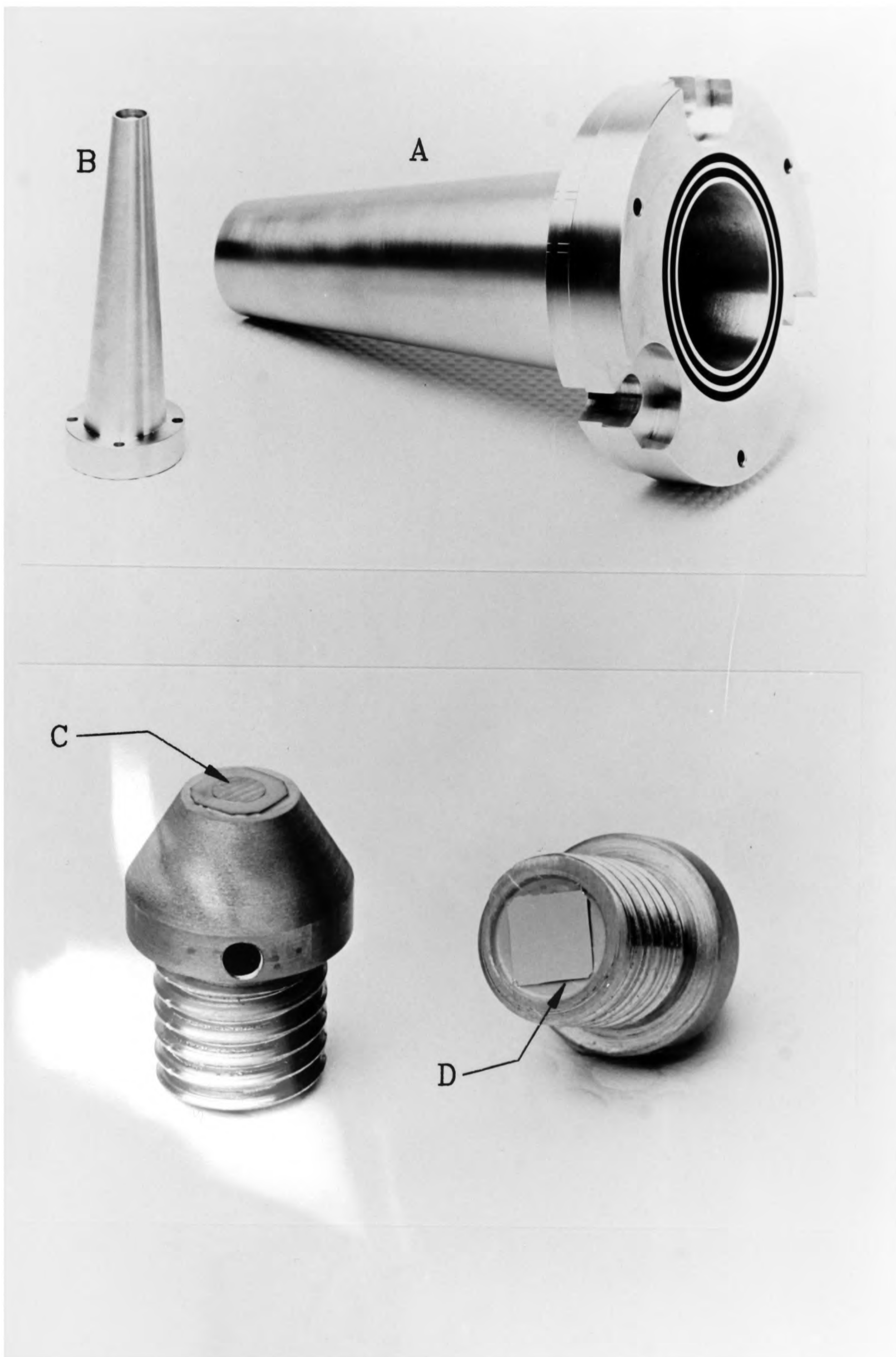
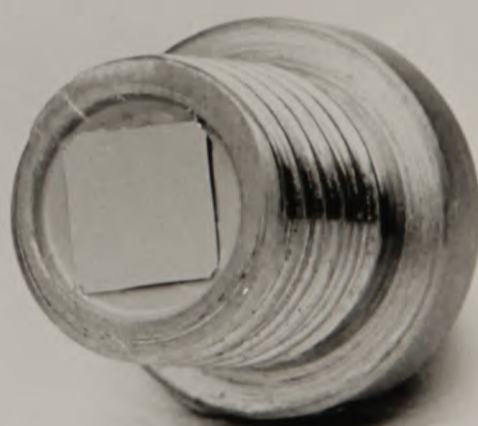
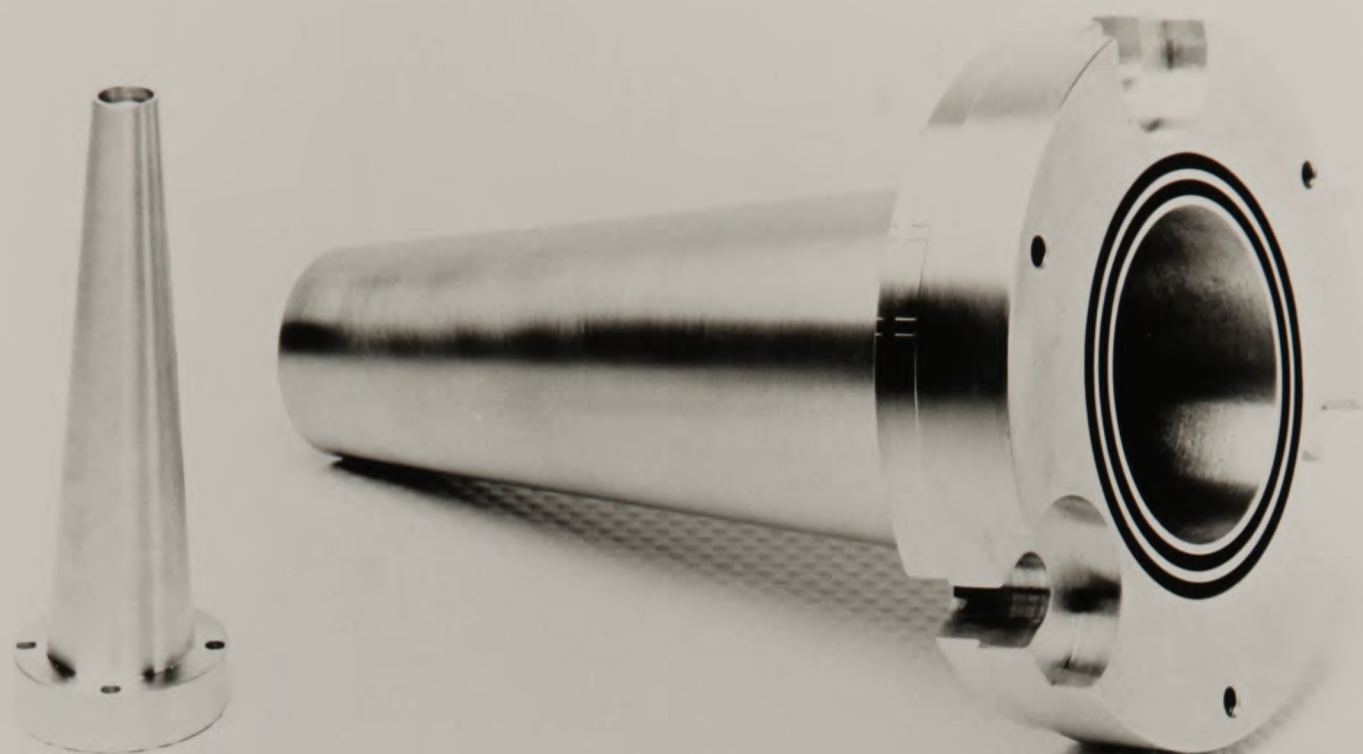


Plate 5.3: The snoot (A) and extension tube (B) used for the pinhole camera.

Plate 5.4: The pinhole holder; pinhole (C) and aluminium coated Si_3N_4 window (D).



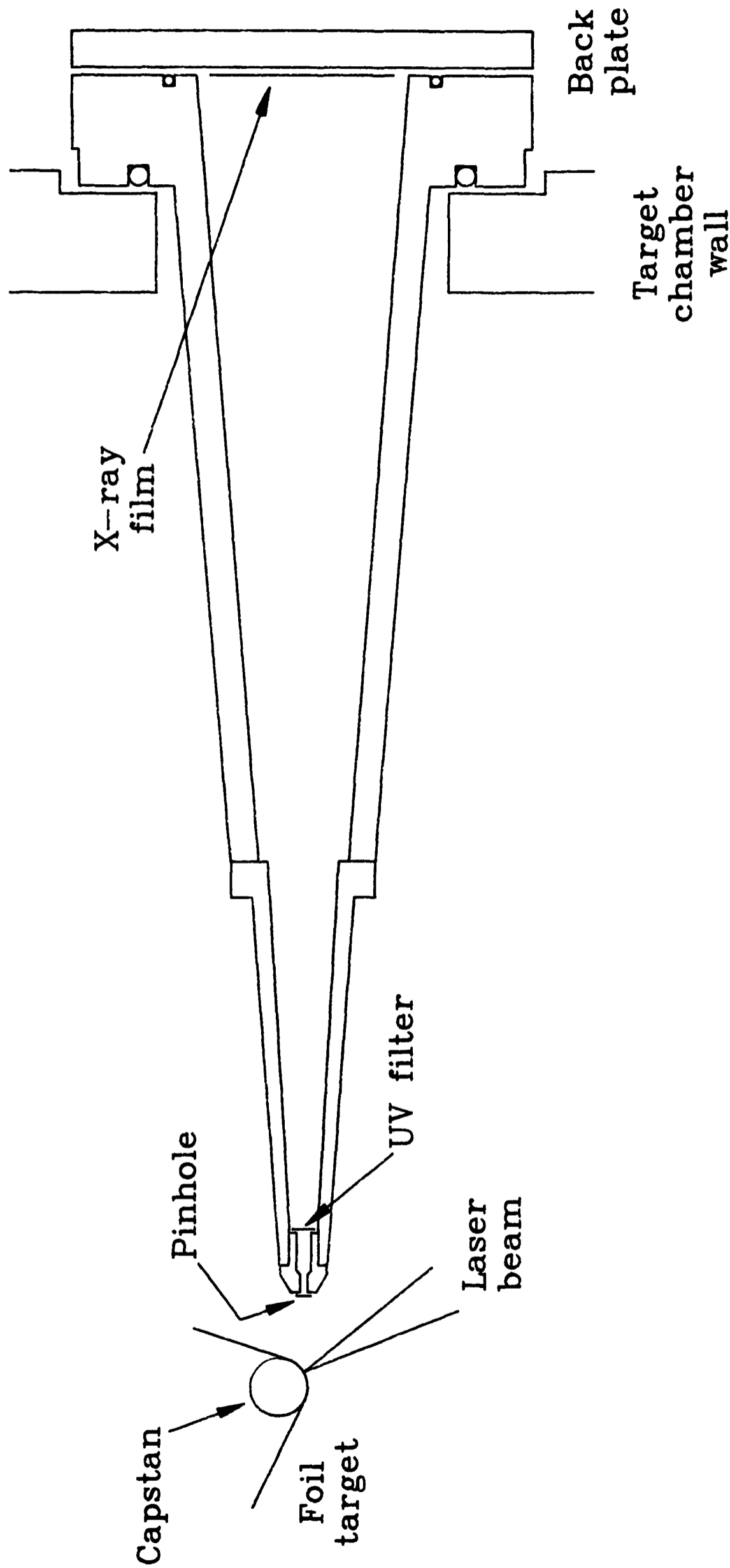
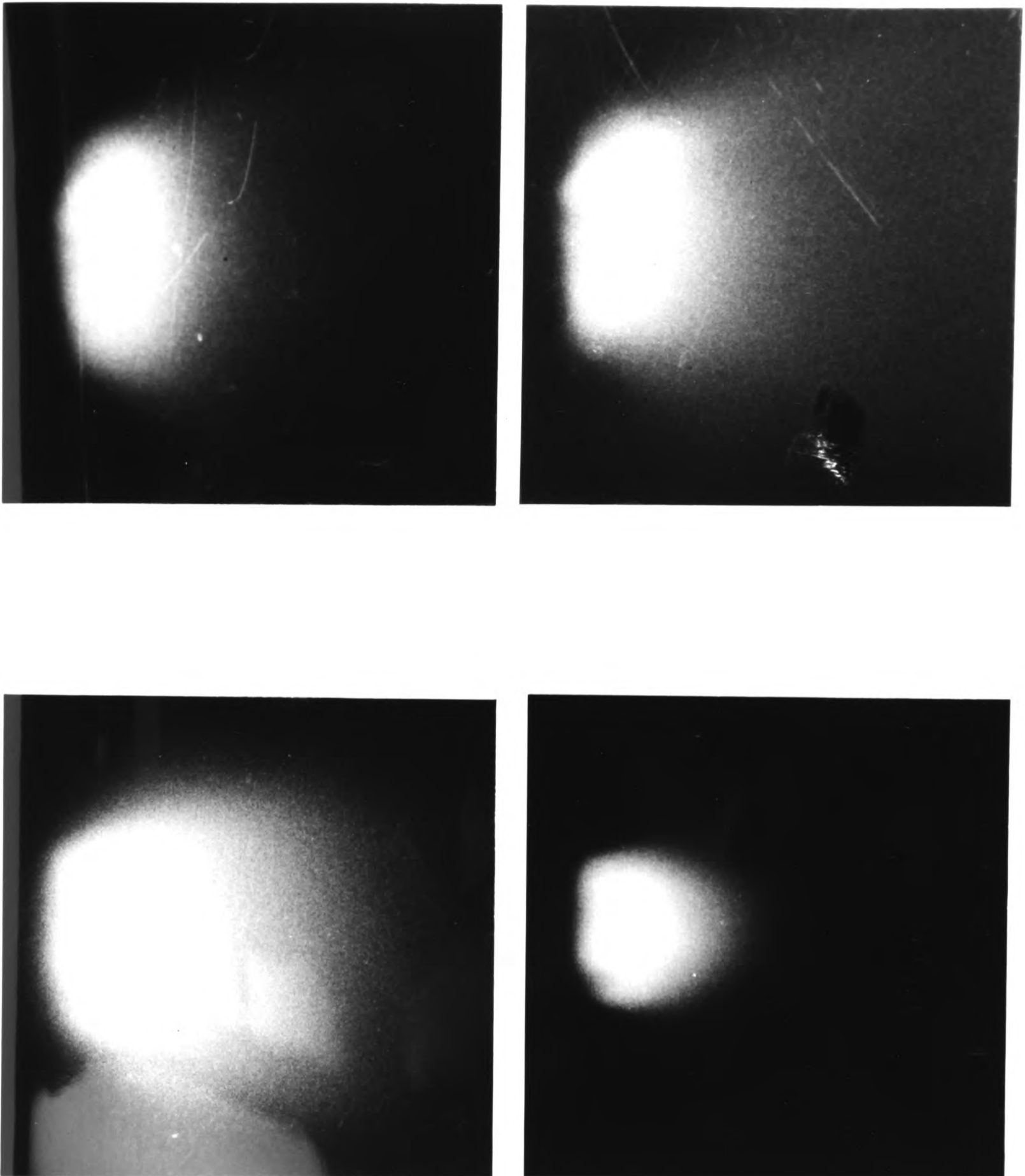
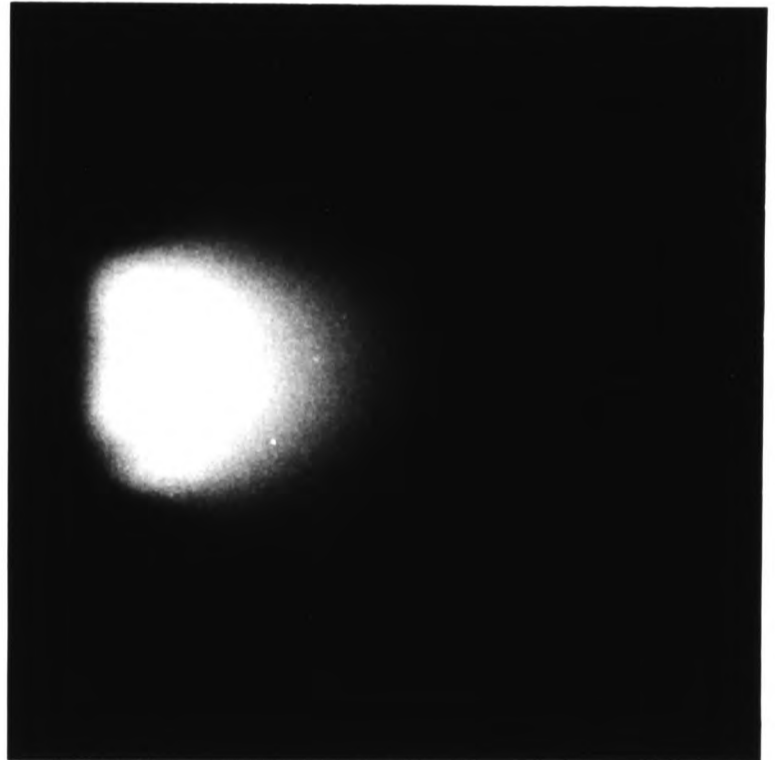
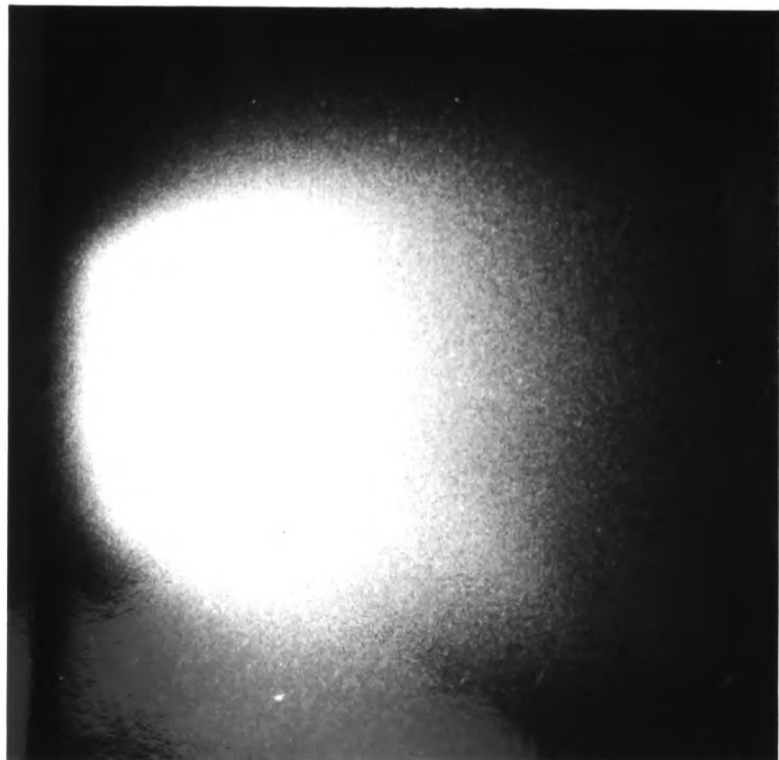
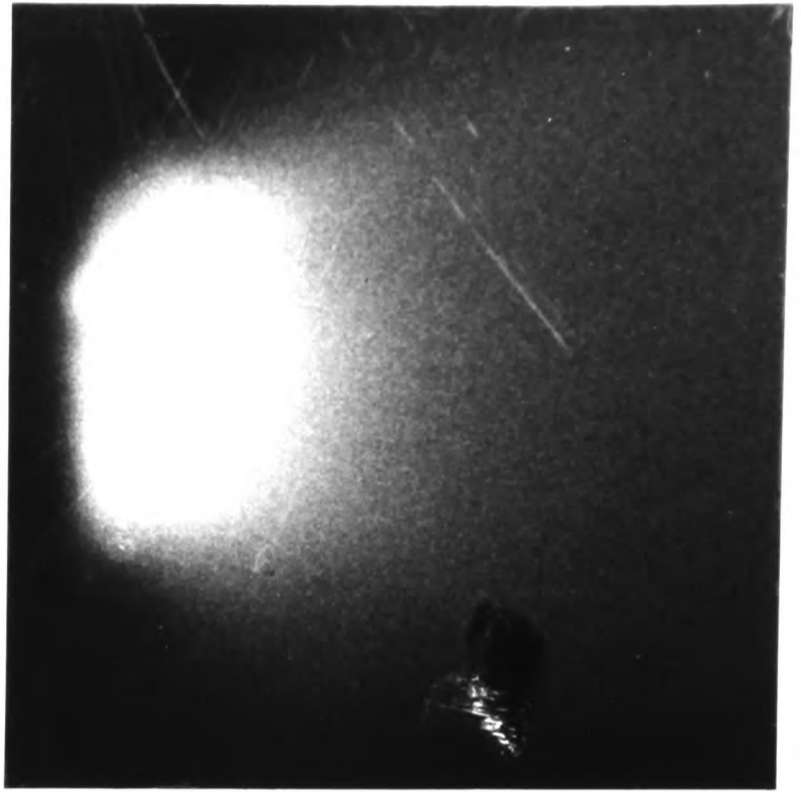
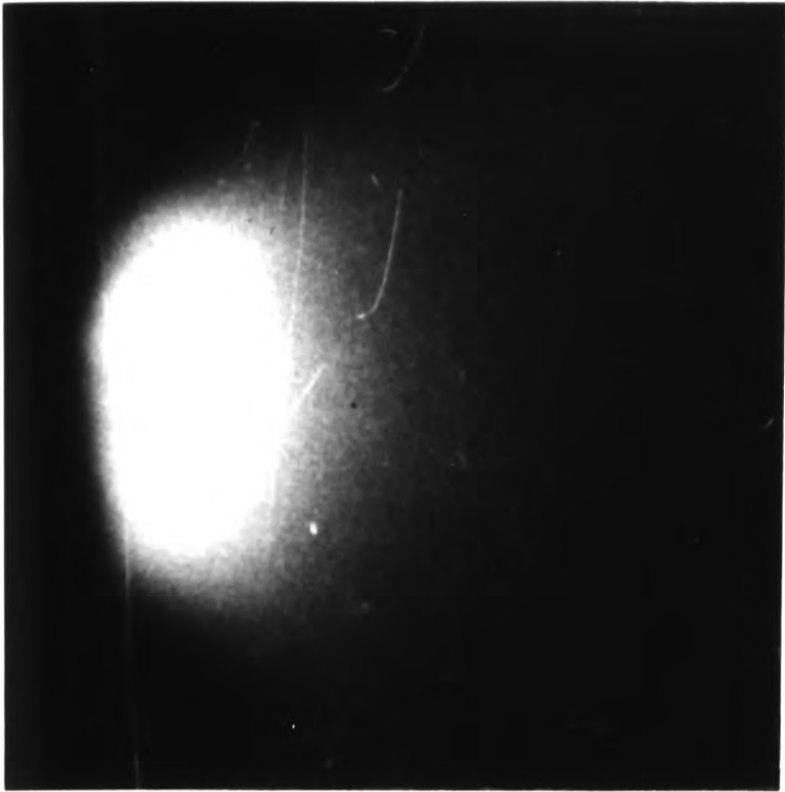


Figure 5.27: Arrangement of the pinhole camera used to photograph the laser generated plasmas.



100 μ m

Plate 5.5: Unfiltered (left) and UV-filtered (right) pinhole camera images of mylar plasmas (top) and titanium plasmas (bottom).



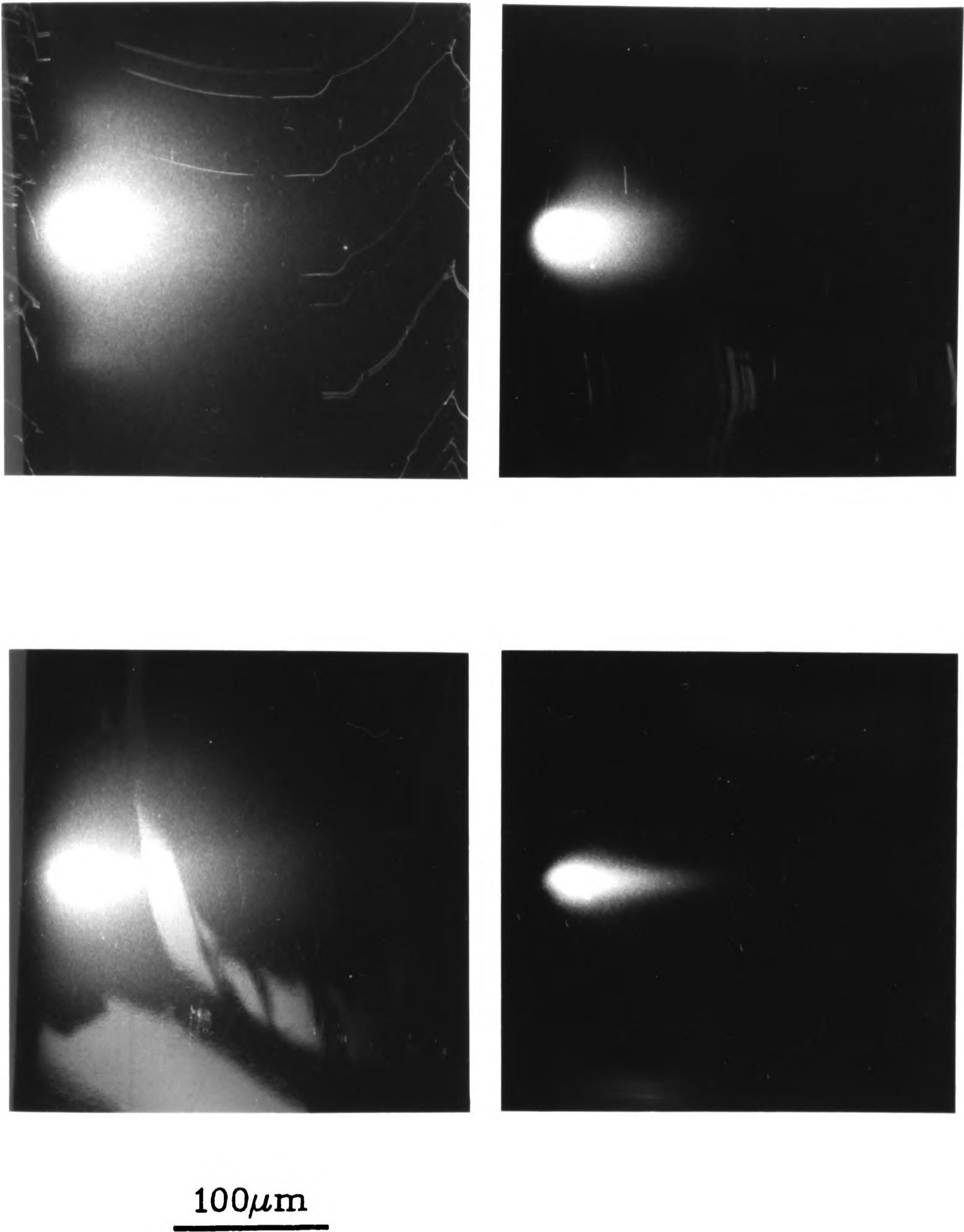
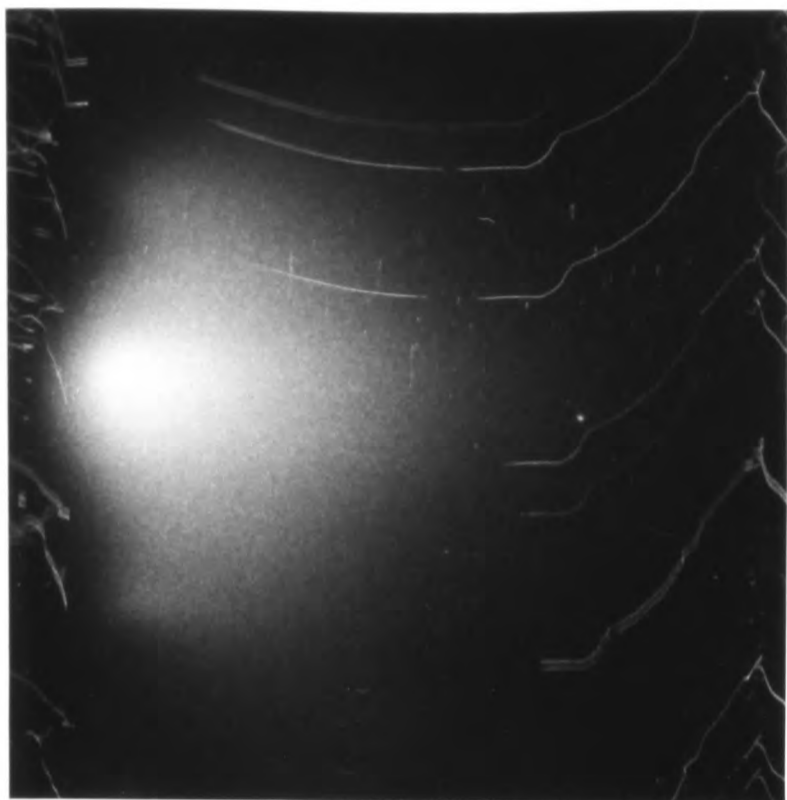


Plate 5.6: Unfiltered (left) and UV-filtered (right) pinhole camera images of molybdenum plasmas (top) and tungsten plasmas (bottom).



overall 'size' of the plasma.

It is also apparent that the plasmas were smaller for the higher Z target materials than for the low Z targets. This arises from the lower intensity threshold for soft X-ray production shown by the low Z elements which meant that X-rays could still be produced when the incident laser beam was focused to a relatively large area on the target surface. This generated a bigger plasma than would have been obtained from a smaller focal spot and lead to a higher emission of X-rays both through this increased plasma volume and through lower radiative losses (which result from the lower temperature of the plasma). For the higher Z materials, the intensity threshold is larger and the surface of the target must be positioned closer to the laser focus to reach this intensity, resulting in the plasmas observed being smaller. Consequently, the soft X-ray emission obtained from molybdenum and tungsten targets is not only larger than that from carbon and titanium by way of larger conversion efficiencies, but it also has the advantage of emanating from a much smaller plasma, thus minimizing the penumbral blurring experienced in the SXCM imaging process. For these two higher Z target materials, the 'size' of the plasma when viewed at 60° to the laser axis was approximately $70\mu\text{m}$ in diameter.

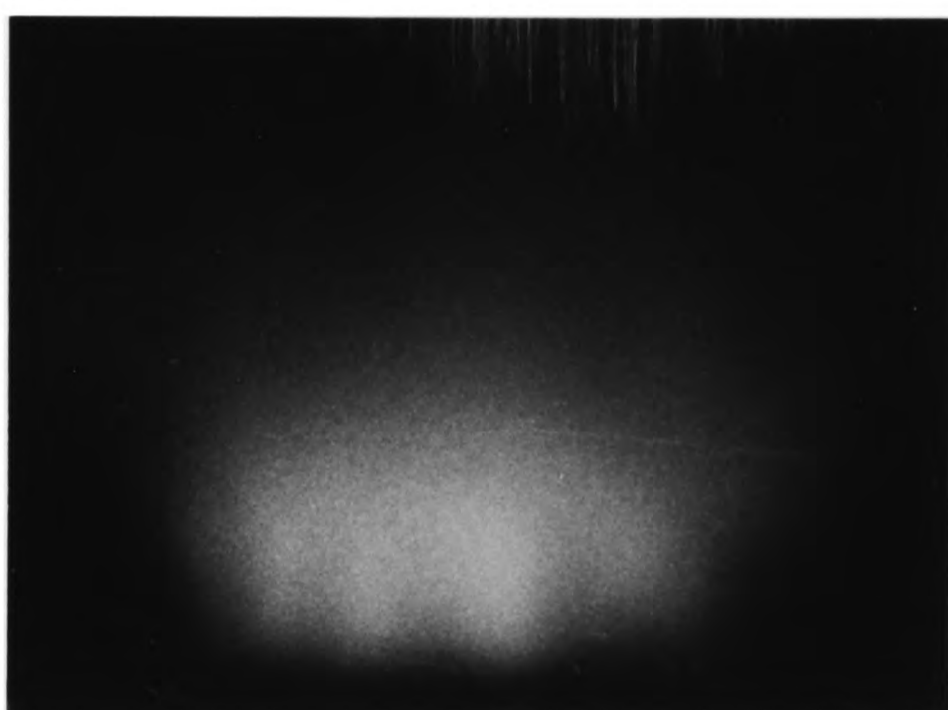
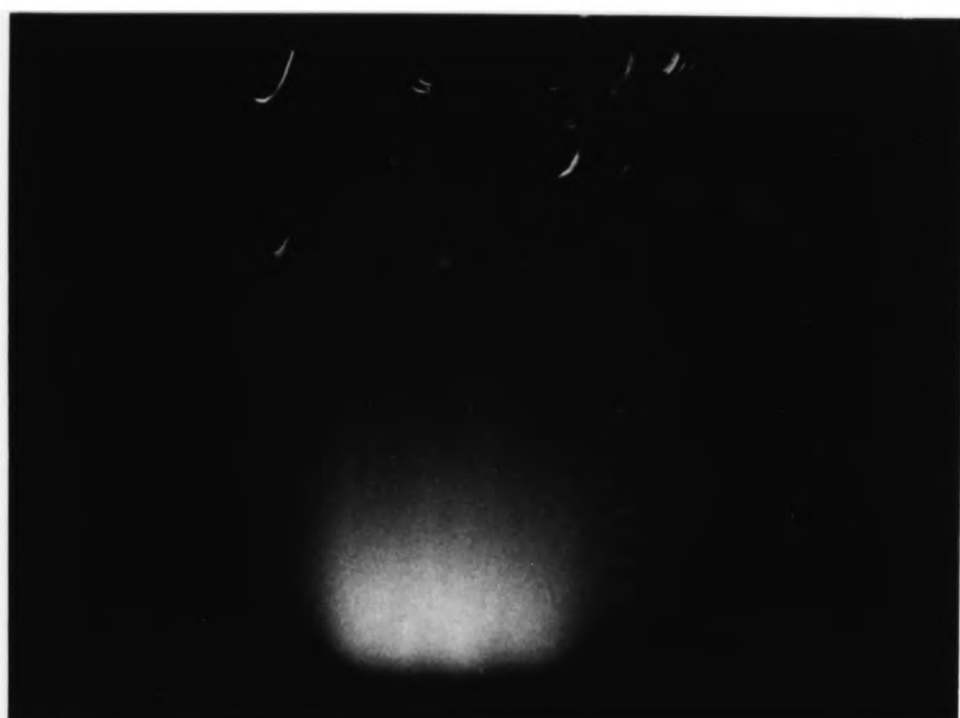
Plate 5.7 shows the unfiltered emission from a mylar target at three focal positions; that which gave the maximum soft X-ray flux (middle image) plus the positions $200\mu\text{m}$ to either side. This illustrates the fact that the optimal position with regard to X-ray emission is not necessarily at the focus of the laser beam, where a small plasma may be generated (as shown in the third image), although moving too far out of focus will result in an incident laser intensity too low to create a plasma of sufficiently high temperature to emit water window X-rays (as is the case in the first image of plate 5.7).

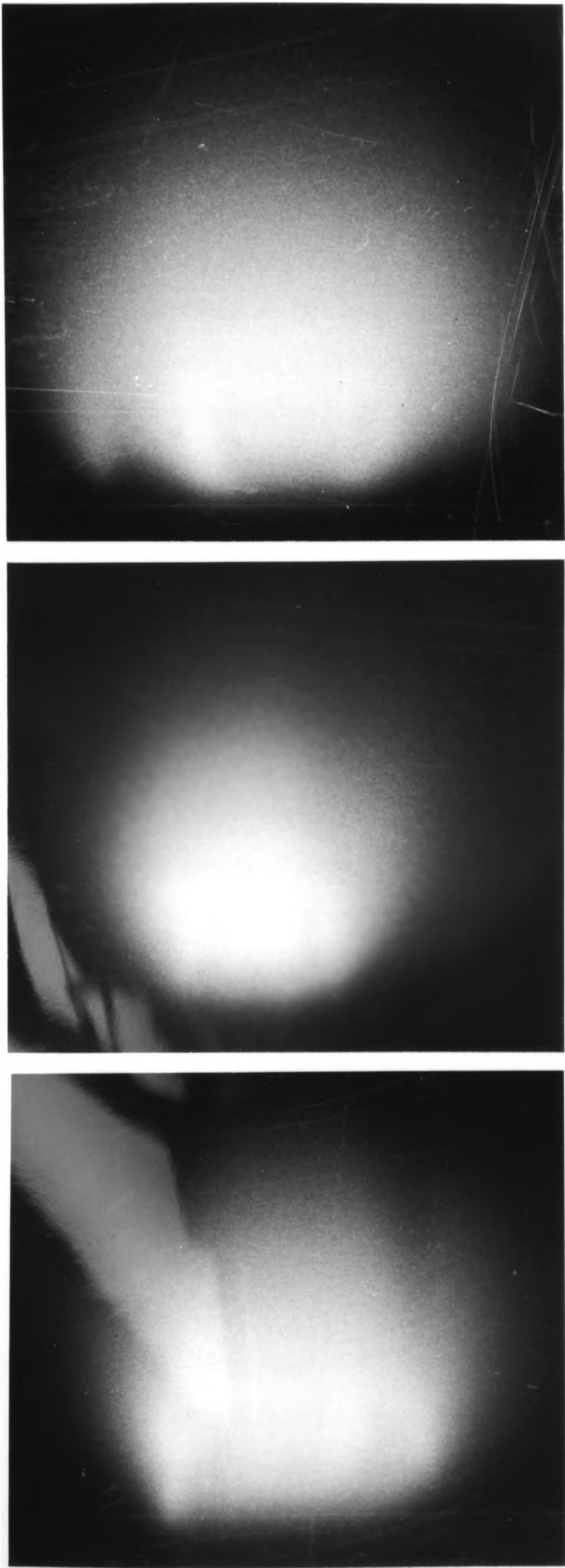
Plate 5.8 shows the unfiltered emission from a molybdenum target at positions of $+360\mu\text{m}$, $-360\mu\text{m}$ and $-720\mu\text{m}$ from that which gave the maximum emission. At such large displacements from the focus of the laser beam, structure is visible within the plasma as large variations in the intensity of the laser beam at the target surface result from the non-uniform intensity profile of the laser output.



100 μ m

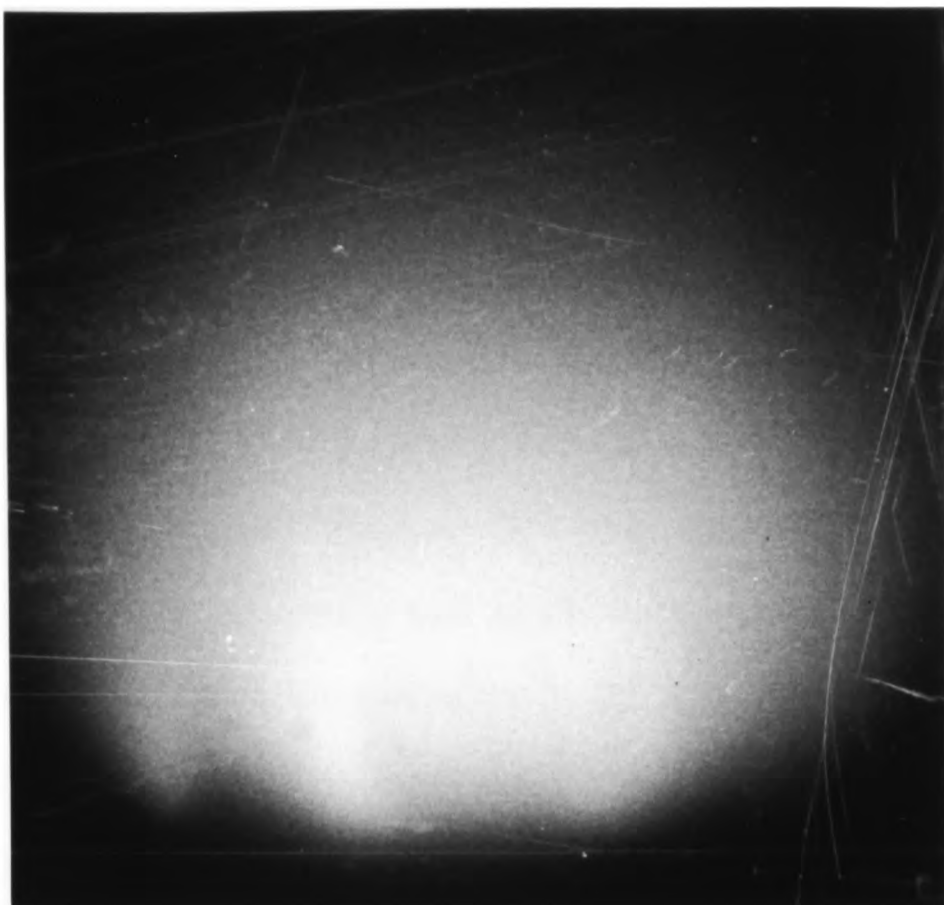
Plate 5.7: Unfiltered pinhole camera images of mylar plasmas at relative positions -200 μ m, 0 μ m and +200 μ m.





100μm

Plate 5.8: Unfiltered pinhole camera images of molybdenum plasmas at relative positions -720 μm, -360 μm and +360 μm.



5.14.2 Estimation of conversion efficiency

In the light of the uncertainty arising from the use of the filtered X-ray photodiodes, an estimation of the conversion efficiency was made from one of the pinhole camera images of a laser generated plasma. The negative of the molybdenum plasma, filtered by 100nm of Si_3N_4 and 200nm of aluminium, was used to obtain a profile of the plasma, as viewed at 60° from the laser axis along that axis. This was converted to an optical density and finally to an intensity, in units of photons/ μm^2 , by use of the calibration curve presented by Henke [1984] and shown in figure 5.28. The Kodak 104-02 film used in the current experiment was taken to have the same characteristics as the 101-07 studied by Henke, save for being only 25% as sensitive. The resultant profile is given in figure 5.29. Assuming an aspect ratio of ~ 2 and an average X-ray wavelength of 3nm, this suggested that $E_n = 1.22 \times 10^{-9} \text{ J}$ had gone to the formation of the image in this particular negative. With a pinhole of diameter d at a distance s from the plasma, this gives a conversion efficiency of incident laser radiation E_i into soft X-rays of

$$\eta = (E_n/E_i) 2\pi(2s/d)^2(1/F) \quad [5.40]$$

where F represents the average transmission of the filter over the water window wavelength range. For the aluminium coated Si_3N_4 window, this has a value of 0.33. Since 3 laser shots were used to register the image, this implies $\eta E_i = 3.35\% \text{ J}$ which compares to a value of $\eta E_i = 3.08\% \text{ J}$ from the measurement made with the RAL1 photodiode and the mylar-supported $0.5\mu\text{m}$ vanadium filter. That is to say, the conversion efficiency calculated from the exposure of the film is approximately equal to that suggested by the X-ray photodiode, lending some support to the absolute accuracy with which X-ray fluxes were able to be measured by the use of this type of device.

5.15 APPLICATION OF ELECTRIC FIELDS TO THE PLASMA REGION

There have been several reports (Farkas [1977], Dinev [1979] and Hontzopoulos [1988]) that the application of a large static electric field to the region of a laser generated plasma may lead to a very large increase in the emitted radiation. By

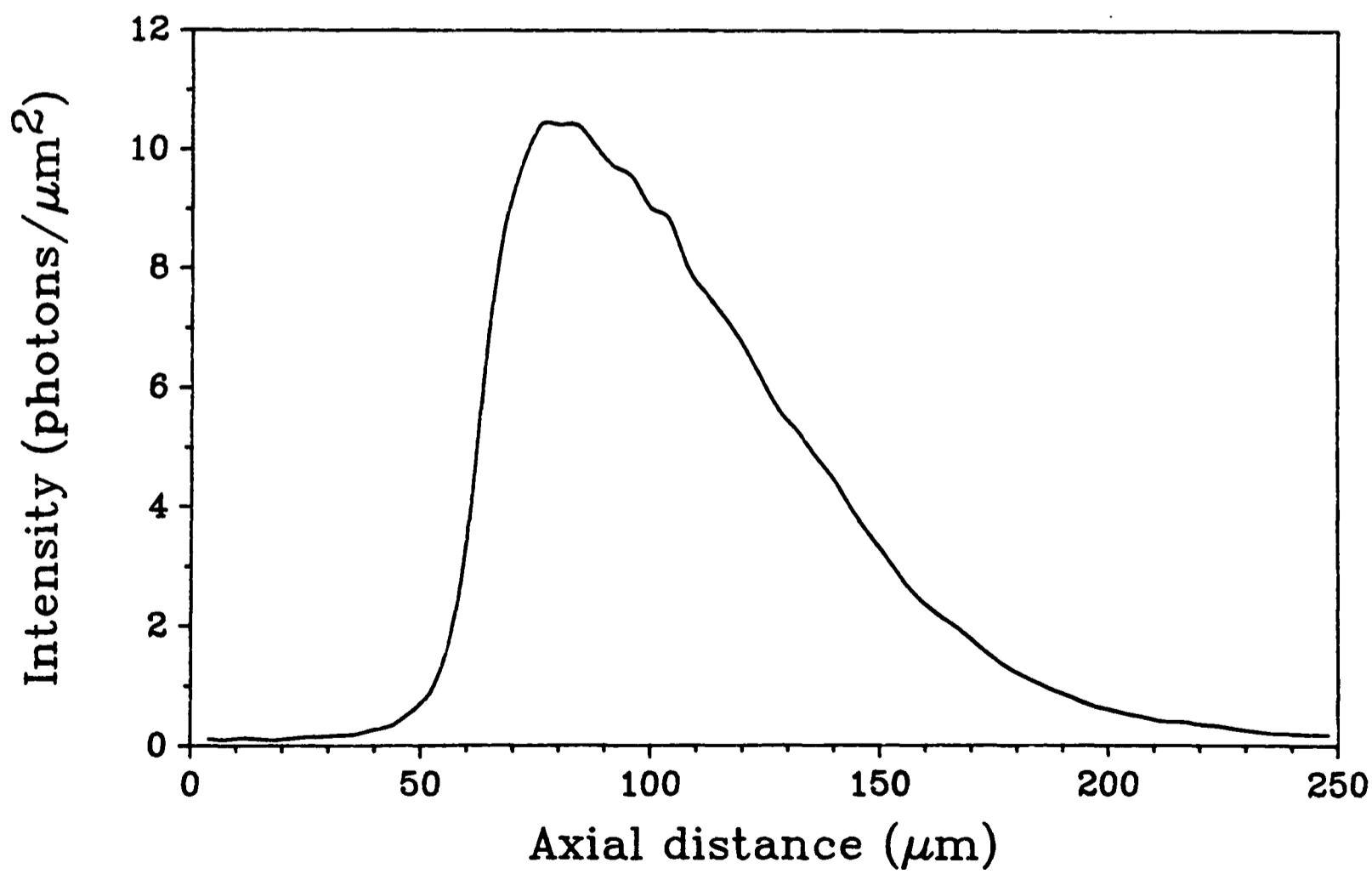
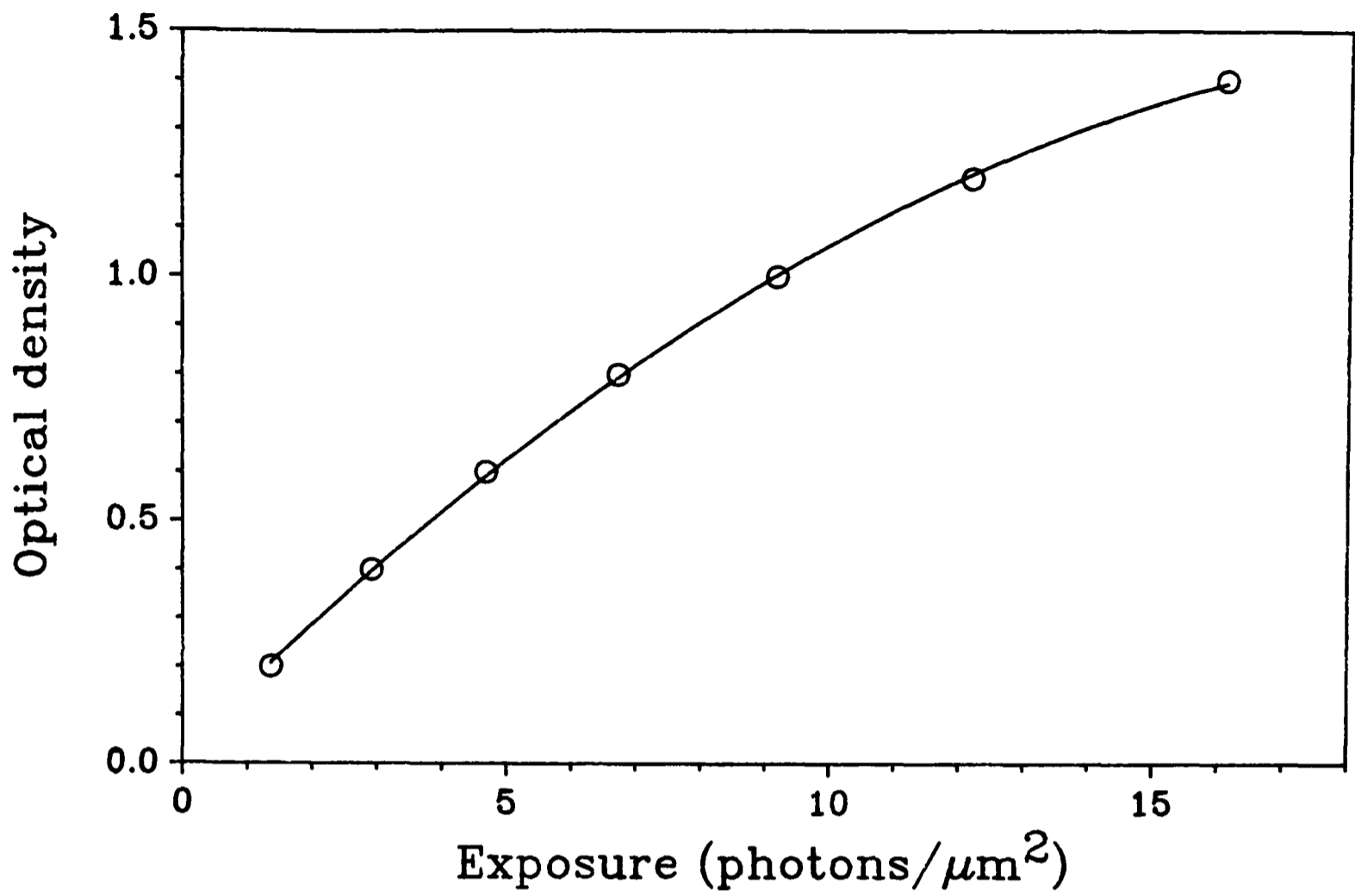


Figure 5.28: Exposure characteristics of the Kodak 104-02 X-ray film.

Figure 5.29: Intensity profile of the pinhole camera image of the molybdenum plasma.

earthing a planar gold target and applying a static field of -25kV/cm to the plasma region, Farkas [1977] claimed an increase in X-ray emission by a factor of 10^3 over that obtained in the absence of any electric field. The laser source used was a train of picosecond pulses from a Nd:glass laser, of unspecified number or energy. Consequently, the conversion efficiency of laser to X-ray energy remains unknown and the possible causes of the observed increase were not discussed. Dinev [1979] limited measurements to those of the current flow between the laser target and the electrode, but nevertheless once again claimed an increase in X-ray flux by 'several orders of magnitude'. Hontzopoulos [1988] measured increases by factors of up to 20 in the UV emission of a plasma created by focusing $\sim 10\text{mJ}$ of KrF laser radiation onto a gold target, when a negative field of $\sim 15\text{kV/cm}$ was applied, relative to the target. It was suggested that this effect arose from the increased recombination probability which resulted from the plasma electrons being repelled by the electrode back into the plasma region.

It was therefore decided to investigate the effect of such an electric field on the plasma region of the current arrangement. A copper electrode was made, consisting of a 1mm thick disk of outside diameter 10mm. A 5mm diameter hole was drilled centrally in the disk to facilitate the passage of the laser beam on to the target, and it was then mounted on a copper rod. The rod was covered with an insulating Perspex sheath and the majority of the copper disk was covered with a Perspex cement (Simplex), in an attempt to prevent electrical breakdown to other components in the vacuum chamber. The cement was removed from the inside of the disk such that only the inside surface of the 5mm hole was exposed; the arrangement is shown in figure 5.30. A 30kV power supply was connected to the end of the supporting copper rod via a vacuum feed-through in the chamber wall. A diffusion pump was also attached to the chamber to enable a pressure of 10^{-3} torr to be reached, thus discouraging electric breakdown between the electrode and the wire target.

The electrode was then placed on the axis of the incident laser, a distance of 5mm from the target, at a potential of 6kV. With this arrangement and using a tungsten wire target, no increase in X-ray yield was observed for either polarity of the

voltage or at any of the detector angles permitted by the configuration of components within the target chamber (ie. 30° to 80°).

This failure to record any increase in the X-ray flux was probably due to the plasma generated in the current application being of sufficient density that the recombination probability for the emitted electrons was already high, and could not be further increased by the effect of an applied electric field. Certainly an increase by a factor of 20, as observed by Hontzopoulos [1988] would not have been possible, and it may well have been the case that the plasmas generated by Dinev [1979] and Hontzopoulos [1988], using only 1mJ and ~ 10 mJ on target respectively, were of much lower density than those obtained with ~ 1400 mJ on target in the current application. In the former cases, the electron recombination probability was probably very low and thus liable to benefit from the applied electric field.

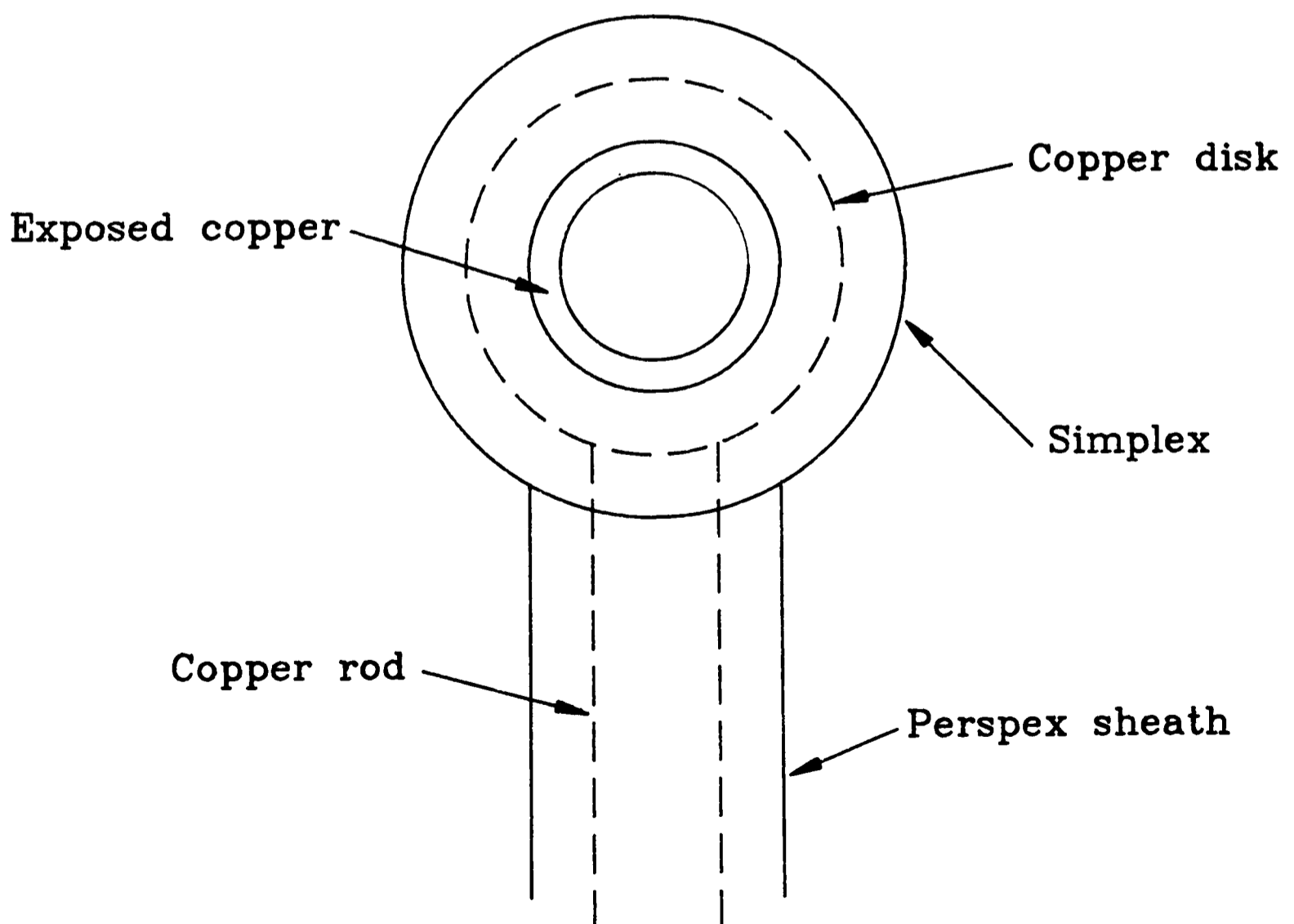


Figure 5.30: The static electric field electrode.

5.16 CONCLUSIONS

From the various measurements made on the laser generated plasmas, it was apparent that the use of a molybdenum or tungsten wire target was the most suitable for the application of SXCM simply by virtue of these resulting in the largest fluxes of water window X-rays of the four target materials investigated. However, the spectra recorded in section 5.9 suggest that the plasmas generated by both of these target materials emit a significant amount of radiation outside the water window. As explained in section 2.7, this will have an adverse effect on the quality of image obtained by the SXCM process. As mentioned previously, the use of a grazing incidence grating to record the spectra is preferable to the transmission grating used here, and it is hoped to make use of such a grating in the near future. It was also evident that the accurate measurement of soft X-rays is by no means a straightforward task. Since the manufacturers of the photodiodes used in the measurements were unable to explain the apparent discrepancies in the signals generated by nominally identical units, the values given for fluxes in this chapter can only be regarded as self consistent. However, estimates of the conversion efficiency made from the pinhole image of a molybdenum plasma, in addition to the calculated efficiencies of section 5.12 do provide a means for comparison with the results published elsewhere. Finally, the measured dissolution rates of exposed PMMA of section 7.3 compare favourably with similar values obtained for resists exposed to equal doses of X-rays by other workers. Irrespective of these problems, the final aim of the investigations described in this chapter was met in that a plasma of sufficient brightness to enable the image of a wet biological specimen to be recorded in the photoresist in a single shot could be generated by the suitable choice of target material and plasma conditions.

CHAPTER SIX

X-RAY OPTICS

6.1	INTRODUCTION
6.2	ZONE PLATES
6.2.1	Resolving power of a zone plate
6.2.2	Collection efficiency
6.3	MULTILAYER MIRRORS
6.4	GRAZING INCIDENCE OPTICS
6.4.1	Kirkpatrick-Baez mirrors
6.4.2	Tapered capillaries
6.4.3	Ellipsoidal mirror
6.4.4	Wolter Type I mirror
6.4.5	Fabrication techniques
6.4.6	Absorption losses at reflection
6.5	USE OF X-RAY OPTICS
6.5.1	Results
6.6	CONCLUSIONS

6.1 INTRODUCTION

Initially, the X-ray flux falling onto the front face of the specimen holder was maximized by bringing it as close as possible to the plasma region at the surface of the target wire. For example, the initial test images of dry diatoms taken by Cotton [1990] were produced with a wire to specimen distance of 21mm and wet cell imaging was subsequently carried out at a separation of between 6mm and 9mm. Tomie [1991] has used a working distance of 6mm in his study of sea urchin sperm using a contact imaging technique similar to that described in chapter 7. Although this has been the arrangement for all contact microscopes currently in operation, this method of flux collection suffers from several drawbacks and limitations:

a) The specimen holder may not be brought so close to the wire target that it obscures the incoming laser beam. Even when the plasma to specimen distance was reduced to 9mm, for example, the solid angle subtended by the $1 \times 1 \text{mm}^2$ entrance window of the specimen holder was still only

$$\begin{aligned}\Omega &\sim 4\pi(1^2/4\pi.9^2) \\ &= 2\pi/570\end{aligned}\quad [6.1]$$

which shows that less than 0.2% of the total X-ray flux emitted by the plasma was used to illuminate the specimen.

b) As the plasma to specimen distance, d , decreases, so the effect of penumbral blurring increases (considered in section 2.7.1). With a $1\mu\text{m}$ thick specimen and $d=9\text{mm}$ as before, this gives $\Delta_p\sim 110\text{nm}$ per millimetre of plasma size. Although plasma sizes of up to 1mm have been reported [Nagel 1984], the plasma diameter in the current application was measured to be $\sim 70\mu\text{m}$ (as shown in section 5.14.1).

c) The problem of debris damage to the specimen increases as it is brought closer to the plasma. This includes breakage of the Si_3N_4 entrance window and damage to the PMMA recording resist, both of which are obviously undesirable in a working microscope system.

In an attempt to overcome these difficulties, the use of an X-ray focusing optic to greatly increase the flux incident on the specimen was investigated. Such an increase would allow specimens of greater thicknesses or carbon densities than previously possible to be studied with the technique. It would also enable investigations to be made on the effect of X-ray filtering on the image quality obtained in the resist (a process which hitherto has not been fully investigated in conjunction with the SXCM technique). For example, measurements made on the dissolution rates of PMMA in section 7.3 indicate that any UV or VUV component in the radiation incident on the resist will make a significant contribution to its exposure (and consequently, its rate of dissolution in MIBK) while leading to a decrease in resolution by means of increased Fresnel diffraction and decreased contrast (described in sections 2.7.2 and 2.7.1). These long wavelength components may be removed by a 100nm thick layer of aluminium, evaporated onto the surface of the Si_3N_4 window, but with the current system, such filters also reduce the soft X-ray component to a level insufficient for satisfactory image formation. Large increases in flux would also lead to a higher resolution being obtained in the final image as a result of improved dosage statistics, as considered in section 2.7.3. Ultimately, it might also greatly reduce the specification requirements

(in particular, the output energy) of the laser used to generate the plasma through more efficient use of those X-rays which are produced to an extent where the performance of a commercially available excimer laser would be sufficient to enable single shot imaging of wet biological specimens.

Since refracting systems are not practicable for X-ray wavelengths, due to the excessive losses which would be experienced through absorption by the material of the lens, the use of optical components has in the past had to rely on zone plates, multilayer or grazing incidence mirrors, each of which is now considered in terms of suitability for use in the Oxford microscope system.

6.2 ZONE PLATES

Much research has been carried out in the field of zone plates for use with X-ray radiation, concentrating on the fabrication of components which permit the very tight focusing of incident fluxes (as described in Michette [1992] for example). These are used in scanning X-ray microscope systems in conjunction with continuous synchrotron sources, where the resolution of the microscope is ultimately limited by the spot size to which the X-rays may be brought to focus. This dimension is approximately equal to the thickness of the outer ring of the zone plate. Coupled with their low efficiencies at these wavelengths, the considerable technical difficulties of producing relatively large structures with outer zone thicknesses of $<100\text{nm}$ has had to be addressed. Furthermore, the focal length of any zone plate is inversely proportional to the wavelength of the incident radiation, leading to extensive chromatic aberration. Nevertheless, we now consider the process by which zone plates act to focus incident radiation, and their performance as condensers, as would be required for the present application.

Initially, we study the propagation of a spherical monochromatic wave, emitted from a point source S. Using the Huygens-Fresnel scalar diffraction theory modified by the Kirchoff inclination factor ($K(\theta) = \frac{1}{2}[1 + \cos(\theta)]$ where θ is the angle between the normal to the primary wavefront and the point of observation), we should be able to sum the secondary wavelets arriving at a point of observation, P, to obtain the

unobstructed primary wave. With reference to figure 6.1, we have the spherical surface of the primary wavefront, at a time t after it has been emitted by S . We represent the disturbance by

$$E = (\epsilon_0/\rho)\cos(\omega t - k\rho) \quad [6.2]$$

We choose to consider the surface as a number of annular regions, corresponding to its intersection with a series of spheres, centred on P , of radii $r_0 + \lambda/2$, $r_0 + \lambda$, $r_0 + 3\lambda/2$, etc. Each is called a Fresnel, or half period, zone. Since ρ is constant for all points on the primary sphere, we assume that the point sources in all zones radiate in phase with each other. Secondary wavelets travel a distance $r = r_0 + n\lambda/2$ to reach P at a time t , with phase $\omega t - k(\rho + r)$. Considering a thin annulus of area dS , in the m th zone, its contribution to the optical disturbance at P will be

$$dE = K(\theta)(\epsilon_a/r)\cos\{\omega t - k(\rho + r)\}dS \quad [6.3]$$

where

$$\epsilon_a = Q\epsilon_0/\rho \quad [6.4]$$

ϵ_0/ρ is the amplitude of the primary wave, and Q a constant to be determined. From figure 6.2, we see that

$$dS = \rho d\phi \cdot 2\pi\rho\sin(\phi) \quad [6.5]$$

$$r^2 = \rho^2 + (\rho + r_0)^2 - 2\rho(\rho + r_0)\cos(\phi) \quad [6.6]$$

and so, by differentiation

$$2rdr = 2\rho(\rho + r_0)\sin(\phi)d\phi \quad [6.7]$$

$$dS = 2\pi\rho r dr / (\rho + r_0) \quad [6.8]$$

Consequently, the disturbance at P from secondary wavelets originating from the m th zone will be

$$E_m = 2\pi K_m \epsilon_a \rho (\rho + r_0)^{-1} \int_{r_{m-1}}^{r_m} \cos\{\omega t - k(\rho + r)\}dr \quad [6.9]$$

We have assumed that K_m is constant over the region of each Fresnel zone. From the definition of $K(\theta)$, we may readily see that

$$K(r) = (r + r_0)(r_0 - r - 2\rho)/4r\rho \quad [6.10]$$

and therefore

$$K_m = (2r_0 + m\lambda/2)(2\rho - m\lambda/2)/4\rho(r_0 + m\lambda/2) \quad [6.11]$$

Since $r_0 \gg \lambda$ and $\rho \gg \lambda$, the value of K_m/K_{m-1} will be approximately equal to 1 for any value of m , even where $r_0 \sim m\lambda$ or $\rho \sim m\lambda$. Therefore,

$$E_m = (-1)^{m+1} \cdot 2K_m \epsilon_a \rho \lambda (\rho + r_0)^{-1} \sin\{\omega t - k(\rho + r_0)\} \quad [6.12]$$

as

$$r_m = r_0 + m\lambda/2 \quad [6.13]$$

Note that $|E_m/K_m|$ is independent of m , the number of the zone under consideration. If we consider q zones, then the disturbance at P will be

$$E = \sum_{n=1}^q E_n \quad [6.14]$$

If the primary wave were to propagate from S to P directly, in time t , then it would

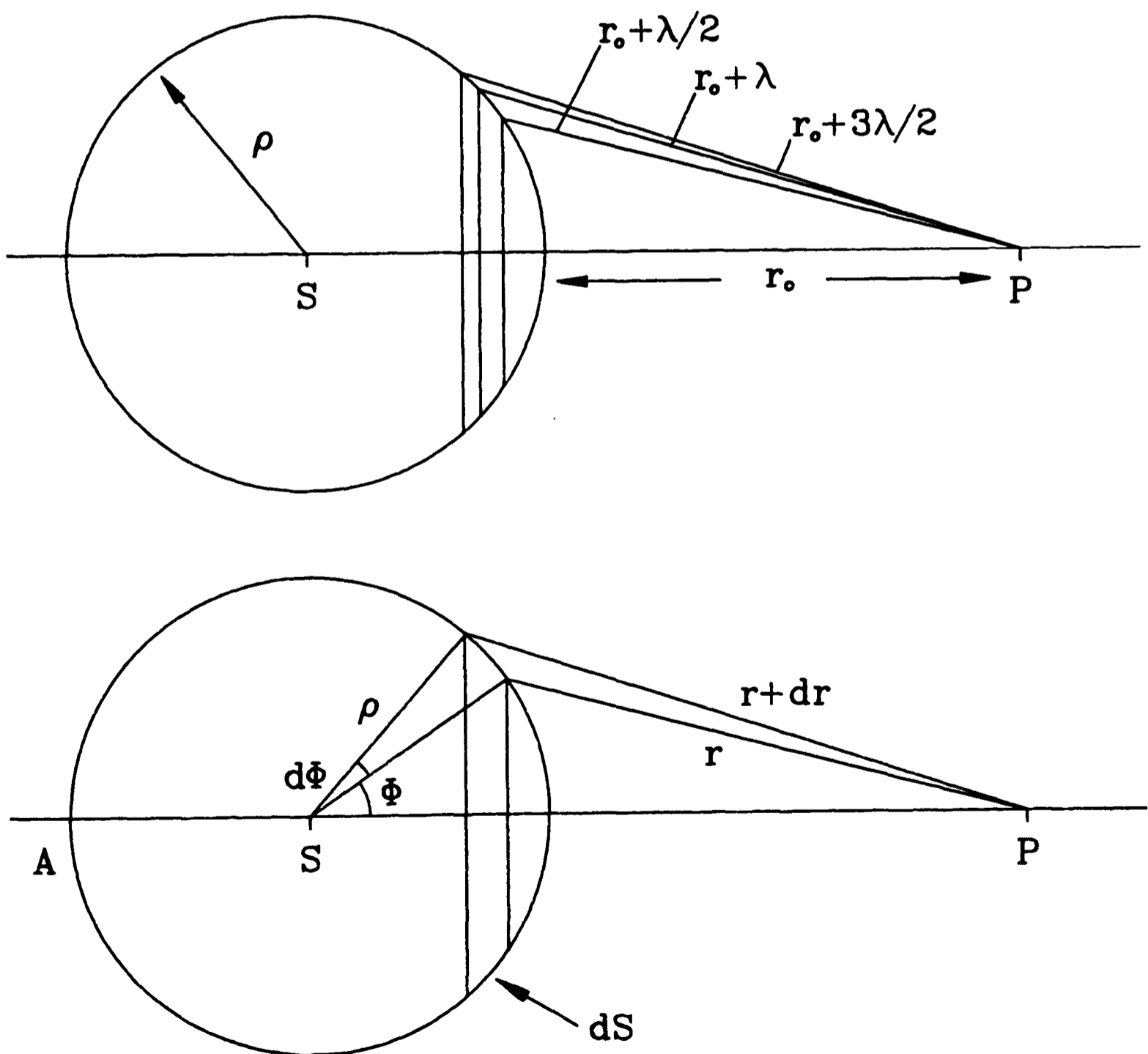


Figure 6.1: The Fresnel zones and associated parameters.

Figure 6.2: The contribution of a thin annulus to the focal intensity.

have the form

$$E = \epsilon_0(\rho + r_0)^{-1} \cos\{\omega t - k(\rho + r_0)\} \quad [6.15]$$

To evaluate the total disturbance from secondary wavelets, we divide the whole sphere into zones, such that the last surrounds A. We then find that, at P,

$$E = K_1 \epsilon_a \rho \lambda (\rho + r_0)^{-1} \sin\{\omega t - k(\rho + r_0)\} \quad [6.16]$$

From equations [6.15] and [6.16], and ignoring the phase difference, we find that, with $K_1=1$,

$$\epsilon_a = \epsilon_0 / \rho \lambda \quad [6.17]$$

At this point, we note that, from equation [6.12], disturbances from adjacent zones would cancel out exactly, owing to the $(-1)^{m+1}$ term, were it not for the contribution from K_m , since E_m is independent of r . Also, from equations [6.15] and [6.12], the total disturbance at P due to the unobstructed wave is

$$E_{un} = \epsilon_0(\rho + r_0)^{-1} \cos\{\omega t - k(\rho + r_0)\} \quad [6.18]$$

while that due to the secondary wavelets of the first zone only is

$$E_1 = 2K_1 \epsilon_0(\rho + r_0)^{-1} \sin\{\omega t - k(\rho + r_0)\} \quad [6.19]$$

Ignoring the phase difference, we see that the disturbance due to the first Fresnel zone only is twice that of the unobstructed wave. If we consider apertures over which K_m varies only slightly, we see that

$$|E_1| \sim |E_m| \quad [6.20]$$

Consequently, it appears that adjacent Fresnel zones tend to cancel each other out. This would suggest that a greatly increased irradiance could be obtained at P by blocking either all of the even, or all of the odd zones. A zone plate which passed only the first 25 odd zones for example

$$\begin{aligned} E &= E_1 + E_3 + E_5 + \dots + E_{49} \\ &\sim 25E_1 \end{aligned} \quad [6.21]$$

would lead to an increase by a factor of 2500 in the disturbance at P over its value (scaling as $E_1^2/4$) which would result in the absence of a zone plate. The radius of the m th zone may be calculated by recalling the requirement that a light ray passing through the m th zone must arrive at P with a path difference of $m\lambda/2$ compared to a wave which travels directly from the source S, to P (as shown in figure 6.3). That is;

$$(\rho_m + r_m) - (\rho_o + r_o) = m\lambda/2 \quad [6.22]$$

With

$$\rho_m = \sqrt{R_m^2 + \rho_o^2} \quad \text{and} \quad r_m = \sqrt{R_m^2 + r_o^2} \quad [6.23]$$

we use the Binomial theorem to obtain

$$\rho_m \sim \rho_o + R_m^2/2\rho_o \quad \text{and} \quad r_m \sim r_o + R_m^2/2r_o \quad [6.24]$$

Then,

$$1/\rho_o + 1/r_o = m\lambda/R_m^2 \quad [6.25]$$

Comparing this with the thin lens equation, we find that, with ρ_o and r_o defining the position of object and image, a zone plate of m zones acts as a lens of focal length

$$f = R_m^2/m\lambda \quad [6.26]$$

illustrating the severe chromatic aberration shown by zone plates.

6.2.1 Resolving power of a zone plate

For a lens of focal length f and diameter d , an incident beam of parallel light which fills the entire lens aperture may be brought to focus with a spot size of

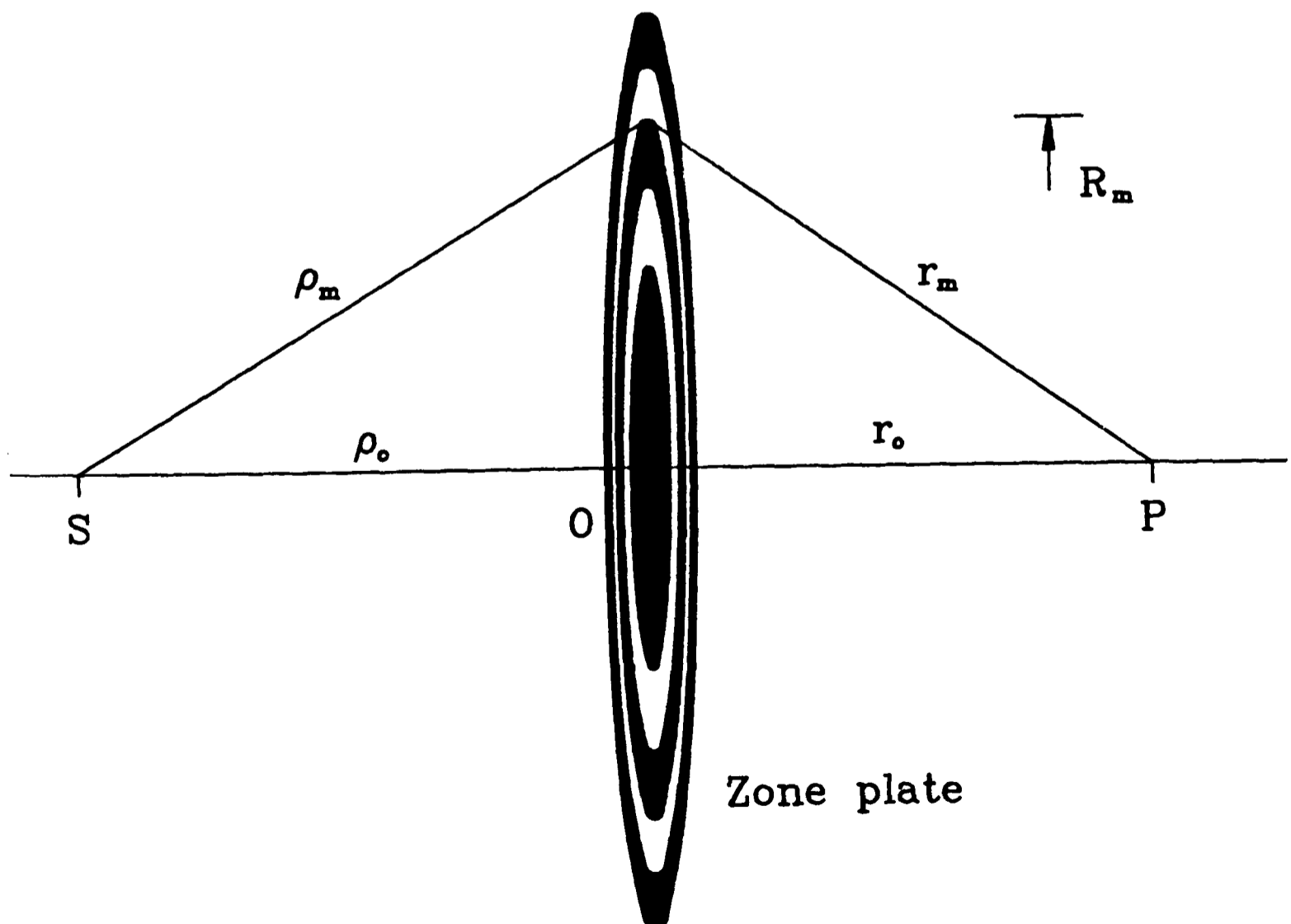


Figure 6.3: The zone plate acting as a lens.

approximately $\lambda f/d$. In the case of a zone plate, the Fresnel-Kirchoff diffraction integral shows that one with over ~ 100 zones behaves like a lens of comparable diameter. Then we have

$$R_m^2 = m\lambda f \quad [6.27]$$

such that

$$\begin{aligned} R_m^2 - R_{m-1}^2 &= \lambda f \\ &= (R_m + R_{m-1})(R_m - R_{m-1}) \\ &\sim 2R_m(R_m - R_{m-1}) \end{aligned} \quad [6.28]$$

We then note that $2R_m = d$, the diameter of the zone plate, so that

$$\lambda f/d = R_m - R_{m-1} \quad [6.29]$$

which is to say that the resolving power of a zone plate is equal to the thickness of the outermost zone of the plate.

6.2.2 Collection efficiency

We have seen that a given zone plate will focus a flux incident upon it in the same manner as a lens of focal length $f = R_m^2/m\lambda$. That is to say, there will be real images at distances of $R_1^2/m\lambda$, where $m=1, 2, 3, 4 \dots$ along the optical axis. These will be accompanied by virtual images, of equal but negative focal positions. By carrying out a Fourier cosine representation of the zone plate, it may be seen that at distances for which m is even, the contributions from various zones cancel out in pairs, so that the intensity of focused X-rays is nought at these positions. Furthermore, the odd numbered foci have relative intensities of $1:1/3^4:1/5^4:1/7^4 \dots$. Their absolute magnitude may be found by considering the fact that $1/2$ of the incident flux is absorbed by the zone plate, $1/4$ is undiffracted (ie. zeroth order, $m=0$), and the remaining quarter is split equally between real and virtual images. So for a zone plate with a reasonably large number of zones,

$$\begin{aligned} \alpha(1 + 1/3^4 + 1/5^4 + 1/7^4 + \dots) &= I_0/8 \\ \alpha\pi^2/8 &= I_0/8 \\ \alpha &= I_0/\pi^2 \end{aligned} \quad [6.30]$$

This indicates that only $1/\pi^2 \sim 0.101$ of the incident flux goes to form the primary

image. The constraint of equation [6.26], coupled with a maximum focal length of $\sim 20\text{cm}$ means that any zone plate used for the current application would have to be of a very small diameter and consequently small collecting area. (For example, the zone plates used in most STXM systems are only a few hundred micrometres in size.) There would also be a very severe problem with debris damage; zone plates are extremely fragile because of the need to have a high transmission in the empty zones and a small aspect ratio in the masked ones. Consequently, it was concluded that the use of zone plates in the current application was not feasible.

6.3 MULTILAYER MIRRORS

There has recently been much effort expended on the fabrication of high reflectance X-ray mirrors by the use of dielectric coatings, stimulated by the requirements associated with the development of the X-ray laser. Several scanning microscope systems have used the Schwarzschild arrangement (illustrated in figure 6.4) to obtain a relatively tightly focused point of X-rays. Here, the X-rays from a small source are reflected twice at near normal incidence to form a demagnified image at the focus of the mirror pair. The reflectivity, R , of all materials generally decreases with

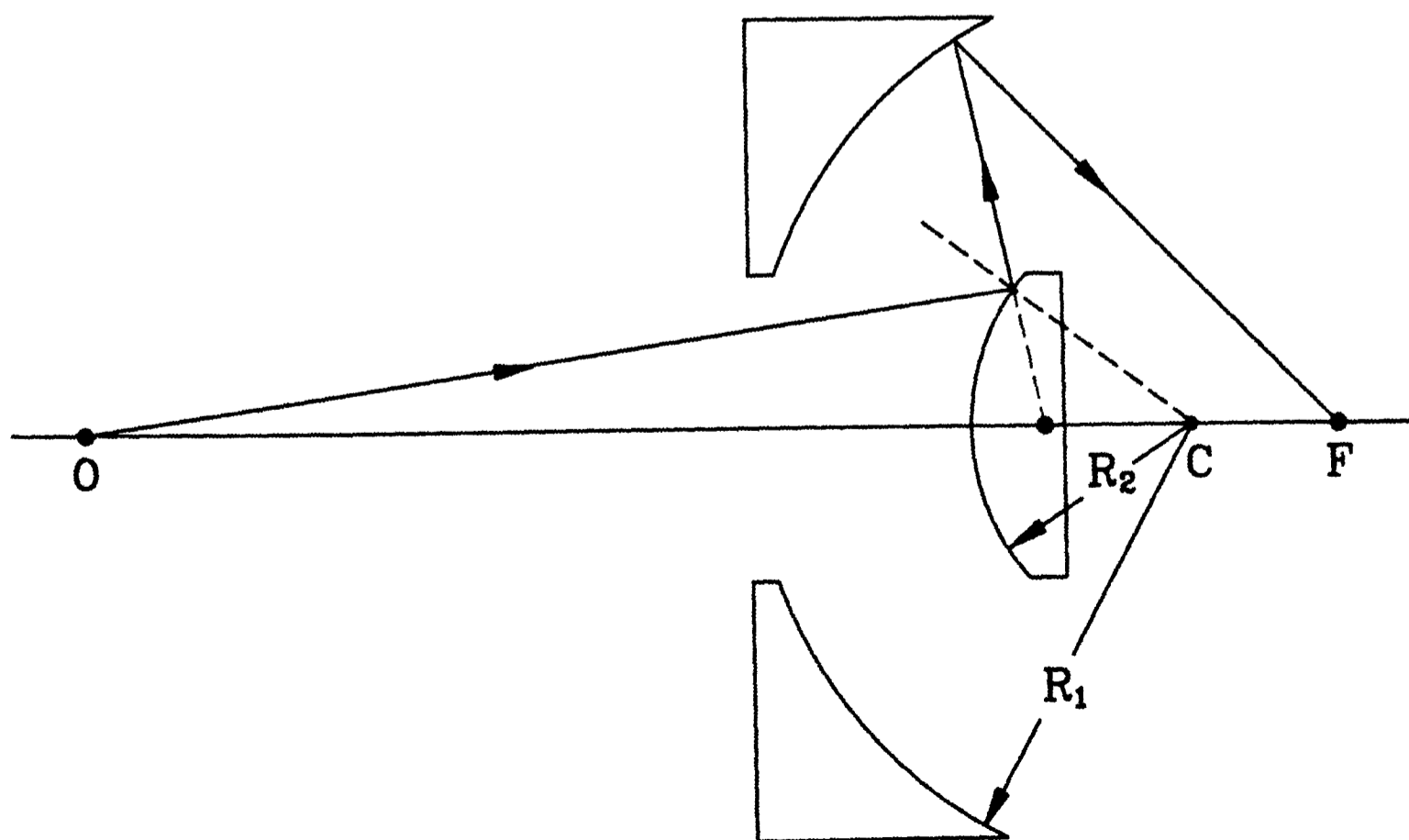


Figure 6.4: The Schwarzschild mirror arrangement.

decreasing wavelength in the soft X-ray region, with a variation given approximately by $R \propto \lambda^4$. For the water window region, normal incidence reflectivities of 10^{-5} are typical, and such a value would obviously make the use of normal incidence mirrors ineffective. However, the reflectivity may be enhanced by the deposition of periodic structures onto the mirror surface, where each period consists of two thin films of differing optical constants. The number of layers required to achieve a given reflectivity then varies approximately as $N \propto 1/\lambda^2$. Such structures have similarities both with Bragg reflectors and the quarter wave stack, where the reflections from all boundaries add in phase to the reflected wave.

The maximum reflectivity achievable by this method is limited by the fact that all materials are absorbing in the X-ray region of the spectrum. Losses may be minimized by positioning the stronger absorber of the two materials as a very thin film (eg. $d < \lambda/4$) at the nodes of the standing wave produced by the superposition of the incident and reflected beams. This results in more layers contributing to the reflected wave by enabling a greater penetration into the multilayer, but requires each layer to be smooth, without imperfection and to be of constant thickness. To achieve this in practice, it has been found that thin films of carbon form stable interfaces with many metals without inter-diffusion. Although such structures of alternating carbon and metal layers of only a few nanometres thickness will operate with a reasonable efficiency for radiation of wavelengths greater than 4.4nm, below this wavelength, the reflectivity falls off very rapidly because of absorption by the carbon layers. It is of course this very absorption which leads to the natural contrast obtained for biological specimens by the use of water window X-rays in the SXCM technique, and consequently is the reason that such optical components are not suitable for the present application. Xu [1991] has suggested that an optimal reflectivity of $<1\%$ can be obtained for water window wavelengths by using 50 layers of nickel and amorphous carbon, while attempts at replacing the carbon elements with an alternative have met with only limited success. Spiller [1980], for example, has demonstrated a reflectance of 1.1% at 2.3nm using 113 layers of rhenium-tungsten/boron.

For wavelengths shorter than 4.4nm, the second Bragg order may be used at the

cost of a lower reflectivity or alternatively, the incidence angle may be decreased and off-axis optical arrangements employed. Evidently, on curved mirrors, the angle of incidence varies across the area of the component, leading to a decrease in overall efficiency if this leads to too large a variation in angle of incidence. This particular problem may be overcome by the deposition of a coating with a variable multilayer period to compensate for this effect (as considered by Chauvineau [1989]).

The fact that coatings with such exacting tolerances are still under development and are by no means readily available, coupled with likely reflectances for water window X-rays of only a few percent, indicates that multilayer optics would not, at present, be suitable for use in the current application.

6.4 GRAZING INCIDENCE OPTICS

Although grazing incidence mirrors are used extensively in X-ray telescopes on board satellite based systems (for which large financial resources are generally available and where performance is often more important than cost), their use in X-ray microscopy has currently been limited to a small number of scanning microscopes which have made use of high brightness synchrotron sources and which required the tight focusing of an initially low divergence beam of X-rays. It does not appear that any work has previously been carried out on the use of such optical components acting as condenser lenses for laser generated plasmas. Because of this, the most appropriate form of and material for such a mirror had to be ascertained from the various tables of data on atomic scattering factors and optical constants currently available.

Since the refractive index of all materials is less than unity in the X-ray region of the spectrum, and assuming that absorption losses within the material are negligible, X-rays incident from a vacuum onto a polished surface will be largely, although not entirely, reflected if the incident grazing angle is less than a certain critical angle, θ_c . According to Snell's law;

$$\begin{aligned}\cos(\theta_c) &= n \\ &= 1 - \delta\end{aligned}\tag{6.31}$$

where n is the refractive index of the material. For an X-ray of wavelength λ which is sufficiently far from any absorption edges exhibited by the reflecting material, we may write [Aschenbach 1985]

$$\delta = N_0 Z r_e \rho \lambda^2 / 2\pi A \quad [6.32]$$

where $N_0 = 6.022 \times 10^{23}$ is Avogadro's number, $r_e = 2.82 \times 10^{-15}$ m is the classical radius of the electron, ρ is the mass density, Z is the atomic number and A is the atomic weight. In the case of gold for example, $\rho = 19.3 \text{ g/cm}^3$, $Z = 79$ and $A = 0.197$, leading to

$$\theta_c = 3.69\lambda \quad [6.33]$$

where θ_c is measured in degrees and λ in nanometres. For our application of soft X-ray microscopy, we wish to focus wavelengths in the range from 2.3 to 4.4 nm, which gives a minimum critical angle of $\theta_c = 8.5^\circ$; any X-ray flux incident on a polished gold surface with a grazing angle of less than this should therefore be reflected with negligible loss in intensity. There are several practical arrangements which use this effect to gather an X-ray flux and focus it to a small point; those which are potentially suitable for our requirements were considered.

6.4.1 Kirkpatrick-Baez mirrors

Perhaps the simplest form of a grazing incidence optic may be achieved by slightly deforming glass flats into parabolic cylinders. To form a point-like focus for incident X-rays, two orthogonal reflecting surfaces are required (shown in figure 6.5). Alternatively, a section of glass tubing, of the desired internal diameter forming the minor radius, may be bent to form a component which will focus incident X-rays with only one reflection [Faldon 1987].

This is probably the least suitable arrangement for the current application in that the solid angle of X-rays which may be collected is very small, owing to the relatively small angle through which the flats may be bent. The bending jig required to deform the flats or tubing would also be heavy, cumbersome and complicated, making the positioning of the mirror in the target chamber both inaccurate and difficult.

6.4.2 Tapered capillaries

Another simple approach to the problem of focusing X-rays is to use tapered capillaries. These may be made relatively simply and cheaply by drawing a section of heat-softened parallel glass tubing along its length so as to form a linear taper. If this is then positioned with its larger open end facing an X-ray source, the flux incident upon it will be focused to some extent as the X-rays are repeatedly reflected from the walls of the tube. The process is illustrated in figure 6.6. From this, we may see that the angle of incidence of the m th reflection will be

$$\theta_m = \alpha + (2m - 1)\gamma \quad [6.34]$$

where γ is the cone angle of the capillary and α is the initial angle between the X-ray beam and axis of the capillary. The total number of reflections experienced by such a beam before emerging from the end of the capillary is

$$n = \frac{1}{2} + \alpha(s + 1)/r_1 \quad [6.35]$$

Consequently, the total reflection coefficient may be put as

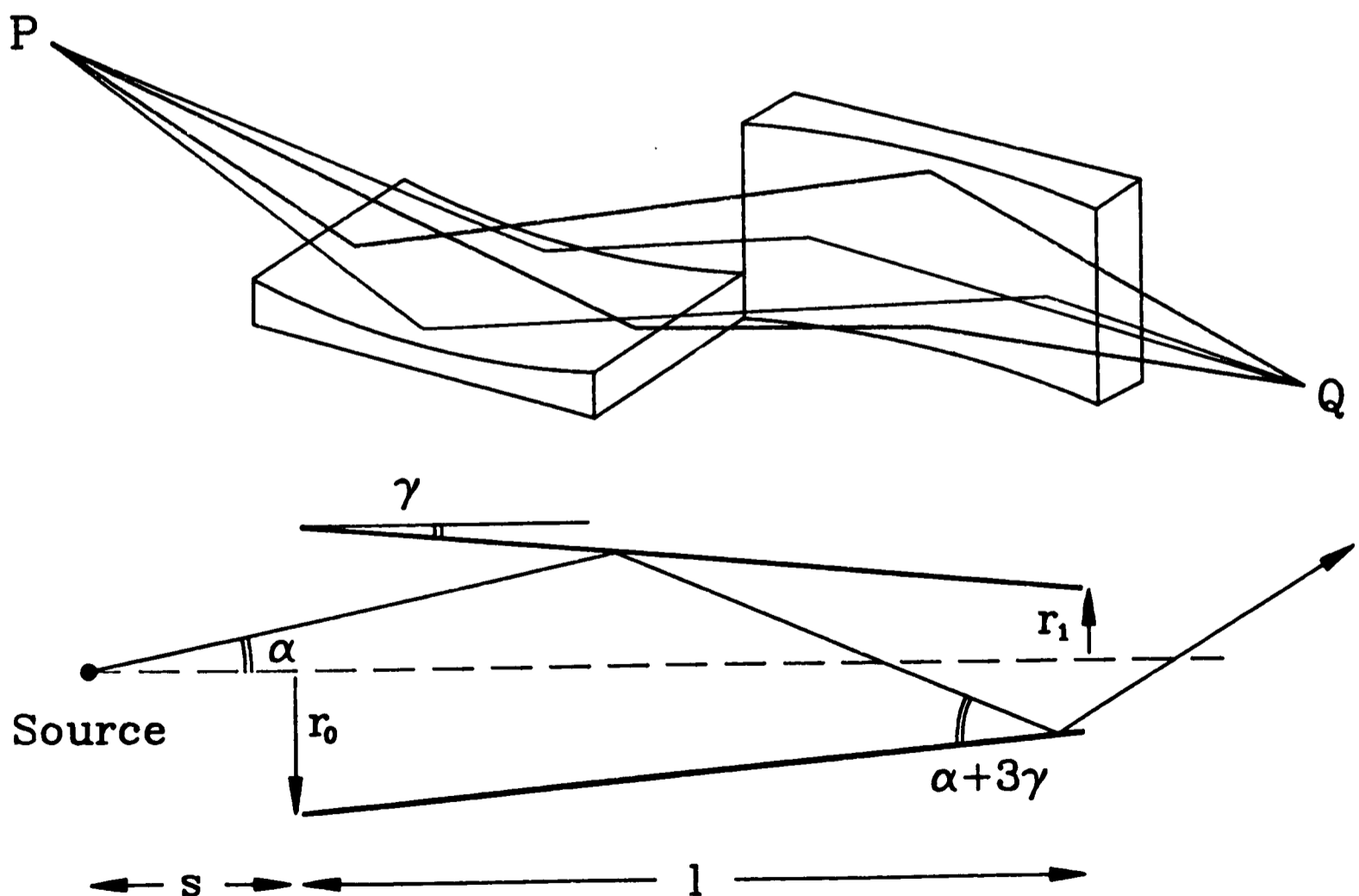


Figure 6.5: The Kirkpatrick-Baez mirror arrangement.

Figure 6.6: Reflection from a tapered capillary.

$$R_n = \prod_{k=1}^n R(\theta_k) \tag{6.36}$$

where $R(\theta_k)$ is the reflectivity at an angle θ_k . Taking a density of $\rho=3\text{g/cm}^3$ for glass and making use of equation [6.32], we find that the critical angle is $\theta_c=1.3^\circ$. Assuming complete reflection for X-rays incident up to this angle, the solid angle collected by a capillary of these parameters will be

$$\Omega = 2\pi\{1 - \cos(\alpha_0)\} \tag{6.37}$$

where α_0 is the angle from the source to the front rim of the capillary. If we make the requirement that at the last reflection before emerging from the capillary, the beam is incident on the wall with an angle θ_c , we may write

$$\alpha_0 = \{r_1\theta_c - 2\gamma(r_1 + l\gamma)\}/(r_1 + 2\gamma l) \tag{6.38}$$

having used

$$s = (r_1 + l\gamma)/\alpha_0$$

In the current application we require $r_1=0.5\text{mm}$ to illuminate the specimen and may have the capillary length $l=20\text{cm}$. Table 6.1 illustrates the variation in solid angle collected as the cone angle γ is adjusted.

From this we may see that the use of tapered capillaries would unfortunately be

γ°	$\Omega \times 10^4$ (sr)	Fraction of 2π	s (mm)	n	r_0 (mm)
0.00	16.172	3885	22.0	10	0.50
0.01	12.046	5216	27.3	9	0.54
0.02	9.202	6828	33.3	8	0.57
0.03	7.161	8774	40.1	7	0.60
0.04	5.651	11118	47.7	7	0.64
0.05	4.505	13947	56.3	6	0.67
0.06	3.616	17374	66.1	6	0.71
0.07	2.916	21545	77.3	5	0.74
0.08	2.357	26657	90.0	5	0.78
0.09	1.905	32978	104.5	5	0.81
0.10	1.537	40875	121.4	4	0.85

Table 6.1: Parameters of a tapered capillary, length 20cm with $\theta_c=1.3^\circ$.

of no use whatsoever for this application, where a large increase in X-ray flux is required. This arises from the fact that more than one reflection is required for the beam to pass through the capillary, and at each reflection the angle of incidence increases by 2γ . For the last reflection to be at or less than the critical angle θ_c , the initial reflection must be at a much smaller angle than this, which severely limits the solid angle which the capillary may present to the plasma source. This is in contrast to the ellipsoidal arrangement (to be considered in section 6.4.3), where only one reflection is required to bring the X-rays to focus and an optic with a much larger effective aperture may be used.

Capillaries are suitable, however, if an increase in the flux at a large and fixed distance is required. For example, the solid angle collected of 7.161×10^{-4} sr for the case of $\gamma = 0.03^\circ$ would decrease by a factor of 35 if the capillary was removed. However, in the current application an increase by a factor of 1.02 in the flux incident on the specimen could be gained simply by removing the capillary and placing the specimen at the position of its opening instead.

6.4.3 Ellipsoidal mirror

One of the simplest configurations of grazing incidence optics is an ellipsoidal mirror. For the figure described in Cartesian coordinates by

$$x = a.\cos(t) \quad \text{and} \quad y = b.\sin(t) \quad [6.40]$$

any ray emerging from one of the points of focus will undergo one reflection only to reach the other point of focus (as shown in figure 6.7), assuming that the angle of incidence and angle of reflection are the same, which will be the case for X-ray reflection. Thus, if a mirror formed by the rotation of an ellipse about its major axis is positioned such that the laser generated plasma is at one focus of the ellipse, then a comparatively large solid angle of the emitted X-rays will be brought to focus at its second focus. The extent of this solid angle will be determined by the critical angle for total external reflection, θ_c , and the values of the parameters a and b .

The eccentricity of an ellipse is defined as

$$e = \sqrt{1 - b^2/a^2} \quad [6.41]$$

and the foci will be a distance $2ae$ apart along the major axis. The mirror need only extend from $x = -x_c$ to $+x_c$, where

$$x_c = a \sqrt{1 - [b/ae \cdot \tan(\theta_c)]^2} \quad [6.42]$$

as beyond this range, X-rays hitting the mirror will do so at angles greater than θ_c , and hence will not be reflected (figure 6.8). We then find that

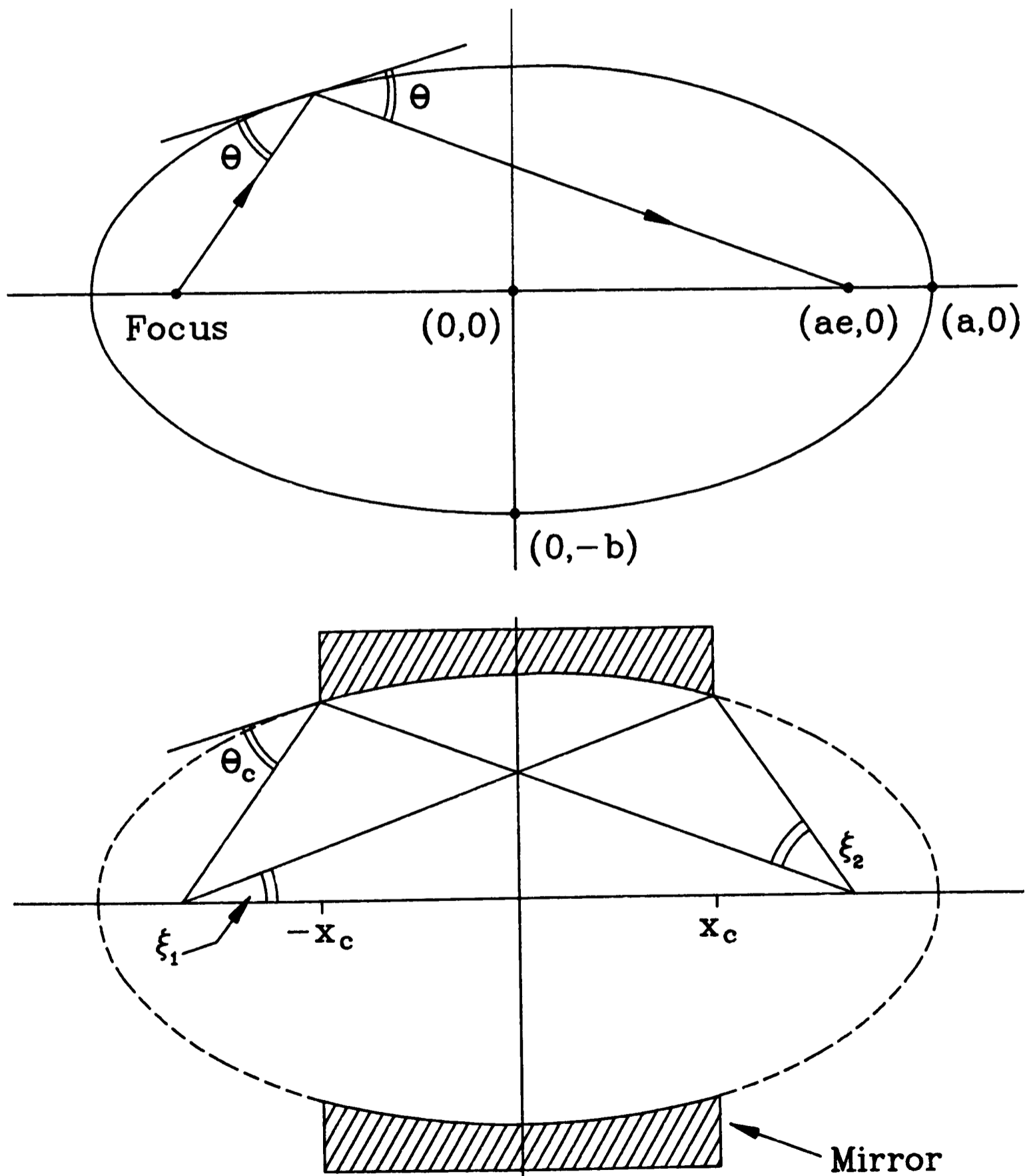


Figure 6.7: The geometry of the elliptical surface as a reflector.

Figure 6.8: The limit imposed by the critical angle on mirror geometry.

$$\xi_2 = \tan^{-1}(y_c/[ae-x_c]) \quad \text{and} \quad \xi_1 = \tan^{-1}(y_c/[ae+x_c]) \quad [6.43]$$

where

$$y_c = b^2/ae.\tan(\theta_c) \quad [6.44]$$

and the solid angle collected by the mirror is given by

$$\Omega = 2\pi\{\cos(\xi_1) - \cos(\xi_2)\} \quad [6.45]$$

For a fixed value of a , which effectively will determine the source to focus distance (since $b \ll a$), the value of Ω increases as b decreases, which causes x_c to increase, requiring the front rim of the mirror to approach the plasma source. As was the case for the specimen holder alone, there will be some minimum distance which will still allow the passage of the incident laser beam onto the wire target. The value of b should therefore be set to as small a value as practicable to obtain the collection of as great a solid angle of X-rays as possible, while not obscuring the target from the laser.

Considering the geometry of the target chamber, the plasma to specimen distance could be increased to $\sim 20\text{cm}$, which would require $a=10\text{cm}$. With this value, and $\theta_c=8.5^\circ$, the required dimensions of a collecting mirror were calculated for various values of the parameter b ; for each, the solid angle collected is shown (table 6.2).

We may compare these solid angles to that gathered by the specimen holder alone, without the aid of any condensing optics. When the specimen holder was brought to a distance of 9mm from the plasma for example, the corresponding solid angle was $2\pi/570$ which is to say that only $1/570$ of the X-rays emitted forward into 2π were used to illuminate the specimen. This compares with $\sim 1/30$ which may theoretically be obtained by the use of a grazing incidence ellipsoidal mirror.

6.4.4 Wolter type I mirror

Devices such as the ellipsoid and Kirkpatrick-Baez mirrors suffer unavoidable aberrations such as coma and astigmatism at grazing incidence. In order to overcome these problems, the Wolter type mirror was developed [Wolter 1952a, 1952b]. The surface of a Wolter type I mirror is a combination of hyperboloid and ellipsoid surfaces (figure 6.9). These are arranged confocally, so that the image of the source on axis is not degraded by any geometrical aberrations; the resolution is theoretically diffraction

b (cm)	Foci separation (cm)	Entrance aperture diameter (cm)	Solid angle collected (sr)	Fraction of 2π	Focus to rim distance (cm)
0.1	20.0	0.01	0.274	22.9	0.02
0.2	20.0	0.05	0.272	23.1	0.08
0.3	20.0	0.12	0.269	23.4	0.20
0.4	20.0	0.21	0.265	23.8	0.36
0.5	20.0	0.33	0.259	24.3	0.57
0.6	20.0	0.48	0.251	25.0	0.83
0.7	20.0	0.66	0.242	25.9	1.15
0.8	20.0	0.86	0.232	27.1	1.53
0.9	20.0	1.09	0.219	28.7	2.00
1.0	19.9	1.34	0.203	30.9	2.55
1.1	19.9	1.63	0.185	34.1	3.22
1.2	19.9	1.94	0.161	38.9	4.05
1.3	19.8	2.28	0.132	47.7	5.12
1.4	19.8	2.65	0.089	70.7	6.66

Table 6.2: Parameters of an ellipsoidal mirror for $a=10.0\text{cm}$ and $\theta_c=8.5^\circ$.

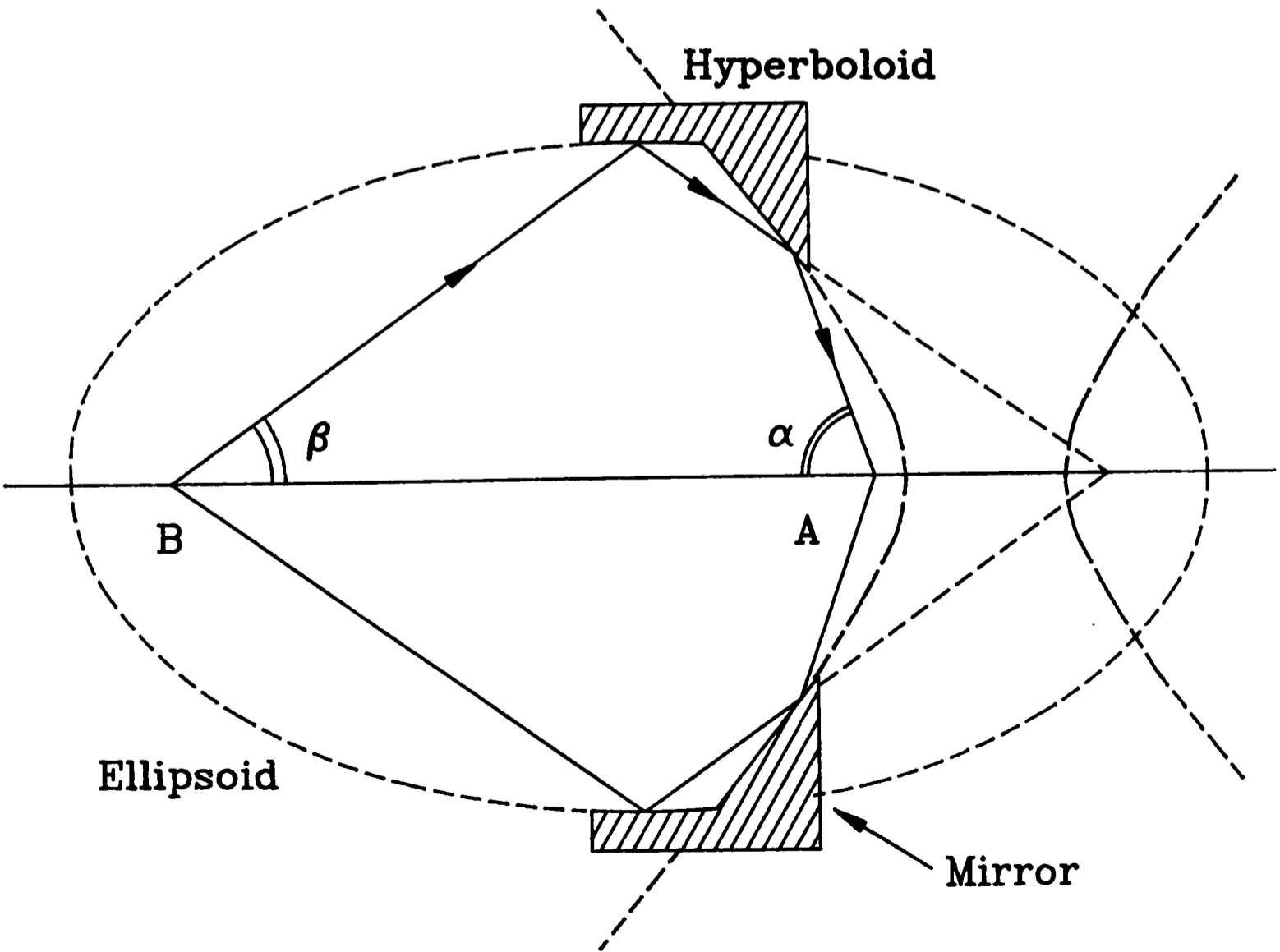


Figure 6.9: The geometry of the Wolter Type I mirror.

limited only, and off-axis aberrations are relatively small.

X-rays emitted from a source at B are reflected twice; once at the ellipsoid and once at the hyperboloid surfaces, to be brought to focus at A. The size of the image at A will be β/α times the source size at B. This arrangement of mirrors has the advantage over a single ellipsoidal surface of allowing magnification, or more importantly, demagnification of the source, and therefore has found uses mainly in astronomical X-ray telescopes [Aschenbach 1985], and scanning X-ray microscopy [Michette 1988b], where the resolution of the instrument is limited to the size to which X-rays may be focused in the image plane. However, for the present application, the collection of a large solid angle with a high efficiency and its focusing to a relatively large ($\sim 1\text{mm}^2$) spot is required, while losses at reflection (investigated in section 6.4.6) would lead to this double reflection optic being too inefficient to be of any use.

6.4.5 Fabrication techniques

There are several production methods which have been used to create grazing incidence optics, each of which addresses the problem of producing highly polished, non-spherical surfaces for the reflection of incident X-rays. The three most appropriate methods for the current application are briefly described below.

i) Diamond turning

The diamond turning technique may only be used to produce surfaces with an aperture to length ratio of at least 1, and is therefore only suitable for the fabrication of Wolter type I, II or III mirrors or other ‘open’ systems. The mirror element has to be relatively thick to withstand the machining process, but very accurate forms may be produced in this way. For use with X-ray wavelengths, however, residual tool marks must be removed by polishing in order to avoid excessive loss on reflection. Furthermore, materials such as stainless steel may not be diamond turned as the heat generated by the machining process causes the tip of the tool to react with the surface of the mirror, forming extremely hard carbide compounds which are highly resistant to further machining.

ii) Epoxy replication

Epoxy replication is an adaptation of a commercial process for producing reflection gratings. A negative mandrel is produced from a material such as glass or Kanigen-plated aluminium to an accuracy and surface finish as required for the X-ray reflector. A 100nm thick layer of gold is evaporated onto the surface over a release agent; this becomes the X-ray reflecting surface. A carrier is then produced with a shape to within $\sim 10\mu\text{m}$ of the actual mirror itself. This carrier is formed over a second negative metal mandrel which need not be of as high quality as the one on which the X-ray reflective surface is laid. Carbon fibre reinforced epoxy may be used to produce the carrier.

The carrier substrate is then placed over the gold plated mandrel, and epoxy is injected between them. Pressure is applied between the carrier and the mandrel while the epoxy cures. The two are then separated by exploiting the difference in the thermal expansion coefficients of the carrier and mandrel. By this method, mirrors with a surface roughness of $\sim 0.3\text{nm}$ RMS have been produced [Aschenbach 1988]. The technique is illustrated in figure 6.10.

iii) Electroforming

In the process of electroforming, a negative mandrel is again produced, with the required surface smoothness obtained either by extended polishing, or by over-coating of the normal polished surface with acrylic lacquer [Gorenstein 1988, de Korte 1988]. A 100nm thick layer of gold is then evaporated onto the surface, to act as the reflector. A layer of nickel is then electrodeposited onto the mandrel, to a thickness of several millimetres, to produce a uniform structural support for the thin gold reflecting surface. This finished mirror is again removed from the mandrel by thermal and mechanical means. This technique is illustrated in figure 6.10.

6.4.6 Absorption losses at reflection

From the previous expression for the critical angle (equation [6.32]), above which radiation will not be reflected, we see that a material with a high density is

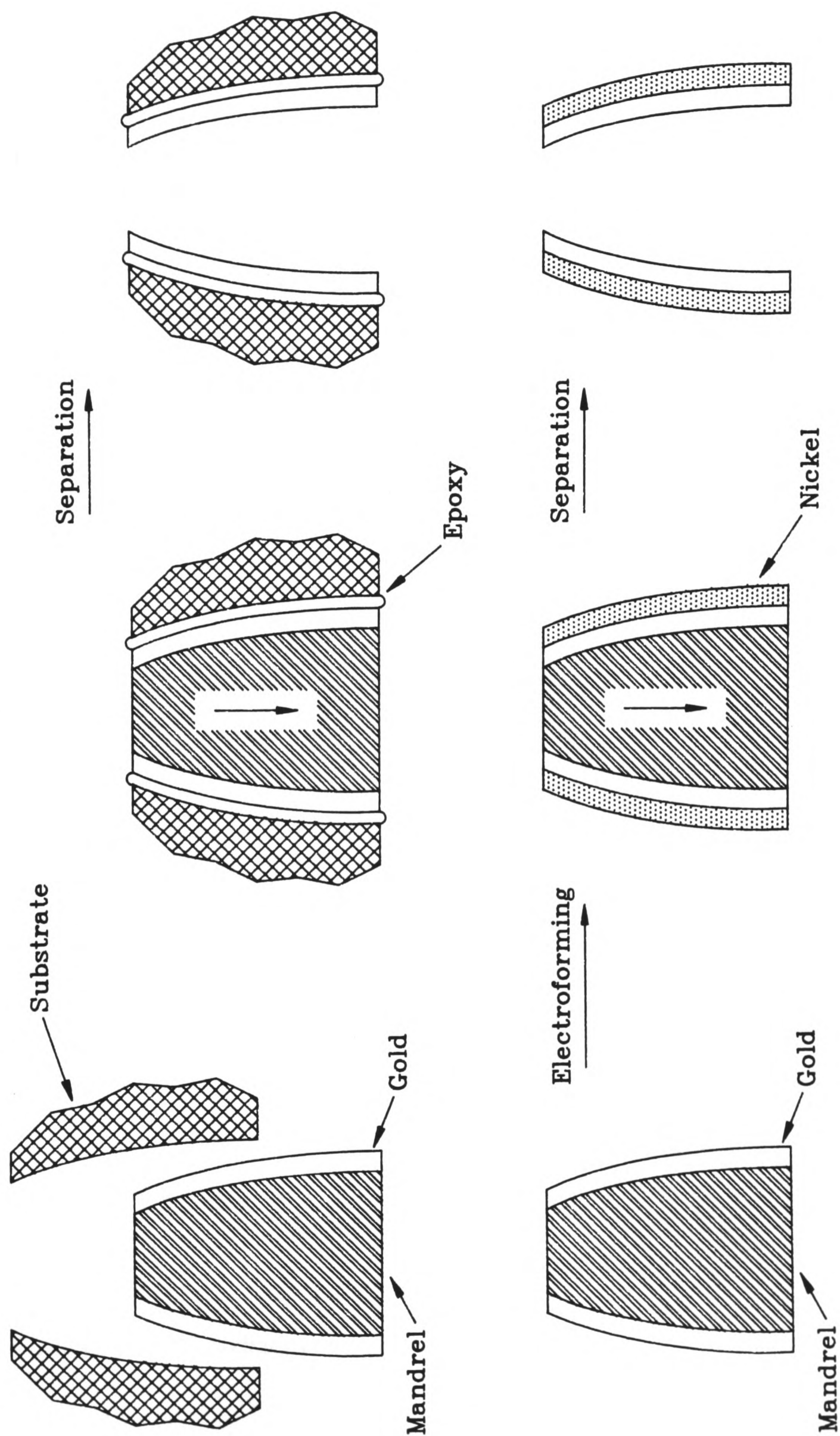


Figure 6.10: Mirror production from a mandrel; epoxy replication (top) and electroforming.

desirable over one with a lower density for the collection of as large a solid angle of X-rays as possible. However, it was assumed that the reflecting material did not absorb radiation of the particular wavelength to be reflected at angles of incidence less than the critical angle. One physical process by which photons in the X-ray region of the spectrum will be absorbed by a material is the promotion of inner shell electrons, from its constituent atoms, to higher empty levels, or effectively, infinity. Figure 6.11 illustrates those elements whose various inner shell electron energy levels correspond to the energies of water window X-rays, and which would therefore be able to absorb them to a greater or lesser extent (from Bearden [1983]). We see that the majority of elements have such levels; in the case of gold, for example, the N_{IV} and N_V levels lie at 359 and 340eV, within the water window. In the vicinity of total reflection cutoff, the attenuation factor in the Poynting vector, which describes the energy flow in the medium, indicates a penetration depth of

$$d_{1/e} = \lambda / 4\pi\beta^{1/2} \quad [6.46]$$

where β is the imaginary part of the complex refractive index of the material at the wavelength λ . This shows that, for example, the depth for gold at 4.4nm is approximately 4nm.

This illustrates the fact that we must take into account the losses at reflection due to absorption, even at grazing incidence. That is to say, we must consider the imaginary part of the refractive index, n , of the reflecting material. The Fresnel equations for the E-field amplitude reflection coefficients are

$$r_p = \left[n^2 \sin(\theta) - \sqrt{n^2 - \cos^2(\theta)} \right] / \left[n^2 \sin(\theta) + \sqrt{n^2 - \cos^2(\theta)} \right] \quad [6.47]$$

$$r_s = \left[\sin(\theta) - \sqrt{n^2 - \cos^2(\theta)} \right] / \left[\sin(\theta) + \sqrt{n^2 - \cos^2(\theta)} \right] \quad [6.48]$$

for the p and s polarizations. The reflectivity for unpolarized incident X-rays will then be

$$R = \frac{1}{2}(r_p^* r_p + r_s^* r_s) \quad [6.49]$$

where the complex refractive index is written

$$n = 1 - \delta - i\beta \quad [6.50]$$

From these equations, we see that if $\beta=0$, then at angles for which $\cos(\theta) > n$, the

$\{n^2 - \cos^2(\theta)\}^{0.5}$ term is imaginary; this leads to a phase change at reflection, but no decrease in intensity, since r_p and r_s will be of the form

$$r = (a - ib)/(a + ib) \tag{6.51}$$

such that $r^*r=1$. The effect of $\beta \neq 0$ is illustrated in figure 6.12; for large values of β , there is no effective cut-off angle, as losses are considerable even at small grazing angles.

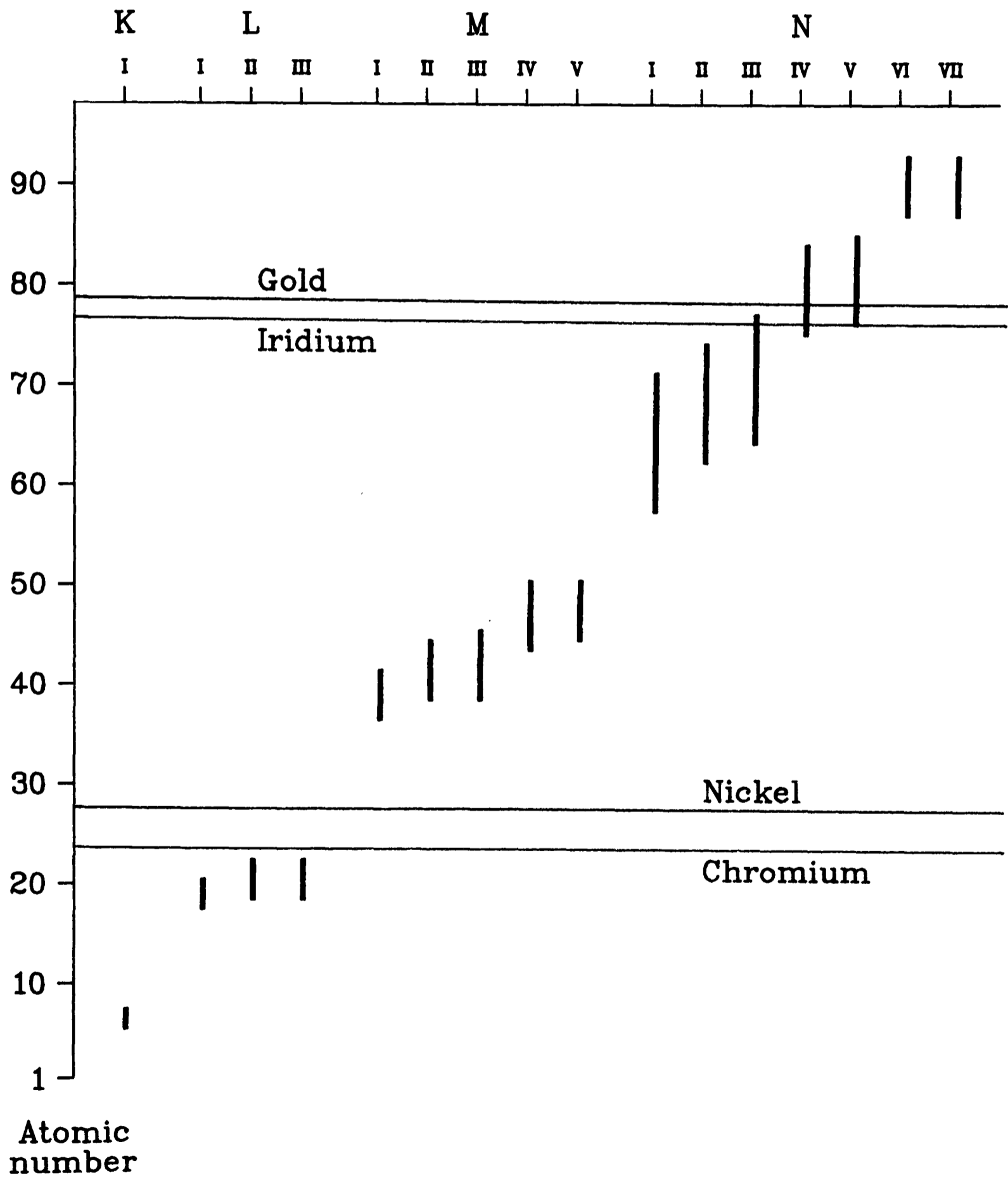


Figure 6.11: Inner shell energy levels which fall within the water widow region, illustrating the suitability of nickel as a reflector.

Two sources for the values of $(1-\delta)$ and β have been used. Firstly, 'direct' values of $(1-\delta)$ and β , obtained by Hagemann [1975] from transmittance measurements, and secondly, via values of the atomic scattering factor f , calculated by Henke [1982]. For the the latter case, writing $f=f_1+if_2$, we have

$$\delta = N_0 \rho r_e \lambda^2 f_1 / 2\pi A \quad [6.52]$$

$$\beta = N_0 \rho r_e \lambda^2 f_2 / 2\pi A \quad [6.53]$$

where, by comparison with equation [6.30], we see that f_1 has taken the place of the atomic number, Z , which is introduced by the anomalous dispersion treatment of the interaction. Agreement between the two sets of data is good, as may be seen from figure 6.13. Unfortunately, measurements of the reflectivity of gold at grazing angles do not appear to have been made for the water window region, and so comparisons were made at 0.834nm and 1.334nm, from the data of Aschenbach [1987]. From figure 6.14, we see that the agreement with the predictions of the Fresnel formulae are excellent. The reflectance for iridium, which is also often used as a reflecting surface, was also calculated for comparison.

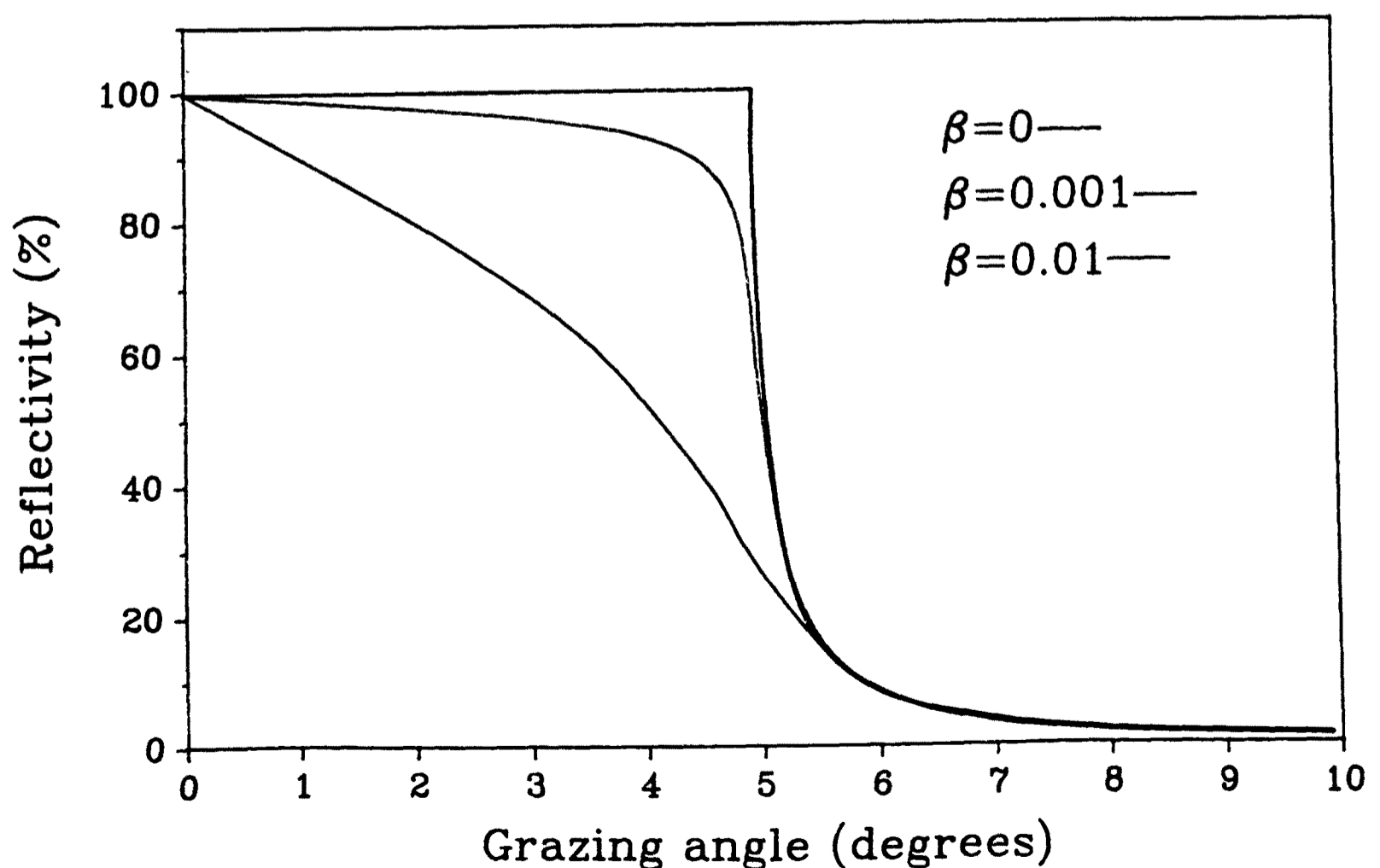


Figure 6.12: The dependence of the critical angle on the value of β .

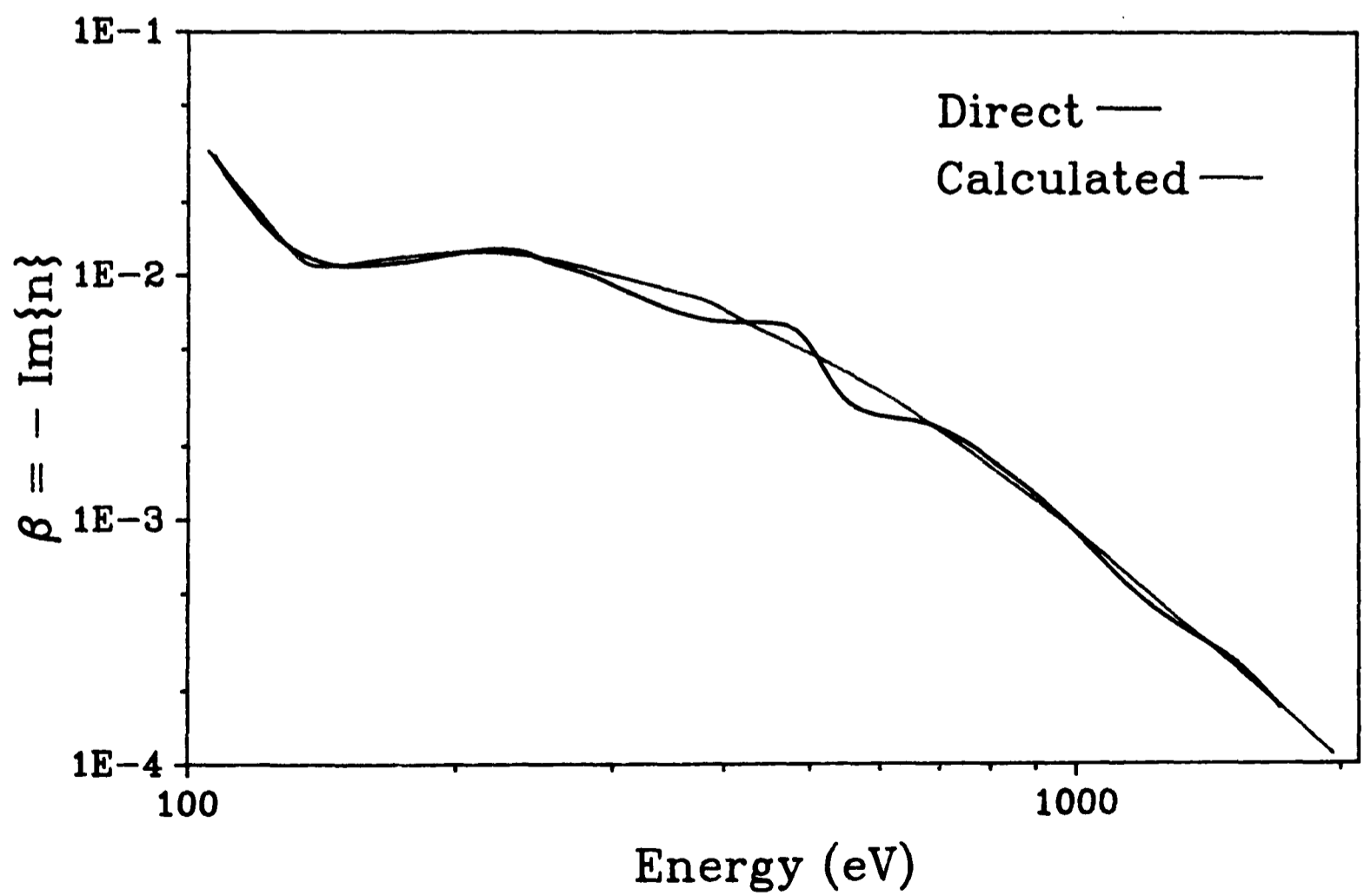
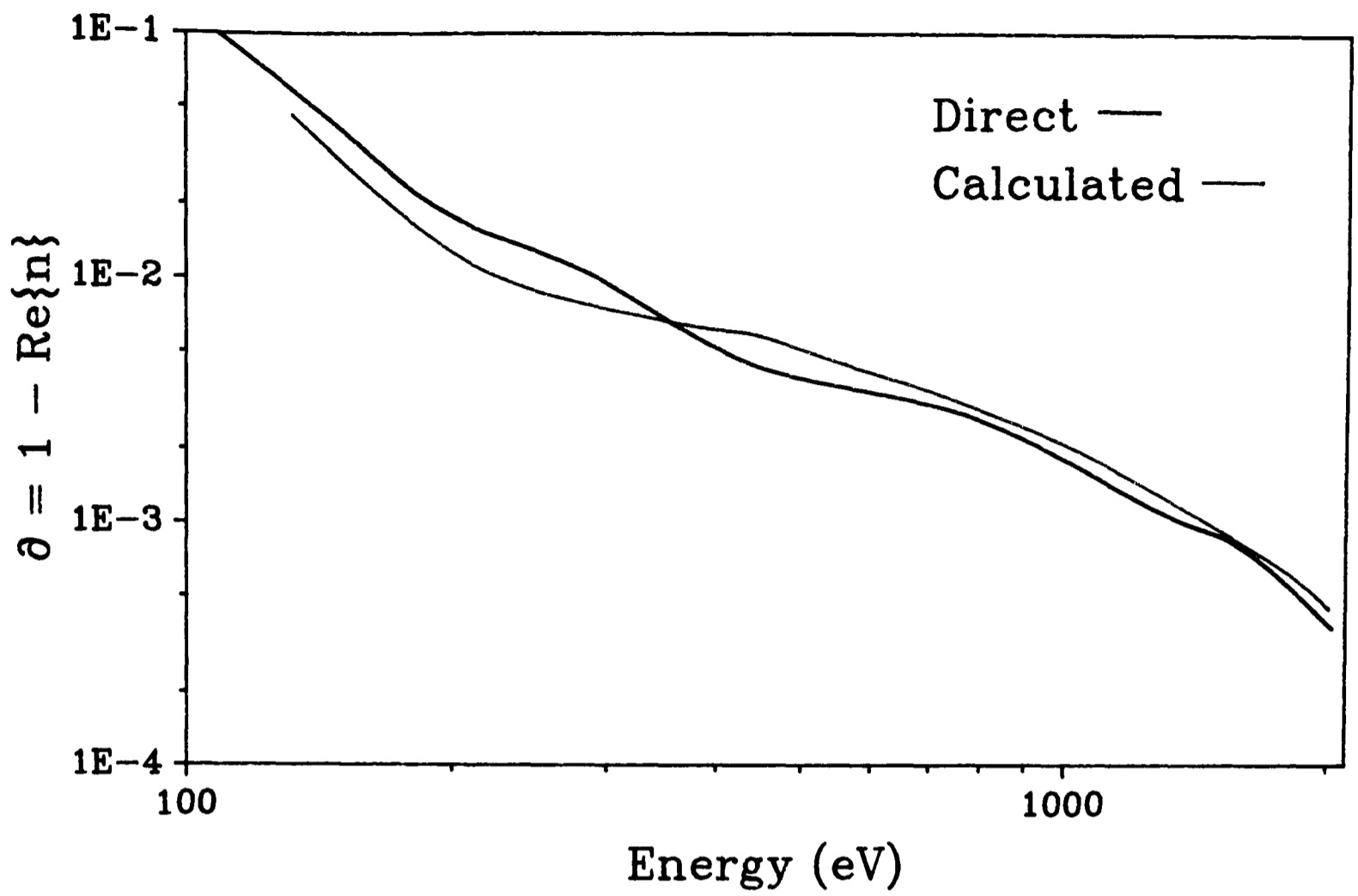


Figure 6.13: A comparison of the measured [Hagemann 1975] and calculated [Henke 1982] values of δ and β for gold.

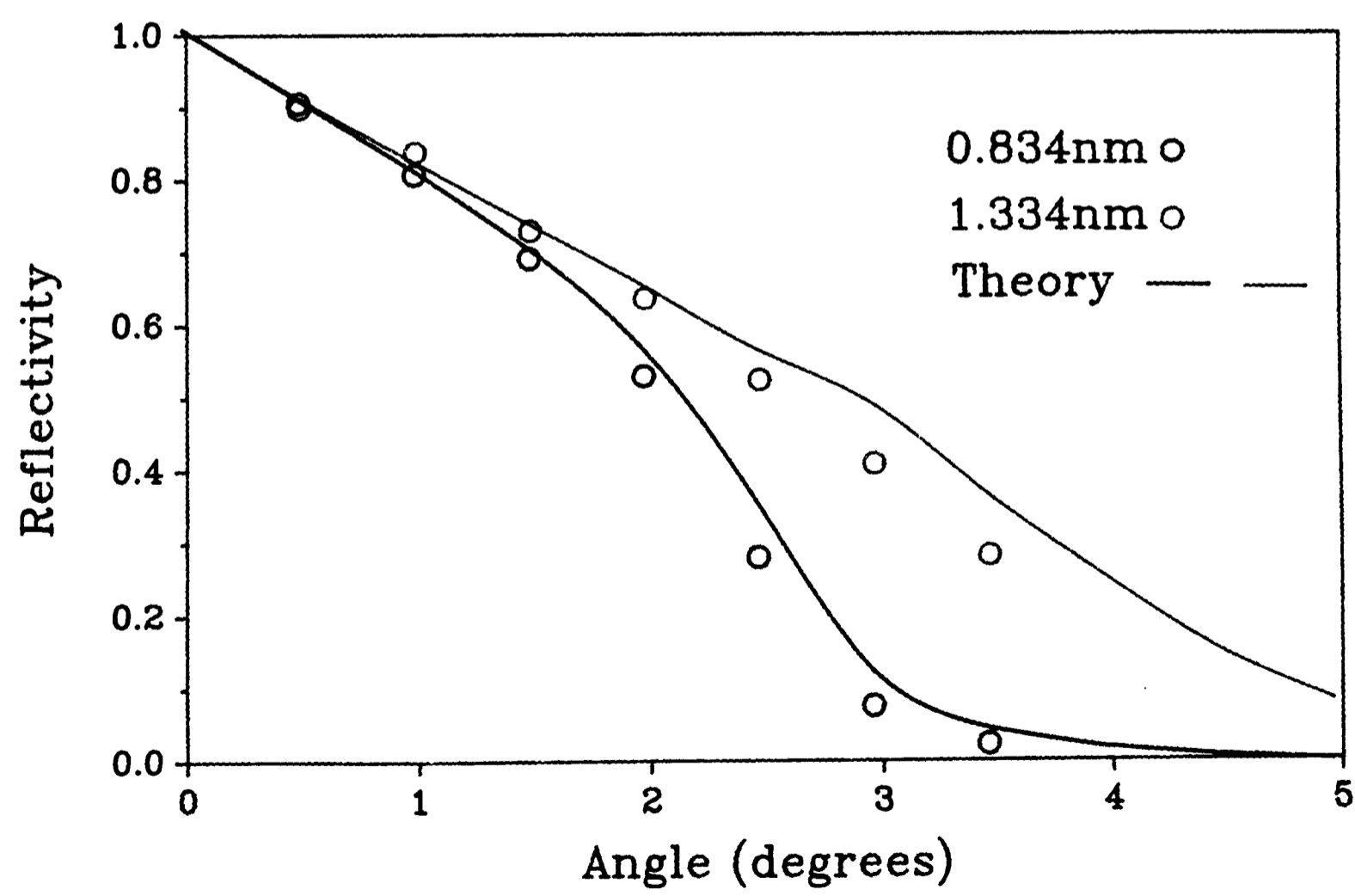
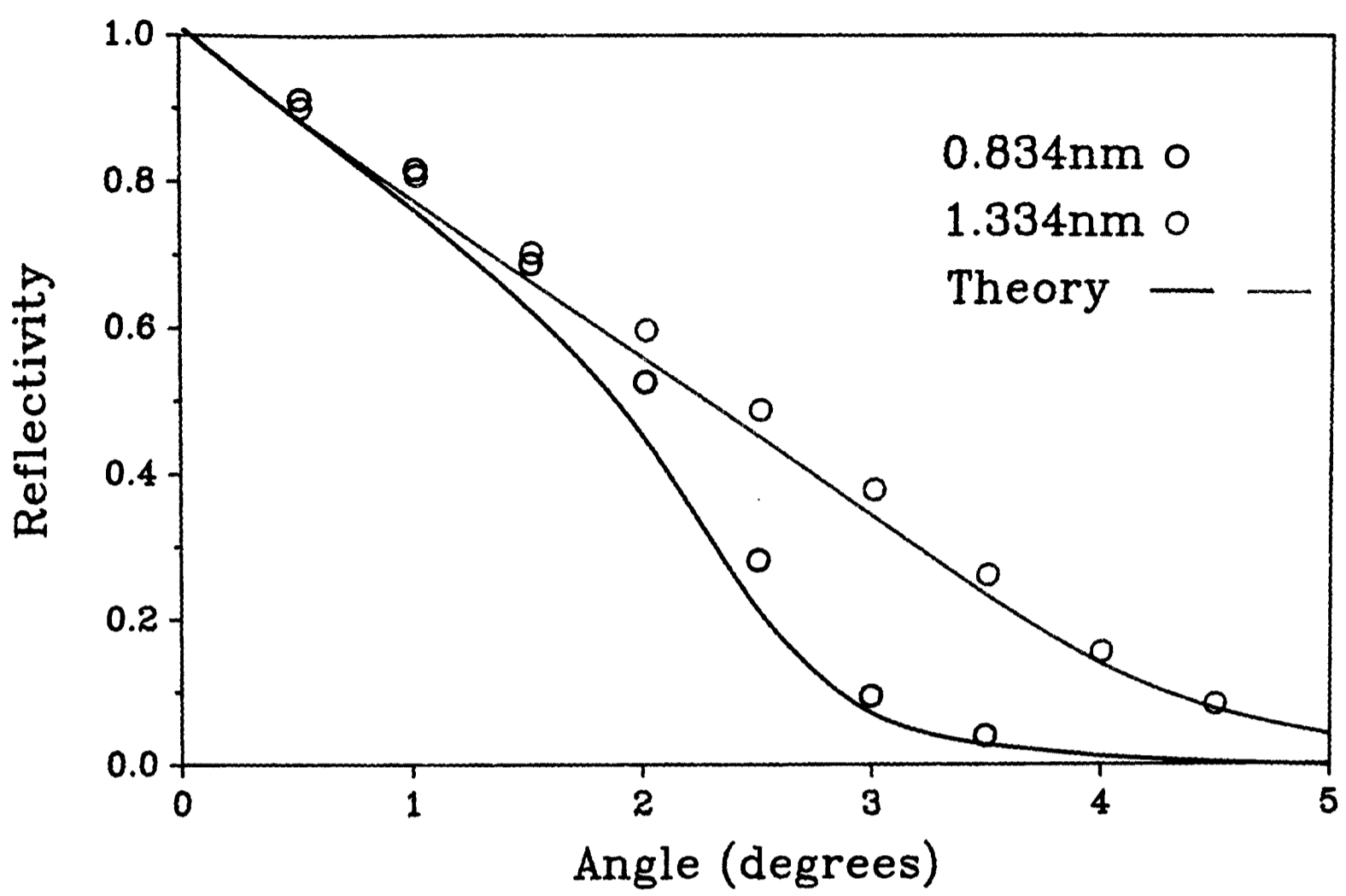


Figure 6.14: Measured [Aschenbach 1987] and theoretical reflectivities for gold (top) and iridium.

Once the data of Henke and the application of the Fresnel equations had been validated, the reflectances at grazing angles were calculated for gold, iridium, chromium and nickel at either end of the water window wavelength range. The results are shown in figures 6.15 to 6.18. From these, we see that nickel or chromium appear to be the most suitable for our application, in that they offer the greatest degree of reflection over the water window range. The values of β for gold and iridium are so large that there is effectively no cut-off angle; for chromium and nickel at 2.36nm, a cut-off is more evident.

The collecting efficiency of an ellipsoidal mirror then had to be recalculated, taking into account these losses at reflection. Previously, we had assumed that the solid angle collected was

$$\Omega = 2\pi\{\cos(\xi_1) - \cos(\xi_2)\} \quad [6.54]$$

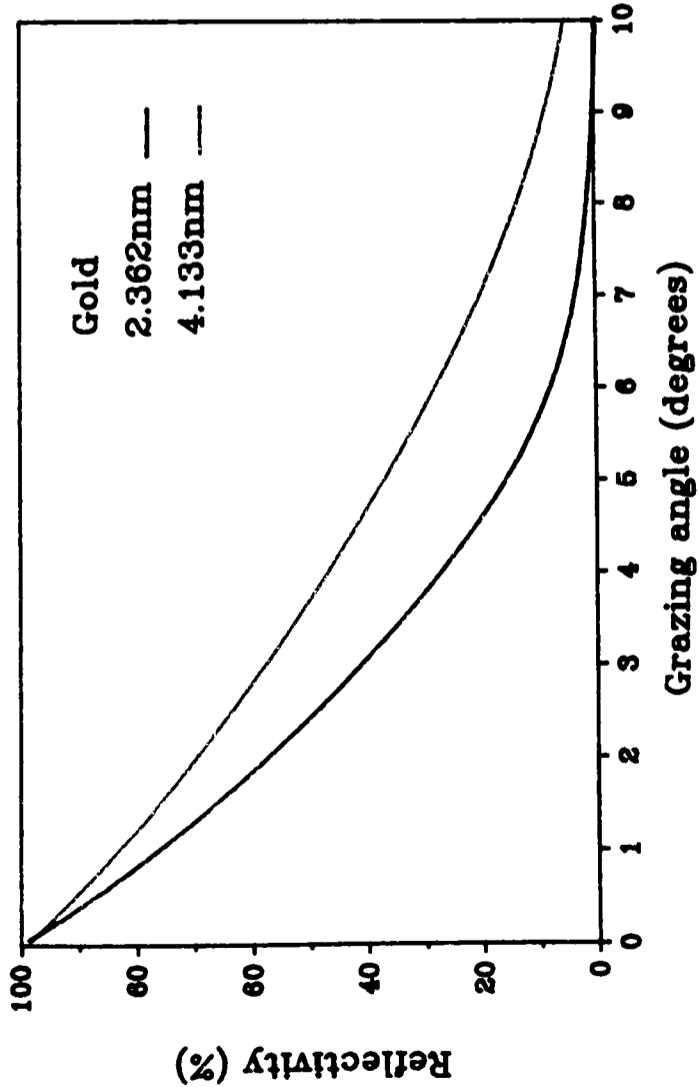
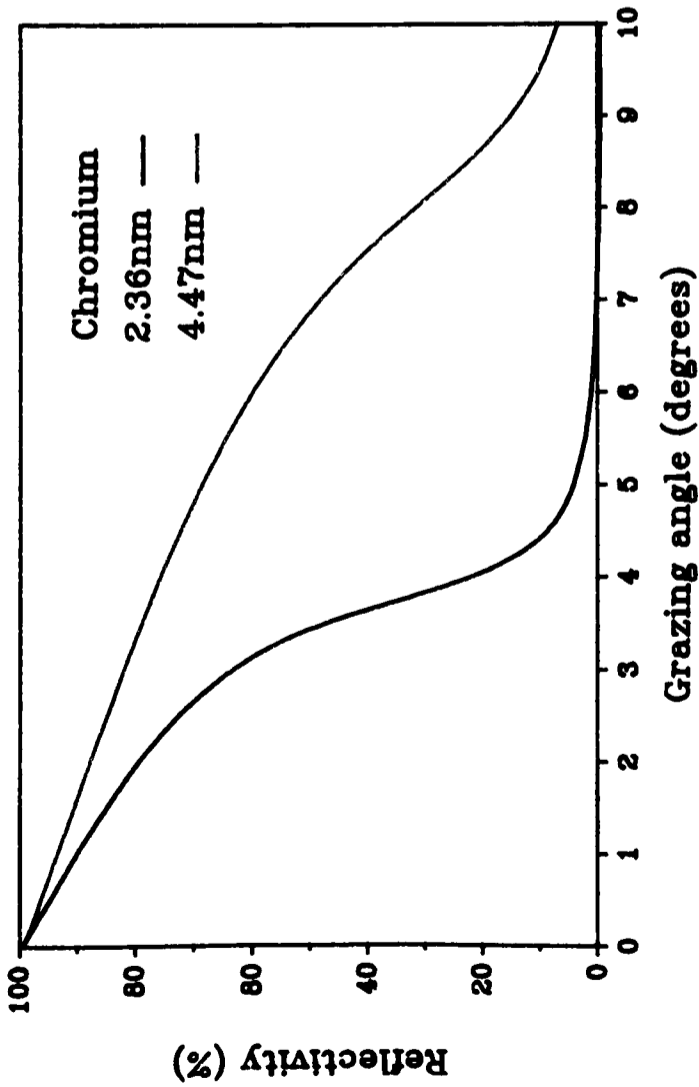
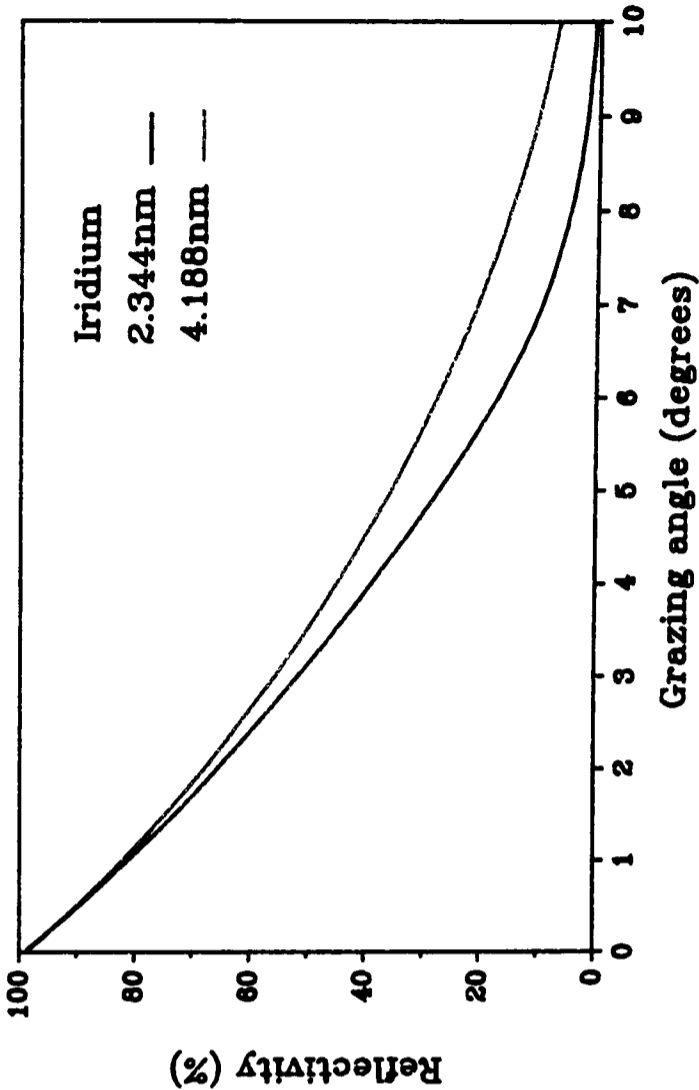
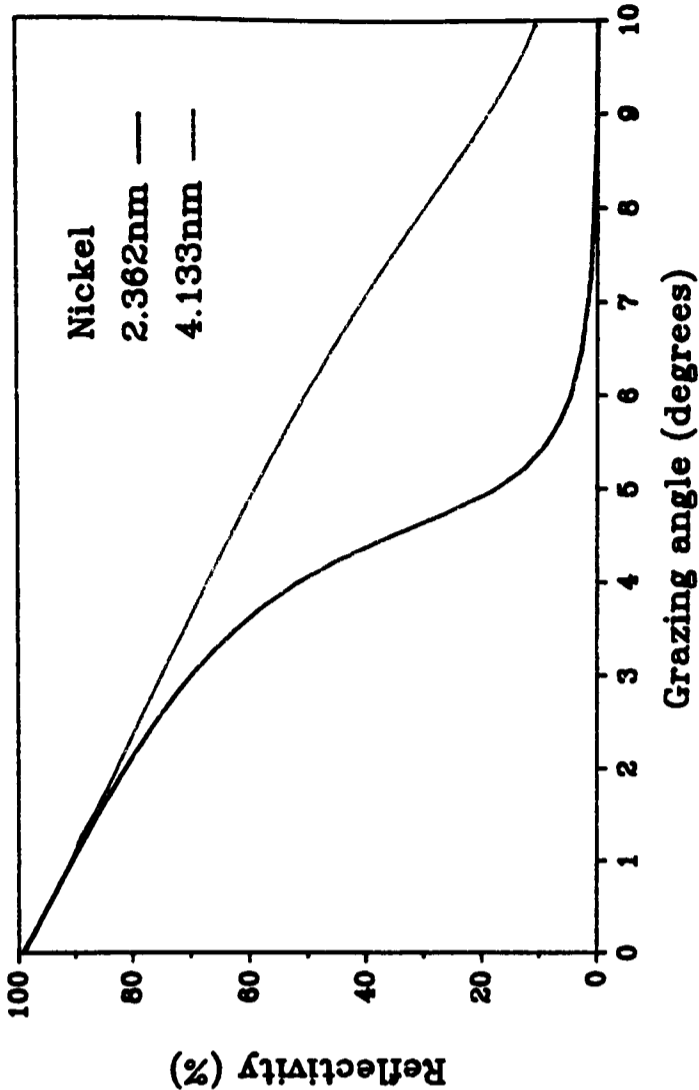
where ξ_1 and ξ_2 were dictated by the cut-off angle of equation [6.31]. Now with a variable reflectivity $R(\theta)$ at a particular wavelength, we may calculate an effective solid angle collected;

$$\Omega_{\text{eff}} = 2\pi \int_{\xi_1}^{\xi_2} R(\theta) \sin(\theta) d\theta \quad [6.55]$$

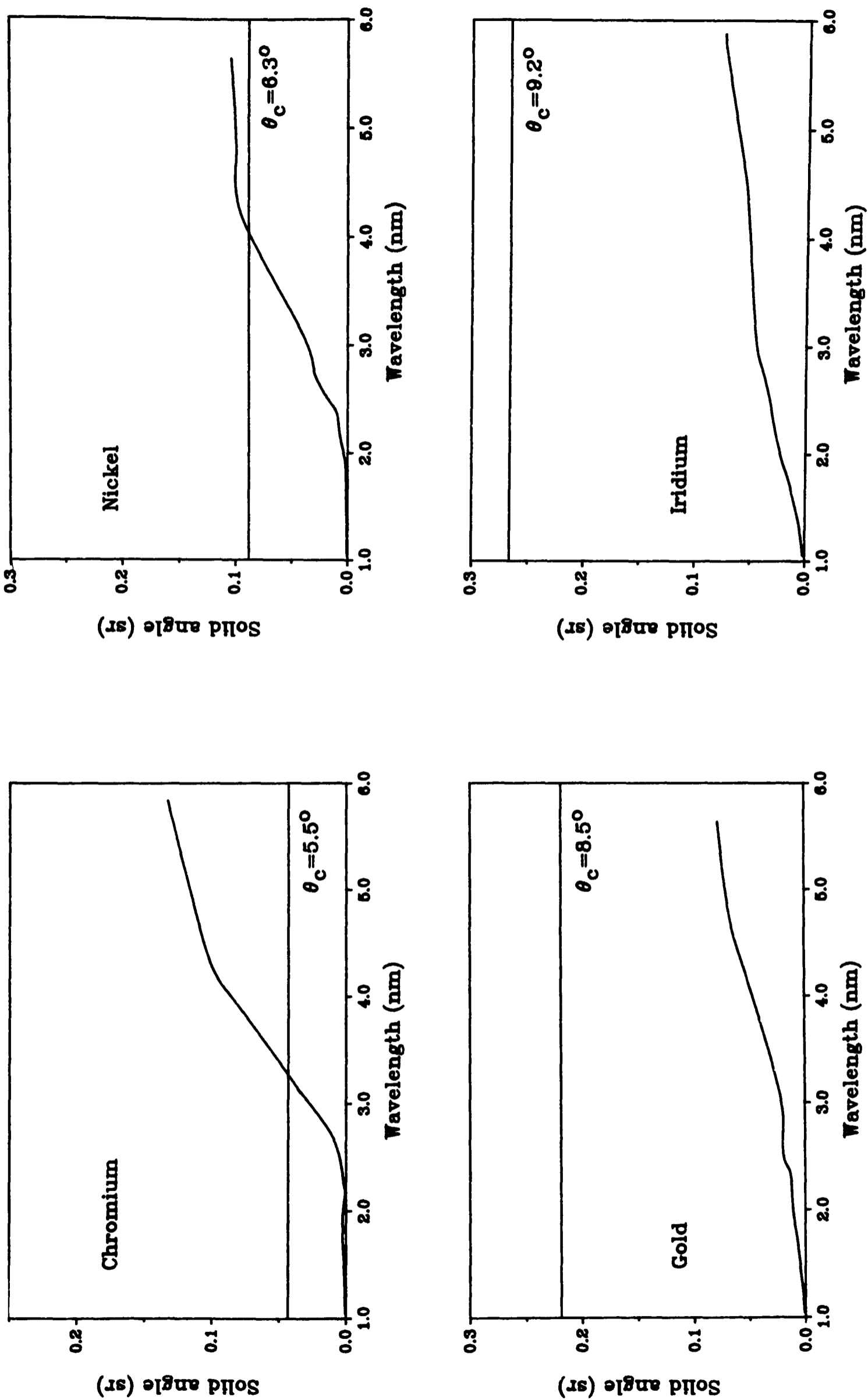
where θ and ξ are linked by the equation

$$\tan(\theta)\tan(\xi) = 1 - \frac{1}{e} \sqrt{1 - \tan^2(\xi) - 2b^2/a^2} \quad [6.56]$$

The integral was performed numerically for a range of wavelengths, to evaluate Ω_{eff} for an ellipsoidal mirror of major axis $a=10\text{cm}$, minor axis $b=0.9\text{cm}$ and overall length 16cm , for the four previously mentioned reflecting surfaces. In the absence of reflection losses (ie. $R(\xi)=1$ for $\xi<8.5^\circ$), a gold surface mirror would be able to completely collect a solid angle of $2\pi/28.7$ (as shown in table 6.2). The resultant efficiencies are illustrated in figures 6.19 to 6.22, in addition to the efficiencies which would result in the absence of any reflection losses up to the critical angle θ_c as defined by equations [6.31] and [6.32]. As indicated by the reflectivities of figures 6.15 to 6.18, mirror surfaces of either nickel or chromium would offer a greater collecting area than either gold or iridium. Assuming a source of X-rays which has a constant intensity throughout the water window region, either of these would offer an efficiency of at least



Figures 6.15 to 6.18: Calculated reflectivities of chromium, nickel, gold and iridium.



Figures 6.19 to 6.22: Calculated solid angles collected by ellipsoidal mirrors with chromium, nickel, gold and iridium reflecting surfaces.

50% of the value assuming no losses. A sharp cut-off at 2nm is also evident, which is desirable, as studies have indicated (for example, those by Spiller [1983]) that shorter wavelength components in the illuminating X-rays may actually decrease the resolution in the final image, due to the emission of secondary electrons in the photoresist, causing collateral exposure.

For a metal to show a high degree of reflectivity (ie. a high reflectance, even at large grazing angles), it is evident that a large value of δ and a small value of β is required. The former ensures that the cut-off angle will be large, while the latter that the reflectivity up to this angle will be high. Table 6.3 shows the values of δ and β for various elements which were considered as possibly suitable for use as reflecting surfaces, as calculated from the data of Henke [1982]. From this, we see that nickel or chromium do indeed appear to be the best choices for the mirror surface.

Element	ρ (g/cm ²)	A	2.36nm		4.47nm	
			$\delta \times 10^3$	$\beta \times 10^3$	$\delta \times 10^3$	$\beta \times 10^3$
Ti	4.51	47.9	1.638	1.873	5.564	1.296
V	6.10	50.9	0.571	2.778	7.968	1.921
Cr	7.19	52.0	2.248	0.424	10.550	2.709
Mn	7.43	54.9	2.660	0.484	10.890	3.031
Ni	8.90	58.7	4.207	0.855	14.480	5.744
Cu	8.96	63.6	4.132	0.994	14.050	5.946
Mo	10.20	95.9	3.770	3.204	4.305	5.964
Pd	12.00	106.4	3.041	3.952	6.805	3.183
Ag	10.50	107.9	2.333	3.646	7.242	3.051
W	19.30	183.5	5.435	3.988	10.990	12.890
Os	22.60	190.2	6.083	4.805	12.350	13.700
Ir	22.50	192.2	5.815	4.940	9.862	13.150
Pt	21.40	195.1	5.226	4.553	9.537	12.210
Au	19.30	197.0	4.762	4.258	7.508	10.430

Table 6.3: Values of δ and β at limits of the water window.

6.5 USE OF X-RAY OPTICS

Although ellipsoidal mandrels of the required shape could be readily made for a

few hundred pounds, the production of a surface smooth to several nanometres proved to be somewhat problematical. The only organization apparently able to meet such specifications was the Czechoslovakian Academy of Science. The cost of a pair of mirrors, of over £7000, unfortunately could not be met from the funds available to the microscopy project, and so several pairs of mirrors were made to a far lower surface quality in an attempt to see whether some degree of focusing could be achieved and whether this would be of any use in the X-ray microscope. Six stainless steel positive mandrels were commissioned from Oxford Engineering Ltd., each consisting of half an ellipsoid of major axis 10cm and minor axis 0.9cm as described in section 6.4.5, on a cylindrical base. The initial surface finish obtained from the machining process was quoted as $0.4\mu\text{m}$. Each mandrel was then re-mounted on a lathe and hand polished by using increasingly fine grades of Scotchbrite abrasive soaked in Brasso. In addition, the mandrels were then electropolished, a process in which each object was placed in a corrosive electrolyte bath as the anode and a current passed from a cathode. The current density is greatest at any sharp edges in the anode, leading to an increased rate of dissolution in the electrolyte; in this way, the surface of the mandrel was further smoothed by the removal of $\sim 20\mu\text{m}$ of material. The improvement in the surface obtained by these processes is apparent from plate 6.1. The elliptical and flange surfaces were then electroplated with nickel to a nominal thickness of 1mm and this nickel shell removed from the stainless steel positive. Two such shells were glued together to produce a complete mirror as illustrated in plate 6.2.

6.5.1 Results

A number of measurements were made to evaluate the extent to which the ellipsoidal mirror was able to focus soft X-rays. From sections 6.4.3 and 6.4.6, it has been shown that the mirror would collect an effective solid angle of $2\pi/126$ assuming it was 100% efficient after considering absorption losses at reflection.

Initially, the flux delivered to an area of 1mm^2 in the focal plane was measured using the RAL1 photodiode, filtered with two 100nm thick Si_3N_4 windows, each of which was coated with 220nm of vanadium. In this situation, the mirror increased the



Plate 6.1: The mandrels used for production of the ellipsoidal mirrors, illustrating the improvements achieved by hand polishing and electropolishing.





Plate 6.2: The grazing incidence ellipsoidal X-ray mirror.



flux to the 1mm^2 area by a factor of 26 over that obtained in its absence. This suggested that it was collecting an effective solid angle of

$$\begin{aligned}\Omega &= 26(4\pi.1^2/4\pi.200^2) \\ &= 2\pi/9700\end{aligned}\tag{6.57}$$

indicating that the mirror was just 1.3% efficient into this area.

In a second experiment, the standard mylar-supported vanadium filter was used with the RAL1 photodiode, with a pinhole of diameter $50\mu\text{m}$ placed on axis in the focal plane of the mirror. This resulted in an increase by a factor of 124 in flux over that obtained in the absence of the mirror, suggesting, by comparison to the previous value of 26 over a larger area in the focal plane, that the mirror was bringing the X-rays to a relatively sharp focus.

Considering this smaller area, the increase in flux obtained by the use of the mirror was equivalent to that which would have resulted if the detector had been moved closer to the plasma source by a factor of $124^{1/2}$; ie. to 18mm. Unfortunately, this increase was not as large as that which was obtained during the imaging experiments, where values of the plasma to resist distance of as little as 6mm could be used. It was presumed that the low efficiency of the mirror was due to relatively large scale deviations of the mirror's form from that of a perfect ellipse and an unacceptably high degree of surface roughness, causing increased losses at reflection.

6.6 CONCLUSIONS

The theoretical calculations made in sections 6.4.3 and 6.4.6 seemed to suggest that the use of a grazing incidence ellipsoidal nickel mirror might offer significant benefits in the application of SXCM. However, the problems associated with its implementation, apparent from the measurements made in section 6.5, indicated that further attention would have to be paid to the production technique used to achieve an optic of sufficiently accurate form and smooth finish before such a component could be of any use in the focusing of soft X-rays.

Unfortunately, time did not permit a more detailed investigation to be made of the use of grazing incidence optics for the application of SXCM. In view of the results

obtained with this optic of length 16cm however, it was realized that a much shorter mirror might well have been more effective in the tight focusing of soft X-rays in that it would be easier to manufacture with smaller deviations from the ideal shape while those deviations which were present would, by the nature of the shorter path lengths that would result, have a less detrimental effect of the quality of focus obtained. It is hoped that work on the use of X-ray optics with the Oxford microscope will continue in the near future.

CHAPTER SEVEN

SOFT X-RAY IMAGING

7.1	INTRODUCTION
7.2	THE IMAGING TECHNIQUE
7.3	RESIST DISSOLUTION RATES
7.3.1	Model of resist dissolution
7.3.2	Results
7.4	USE OF THE ATOMIC FORCE MICROSCOPE
7.4.1	Operation of the AFM
7.4.2	Image processing
7.5	BIOLOGICAL IMAGING
7.5.1	<i>Rhytidiadelphus loreus</i>
7.5.2	<i>Schizosaccharomyces pombe</i>
7.5.3	<i>Bacillus cereus</i>
7.5.4	<i>Chlamydomonas</i>
7.6	FUTURE BIOLOGICAL INVESTIGATIONS
7.6.1	Electroporation processes
7.6.2	<i>Escherichia coli</i>
7.6.3	Chromosomes
7.7	SUMMARY

7.1 INTRODUCTION

Once the entire laser system had been upgraded from the initial '1 Joule' design and the plasmas generated by each of the four target materials fully characterized, a number of different biological specimens were imaged with the microscope. Initially, two subjects were chosen for ease of handling in order to test the microscope equipment and gain familiarity with the process of working the system. Once satisfactory results had been obtained and a few minor technical difficulties overcome, studies were commenced on biological systems brought to the Clarendon Laboratory for imaging by external users. The microscope could be ready for operation at a day's notice, and typically a dozen resists would be exposed one a session. Once the AFM had become available within the University for use in conjunction with the X-ray microscope, the entire imaging process could be completed within a single working day.

This rapid accessibility highlighted the advantages of a dedicated system over X-ray microscopes set up at national facilities, which frequently may only be used for a limited period of time which has to be booked well in advance.

7.2 THE IMAGING TECHNIQUE

The laser generated plasmas used as a source of X-rays in this experiment were created in a large target chamber designed and built specifically for this type of application. A schematic diagram of the arrangement is given in figure 7.1. A vacuum feed-through port (described by Cotton [1990]) enabled a specimen holder, loaded with a Si_3N_4 window, polymethyl methacrylate (PMMA) coated wafer and biological specimen, to be introduced into the vacuum environment of the chamber and positioned a fixed distance from the laser generated plasma. By using this device, an exposure could be made every 4 minutes once the laser system had been set up, although in practice this was limited by the speed with which new specimens could be loaded into the specimen holder.

A cross-section of the specimen holder is shown in figure 7.2. Two O-ring seals ensured that the subject was kept under atmospheric conditions up to the point of exposure even when the holder itself was placed in the vacuum chamber. Before securing the back plate of the holder, the nylon plunger was advanced so as to bring the specimen up to the 100nm thick Si_3N_4 window and into close contact with the PMMA-coated wafer. Care had to be taken not to over-tighten however, as the thin Si_3N_4 windows were extremely fragile, despite being able to withstand a pressure difference of 1 atmosphere. Debris emitted by the wire target did, in every case, cause this window to break; however, the image of the specimen was recorded before the debris reached the holder and so a representation of the living specimen still resulted nevertheless. Cases where the window broke before exposure (as a result of mishandling during the introduction of the holder into the chamber) were easily identifiable in that the PMMA dissolution rate during development was far greater than that for resists exposed behind intact windows and also the recorded image showed fragments of the broken window.

7.3 RESIST DISSOLUTION RATES

To obtain an approximate indication of the relationship between the rate of resist dissolution and the X-ray flux incident upon it, a Leitz MPV-SP microspectrophotometer was used to measure the thickness of the resist remaining on a number of silicon wafers after increasing amounts of development, using a 1:1 mixture

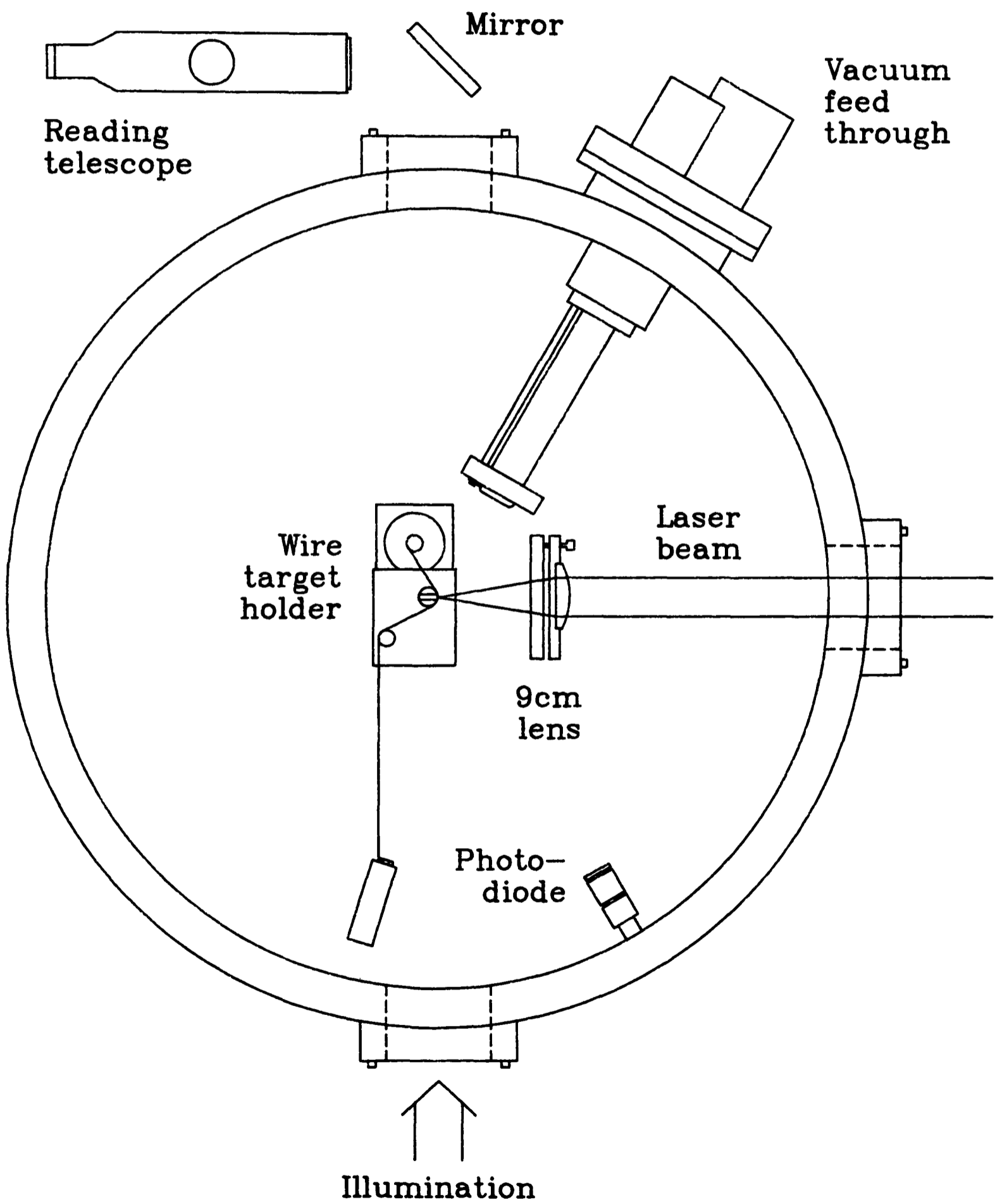


Figure 7.1: The target chamber and associated equipment used for X-ray imaging.

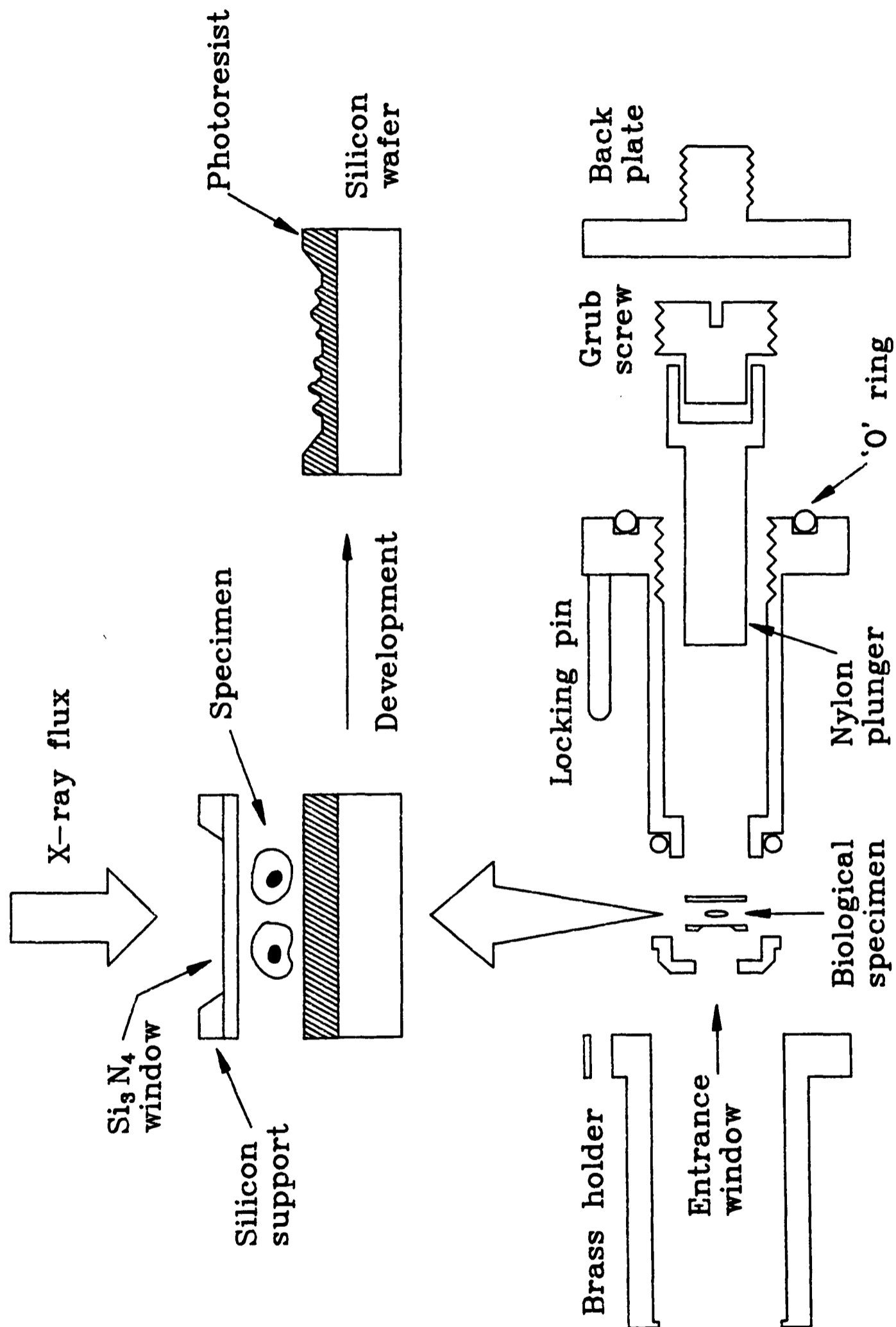


Figure 7.2: The specimen holder used in the target chamber and the SXCM process.

of methyl isobutyl ketone (MIBK) and isopropyl alcohol (IPA) at 18°C. Twenty one resists were examined, each having been exposed to various amounts of soft X-rays, generated either by a molybdenum or tungsten target, and subject to various types of filtering. Table 7.1 lists the range of parameters involved in the measurements; the values for incident flux are based on readings from the RAL1 photodiode used with a mylar-supported vanadium filter.

Target material	Filtering	Plasma to resist (mm)	WW flux on resist (mJ/cm ²)
Molybdenum	Si ₃ N ₄ +Al	9.0	6.2
	Si ₃ N ₄	9.0	7.3
	none	9.0	12.5
	Si ₃ N ₄	10.0	6.0
	none	11.6	7.3
	none	13.0	5.9
Tungsten	Si ₃ N ₄ +Al	9.0	9.4
	Si ₃ N ₄	9.0	11.1
	none	9.0	18.0
	Si ₃ N ₄	10.0	8.8
	none	11.6	11.1
	none	13.0	8.8

Table 7.1: Conditions employed for the exposure of the photoresists.

The Si₃N₄ windows used were 100nm thick and transmitted an average of 62% of X-rays within the water window region; when coated with 50nm of aluminium, the water window transmission was reduced to 52%. The transmission of 50nm of aluminium is given in figure 7.3.

7.3.1 Model of resist dissolution

If a resist is exposed to an incident flux, E_0 (measured in energy per unit area), of radiation within the water window region , then at a distance x below the surface,

the exposure will be given by

$$E_x = E_0 e^{-\alpha x} \quad [7.1]$$

where α is the average linear absorption coefficient of PMMA for that wavelength range. For water window X-rays, this has a value of $2.62 \times 10^6/\text{m}$ [Kirz 1985]. The rate of resist dissolution in a solvent such as MIBK is generally modelled by the expression

$$R = R_c (E/E_c)^n \quad [7.2]$$

[Jacobsen 1988] where n and R_c are constants and we choose $E_c = 1 \text{ mJ/cm}^2$ in this particular application for convenience. We would then expect a thick film of PMMA to dissolve by an amount x in a time t according to the formula

$$x = (1/\alpha n) \ln(R_c [E_0/E_c]^n \alpha n t + 1) \quad [7.3]$$

The dissolution rate may also be measured as a function of the dose absorbed per unit mass by the PMMA resist. In this case, considering a square of unit area exposed to a flux of E_0 as before, a small depth, x , of resist will absorb an amount of energy given by

$$E_0(1 - e^{-\alpha x}) \sim E_0 \alpha x \quad [7.4]$$

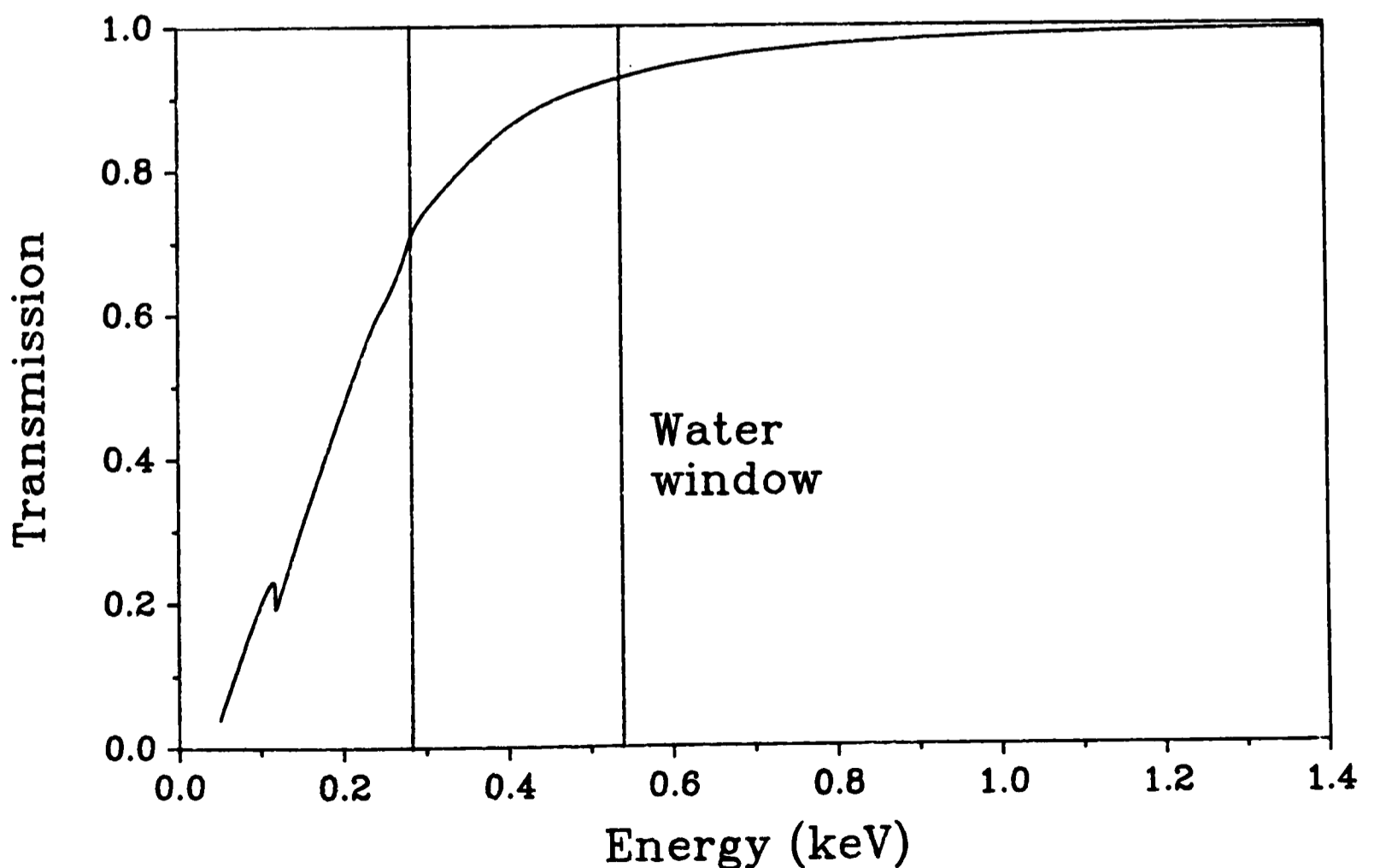


Figure 7.3: The transmission of 50nm of aluminium.

Consequently, the dose received will be

$$D = E_0 \alpha / \rho \quad [7.5]$$

where $\rho = 1.18 \times 10^3 \text{ kg/m}^3$ is the density of PMMA. This may be expressed in the unit most widely used in the biological sciences to measure absorbed radiation dose;

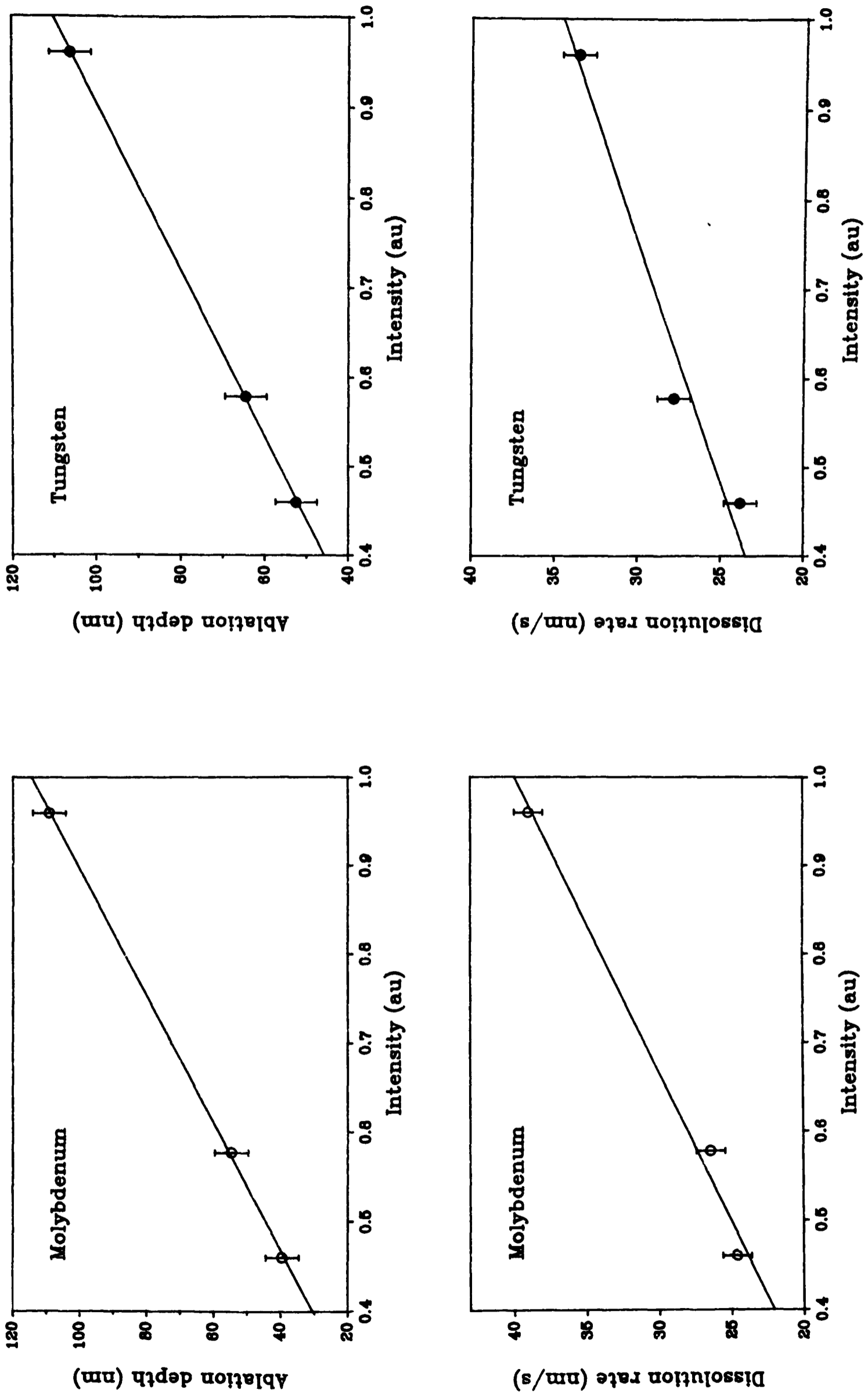
$$D = 2.22 E_0 \text{ Mrad} \quad [7.6]$$

if E_0 is expressed in units of mJ/cm^2 .

7.3.2 Results

From the measured dissolution rates, it was immediately apparent that for both molybdenum and tungsten targets, there was a very significant UV and VUV component to the laser generated plasma source. Those resists which were exposed to unfiltered radiation showed an initial dissolution rate of at least 24nm/s compared to a maximum rate of 2nm/s for any of the resists filtered by 100nm of Si_3N_4 alone. It was also noted that, in the case of unfiltered exposure, up to 100nm of the resist material had been removed, probably by photoablation, before any chemical development was undertaken. Since the photodiode did not measure this long wavelength component, its absolute magnitude for each resist is not known. However, its relative intensity between resists could be calculated from the measured plasma to resist distances, and so the initial rates of dissolution and amounts of photoablation could be given as a function of intensity in arbitrary units, and these are presented in figures 7.4 to 7.7. The dissolution of a typical unfiltered resist is shown in figure 7.8.

For those resists which had been exposed to radiation filtered either by a Si_3N_3 window alone or by an aluminium-coated Si_3N_4 window, the formula of [7.3] was fitted to the data by means of a least squares fit, varying the values of the parameters n and R_c . For these resists, it was also found necessary to introduce a time offset, representing an initial period of up to 30s during which there appeared to be little or no dissolution in MIBK, as illustrated in figure 7.9. The cause of this initial passivation, in contrast to those resists which had not been filtered, was not clear, although it may have resulted from a thin layer of some semi-inert material being present on the surface of the PMMA resist, which was ablated by the unfiltered



Figures 7.4 to 7.7: Photoablation depths and dissolution rates for unfiltered resists exposed to molybdenum and tungsten plasmas.

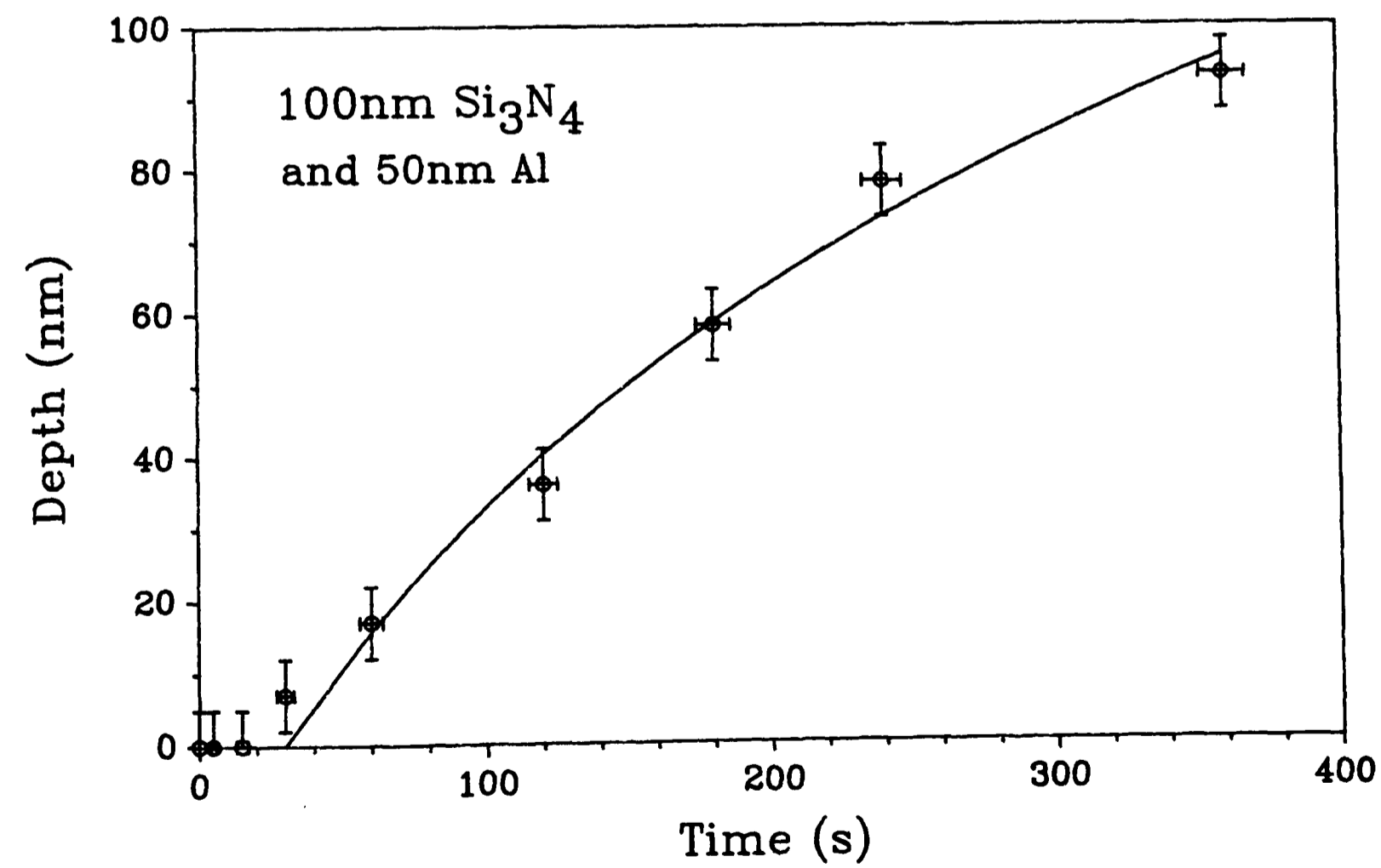
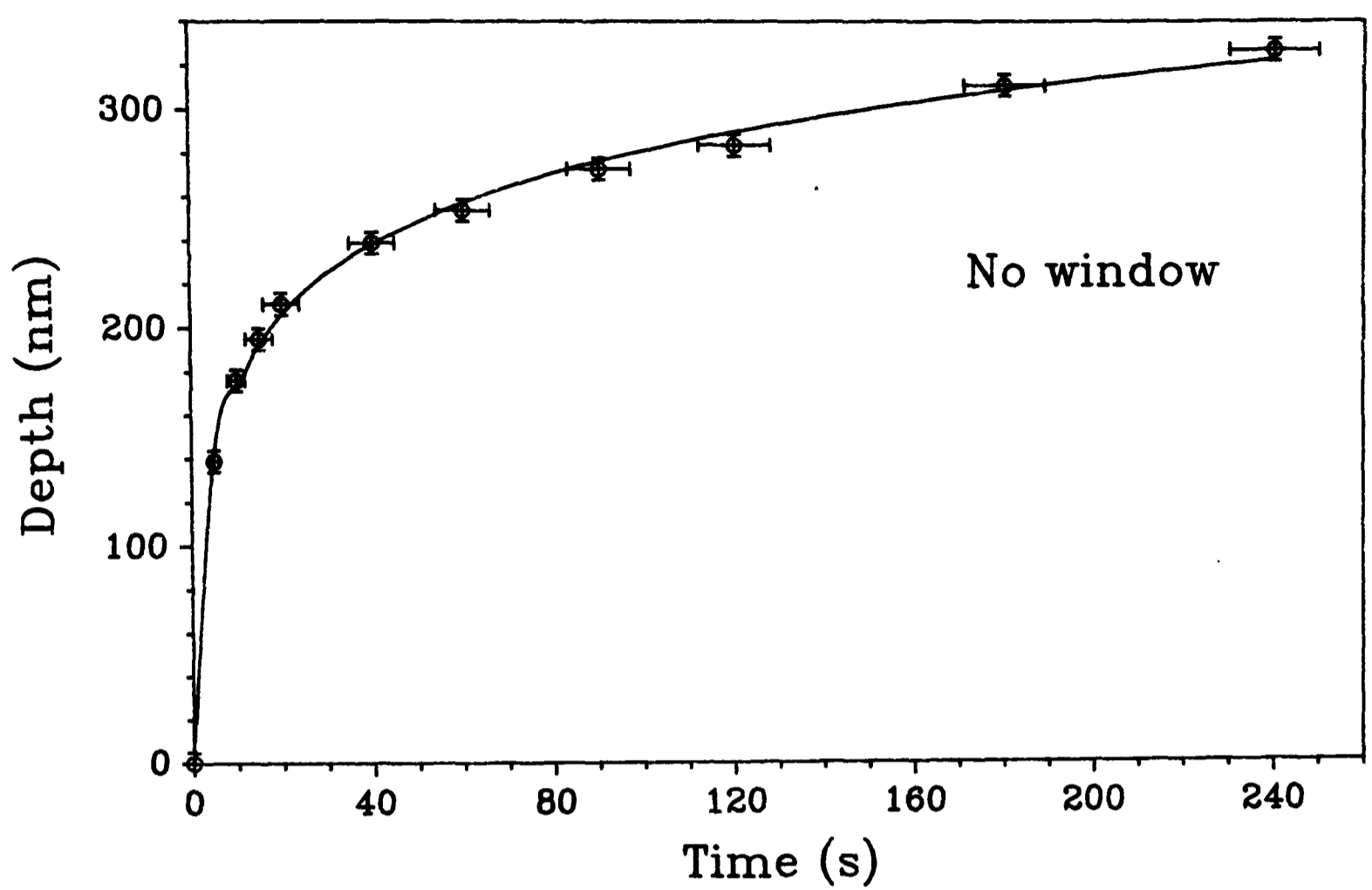


Figure 7.8: The dissolution of a typical unfiltered resist, with theoretical fitted curve.

Figure 7.9: The dissolution of a typical resist, filtered by Si_3N_4 and aluminium, with theoretical fitted curve.

radiation but which temporarily delayed the dissolution of those which had been filtered. Table 7.2 gives the mean values for the parameter n obtained with each of the various arrangements used to expose the resists in addition to a mean dissolution rate for the time period over which the measurements were made.

Target material	Filtering	WW flux (mJ/cm ²)	n	Dissolution rate (nm/s)
Mo	Si ₃ N ₄ +Al	6.2	3.36±0.59	0.34±0.05
	Si ₃ N ₄	7.3	3.45±0.58	0.79±0.13
	Si ₃ N ₄	6.0	3.21±0.45	0.58±0.04
W	Si ₃ N ₄ +Al	9.4	6.29±0.48	0.29±0.01
	Si ₃ N ₄	11.1	4.89±0.06	0.71±0.12
	Si ₃ N ₄	8.8	3.35±0.93	0.56±0.06

Table 7.2: Dissolution rates measured from the various resists.

As expected, the rates obtained for the Si₃N₄ filtered resists show a decrease with decreasing flux. The lower dissolution rates for resists filtered by Si₃N₄ and aluminium compared to those exposed to a flux of equal magnitude (within the water window range of wavelengths), but with only Si₃N₄ filtering, indicate that the 50nm of aluminium did remove longer wavelength components (ie. VUV) which were present in the plasma emission which were not removed by the Si₃N₄ alone. The aluminium will have also greatly attenuated any UV wavelengths which may have resulted from reflection of the incident laser beam by the target wire. The contribution of such radiation to the SXCM imaging process would decrease the resolution obtained, both by way of decreasing the contrast (VUV components, for which the cross-sections for absorption shown by water and carbon are similar) and increasing the Fresnel diffraction (longer wavelength components, relevant to equation [2.13]). These observations illustrate the importance of filtering in SXCM in order to obtain high resolution images.

Spiller [1977], using 0.83nm radiation and a much larger flux of 1J/cm², observed a dissolution rate of 3.8nm/s and variation $R=kE^2$ using a 1:1 mixture of

MIBK and IPA developer. At a smaller exposure of $10\text{mJ}/\text{cm}^2$ and 100% MIBK developer, the rate was reduced to only $\sim 0.15\text{nm}/\text{s}$. This is in rough agreement with the results of Tomie [1991] who observed a rate of $\sim 0.5\text{nm}/\text{s}$ and variation $R=kE^{1.5}$ for an incident flux of $10\text{mJ}/\text{cm}^2$ of water window X-rays. Haelbich [1984] also measured a rate of $0.5\text{nm}/\text{s}$ for a flux of $10\text{mJ}/\text{cm}^2$ at 1nm wavelength using 100% MIBK to develop the exposed PMMA.

These results indicate that to obtain an appreciable depth of development, as suitable for viewing with an SEM or AFM for example, at least 3 minutes of treatment with a 1:1 solution of MIBK and IPA is required.

7.4 USE OF THE ATOMIC FORCE MICROSCOPE

As mentioned in section 2.5, a consortium of groups within the University, including the Laser Group, made a successful bid for University support to purchase a Park Scientific Instruments scanning probe microscope system. This instrument has facilities for repulsive and attractive mode AFM as well as scanning tunneling microscopy (STM). A wet cell holder for AFM was also provided, and the entire system was installed by Dr. Cotton and this author. At the time, this was one of only two such systems operating in the United Kingdom.

For the viewing of uncoated resists, the repulsive mode AFM was used, since the samples were not electrically conducting and therefore could not be viewed with the STM module. Although the operation of the repulsive mode AFM is considered more difficult than STM, it was found that, with practice, a new resist could be loaded into the microscope head and imaged within about 5 minutes.

7.4.1 Operation of the AFM

The AFM working in repulsive mode is similar in principal to a profilometer. The specimen, mounted on an SEM stub, is held in an xyz piezo tube (which typically has an xy range of $\sim 50\mu\text{m}$ and z range of $\sim 10\mu\text{m}$) and is repeatedly scanned in the x-y plane. The height measurement device is a small pyramidal tip of crystalline Si_3N_4 , approximately $2\mu\text{m}$ tall, which is grown on the face of a 600nm thick triangular Si_3N_4

cantilever. For ease of handling, each cantilever is attached to a small, $600\mu\text{m}$ thick pyrex chip, which is inserted into the AFM head. This is then grossly positioned, using an on-axis optical microscope, so that the sharp tip of the pyramid is close to the surface which is to be viewed. A visible laser diode beam is focused onto the back surface of the cantilever, above the position of the pyramid tip, and a position sensitive photodiode (PSPD) then monitors the reflection of the laser beam from the back of the cantilever. During the scanning process, the specimen is raised or lowered in the z direction so as to cause a constant fixed deflection of the cantilever, as measured by the PSPD; a feedback loop between the piezo and the PSPD is used to maintain this condition. The extension of the piezo in all three directions is monitored by a computer in order to build up a height profile of the specimen. The technique is represented schematically in figure 7.10.

7.4.2 Image processing

The data generated by this process is initially presented as a grey-scale picture,

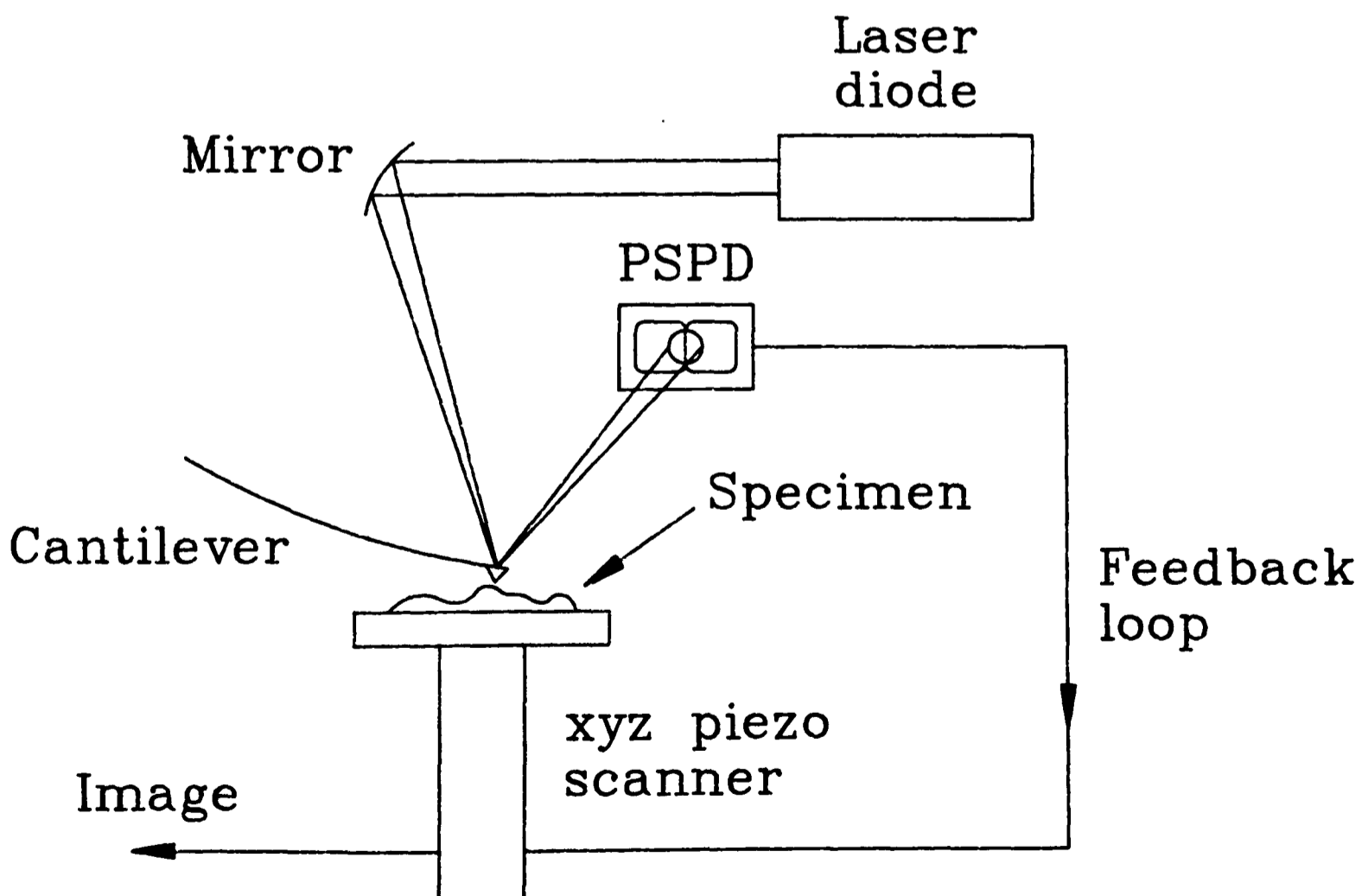


Figure 7.10: A schematic representation of the atomic force microscope image formation process.

with the height of the resist at each point proportionally represented by an intensity. In order to make the image easier to interpret visually, it may be 'shaded' (an option available within the software package which controlled the various functions of the microscope) so that a 'solid surface' is generated. In this way, the image may be made to more closely resemble that which would have been obtained had the resist been viewed with an SEM, and as such, was felt to be most suitable for those using the X-ray microscope who were generally more familiar with the output obtained from an SEM than an AFM.

7.5 BIOLOGICAL IMAGING

Once the entire laser system had been upgraded from the initial '1 Joule' system and the various target materials investigated, there was unfortunately not as much time available as might have been wished for to carry out biological studies using the microscope. However, it is hoped to continue work with the microscope now that it has been developed to a point where imaging of biological specimens can readily be performed. Initially, two specimens were chosen for ease of handling to test the imaging process and the microscope system. These also provided the opportunity to make a direct comparison between the use of an SEM and AFM for the study of exposed and developed resists. The X-ray fluxes incident on the specimens viewed in this chapter were all calculated from measurements made with the RAL1 photodiode with a mylar-supported $0.5\mu\text{m}$ thick vanadium filter.

The next specimen to be studied was *Bacillus cereus*, provided by Dr. G.W. Gould from the Biomaterials Science Department of the Unilever Research Laboratory at Bedford. Considerable interest in the study of these spores by SXCM had been shown because of the possibility of viewing structures at sub-optical resolutions without the need for any type of specimen preparation.

Finally, the algae *Chlamydomonas* was imaged, and comparison made between the results obtained from SXCM and TEM.

7.5.1 *Rhytidiadelphus loreus*

As an initial test of the system, the moss *Rhytidiadelphus loreus* was chosen for study. A tungsten target was used and the plasma to specimen distance was 6mm. The flux transmitted through the Si_3N_4 window and incident on the specimen was $\sim 17\text{mJ}/\text{cm}^2$. Plate 7.1 shows images of the developed resist as viewed with an AFM.

The filaments observed here result from the first stage of growth following germination of the moss spores. At maturity, each cell may be several hundred micrometres long and $\sim 30\mu\text{m}$ in diameter. The numerous small ‘bumps’ within these protonemal filaments are chloroplasts (the photosynthetic organelles), indicating that these are of the chloronemal type, as opposed to caulonemal, which contain relatively few chloroplasts. All of the images show the cellulose cell wall as a ridge along the edge of the cell, and the transverse wall between adjacent filament cells may also be seen.

In cells undergoing lateral division, the nucleus migrates to this transverse wall before undergoing division itself (mitosis) and returning to the centre of the original filament cell. No such nucleus appears to have been recorded here, from which it may be deduced that these particular cells were not undergoing cell division at the time of imaging.

Finally, the linear ridges within the cell body are probably cytoplasmic strands traversing the vacuole up to the cell junction. In mature cells such as these, the body is highly vacuolate and the cytoplasm is arranged around the cell wall.

The fact that internal structure can be easily seen, even for a specimen thickness of $\sim 30\mu\text{m}$ such as these, suggests that the fluxes generated by the system were of a sufficient intensity to view a wide range of biological specimens.

7.5.2 *Schizosaccharomyces pombe*

A far smaller organism was then chosen; *Schizosaccharomyces pombe*, commonly known as ‘fission yeast’. A number of different strains were imaged using a tungsten target and a plasma to specimen distance of 6mm. In each case, the flux incident on the specimen was calculated to be $\sim 15\text{mJ}/\text{cm}^2$. Plate 7.2 shows images in the resist as obtained with a Cambridge S100 SEM. As explained previously, the

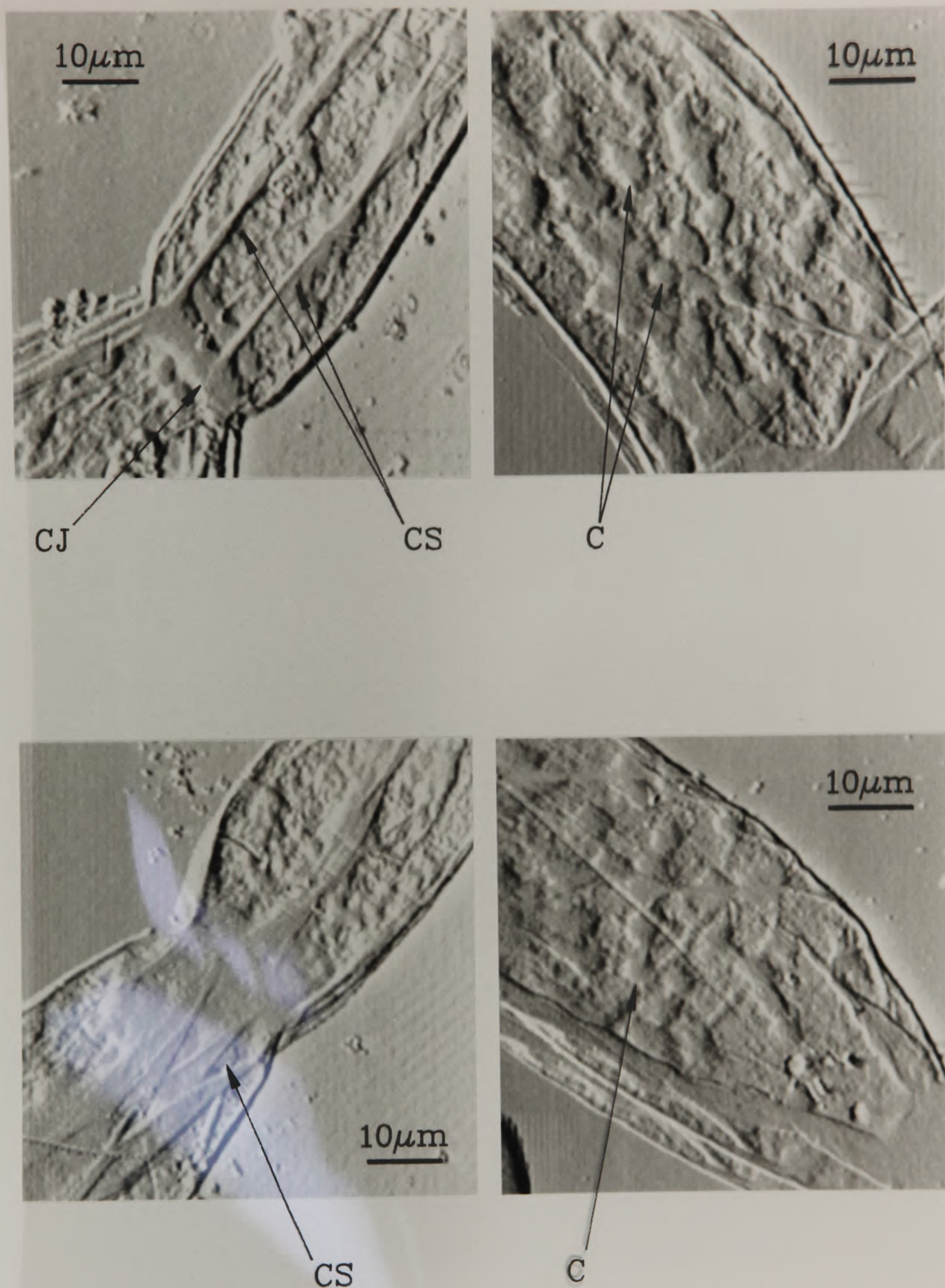
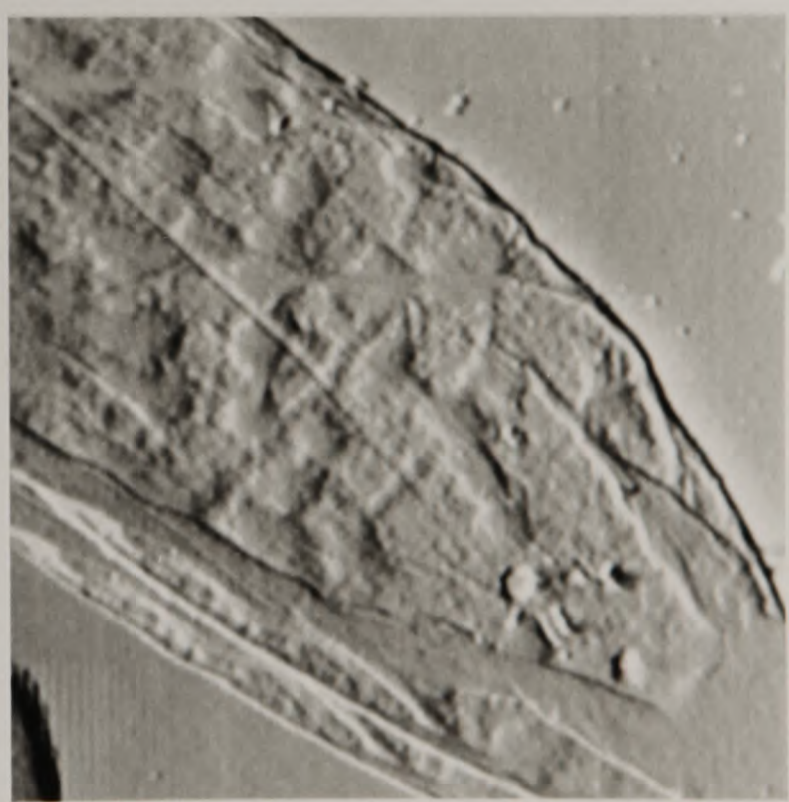
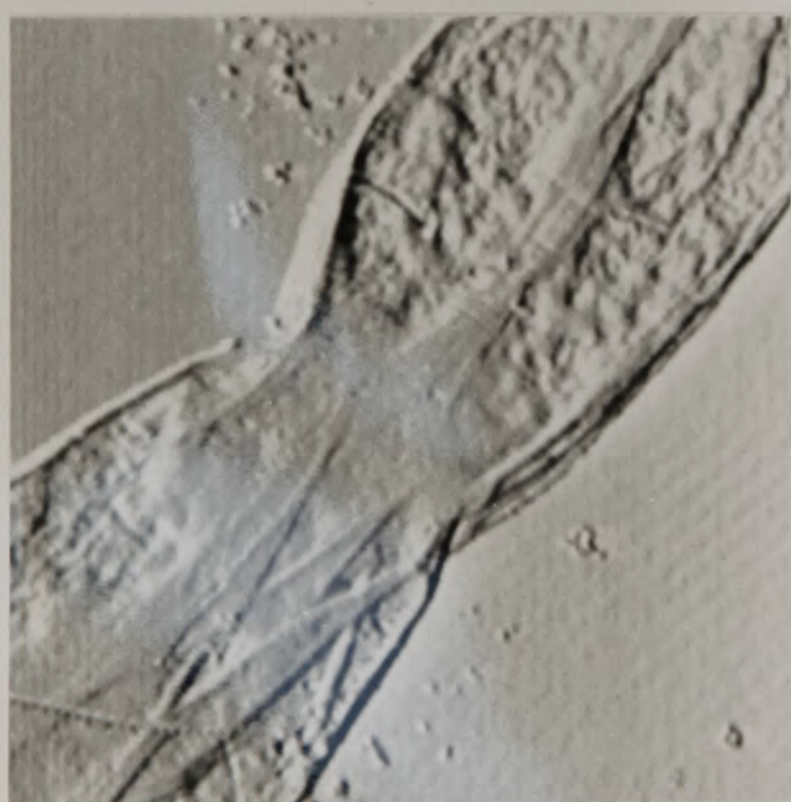
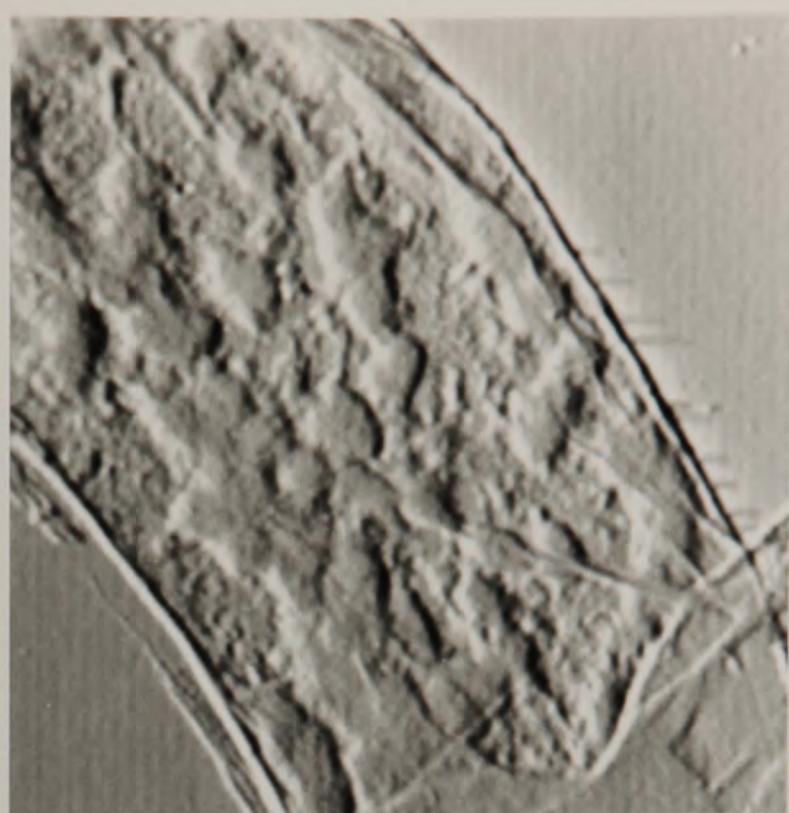
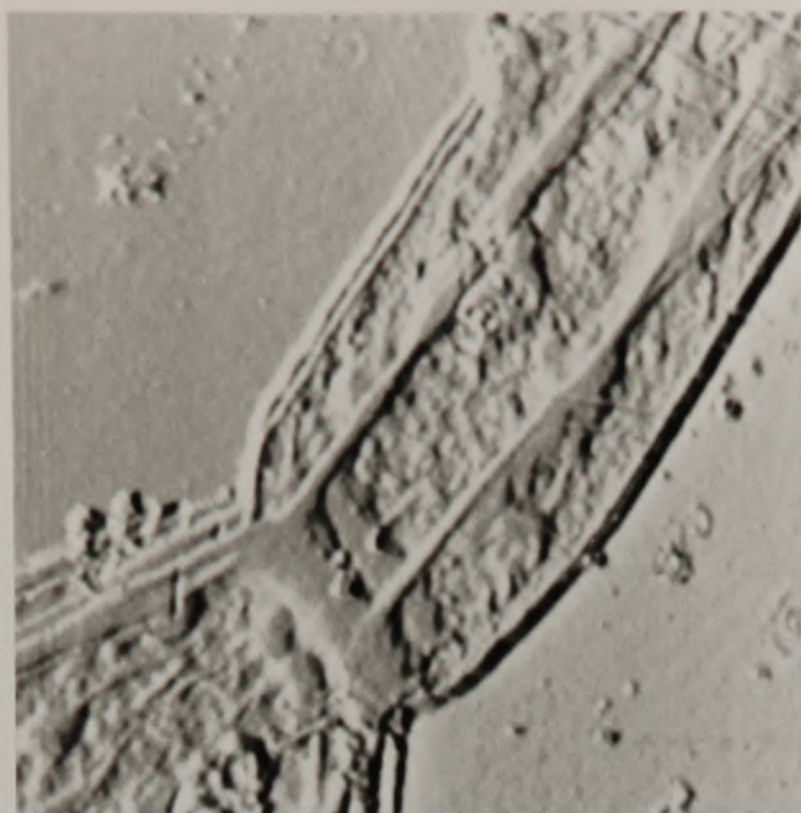


Plate 7.1: Images of the moss *Rhytidiadelphus loreus* obtained with an AFM.
CS - cytoplasmic strands; CJ - cell junctions; C - chloroplasts.



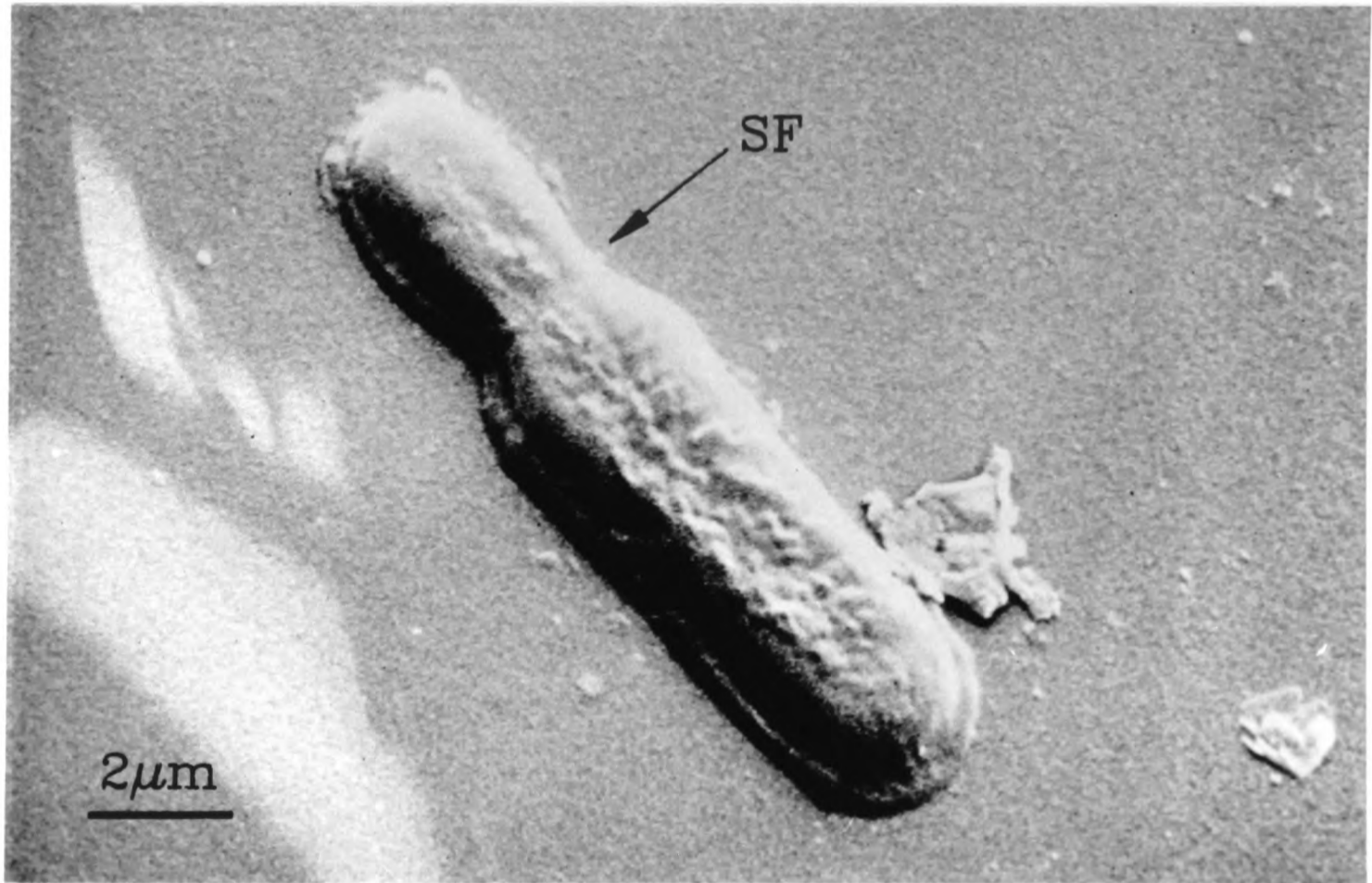
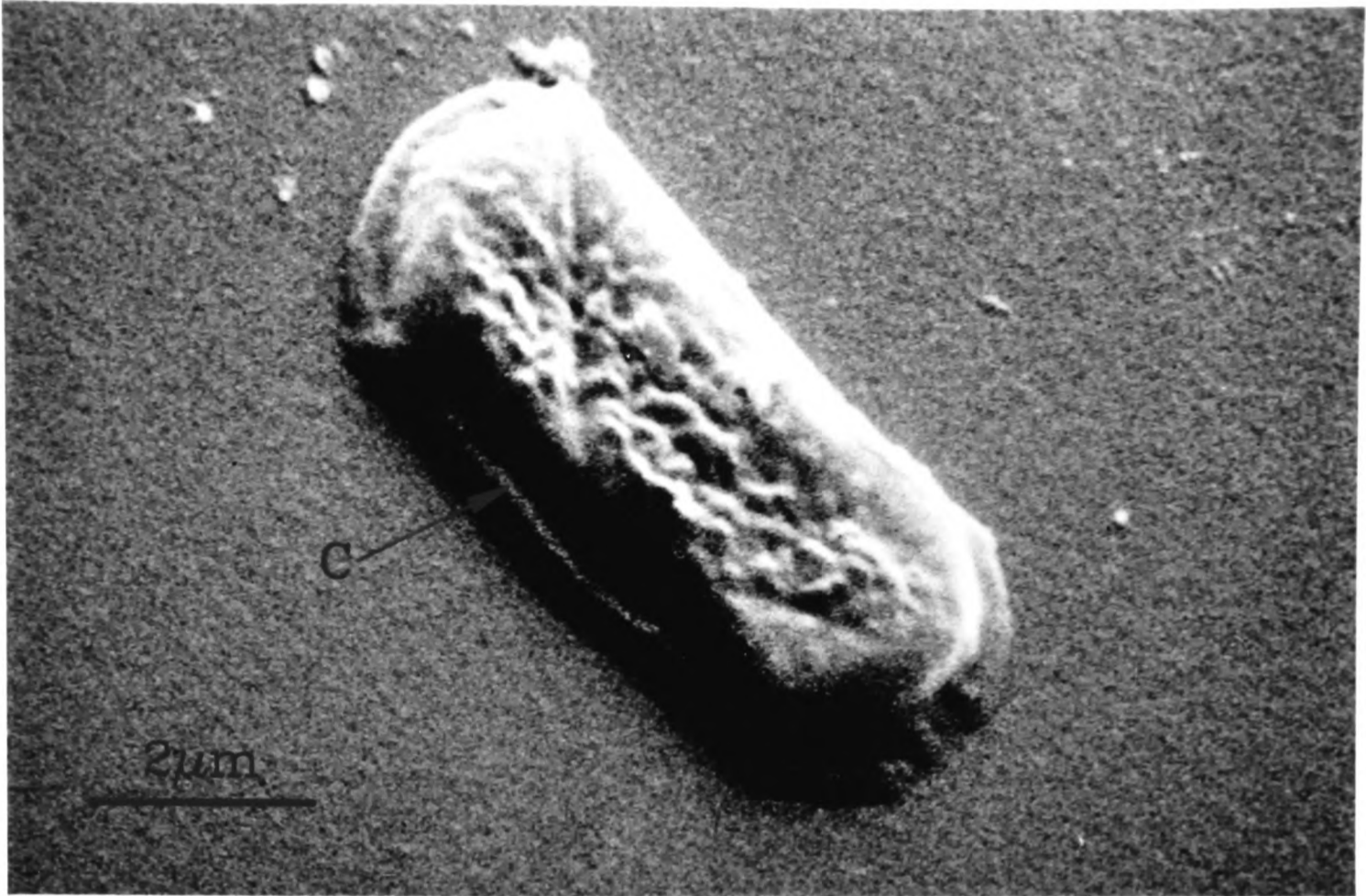


Plate 7.2: Images of *Schizosaccharomyces pombe*, recorded in a resist and viewed with an SEM, showing the cell wall (C) and septum formation (SF).



constraints imposed on the operating conditions of the SEM by the risk of beam damage to the photoresist has resulted in relatively 'noisy' images. Nevertheless, the central granular structure, typical of cells with ribosomal defective content such as these, is clearly visible along with a cell wall, which has a much lower carbon content than the rest of the organism. Septum formation is also apparent, this structure being present in cells undergoing the process of division. Features of 100nm in size are present in the image, a limit which may have been imposed by the SEM readout stage of the process.

In plate 7.3, images obtained with the AFM show similar features, in addition to bud scars along the side of the cells. These scars are formed during binary fission of the cells as they undergo a replication process. The cell wall is shown in greater detail in plate 7.4 along with a close-up of the central granular structure. As an indication of the resolution obtained in this particular series of images, the 25-75% points in the cross-section profile of a number of these granular structures represented in plate 7.4 were measured. A value of (66 ± 10) nm was obtained for the width between these points. Once the resists had been viewed with the AFM, they were subjected to further chemical development and then studied again with the AFM. As may be seen from plates 7.4 (bottom) and 7.5a, this resulted in the loss of some features as the larger-scale variations in carbon density became more apparent. In plate 7.5a, it is believed that the structure running along the length of the cell might be a mitotic spindle. During nuclear division, these microtubules draw the cell's chromosomes apart to opposite ends of the cell prior to the formation of the daughter nuclei, although the exact manner in which this process occurs is not fully understood. Finally, after further development, plate 7.5a shows the image of a cell which has been almost fully dissolved away.

7.5.3 *Bacillus cereus*

One of the most widely distributed soil saprophytes is *Bacillus cereus*, an organism, typically about $1\mu\text{m}$ in diameter, generated within the vegetative cells of particular types of bacteria. Once ingested, they multiply in the gut; producing large



2 μm



2 μm



1 μm



2 μm

Plate 7.3: Images of *Schizosaccharomyces pombe*, viewed with an AFM.
C - cell wall; BS - bud scars.



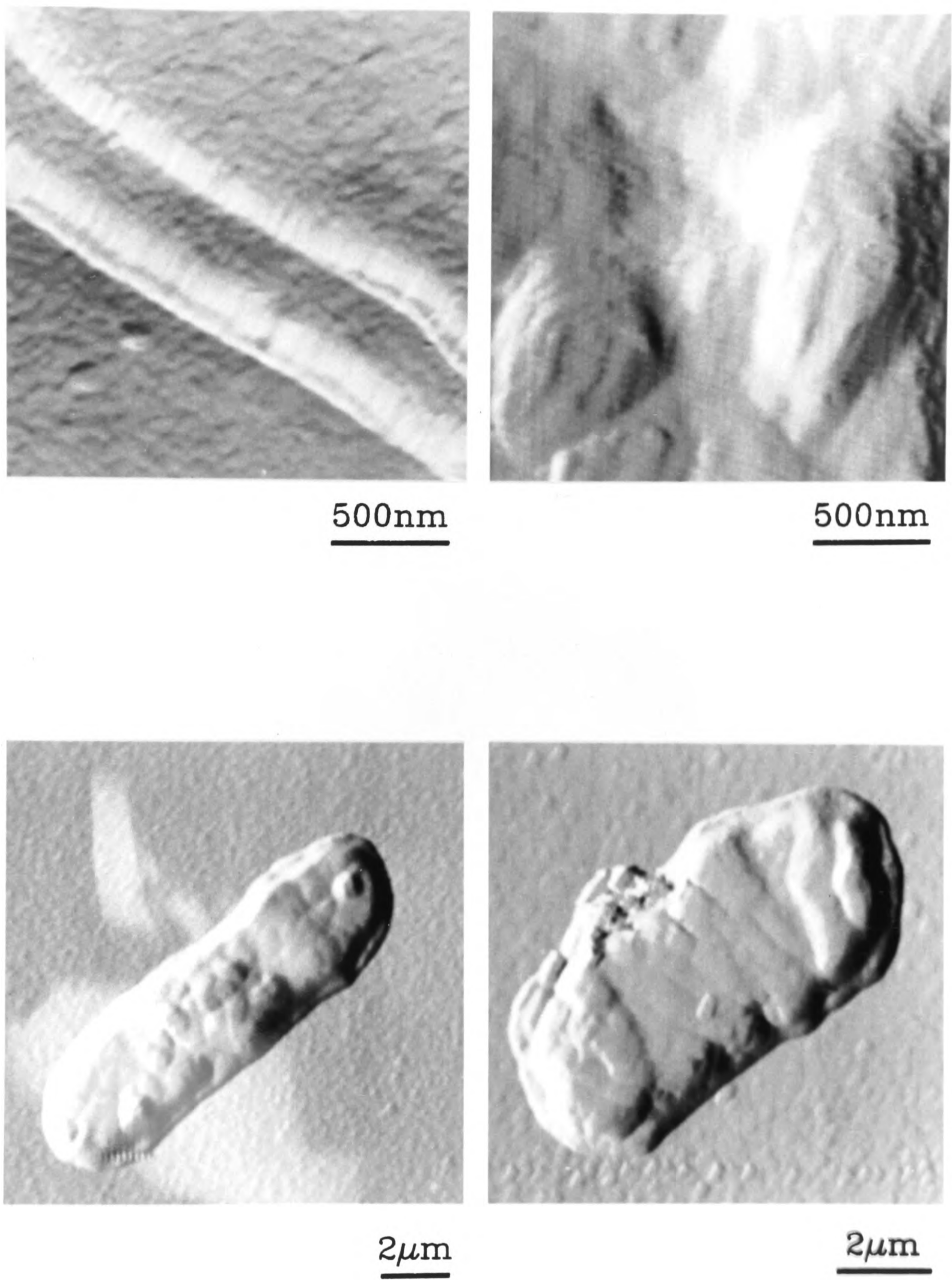
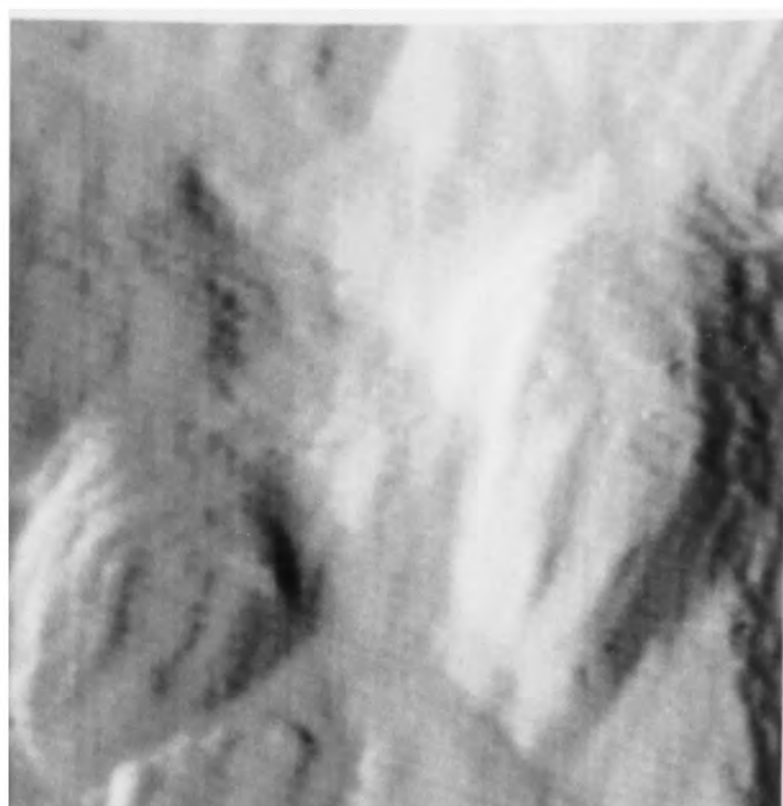
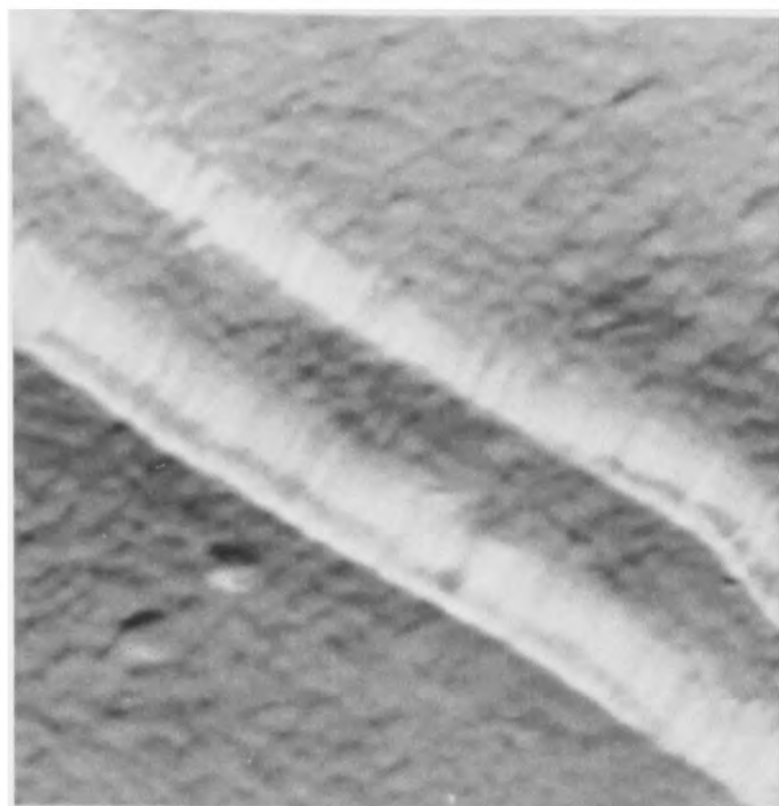


Plate 7.4: Images of *Schizosaccharomyces pombe*, viewed with an AFM.



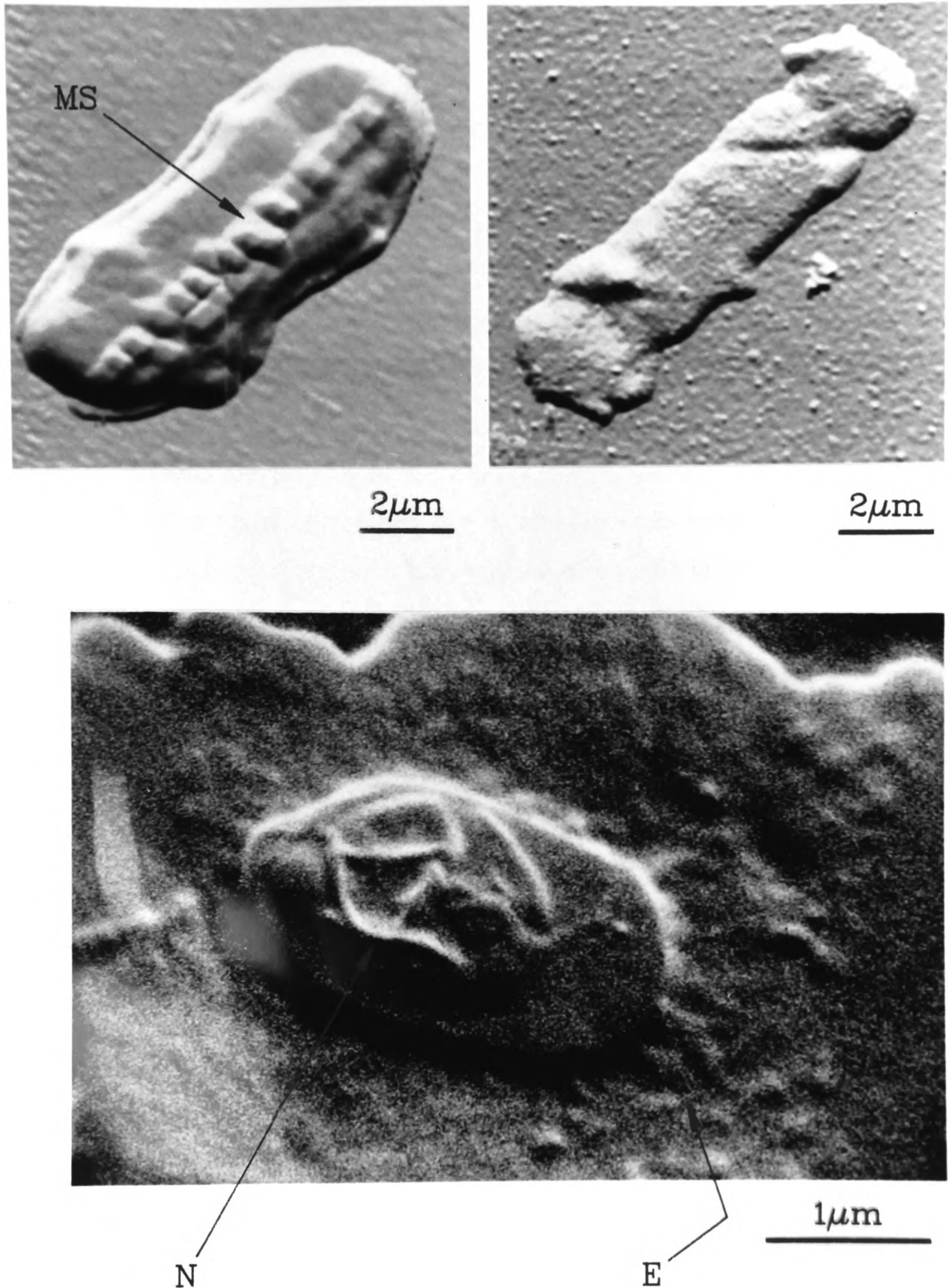
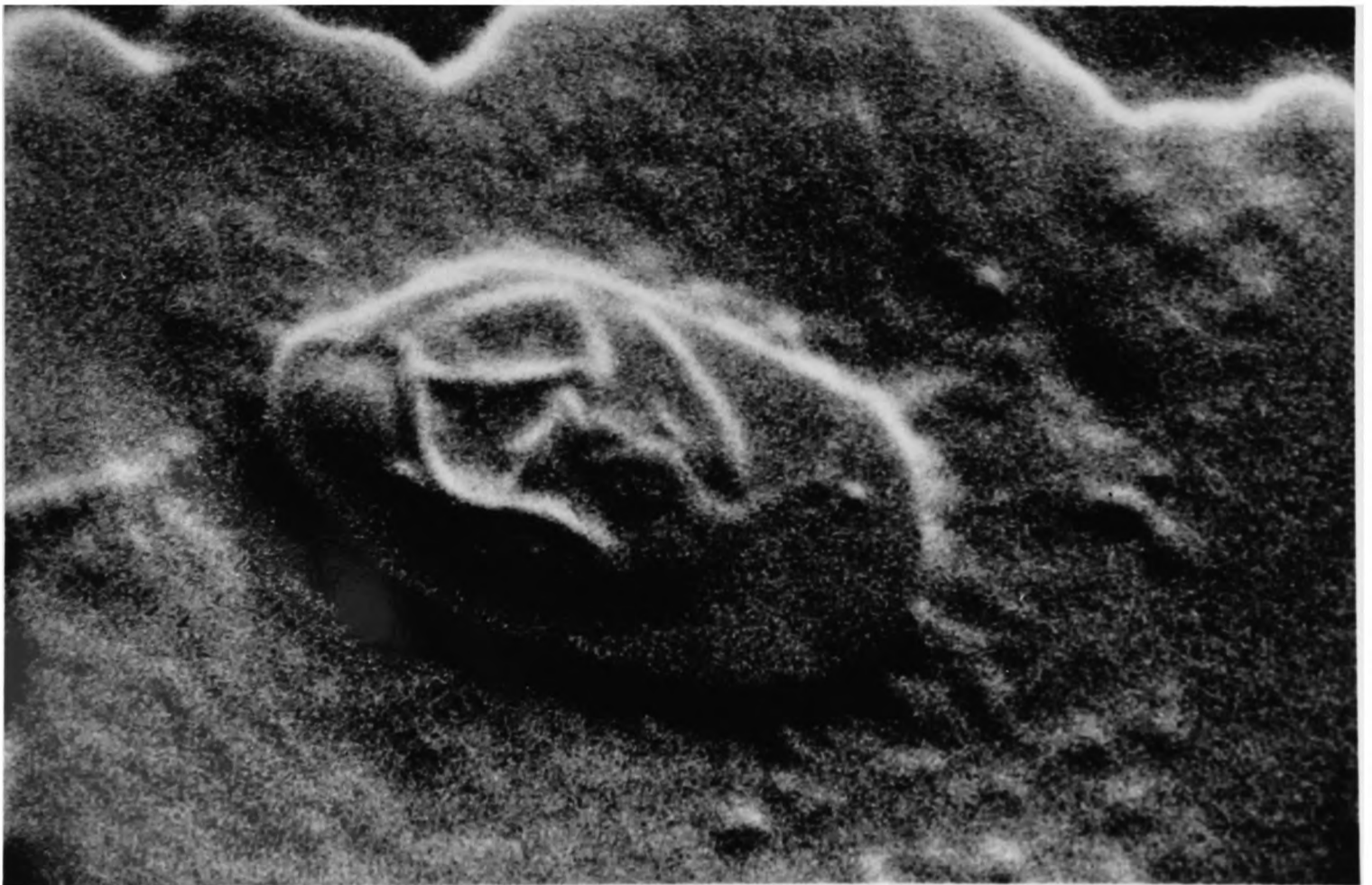
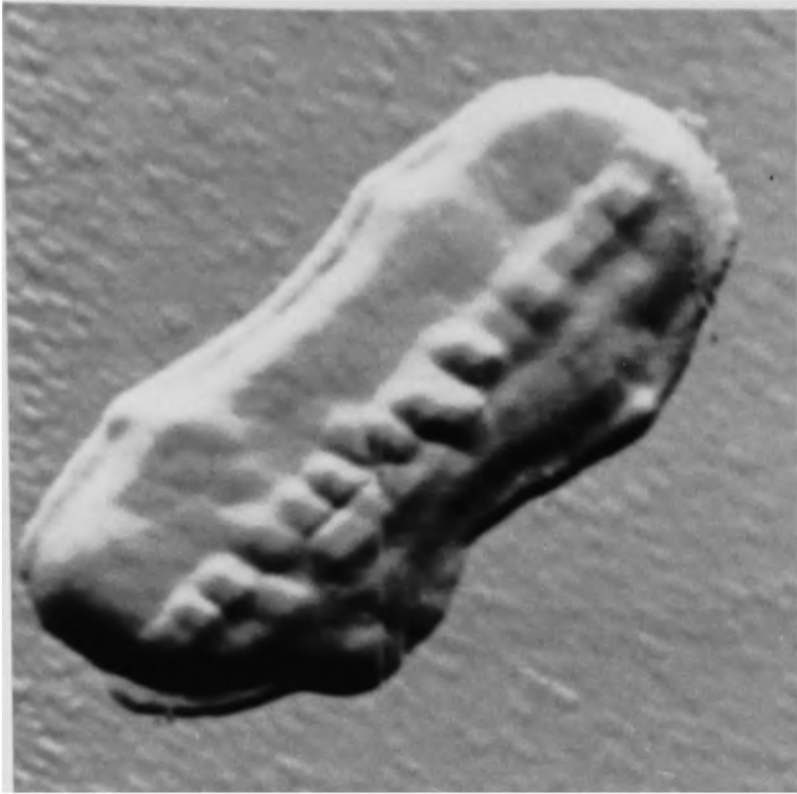


Plate 7.5a: Images of *Schizosaccharomyces pombe*, viewed with an AFM (top).
 MS - mitotic spindle.

Plate 7.5b: Image of a *Bacillus cereus*, viewed with an SEM (bottom).
 N - nucleus; E - exosporium.



amounts of phospholipase, which may kill small hosts such as insects, or lead to 'food poisoning' in larger mammals such as humans. A characteristic of particular importance is their extreme resistance to chemical and physical agents, specifically, heat. They normally are able to resist temperatures about 50°C higher than those which are sufficient to destroy their isolated components (such as enzymes etc.). This suggests that the spore is able somehow to impose a significant degree of heat resistance on its contents.

One practical consequence of this effect is the need to heat foods to temperatures in excess of 120°C prior to canning in order to sterilize any bacterial spores present. This is both costly in terms of time and energy and also frequently detrimental in terms of nutrition and 'taste'. Extensive NMR, light and electron microscope studies of the spores have yet to enable a satisfactory explanation of this dormancy process to be formulated, although there is evidence which suggests that the internal core of the spore is of particular importance. This is maintained in a dehydrated state by an enveloping cortex, consisting of a cross-linked polymer. The cortex is surrounded by a protein-rich enzyme resistant coat, beyond which there is a large, loose exosporium for which no function has ever been discovered. Up to 10% of the spore's dry weight consists of calcium dipicolinate (pyridine 2,6-dicarboxylate) which is known to be important in the maintenance of dormancy, although it is not known by what process.

A number of resists were exposed using the plasma generated by a tungsten target and a plasma to specimen distance of 6mm. A 100nm thick Si₃N₄ window was used, and the water window flux incident on the specimen was measured to be ~20mJ/cm². The image of a single spore in the resist, as viewed with an SEM, is shown in plate 7.5b; the core and surrounding coat are visible and there is a faint image of an exosporium. In the central core there are several structures which it is believed may be solid concentrations of calcium dipicolinate. If this is the case, then those hypotheses which propose extensive interactions of the compound with proteins and other macromolecules within the spores may have to be discarded. It is hoped that further investigations to be undertaken either with the Oxford or RAL microscopes will

confirm or invalidate this observation; mutant spores which contain no calcium dipicolinate will be viewed along with further samples of the normal types to enable comparisons to be made between their images.

7.5.4 *Chlamydomonas*

The single-celled organism *Chlamydomonas* is one of the many chlorophyte genera, the largest and most complex group of freshwater algae. Members of the species may be found in freshwater ponds and lakes, sewage ponds, marine and brackish water, agricultural soil, peat bogs and a large number of other habitats. A typical TEM micrograph of a *Chlamydomonas* is shown in plate 7.6 (kindly provided by Dr. Tom Ford of RHBNC). This thin section shows many internal components, the most important of which are labelled. Not present in this micrograph, however, are the two flagellum, which would be joined to the cell at the top right corner. In a living *Chlamydomonas*, the flagellum enable the cell to be motile and also play a part in the reproductive cycle.

To compare the representations of the cell obtained by TEM and SXCM, several exposures were made using the Oxford microscope, and the developed resists viewed with the AFM. Although the resultant images do not match the very high resolution apparent in the TEM micrograph, they do have the advantage of representing a living cell; for TEM, an extensive and elaborate specimen preparation procedure (including thin sectioning) had to be carried out. Plates 7.7 and 7.8 show the images obtained. A plasma to specimen distance of 6mm was used with a molybdenum target wire, and the water window flux incident on the specimen in each case was $\sim 10\text{mJ}/\text{cm}^2$. An uncoated, 100nm thick Si_3N_4 window was used in the specimen holder.

The flagella, which are just discernible under conventional light microscopy, may be clearly seen in plate 7.7, having a width of $\sim 500\text{nm}$. Plates 7.7 and 7.8 show the internal structure of a number of other *Chlamydomonae*, from which it can be seen that, apart from the presence of a thick cell wall, there appears to be little in common with the images obtained by TEM. As yet, the identification of the many internal structures has not proved possible although in plate 7.8, there is some suggestion that

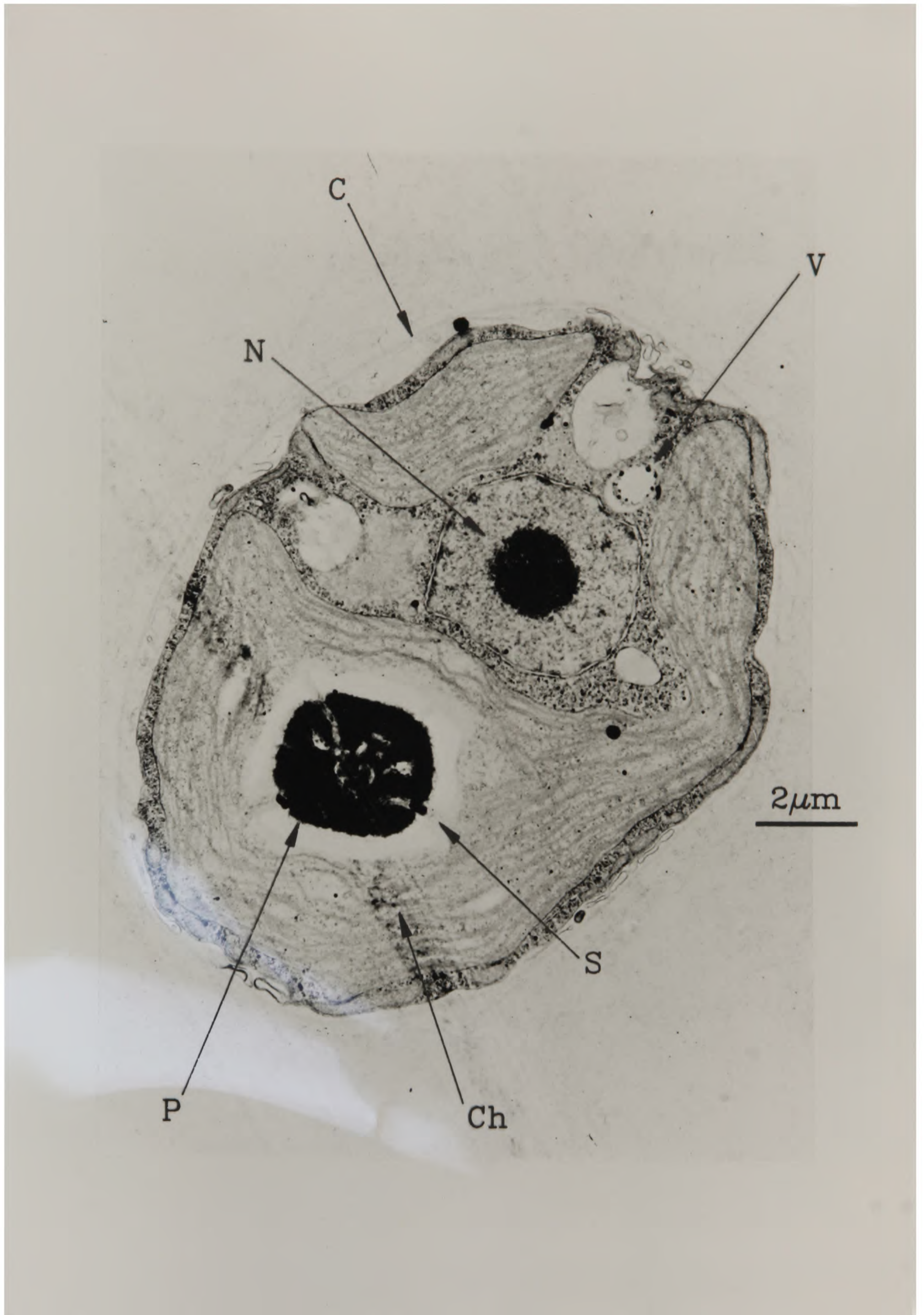
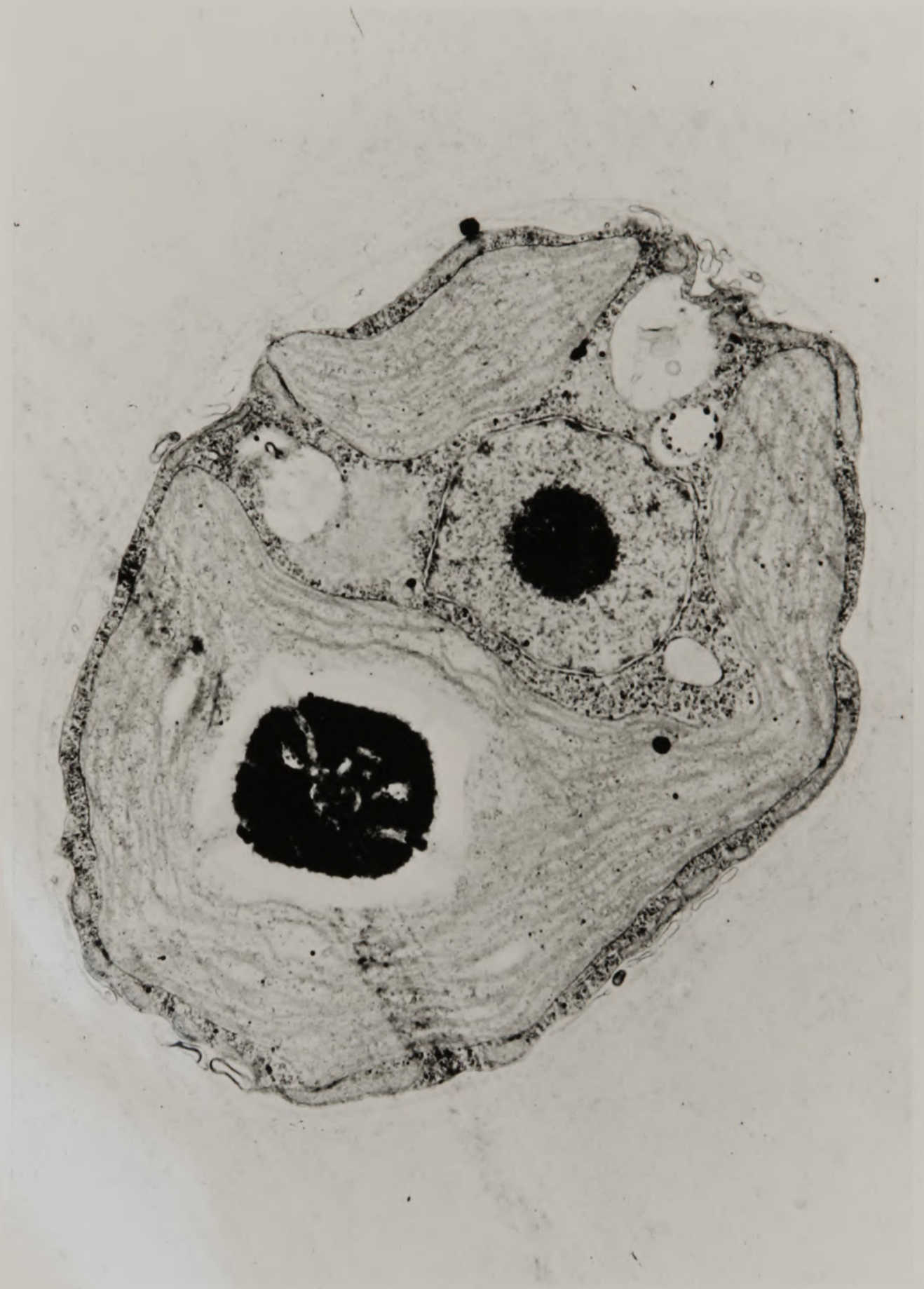
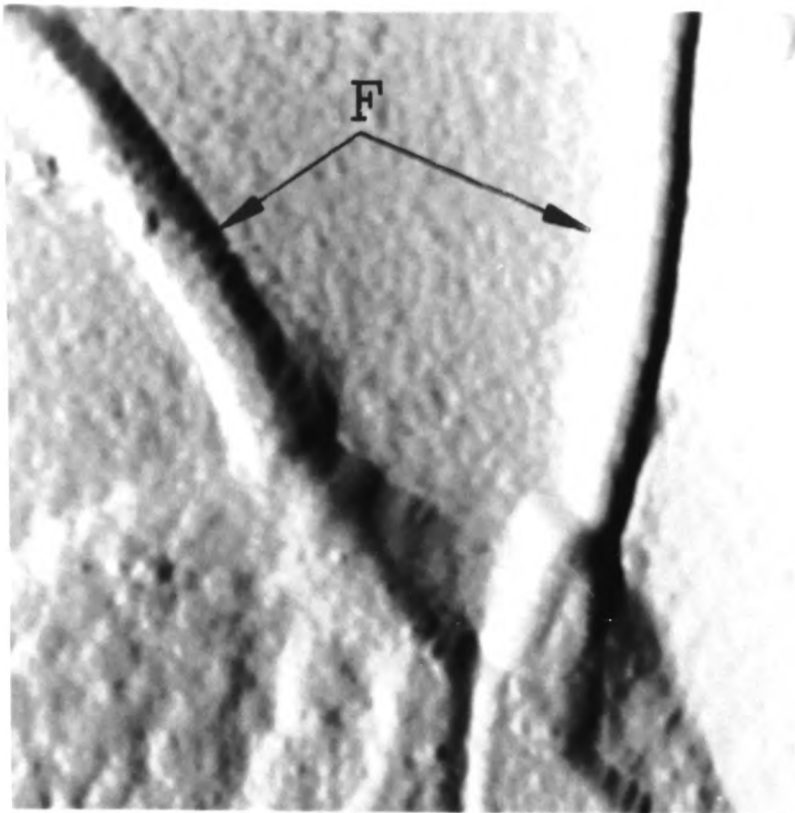
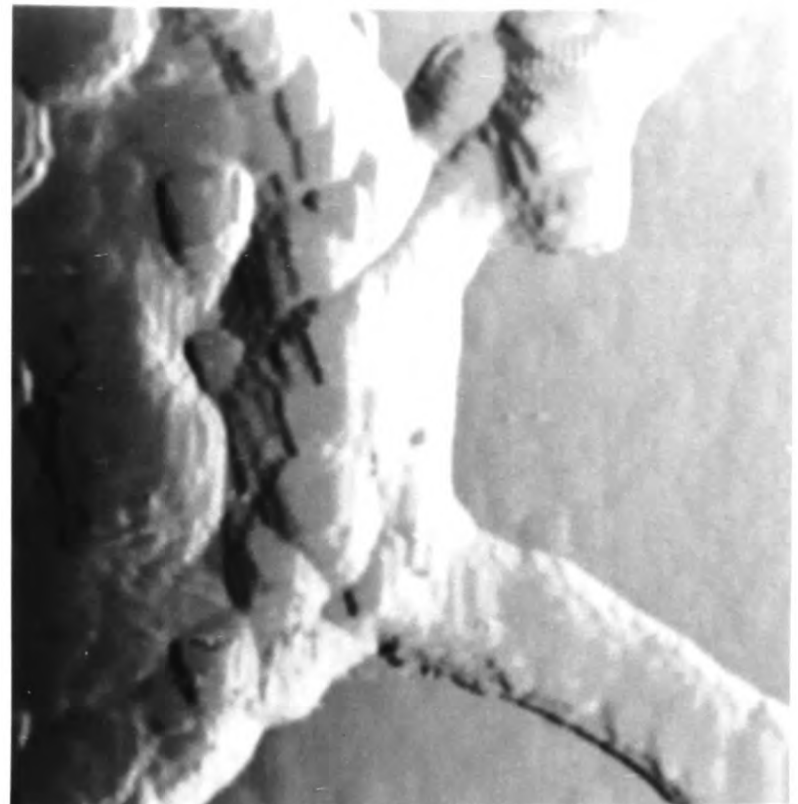


Plate 7.6: A TEM image of a thin section of *Chlamydomonas*, showing C - cell wall; Ch - chloroplast; N - nucleus; V - vacuole; P - pyrenoid; and S - starch granules.

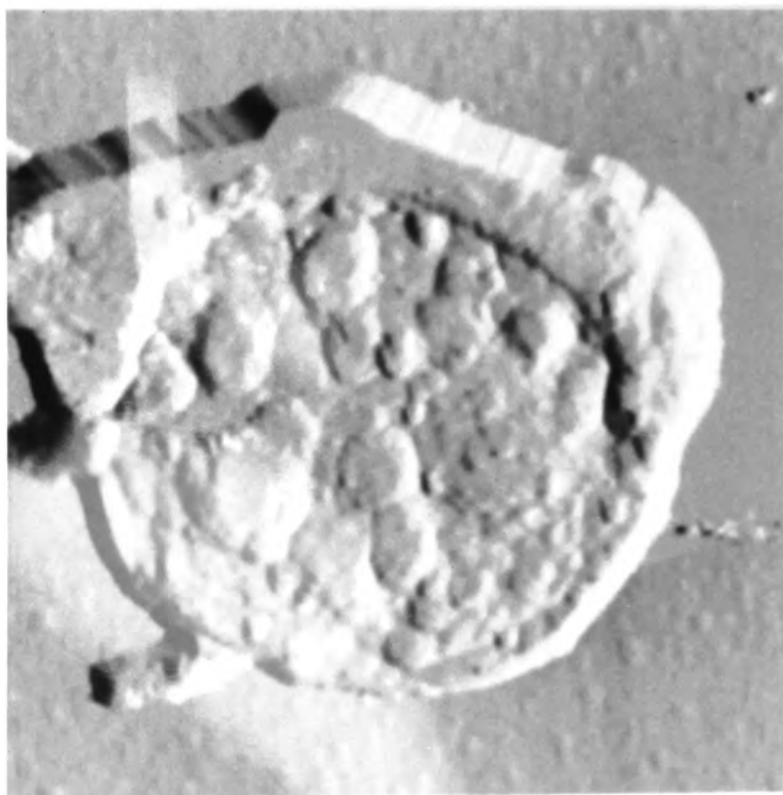




1μm



1μm

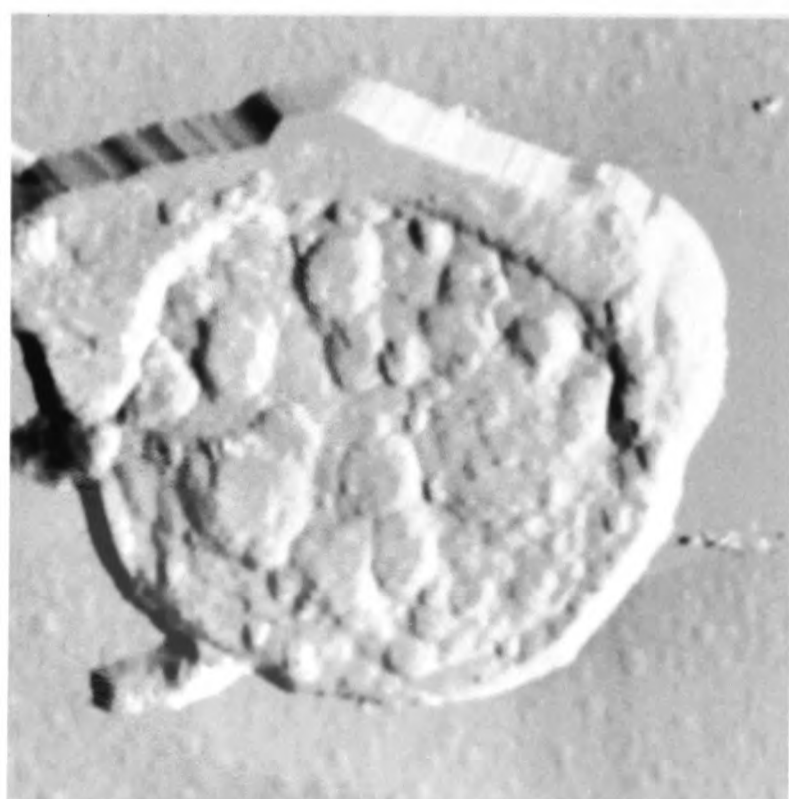
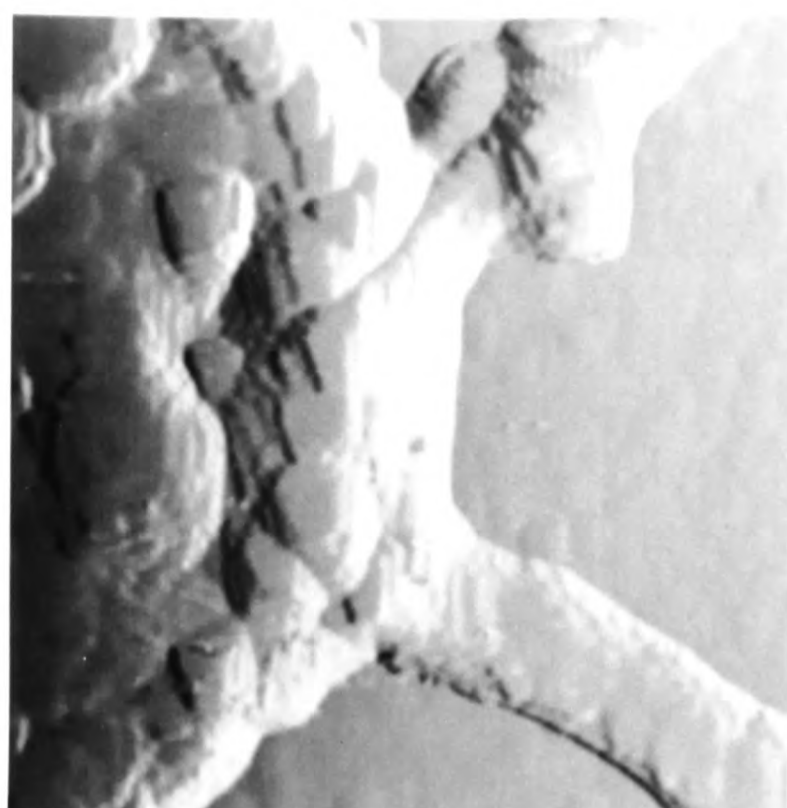
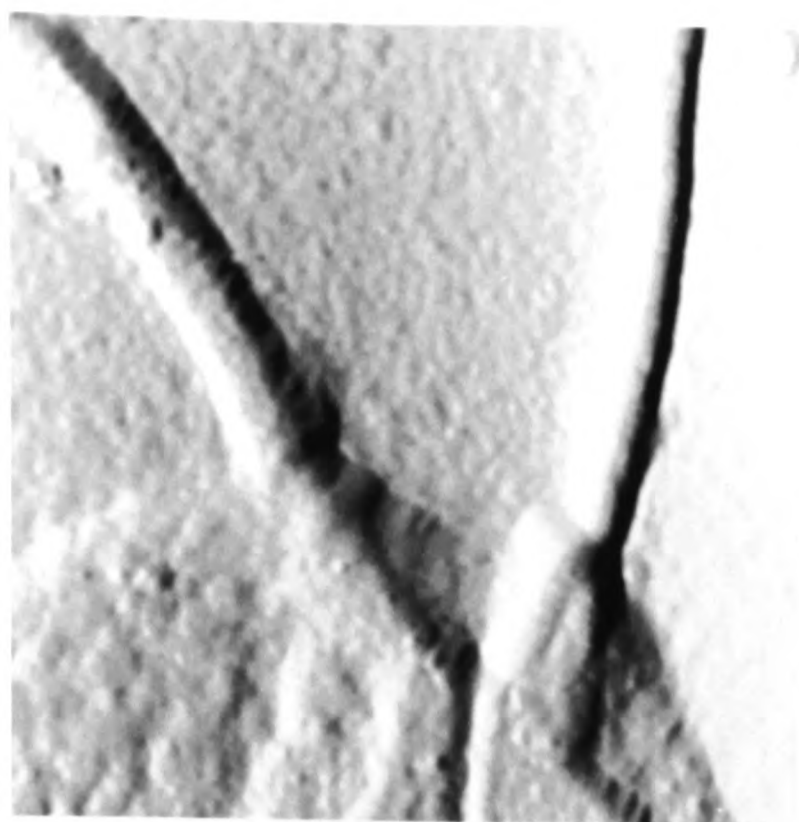


2μm



2μm

Plate 7.7: Soft X-ray contact microscope pictures of *Chlamydomonas* obtained with an AFM, showing flagellum (F) and the cell wall (C).



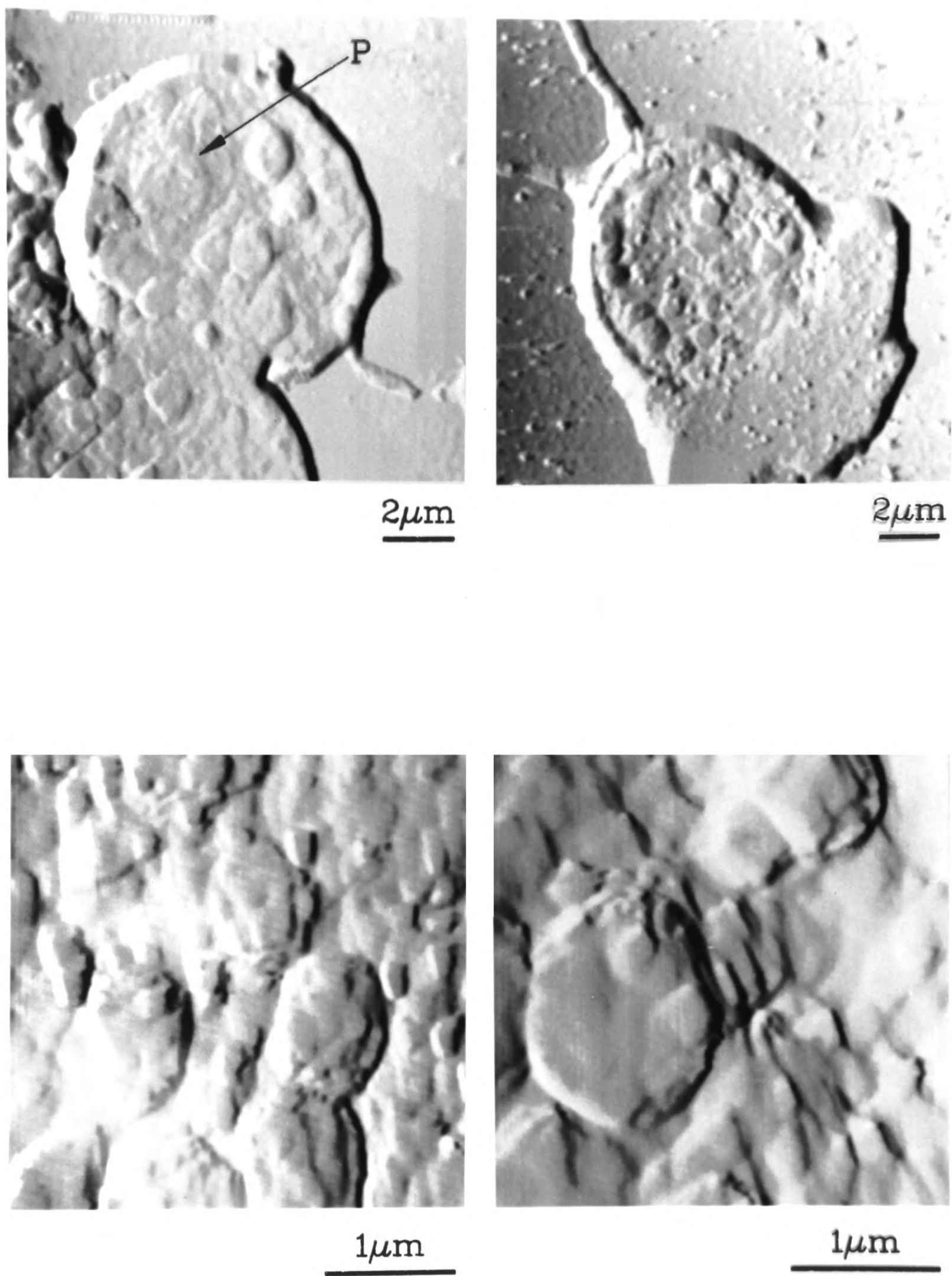
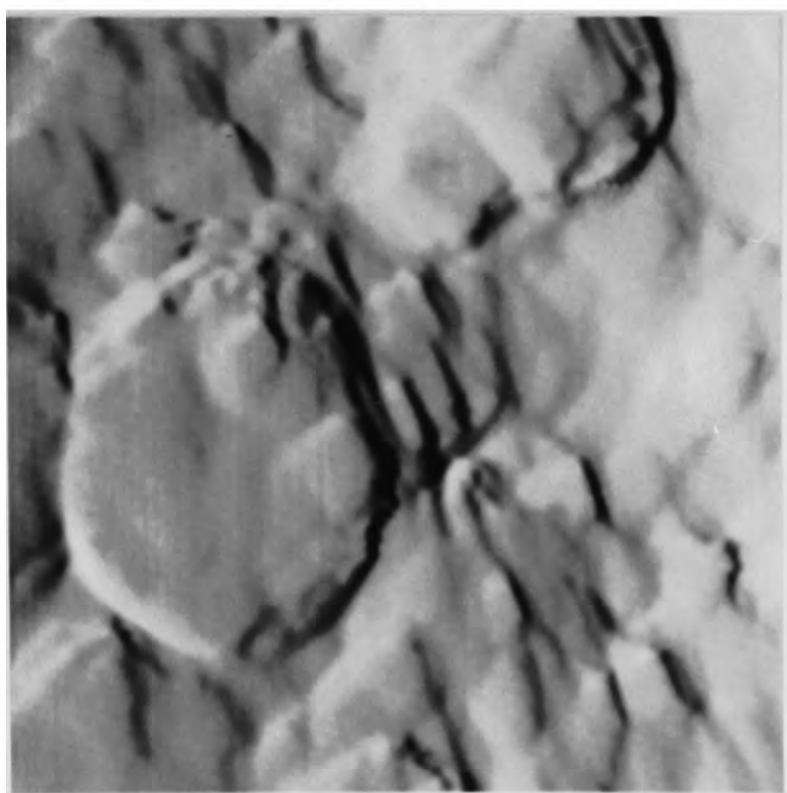
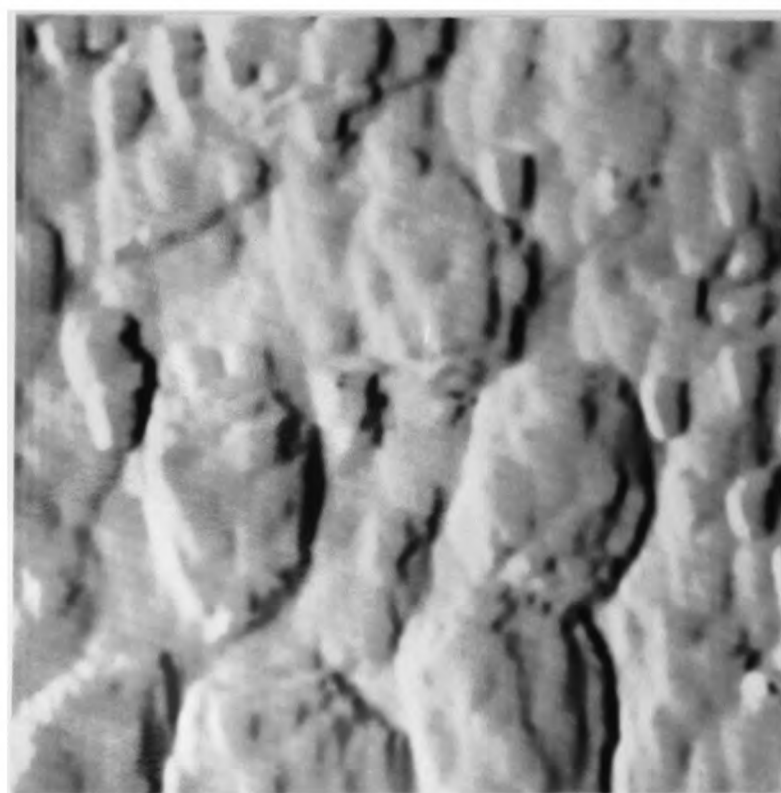


Plate 7.8: Soft X-ray contact microscope pictures of *Chlamydomonas* obtained with an AFM, possibly showing the pyrenoid (P).



the pyrenoid has been imaged. The presence of such a large number of spherical objects in all of the *Chlamydomonae* imaged with both the Oxford and RAL microscopes does suggest that there are further internal components in this organism which hitherto have not been observed by either conventional light microscopy (because of limited resolution) or by TEM (because of structural changes brought about by preparation techniques). Plate 7.8 shows higher magnification images of these internal bodies, and indicate that these themselves have some internal structures. (The near horizontal stripes in the image arise from electronic interference suffered by the AFM, which unfortunately had not been eliminated at the time of imaging.) Further imaging experiments are planned in an attempt to identify these intra-cellular components.

The 25-75% points on a number of different features shown in plate 7.8 (bottom) were measured, and a mean value of (39 ± 22) nm was obtained. The 25-75% points on the image of the flagella in plate 7.7 were also measured, and a value of 50nm obtained. While this is by no means an accurate estimation of the resolution obtained in the imaging process, it does provide some indication of the 'size' of object which could be seen in the developed resist.

7.6 FUTURE BIOLOGICAL INVESTIGATIONS

With the microscope system fully operational and readily available for imaging experiments, further contacts were made with members of groups in other departments. Interest was frequently shown in the imaging capabilities offered by the SXCM technique, and as a consequence, several projects were set up in which biological material supplied by these groups will be imaged with both the Oxford and RAL microscopes. This will enable images taken on the two systems to be compared, and if these initial images prove to be of interest, further biological studies will be undertaken in order to meet the requirements of those investigating the various different specimens.

7.6.1 Electroporation processes

Fibroblasts have already been viewed by SXCM by Skinner [1990] using

radiation of 18.2nm wavelength. However, work currently being undertaken in collaboration with Dr. R. Meldrum of the University of Birmingham School of Biochemistry may enable information about dynamic processes occurring within cells to be investigated. In particular, it is known that the application of a small electric shock to fibroblast cells in solution causes pores to temporarily form in the membrane. These pores enable large or negatively charged molecules such as pieces of DNA or proteins, which would not normally be able to pass through the cell membrane, to enter the cell. As yet, the precise nature of the formation and structure of these pores is not well understood.

Evidently, electron microscopy is totally unsuitable for the study of this dynamic process, while the resolution available from conventional light microscopy is too low for the pores to be observed. By employing SXCM however, it is hoped that, by synchronizing the application of a small electrical shock to the specimen with the production of the plasma, a series of images may be obtained from a number of different specimens to illustrate the temporal formation of these pores. Studies will be undertaken either on the Oxford or RAL microscope systems in the near future.

7.6.2 *Escherichia coli*

At the Department of Biochemistry, Oxford University, there is an ongoing programme of investigation into various strains of the bacterium *Escherichia coli*. In particular, a strain derived from a wild type of *Escherichia coli* by mutagenesis, which is dependent of the antibiotic erythromycin for growth, is being studied. At a sufficiently high temperature, growth appears to proceed normally, but at lower temperatures ($\sim 30^{\circ}\text{C}$), growth becomes erratic and the cells develop abnormal morphologies.

Since these bacteria are only a few micrometres in length and less than a micrometre wide, observation by light microscopy only provides a rough guide of any given cell's overall structure, making the differentiation between normal and abnormal morphologies particularly difficult. However, this type of specimen is an ideal subject for SXCM; it should be possible not only to differentiate between the various types,

but also to actually study the morphological abnormalities of the mutagen strains. It is planned to investigate these bacteria with the Oxford microscope within the next few months.

7.6.3 Chromosomes

Although hydrated, unfixed chromosomes have been imaged previously [Shinohara 1993], using a pulsed plasma source and the SXCM technique, the results obtained were not of sufficient quality to enable any meaningful biological interpretation to be made. Radiation damage studies have been performed by Williams [1993], but these have been on either freeze-dried or fixed specimens.

Samples of chromosomes, prepared by Dr. Brown and Dr. Porter of the Biochemistry Department of Oxford University will be imaged with both the Oxford and RAL microscopes in the near future to see whether the SXCM process will be of any use for the investigation of chromosomes, and specifically, the identification and classification of mutations. The lateral thickness of such specimens will be less than 50nm, and will therefore provide an excellent test of the ability of the SXCM technique to image biological objects which cannot be seen by any form of visible light microscopy.

7.7 SUMMARY

As may be seen from the images presented in this chapter, the Oxford X-ray microscope has been successfully used to image a number of different biological specimens. The exposed resists show detail at a resolution higher than would be obtained by conventional light microscopy (including confocal microscopy), and represent living specimens which have not undergone any form of preparation. In several cases, the images produced have shown features which were not expected to be present, and which may not have been previously observed. In these cases, further imaging will soon be undertaken in an attempt to identify these components. In addition, a number of further experiments are planned, in collaboration with workers in various biochemistry departments, and it is hoped that, in the near future, an

increasing number of such joint investigations will be instigated, thereby drawing the attention of workers in the biological sciences to the advantages and facilities offered by SXCM. In the longer term, this may lead to the greater availability and more widespread use of X-ray microscopy as an imaging tool for biological material.

REFERENCES

Abbe 1884

"Note on the proper definition of the amplifying power of a lens or lens system."
E. Abbe, *J. Roy. Microsc. Soc.* 4(1), p348.

Alaterre 1986

"X-ray conversion efficiency as a function of atomic number for 0.26 μ m laser irradiated targets."
P. Alaterre et al, *Phys. Rev. A* 34(5), pp4184-4194.

Aschenbach 1985

"X-ray telescopes."
B. Aschenbach, *Rep. Prog. Phys.* 48, pp579-629.

Aschenbach 1987

"Grazing incidence X-ray reflectivity of gold and iridium coated flat mirrors."
B. Aschenbach et al, *Proc. SPIE Conf. 'Grazing incidence optics for astronomical and laboratory applications'* 830, pp284-287.

Aschenbach 1988

"Design, construction and performance of the ROSAT high resolution X-ray mirror assembly."
B. Aschenbach, *Appl. Opt.* 27(8), pp1404-1413.

Bearden 1983

"X-ray atomic energy levels."
J. A. Bearden and A. F. Burr, *Handbook of Chemistry and Physics 64th Edition*,
Ed. R. C. Weast, Publ. CRC Press Florida, ppE171-E176.

Chauvineau 1989

"Multilayers for X-UV optics."
J. P. Chauvineau, *Proc. SPIE Conf. 'X-ray instrumentation'* 1140, pp440-447.

Cheng 1986

"Soft X-ray contact microscopy."
P. C. Cheng et al, *Nucl. Instrum. Meth. Phys. Res.* A246, pp668-674.

Compton 1935

X-rays in theory and experiment (2nd. edition).
A. H. Compton and S. K. Allison, Publ. Van Nostrand.

Cotton 1990

Pulsed UV gas lasers and their applications.
R. A. Cotton, *DPhil. Thesis*, University of Oxford.

Cotton 1992a

"Bringing soft X-ray contact microscopy to the biologist."
R. A. Cotton and J. H. Fletcher, *Proc. RMS* 27(2), pp77-80.

Cotton 1992b

"Using soft X-rays from laser generated plasmas for the contact imaging of living biological specimens."
R. A. Cotton et al, *Int. Conf. on X-ray optics and microanalysis XIII*.

Cotton 1993

"Atomic force microscopy employed as the final imaging stage for soft X-ray contact microscopy."
R. A. Cotton et al, *Proc. SPIE Conf. 'Soft X-ray microscopy'* 1741, pp204-212.

Daido 1992

"Spatial coherence of a repetitive laser plasma point X-ray source in the water window spectral region."
H. Daido et al, *Appl. Phys. Lett.* 60(10), pp1155-1157.

Da Silva 1992

"Demonstration of X-ray microscopy with an X-ray laser operating near the carbon K edge."
L. B. Da Silva et al, *Opt. Lett.* 17(10), pp754-756.

de Korte 1988

"High throughput replica optics."
P. A. J. de Korte, *Appl. Opt.* 27(8), pp1440-1446.

Dinev 1979

"X-ray emission from a laser irradiated target in the presence of a high electric field."
S. G. Dinev et al, *Opt. Comm.* 30(2), pp219-223.

Dupouy 1966

G. Dupouy et al, *J. Microsc. Spectrosc. Electron.* **5**, p655.

Eidmann 1986

"Absolutely measured X-ray spectra from laser plasmas with targets of different elements."

K. Eidmann and T. Kishimoto, *Appl. Phys. Lett.* **49**(7), pp377-378.

Fabbro 1985

"Planar laser driven ablation: Effect of inhibited electron thermal conduction."

R. Fabbro et al, *Phys. Fluids* **28**(5), pp1463-1481.

Faldon 1987

The production and testing of a bent glass relay optic for soft X-ray use.

M. Faldon, *MSc. Thesis*, Imperial College, University of London.

Farkas 1977

"Picosecond laser plasma creation in the presence of high electrostatic field on the surface of metals."

Gy. Farkas and Z. Gy. Horvath, *Opt. Comm.* **21**(3), pp408-410.

Fedosejevs 1987

"Characterization of X-ray production from krypton fluoride laser produced plasma."

R. Fedosejevs et al, *Proc. SPIE Conf. 'X-rays from laser plasmas'* **831**, pp66-72.

Fletcher 1993

"Soft X-ray contact microscopy using laser generated plasma sources."

J. H. Fletcher et al, *Proc. SPIE Conf. 'Soft X-ray microscopy'* **1741**, pp142-153.

Folkard 1992

"Radiation damage to cells by ultrasoft X-rays."

M. Folkard, *'X-ray Microscopy III', Springer Series in Optical Sciences* **67**, Eds.

A. Michette et al, Publ. Springer-Verlag Berlin, pp306-312.

Fox 1964

"Modes in a maser interferometer with curved mirrors."

A. G. Fox and T. Li, *Quant. Electron. Proc. Third Int. Congress Paris*, Eds. P. Grivet and N. Bloembergen, Publ. Columbia University Press New York, pp1263-1270.

Freiberg 1972

"An experimental study of unstable confocal CO₂ resonators."

R. J. Freiberg et al, *IEEE J. Quant. Electron.* QE8(12), pp882-892.

Gerritsen 1986

"Laser generated plasma as soft X-ray source."

H. C. Gerritsen et al, *J. Appl. Phys.* 59(7), pp2337-2344.

Gobbi 1984

"A novel unstable resonator configuration with a self filtering aperture."

P. G. Gobbi and G. C. Reali, *Opt. Comm.* 52(3), pp195-198.

Gobbi 1985

"Novel unstable resonator configuration with a self filtering aperture: experimental characterization of the Nd:YAG loaded cavity."

P. G. Gobbi et al, *Appl. Opt.* 24(1), pp26-33.

Goby 1913

"Une application nouvelle des rayons X: la microradiographie."

P. Goby, *CR Hebd. Seances Acad. Sci. Paris* 156, pp686-688.

Gorenstein 1988

"High throughput X-ray optics: an overview."

P. Gorenstein, *Appl. Opt.* 27(8), pp1433-1439.

Green 1961

"The efficiency of production of characteristic X-radiation in thick targets of a pure element."

M. Green and V. E. Cosslett, *Proc. Phys. Soc.* 78(2), pp1206-1214.

Guttmann 1993

"X-ray microscopy studies with the Göttingen X-ray microscopes."

P. Guttmann et al, *Proc. SPIE Conf. 'Soft X-ray microscopy'* 1741, pp52-61.

Haelbich 1984

"Synchrotron radiation X-ray lithography."

R. P. Haelbich et al, *Nucl. Inst. Meth. Phys. Res.* **222**, pp291-301.

Hall 1991

"Confocal microscopy - the basics explained."

A. Hall et al, *Proc. RMS* **26**(2), pp63-70.

Hagemann 1975

"Optical constants from the far infrared to the X-ray region: Mg, Al, Cu, Ag, Au, Bi, C and Al₂O₃."

H. J. Hagemann et al, *J. Opt. Soc. Am.* **65**(6), pp742-744.

Henke 1982

"Low energy X-ray interaction coefficients."

B. L. Henke et al, *At. Data Nucl. Data Tables* **27**(1), pp1-144.

Henke 1984

"Low energy X-ray response of photographic films. II Experimental characterization."

B. L. Henke et al, *J. Opt. Soc. Am. B* **1**(6), pp828-849.

Hirst 1987a

"Spatially resolved gain measurements in a discharge pumped KrF laser amplifier."

G. J. Hirst et al, *J. Appl. Phys.* **61**(7), pp2438-2444.

Hirst 1987b

Ionic species in gas lasers.

G. J. Hirst, *DPhil. Thesis*, University of Oxford.

Hontzopoulos 1988

"Enhancement of ultraviolet laser plasma emission produced in a strong static electric field."

E. Hontzopoulos et al, *Opt. Comm.* **67**(2), pp124-128.

Horowitz 1972

"A scanning X-ray microscope using synchrotron radiation."

P. Horowitz and J. A. Howell, *Science* **178**, pp608-611.

Hughes 1979

"An introduction to the absorption of laser light in plasmas."

T. P. Hughes, *Proc. Scottish University Summer School in Physics 'Laser plasma interactions'* 20, pp1-90.

Hui 1974

"Electron diffraction of wet phospholipid bilayers."

S. W. Hui et al, *Proc. Nat. Acad. Sci. USA* 71(12), pp5068-5072.

Jacobsen 1988

X-ray holographic microscopy of biological specimens using an undulator.

C. Jacobsen, *PhD. Dissertation*, State University of New York.

Jacobsen 1991

"Diffraction limited imaging in a scanning transmission X-ray microscope."

C. Jacobsen et al, *Opt. Comm.* 86(3-4), pp351-364.

James 1979

"High magnification unstable resonator excimer laser."

D. James et al, *IEEE J. Quant. Electron.* QE15(5), pp335-336.

Jianwen 1990

"Experimental study of positive and negative branch unstable resonators applied to a XeCl laser."

C. Jianwen et al, *J. Mod. Opt.* 37(1), pp75-83.

Kado 1991

"Development of a Schwarzschild type X-ray microscope."

M. Kado et al, *Opt. Lett.* 16(2), pp109-111.

Kagoshima 1992

"Present status and future plan of soft X-ray microscopy at the Photon Factory."

Y. Kagoshima et al, *Rev. Sci. Instrum.* 63(1), pp605-608.

Kearsley 1979

"A novel pre-ionization technique for discharge excited rare gas halide lasers."

A. J. Kearsley et al, *Opt. Comm.* 31(2), p181-184.

Kearsley 1980

Gas laser efficiency.

A. J. Kearsley, *DPhil. Thesis*, University of Oxford.

Kinjo 1992

"Comparative study by soft X-ray contact microscopy of the images of human chromosomes treated with various conditions."

Y. Kinjo et al, '*X-ray Microscopy III*', *Springer Series in Optical Sciences* 67, Eds. A. Michette et al, Publ. Springer-Verlag Berlin, pp442-446.

Kirz 1985

"Soft X-ray microscopes."

J. Kirz and H. Rarback, *Rev. Sci. Instrum.* 56(1), pp1-13.

Kirz 1992

"Soft X-ray microscopy with coherent X-rays."

J. Kirz et al, *Rev. Sci. Instrum.* 63(1), pp557-563.

Kühnle 1988

"X-ray production by irradiation of solid targets with sub-picosecond excimer laser pulses."

G. Kühnle et al, *Appl. Phys. B* 47, pp361-366.

Letokhov 1970

"Dynamics of a Q-switched laser."

V. S. Letokhov and A. F. Suchkov, *Proc. P. N. Lebedev Phys. Inst.* 43, pp155-170.

Lindaas 1993

"Development of a linear scanning force microscope for X-ray Gabor hologram readout."

S. Lindaas et al, *Proc. SPIE Conf. 'Soft X-ray microscopy'* 1741, pp213-222.

London 1989

"Wavelength choice for soft X-ray laser holography of biological samples."

R. A. London et al, *Appl. Opt.* 28(15), pp3397-3404.

McCown 1988

"Enhancements in the output energy of a KrF oscillator."

A. W. McCown and J. A. B. Godard, *J. Appl. Phys.* 64(6), pp2879-2884.

McKee 1988

"Performance comparison of positive branch unstable resonator cavities for excimer lasers."

T. J. McKee and G. T. Boyd, *Appl. Opt.* 27(9), pp1840-1843.

Maruyama 1992

"Characteristics of high power excimer laser master oscillator power amplifier system for dye laser pumping."

Y. Maruyama et al, *Opt. Comm.* 87, pp105-108.

Masui 1993

"Evaluation of the Schwarzschild X-ray microscope using the compact SR ring AURORA."

S. Masui et al, *Proc. SPIE Conf. 'Soft X-ray microscopy'* 1741, pp94-103.

Mead 1981

"Laser plasma interactions at $0.53\mu\text{m}$ for disk targets of varying Z."

W. C. Mead et al, *Phys. Rev. Lett.* 47(18), pp1289-1292.

Michette 1988a

"A laser generated plasma source for X-ray lithography and VLSI."

A. G. Michette et al, *J. Phys. E: Sci. Instrum.* 21, pp959-965.

Michette 1988b

"X-ray microscopy."

A. G. Michette, *Rep. Prog. Phys.* 51, pp1525-1606.

Michette 1992

X-ray microscopy III.

Eds. A. Michette et al, *Springer Series in Optical Sciences* 67, Publ. Springer-Verlag Berlin.

Mochizuki 1986

"Atomic number dependence of soft X-ray emission from various targets irradiated by a $0.53\mu\text{m}$ wavelength laser."

T. Mochizuki et al, *Phys. Rev. A* 33(1), pp525-539.

Morrison 1992

"Recent progress with the King's College scanning transmission X-ray microscope."

G. R. Morrison et al, '*X-ray Microscopy III*', *Springer Series in Optical Sciences* 67, Eds. A. Michette et al, Publ. Springer-Verlag Berlin, pp139-142.

Nagel 1984

"Repetitively pulsed plasma soft X-ray source."

D. J. Nagel et al, *Appl. Opt.* 23(9), pp1428-1433.

Nicholas 1982

"The development of fluid codes for the laser compression of plasmas."

D. J. Nicholas, *Proc. Scottish University Summer School in Physics 'Laser plasma interactions 2'* 24, pp129-183.

Niemann 1992

"X-ray microscopy with the Göttingen scanning X-ray microscope at 2.4nm."

B. Niemann, '*X-ray Microscopy III*', *Springer Series in Optical Sciences* 67, Eds. A. Michette et al, Publ. Springer-Verlag Berlin, pp143-146.

O'Neill 1987

"Plasma X-ray sources for lithography generated by 0.5J KrF laser."

F. O'Neill et al, *Proc. SPIE Conf. 'X-rays from laser plasmas'* 831, pp230-236.

Polak 1987

"First images with the soft X-ray image converting microscope at LURE."

F. Polak and S. Lowenthal, '*X-ray microscopy*', *Springer Series in Optical Sciences* 43, Eds. G. Schmahl and D. Rudolph, Publ. Springer-Verlag Berlin, pp251-260.

Popil 1987

"Measurement of KrF laser-plasma X-ray radiation from targets with various atomic numbers."

R. Popil et al, *Phys. Rev. A* 35(9), pp3874-3882.

Present 1958

Kinetic theory of gases.

R. D. Present, *International Series in Practical and Applied Physics*, Publ. McGraw-Hill New York.

Rogoyski 1989

"Characterization of soft X-ray emission in the water window from a KrF laser generated plasma."

A. M. Rogoyski et al, *RAL annual report of the laser facility RAL-89-045*, pp366-368.

Rosser 1985

"Soft X-ray contact microscopy using a laser produced plasma X-ray source."

R. J. Rosser et al, *RAL annual report of the laser facility RAL-85-047*, ppA4.12-A4.16.

Rothman 1992

"Following protein transport with the high resolution X-ray microscope."

S. S. Rothman et al, '*X-ray Microscopy III*', *Springer Series in Optical Sciences* 67, Eds. A. Michette et al, Publ. Springer-Verlag Berlin, pp373-383.

Sayre 1987

X-ray microscopy II.

Eds. D. Sayre et al, *Springer Series in Optical Sciences* 56, Publ. Springer-Verlag Berlin.

Schmahl 1984

X-ray microscopy.

Eds. G. Schmahl and D. Rudolph, *Springer Series in Optical Sciences* 43, Publ. Springer-Verlag Berlin.

Schmahl 1992

"A laboratory X-ray microscope with a plasma X-ray source."

G. Schmahl et al, '*X-ray Microscopy III*', *Springer Series in Optical Sciences* 67, Eds. A. Michette et al, Publ. Springer-Verlag Berlin, pp66-69.

Schneider 1992

"Environmental chamber for X-ray imaging of wet biological specimens."

G. Schneider and B. Niemann, '*X-ray Microscopy III*', *Springer Series in Optical Sciences* 67, Eds. A. Michette et al, Publ. Springer-Verlag Berlin, pp350-354.

Shaw 1983

"The bi-directional amplifier in the constant intensity approximation and its application to KrF lasers."

M. J. Shaw, *Appl. Phys. B* **30**, pp5-10.

Shinohara 1993

"Observation of human chromosome fibres in a water layer by laser plasma X-ray contact microscopy."

K. Shinohara et al, *Proc. SPIE Conf. 'Soft X-ray microscopy'* **1741**, pp386-392.

Siegman 1965

"Unstable optical resonators for laser applications."

A. E. Siegman, *Proc. IEEE* **53**, pp277-287.

Siegman 1967

"Modes in unstable optical resonators and optical waveguides."

A. E. Siegman and R. Arrathoon, *IEEE J. Quant. Electron.* **QE3**(4), pp156-163.

Sigel 1987

"Laser generated soft X-rays."

R. Sigel et al, *Proc. SPIE Conf. 'X-rays from laser plasmas'* **831**, pp73-83.

Skinner 1990

"Contact microscopy with a soft X-ray laser."

C. H. Skinner et al, *J. Microsc.* **159**(1), pp51-60.

Spiller 1976

"X-ray microscopy of biological objects with carbon K α and with synchrotron radiation."

E. Spiller et al, *Science* **191**, pp1172-1174.

Spiller 1977

"X-ray lithography."

E. Spiller and R. Feder, *'X-ray Optics', Topics in Applied Physics* **22**, Ed. H. J. Queisser, Publ. Springer-Verlag Berlin, pp35-92.

Spiller 1980

"Controlled fabrication of multilayer soft X-ray mirrors."

E. Spiller et al, *Appl. Phys. Lett.* **37**(11), pp1048-1050.

Spiller 1983

"Soft X-ray optics and microscopy."

E. Spiller, *Handbook of synchrotron radiation* 1, Ed. E. E. Koch, Publ. North-Holland, pp1091-1129.

Spitzer 1953

"Transport phenomena in a completely ionized gas."

L. Spitzer and R. Härm, *Phys. Rev.* **89**(5), pp977-981.

Spitzer 1962

Physics of fully ionized gases.

L. Spitzer, *Interscience Tracts on Physics and Astronomy* 3, Publ. Interscience Publishers Inc. New York.

Stead 1993

"Visualisation of the effects of electron microscopy fixatives on the structure of hydrated epidermal hairs of tomato (*Lycopersicum peruvianum*) as revealed by soft X-ray contact microscopy."

A. D. Stead et al, *Proc. SPIE Conf. 'Soft X-ray microscopy'* **1741**, pp.351-362.

Suzuki 1992

"Hard X-ray microprobe with total reflection mirrors."

Y. Suzuki and F. Uchida, *Rev. Sci. Instrum.* **63**(1), pp578-581.

Tomie 1991

"Three dimensional readout of flash X-ray images of living sperm in water by atomic force microscopy."

T. Tomie et al, *Science* **252**, pp691-693.

Tomie 1993

"Flash contact X-ray microscopy of biological specimen in water."

T. Tomie et al, *Proc. SPIE Conf. 'Soft X-ray microscopy'* **1741**, pp118-128.

Trail 1989

"Compact scanning soft X-ray microscope using a laser produced plasma source and normal incidence multilayer mirrors."

J. A. Trail and R. L. Byer, *Opt. Lett.* **14**(11), pp539-541.

Turcu 1987

"Calibration of a KrF laser plasma source for X-ray microscopy applications."

I. C. E. Turcu et al, *Proc. SPIE Conf. 'X-rays from laser plasmas'* **831**, pp211-216.

Turcu 1992

"High repetition rate laser plasma X-ray source for microscopy."

I. C. E. Turcu et al, '*X-ray Microscopy III*', *Springer Series in Optical Sciences* **67**, Eds. A. Michette et al, Publ. Springer-Verlag Berlin, pp54-57.

Watanabe 1992

"Observation of wet biological specimen by soft X-ray microscope with zone plates at UVSOR."

N. Watanabe et al, *Jpn. J. Appl. Phys.* **31**(2,11A), ppL1571-L1573.

Williams 1993

"Radiation damage to chromosomes in the scanning transmission X-ray microscope."

S. Williams et al, *Proc. SPIE Conf. 'Soft X-ray microscopy'* **1741**, pp318-324.

Winick 1987

"Synchrotron radiation."

H. Winick, *Sci. America* **257**(5), pp72-81.

Wolter 1952a

"Spiegelsysteme streifenden Einfalls als abbildende Optiken für Röntgenstrahlen."

H. Wolter, *Ann. Phys.* **10**(1-2), pp94-114.

Wolter 1952b

"Verallgemeinerte Schwarzschildsche Spiegelsysteme streifender Reflexion als Optiken für Röntgenstrahlen."

H. Wolter, *Ann. Phys.* **10**(4-5), pp286-295.

Xu 1991

"Normal incidence multilayer mirrors for the wavelength range 2.3 to 4.6nm."

S. Xu and B. L. Evans, *J. Mod. Opt.* **38**(8), pp1631-1654.

Zeng 1991

"Water window X-ray source produced by a slab glass laser."

G. Zeng et al, *J. Appl. Phys.* **69**(11), pp7460-7464.

ERRATA

- Page 14, 7th. line of section 2.3.3: remove ‘(commonly a CCD)’.
- Page 16, 1st. line: ‘region in’ to ‘region’.
- Page 17, 8th. line: remove ‘CCD’.
- Page 18: ‘2.5.2 Contact microscopy’ to ‘2.5.3 Contact microscopy’.
- Page 31, 10th. line: ‘~20nm’ to ‘~200nm’.
- Page 68, 8th. line: ‘pre-ionisating’ to ‘pre-ionizing’.
- Page 115, 1st. line of section 5.4: ‘spectra’ to ‘spectrum’.
- Page 139, 3rd. line: ‘angle’ to ‘solid angle’.
- Page 182: equation [6.46] to ‘ $d_{1/e} = \lambda/4\pi\beta$ ’ and line 17: ‘4nm’ to ‘34nm’.

Target material	Laser $\lambda(\text{nm})$	Intensity (W/cm^2)	Energy range (eV)	η (%)	Reference
Carbon	248	1×10^{14}	282-539	8	Present work
Titanium	248	1×10^{14}	282-539	10	Present work
Molybdenum	248	1×10^{14}	282-539	19	Present work
Tungsten	248	1×10^{14}	282-539	35	Present work

Table 5.7: Comparison of conversion efficiencies obtained here with those from other laser systems.

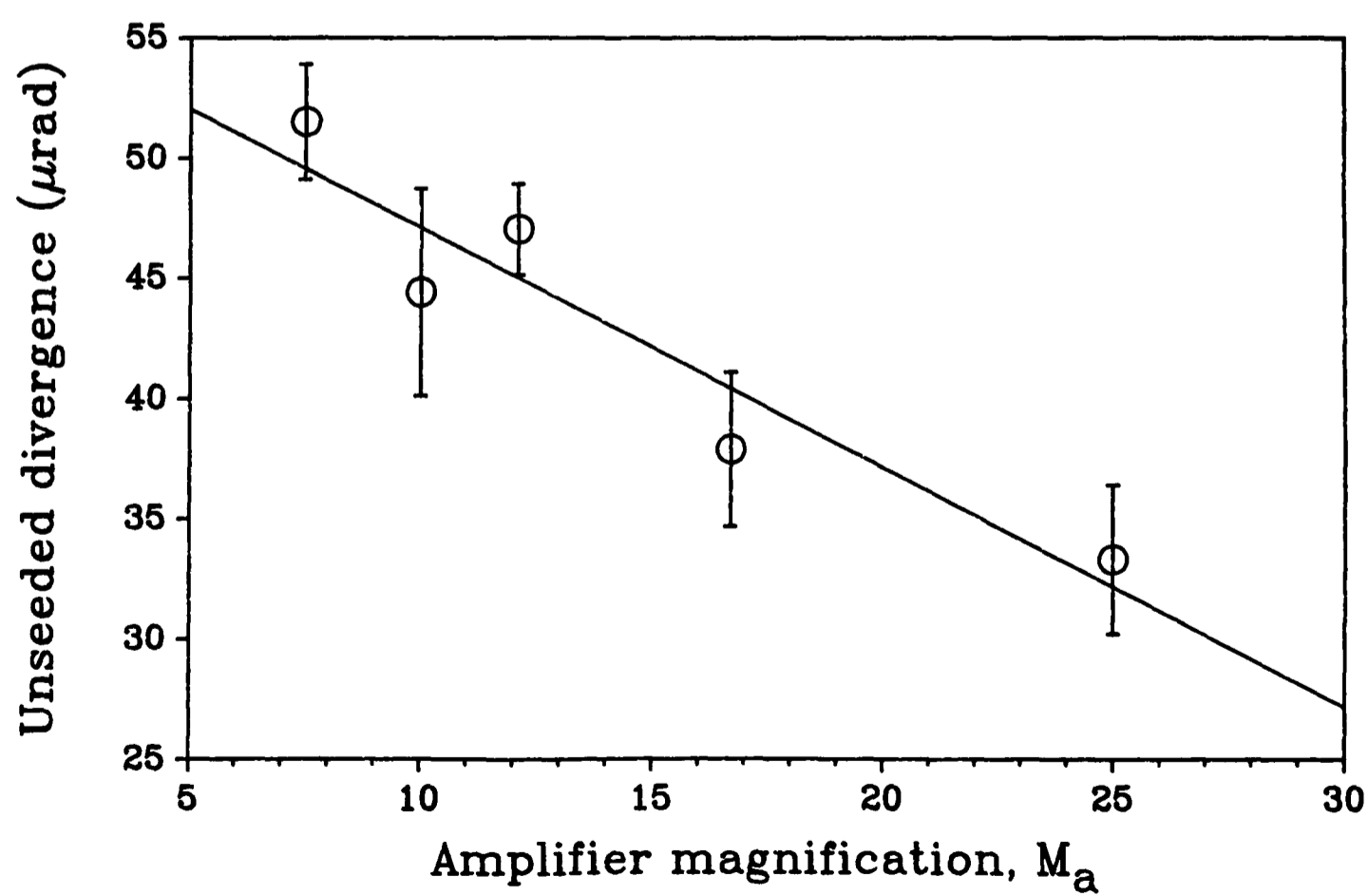


Figure 4.24: Divergences obtained from the various unseeded cavity arrangements.

